UNIVERSITY OF CORDOBA

THESIS

HYDRAULIC MODELLING OF SUSPENDED AND BED-LOAD TRANSPORT IN EROSIVE FLOWS

FRANCISCO NICOLÁS CANTERO CHINCHILLA

DEPARTMENT OF AGRONOMY

Córdoba, Spain

2016

Advisors

OSCAR CASTRO ORGAZ

JOSÉ LUÍS AYUSO MUÑOZ

TITULO: *Hydraulic modelling of suspended and bed-load transport in erosive flows*

AUTOR: *Francisco Nicolás Cantero Chinchilla*

Campus de Rabanales
Ctra. Nacional IV, Km. 396 A
14071 Córdoba

www.uco.es/publicaciones
publicaciones@uco.es

Advisors' Report

TÍTULO DE LA TESIS: Hydraulic modelling of suspended and bed-load transport in erosive flows

DOCTORANDO/A: Francisco Nicolás Cantero Chinchilla

INFORME RAZONADO DEL/DE LOS DIRECTOR/ES DE LA TESIS
(se hará mención a la evolución y desarrollo de la tesis, así como a trabajos y publicaciones derivados de la misma).

Oscar Castro Orgaz y José Luis Ayuso Muñoz, profesor contratado Ramón y Cajal del Departamento de Agronomía, y Catedrático del Departamento de Ingeniería Rural, de la Universidad de Córdoba, como directores de la tesis doctoral del alumno del Programa de Doctorado "Dinámica de Flujos Bioqeoquímicos y su Aplicación", Francisco Nicolás Cantero Chinchilla,

INFORMAN,

Que el doctorando ha cubierto los objetivos marcados en la tesis, estudiando el uso de modelos promediados verticalmente para la simulación de flujos con sedimento suspendido, y lecho móvil, mediante la inclusión de hipótesis mas avanzadas para la caracterización de la estructura vertical del flujo. En concretó, se han estudiado diversos casos de gran importancia en hidráulica fluvial, como el flujo en canales de sección compuesta, típica en problemas de inundaciones, así como la generación de peligrosas ondas de rotura de embalses, tanto sobre lecho rígido, como sobre lecho erosivo, lo cual da lugar a flujos geomórficos agua-sedimento. Para el desarrollo de los trabajos ha sido necesario el uso de técnicas avanzadas propias de la mecánica de fluidos, desarrollándose, como resultado principal, una serie de códigos numéricos con solucionas avanzadas, novedosas, y eficientes, a los problemas tratados. Prueba de la calidad, e impacto científico-tecnológico a nivel internacional, de las investigaciones realizadas, es la publicación de la totalidad de los trabajos de la tesis en forma de 5 artículos científicos en revistas indexadas Q1.

Por todo ello, se autoriza la presentación de la tesis doctoral.

Córdoba, 7 de junio de 2016

Firma del/de los director/es

Fdo.: Oscar Castro Orgaz

Fdo.: José Luis Ayuso Muñoz

Abstract

Depth-averaged modelling of river flows is a widely used technique in hydraulic engineering, given the reduced computational work as compared to a three dimensional numerical solution. Typically, depth-averaged models rely on the assumptions of a hydrostatic pressure distribution, and depth-independent velocity and concentration distributions. However, even though Saint-Venant type models produce good results for the solution of a wide range of engineering problems, a significant increase in accuracy is achieved by using more realistic assumptions for the vertical structure of the flow. The main objective of this thesis is to study the effect of higher-order closure hypothesis for the vertical distributions of pressure, velocity and concentration, on the solution of one-dimensional depth-averaged models for river flow problems. This main objective is developed in the following specific studies: (i) The effect of the non-hydrostatic pressure distribution is first investigated in a basic section of river flow, namely the compound channel. Here, the energy and momentum balances in steady-state are investigated; (ii) Unsteadiness is introduced using the dam break flood wave over a rigid bed as a test case. Here, the accuracy of the velocity and pressure distributions of Serre-type, depth-averaged, non-hydrostatic flows is assessed; (iii) The finite-volume numerical model developed for dam break waves over rigid beds is expanded to dam break wave flows over movable beds by introducing a non-equilibrium sediment transport model, and the suspended sediment flux; (iv) An analytical solution for the equilibrium suspended-load flux is proposed used a power-law for the turbulent velocity profile, and a wall-wake concentration profile; (v) The effect of highly non-uniform distributions of velocity and concentration is investigated introducing a similarity approximation for erosive/depositional flows in turbidity currents.

Acknowledgements

Foremost, I am thankful to my advisors Dr. Oscar Castro Orgaz and Dr. José Luís Ayuso Muñoz for their continuous and valuable advice throughout the course of this study. Because of their wisdom, kind patience, and understanding, I am able to present these lines.

I wish to specially thank to professor Dr. Subhasish Dey, Indian Institute of Technology (IIT), Kharagpur, India, for his hearty reception and treat during my doctoral stay in India. His nice suggestions guided me all over tough moments to find inspiration and motivation. My thankful is also extended to those doctoral fellows in the IIT-Kharagpur who friendly received me during my doctoral stay and for the joyful time. There are not enough lines to express my gratitude to all of you here, but a special mention to my friend Sk Zeeshan Ali is obligated.

Thanks are due to the Ministerio de Educación, Cultura y Deporte, Spain, for grant (FPU12/04795) to develop this study and to visit to the IIT-Kharagpur. Besides, this study was supported by the Spanish project CTM2013-45666-R, Ministerio de Economía y Competitividad, to which I am also thankful.

My thankful is also extended to all institutional staff at the University of Córdoba as well as the IIT-Kharagpur that kindly assisted my requests in terms of PhD information and documentation.

I would like to thank to my parents, Francisco and Adoración, for their unlimited support and love. Your encouragement to study and go beyond limits helped me to achieve this goal. These thanks are extended to my brother Sergio and all my family indeed, from whom I always found support.

Finally, I specially thank you, Cristina, for always being there. Your love and understanding are my source of inspiration, pushing me to overcome tough moments all throughout these years.

To my parents.

In loving memory of my grandfather.

Table of Contents

Chapter 1

Introduction

Mathematical modelling of open-channel flows for engineering applications is routinely conducted using vertically-integrated models, given the reduction of the computational work as compared to a complete three-dimensional analysis (Steffler and Jin 1993, Chaudhry 2008, Castro-Orgaz et al. 2015). Most of these computational models numerically solve the Saint-Venant equations (implying a hydrostatic pressure distribution) in 1D or 2D, using finite-difference, finite element or finite volume schemes (Toro 2001, Chaudhry 2008). For sediment transport problems, the generalization of the Saint-Venant equations for a mixture of fluid and sediments over an erodible bed is available (Wu 2008). However, the assumption of a hydrostatic pressure distribution is not accurate for flows where the vertical length scale is of the order of the horizontal length scale, or, if the shallowness parameter is not asymptotically tending to zero. Typical problems are the flow in open channel structures like weirs and overfalls, water wave motion, and bed-form development and migration (Steffler and Jin 1993, Castro-Orgaz et al. 2015). Given the importance of modelling non-hydrostatic flows, this feature has been a topic of intense research since the 1980's, starting with the classical work of Hager and Hutter (1984). Most of the research conducted focussed on steady flows in a vertical plane (see Castro-Orgaz et al. 2015 for a recent review), but no extensions to cross-sectional shapes relevant for river-flows, like a compound channel (Blalock and Sturm 1981), are available. Unsteady non-hydrostatic flow solutions are rare, with the accurate development of Khan and Steffler (1996) as a notable exception. However, this model is limited to clear-water flows over rigid beds. Non-hydrostatic computations for sediment-laden flows over movable beds remain unaddressed (Wu 2008). Even though some erosion-deposition flows can be tackled using a hydrostatic pressure assumption, the velocity and concentration distributions in turbulent flow can be relevant (Dey 2014), like those in turbidity currents.

Therefore, a sediment transport model for non-uniform flow conditions should allow for the inclusion of a non-hydrostatic pressure distribution, and non-uniform velocity and concentration distributions. Typically, a non-equilibrium sediment transport model is required, and an accurate finite-volume or finite-element solution is desirable. At the current state-of-the-art, these issues are not addressed in the literature in a single and structured research work (Wu 2008), and, thus, this is the starting point of the present work.

References

Castro-Orgaz, O., Hutter, K., Giraldez, J. V., & Hager, W. H. (2015). Nonhydrostatic granular mass flow over 3-D terrain: New Boussinesq-type gravity waves?. *Journal of Geophysical Research: Earth Surface*, 120(1), 1–28.

Chaudhry, M. H. (2008). Open-channel flow. Springer, Berlin, Germany.

Dey, S. (2014). Fluvial Hydrodynamics: Hydrodynamic and Sediment Transport Phenomena. Springer, Berlin.

Hager, W. H., & Hutter, K. (1984). On pseudo-uniform flow in open channel hydraulics. *Acta Mechanica*, 53(3–4), 183-200.

Khan, A. A., Steffler, P. M. (1996). Vertically averaged and moment equations model for flow over curved beds. *Journal of Hydraulic Engineering*, 122(1), 3–9.

Steffler, P. M., & Jin, Y. C. (1993). Depth averaged and moment equations for moderately shallow free surface flow. *Journal of Hydraulic Research*, 31(1), 5̃17.

Wu, W. (2008). Computational river dynamics. CRC Press.

Blalock, M. E., & Sturm, T. W. (1981). Minimum specific energy in compound open channel. *Journal of the Hydraulics Division*, 107(6), 699–717.

Toro, E .F. (2001). Shock-capturing methods for free-surface shallow flows. John Wiley and Sons, Singapore.

Chapter 2

Objectives

The general objective of this work is to study the use of higher-order physical closure hypothesis, as compared to Saint-Venant type models, for the vertical distributions needed mathematically in a depth-averaged model. Specific objectives are as follows:

i. Studying the effect of including the non-hydrostatic pressure distribution in compound channel flows. This problem was selected as a basic section in river-type flows. This work is presented in Appendix I.

ii. Studying the effect of including the non-hydrostatic pressure distribution in unsteady dam break flows over rigid beds. This is a basic water wave including rarefaction and shock-waves. This work is presented in Appendix II.

iii. Studying the effect of including the non-hydrostatic pressure distribution in unsteady dam break flows over movable beds, with suspended and bed-load sediment transport modes. This is a key problem is fluvial hydrodynamics. This work is presented in Appendix III.

iv. Developing an analytical model for suspended load computations based on a power-law turbulent velocity profile. This work is presented in Appendix IV.

v. Including the velocity and suspended-load concentration distributions in erosion/deposition models. This work is presented in Appendix V.

Chapter 3

General Conclusions

The general conclusions drawn from this work are:

i. Inclusion of the non-hydrostatic pressure distribution in compound open channel flows produces energy and momentum equations that can simulate flow profiles not described by the gradually-varied (hydrostatic) flow theory. The momentum model was found to yield better results, using as a test case the free overfall in a compound channel.

ii. A high-resolution finite-volume model was developed to solve the weakly dispersive, fully non-linear Serre equations, for the dam break flood wave. The model was used to show that velocity and pressure distributions predicted by the theory are accurate, and that it is not needed to enhance the linear frequency dispersion relation in shallow flows, given the dominant role of non-linear effects as the ratio of wave amplitude to depth increases.

iii. A generalized Serre-type model was formulated for unsteady flow over movable beds, accounting for suspended and bed-load sediment transport modes. The model was solved using a high-resolution finite-volume scheme, and the results compared well with experimental observations and 3D numerical results available in the literature. The model produced a significant improvement in free surface predictions as compared to Saint-Venant type simulations.

iv. Using a power-law model for the turbulent velocity profile, an analytical solution to the suspended-load concentration profile was produced using a wall-wake approximation. The proposed velocity and concentration distributions were used to find an analytical solution to the suspended-load transport rate, which is an alternative to the numerical solution to Einstein's integrals.

v. An accurate description of the velocity and suspended-load concentration distributions using self-similarity functions produced a significant increase in

accuracy for turbidity current modelling (a strong erosion/deposition flow), as compared to classical models based on depth-independent distributions.

Appendix I

Free surface profiles in river flows: Can standard energy-based gradually-varied flow computations be pursued?

Francisco Nicolás Cantero-Chinchilla[1]; Oscar Castro-Orgaz[2], Amanda Garcia-Marín[3], José Luis Ayuso-Muñoz[3], Subhasish Dey[4]

Journal of Hydrology, 529(1), 1644–1656, doi:10.1016/j.jhydrol.2015.07.056. Impact factor (JCR 2014): 3.053 / Q1 (4/125 Civil Engineering)

Summary

Is the energy equation for gradually-varied flow the best approximation for the free surface profile computations in river flows? Determination of flood inundation in rivers and natural waterways is based on the hydraulic computation of flow profiles. This is usually done using energy-based gradually-varied flow models, like HEC-RAS, that adopts a vertical division method for discharge prediction in compound channel sections. However, this discharge prediction method is not so accurate in the context of advancements over the last three decades. This paper firstly presents a study of the impact of discharge prediction on the gradually-varied flow computations by comparing thirteen different methods for compound channels, where both energy and momentum equations are applied. The discharge, velocity distribution coefficients, specific energy, momentum and flow profiles are determined. After the study of gradually-varied flow predictions, a new theory is developed to produce higher-order energy and momentum equations for rapidly-varied flow in compound channels. These generalized equations enable to describe the flow profiles with more generality than the gradually-varied flow computations. As an outcome, results of gradually-varied flow provide realistic conclusions for computations of flow in compound channels, showing that momentum-

[1] PhD Student, Hydraulic Engineering Area, Dept. of Agronomy, Univ. of Cordoba, Campus Rabanales, Edif. da Vinci, Cra Madrid Km 396, 14071 Cordoba, Spain.
[2] Professor, Hydraulic Engineering Area, Univ. of Cordoba, Campus Rabanales, Edif. da Vinci, Cra Madrid Km 396, 14071 Cordoba, Spain. E-mail: oscarcastro@ias.csic.es (author for correspondence)
[3] Professor, Dept. of Rural Engineering, Univ. of Cordoba, Campus Rabanales, Edif. da Vinci, Cra Madrid Km 396, 14071 Cordoba, Spain.
[4] Professor and Head, Dept. of Civil Engineering, Indian Institute of Technology, Kharagpur 721302, West Bengal, India.

based models are in general more accurate; whereas the new theory developed for rapidly-varied flow opens a new research direction, so far not investigated in flows through compound channels.

1. Introduction

Discharge hydrographs from heavy rainfall events are conveyed as a free surface flow through natural waterways and rivers, which are normally compound channels. The cross-sections of these channels are complex and can be divided into a main channel and the flood plains, with a large variation of hydraulic roughness between them (Sturm, 2001). The computation of free surface levels in natural channels is an important procedure and it is required to demarcate the flow inundation areas as a function of the return period of peak flood (Chow et al., 1988; Brutsaert, 2005). The accuracy in flow profile predictions relies on hydraulic computations based on one-dimensional gradually-varied flow models (Chow et al., 1988). Programs like HEC-RAS (Hydrologic Engineering Center-River Analysis System) are used to compute one-dimensional gradually-varied flow in natural channels by using the energy equation (Sturm, 2001; Chaudhry, 2008). A decisive aspect in these computations is the selection of an appropriate method to calculate the discharge taking into account the variation of hydraulics roughness within the cross-section. The HEC-RAS program, for example, subdivides the channel cross-section with vertical planes and turbulent stresses are neglected along the division lines. This is a traditional approximation in open channel flows (Chow, 1959; Montes, 1998; Sturm, 2001; Chaudhry, 2008). However, in the past 30 years, a large number of studies analyzed the discharge prediction method for compound channel sections. Most of them argued that the subdivision method is not accurate for the discharge prediction. The strong lateral velocity gradients and turbulence result in a significant linear momentum transfer between the main channel and the flood plains (Sellin, 1964; Myers, 1978; Rajaratnam and Ahmadi, 1981; Wormleaton et al., 1982; Knight and Demetriou, 1983; Shiono and Knight, 1991; Knight and April, 1996; Lambert and Sellin, 1996; Bousmar and Zech, 1999; Kathua et al., 2011). Prinos (1985) and Chatila and Townsend (1996) compared the methods based on virtual plane divisions between the main channel and the floodplains. The interaction between the flood plain and the main channel flows induces secondary flows and turbulent stresses at the virtual planes, which can be introduced in the governing equations by a momentum balance (Wormleaton et al., 1982). Wormleaton et al. (1982),

Prinos and Townsend (1984) and Wormleaton and Merrett (1990) solved the momentum equation by introducing an apparent shear stress at the interfaces, and parameterized it in terms of velocity of the main channel and the floodplains. Dracos and Hardegger (1987) suggested the use of the ratio of hydraulic radius to total depth for the single-channel method, which involves several empirical parameters related to the geometry of the cross-sections. Ackers (1993a, b) proposed the coherence method, that introduces an empirical correction to the vertical (virtual) division method. Khatua et al. (2011) developed an equation to quantify the momentum transfer in terms of an appropriate interface length. Thus, despite it is well established that the momentum transfer between the main channel and the flood plains must be considered for an accurate determination of the discharge, this knowledge has so far been hardly transmitted to the basic hydraulic computations involving free surface flows. It is, however, unclear amongst various available methods, which discharge prediction method should be included in one-dimensional compound channel models. Further, it is also unclear, which is the best, whether the use of momentum or energy principle for the computations of flow in compound channels.

The prediction of the stage-discharge relationship in a compound channel directly influences other relevant gradually-varied flow computations. The discharge curve is needed to perform flow profile computations using gradually-varied energy or momentum models (Sturm and Sadiq, 1996; Sturm, 2001; Chaudhry, 2008). An aspect that particularly makes these computations in compound channels complicated relates to the nonuniform lateral velocity distribution within the cross-section induced by the large variation of hydraulic roughness. It results in velocity distribution coefficients much larger than unity that needs to be accounted for (Sturm and Sadiq, 1996; Sturm, 2001). The computations of these coefficients as well as the determination of the energy line slope are highly dependent on the discharge prediction method. Thus, the flow profile computations are reliant on the discharge predictor model. Critical depth is used to compute stage-discharge rating curves by using the energy or momentum principles (Petryk and Grant, 1978; Blalock and Sturm, 1981; Schoellhamer et al., 1985; Chaudhry and Ballamudi, 1988; Yuen and Knight, 1990; Lee et al., 2002), and it is as well a boundary condition to initiate flow profile computations (Sturm and Sadiq, 1996; Field et al., 1998). The impact of the discharge predictor on the critical depth computations is also unclear. Field et al. (1998) compared energy and momentum equations of

gradually-varied flows for the computation of flow profiles in compound channels. They concluded that more research was needed to evaluate both approximations, that give large differences. Errors in discharge prediction may result in large inaccuracies in computing energy and momentum fluxes, thereby provoking problems when solving the dynamic flow equations (Wormleaton and Hadjipanos, 1985). Further, the flow discharge measurement in open channels is usually done by weirs and flumes (Clemmens et al., 2001). If a long throated flume is installed into a compound channel to measure discharge, then the rating curve of the flume relates flow discharge Q to the specific energy E in the upstream compound channel (Montes, 1998; Clemmens et al., 2001). Given the large magnitude of the energy correction coefficient of flow in this type of channel, the measurement of discharge may be highly sensitive to errors in the computation of E. However, like in the former problems, no assessment of the impact of discharge prediction methods in the computation of the specific energy and momentum is so far available in the literature to the best of authors' knowledge. In short, no assessment of the impact of the discharge prediction method on the computation of velocity distribution coefficients, uses of energy and momentum principles, critical depth and flow profile computations appears to be available in the literature in a single and structured study.

The compound channel studies summarized above are related to gradually-varied flow, where the pressure distribution is assumed to preserve a hydrostatic variation. Within the range of multiple critical depths, the free surface at the cross-sectional plane in a compound channel is no longer horizontal in the vicinity of free overfalls (Dey and Lambert, 2006); the velocity field is then three-dimensional and the pressure non-hydrostatic (Sturm and Sadiq, 1996). For a higher discharge outside this range, there is only one critical depth in the specific energy curve and the free surface is horizontal at the cross-sectional plane. In this case, the free surface is only a function of the longitudinal distance (or streamwise coordinate); and thus one-dimensional models apply. Near overfalls, however, there is a significant vertical velocity component and hence the velocity field is two-dimensional despite the flow depth is a one-dimensional magnitude. Given the non-hydrostatic pressure, this type of flow cannot be solved by standard gradually-varied flow computations so far dominating this field of research. One-dimensional non-hydrostatic, or rapidly-varied, flows have been successfully modelled in open channel hydraulics by means of the Boussinesq-type approximation

(Serre, 1953; Hager and Hutter, 1984a; Chaudhry, 2008; Castro-Orgaz and Hager, 2011). Experimental flow profiles measured by Sturm and Sadiq (1996) indicated the presence of non-hydrostatic pressure effects near the drawdown at a free overfall and at the oscillatory wave train around the normal depth. Both free surface flow configurations were explained by Serre (1953) in rectangular channels using the higher-order energy and momentum equations. However, there exists no work in the literature making such an analysis for flows in compound channels. In particular, the higher-order Boussinesq-type non-hydrostatic pressure equations for compound channels were so far not developed to the best of authors' knowledge.

The objective of this research is twofold:

(i) The first objective relates to gradually-varied flow and the impact of the discharge prediction method. For this purpose, thirteen relevant discharge prediction methods available in the literature are analyzed to reveal the impact of momentum transfer on basic flow profile computations. The methods are first compared in terms of discharge prediction to highlight their accuracy to predict the stage-discharge rating curve under uniform flow conditions. The methods are then used to compute the velocity distribution coefficients, namely, Coriolis (energy) and Boussinesq (momentum) coefficients. After evaluating the discharge and the velocity correction coefficients, their interaction is investigated computing the specific energy and momentum functions of gradually-varied flow in open channels. Critical flow computations are presented using the energy and the momentum equations; and the impact of the discharge prediction method is then analyzed. Further, the discharge prediction methods are used to solve numerically the differential equations of gradually-varied flow describing the flow profiles, using both energy and momentum principles.

(ii) The second objective is the theoretical development of the higher-order energy and momentum equations for flow in compound channels. The computation of rapidly-varied flow profiles using the higher-order energy and the dynamic momentum equations requires simultaneous consideration of the vertical distribution of non-hydrostatic pressure and the nonuniform lateral velocity of flow in compound channels. A new theoretical development is introduced and the higher-order specific energy E and momentum S of flow in compound channels are presented for the first time. This permits to simulate the flow profiles in a wider range of flow conditions as compared to previous methods. In particular, the new theoretical equations are found to describe the

drawdown curve near the free overfall in a compound channel and the undulating flow around the normal depth. These flow profiles are not predicted by the gradually-varied flow formulations, showing the physical relevance of the new set of equations. The higher-order flow profiles are the result of a complex interaction between the non-hydrostatic pressure, the nonuniformity of the velocity profile originating from the variation of hydraulic roughness and the linear momentum transfer between the main channel and the flood plains.

Based on the analysis of gradually-varied flow, practical recommendations for the use in flood inundation hydraulic studies are given, whereas the new theoretical development of rapidly-varied flow opens a new research direction.

2. Gradually-varied flow

2.1. Discharge prediction methods

The discharge prediction methods evaluated, in this study, are divided into two groups: single channel and separate channel methods (Table 1). For specific details of each method, one may consult the corresponding publications. Here, the primary focus is to the use of the methods. Single channel methods are based on the Manning equation to predict Q as

$$Q = \frac{1}{n_e} A R^{2/3} S_0^{1/2} \tag{1}$$

where n_e = equivalent manning coefficient for the entire cross-section, A = flow cross-sectional area, R = hydraulic radius of the cross-section and S_0 = channel slope. The Manning roughness n_e is given by the equation (Chow, 1959; Prinos and Townsend, 1984)

$$n_e = \left(\sum_i \frac{p_i n_i^{3/2}}{P} \right)^{2/3} \tag{2}$$

where p_i, n_i = wetted perimeter and Manning coefficient of the i-th subsection, respectively. Equation (2) is obtained assuming that the average velocity at each subsection is constant (Prinos and Townsend, 1984). In this work, two additional single channel methods by Dracos and Hardegger (1987) and French (1987), who used a weighted hydraulic radius proposal, are evaluated.

Nomenclature	Method	Reference
SGCM	Single channel method	Prinos and Townsend (1984)
SGCME	Single channel method empirical hydraulic radius	Dracos and Hardegger (1987)
SGCMW	Single channel method weighted hydraulic radius	French (1987)
SCMV	Separate channel method vertical divisions	Chow (1959)
SCMH	Separate channel method horizontal divisions	Chatila and Townsend (1996)
SCMI	Separate channel method inward diagonal divisions	Yen and Overton (1973)
SCME	Separate channel method extended side slope	Chow (1959)
SCMO	Separate Channel Method Outward diagonal	Chatila (1992)
SCMASSP	Separate channel method apparent shear stress Prinos	Prinos and Townsend (1984)
SCMASSW	Separate channel method apparent shear stress Wormleaton	Wormleaton et al. (1982)
SCMASSM	Separate channel method apparent shear stress Merrett	Wormleaton and Merrett (1990)
SCMA	Separate channel method Ackers	Ackers (1993)
SCMK	Separate channel method Khatua	Khatua et al. (2011)

Table 1. Discharge prediction methods

The second group of methods divides the channel into main channel and floodplains by virtual division planes. Depending on the slope of the virtual planes and its location within the cross-section, a number of methods are available in the literature (SCMV, SCMH, SCMI, SCME and SCMO in Table 1) (Fig. 1a). In Fig. 1(a), the point-dot lines represent the virtual division planes (O=outwards, I=inwards, H=horizontal, V=Vertical, E=Extended) using in each method. Following Chatila and Townsend (1996), the discharge is predicted by

$$Q = \sum_i \frac{1}{n_i} A_i R_i^{2/3} S_0^{1/2} \tag{3}$$

Equation (3) neglects the turbulent stresses at virtual divisions, that are accounted for in other methods by using a momentum approach (methods SCMASSP, SCMASSW and SCMASSM in Table 1). A momentum balance yields an averaged velocity U in main channel and flood plain as (Wormleaton et al., 1982)

$$U_c^{\,2} = \frac{8}{\rho f_c}\left(\gamma R_c S_e - \frac{2\tau_a y}{P_c}\right) \tag{4}$$

$$U_f^{\,2} = \frac{8}{\rho f_f}\left(\gamma R_f S_e + \frac{\tau_a y}{P_f}\right) \tag{5}$$

where ρ = density of water, f = Darcy-Weisbach friction factor, γ= specific weight, y = flood plain water depth (Fig.1) and τ_a = apparent shear stress acting at the virtual planes. Subscripts c and f refer to the main channel and floodplain, respectively. For the computation of P_c, P_f, A_c and A_f in this method vertical division lines are taken. Note that these virtual division lines are excluded for the computation of both P_c and P_f. The apparent stress can be estimated by empirical relationships available in the literature (Rajaratnam and Ahmadi, 1981). From equations (4) and (5), the discharge for symmetrical flood plains is given by

$$Q = A_c U_c + 2A_f U_f \tag{6}$$

Two additional methods which originated from the study of Wormleaton et al. (1982) are due to Ackers (1993a, b) and Khatua et al. (2011), SCMA and SCMK, respectively (Table 1). Ackers (1993a, b) improved discharge prediction by introducing a corrector factor which depends on the relative depth between the main channel and the flood plain. Khatua et al. (2011) developed two wetted perimeter coefficients derived from a new momentum transfer approach at the interfaces. These coefficients, X_c and X_f, are

$$X_c = P_c\left(\frac{100}{(100-\lambda)}\frac{A_c}{A} - 1\right) \tag{7}$$

$$X_f = P_f\left(\frac{100}{\lambda}\left(\frac{A_c}{A} - 1\right) - 1\right) \tag{8}$$

where λ=4.1045$(100A_f/A)^{0.6917}$, which is an empirical correlation. The discharge is then given by

$$Q = \frac{S_0^{\,1/2}}{n_c} A_c^{\,5/3}\left(P_c + X_c\right)^{-2/3} + 2\frac{S_0^{\,1/2}}{n_f} A_f^{\,5/3}\left(P_f - X_f\right)^{-2/3} \tag{9}$$

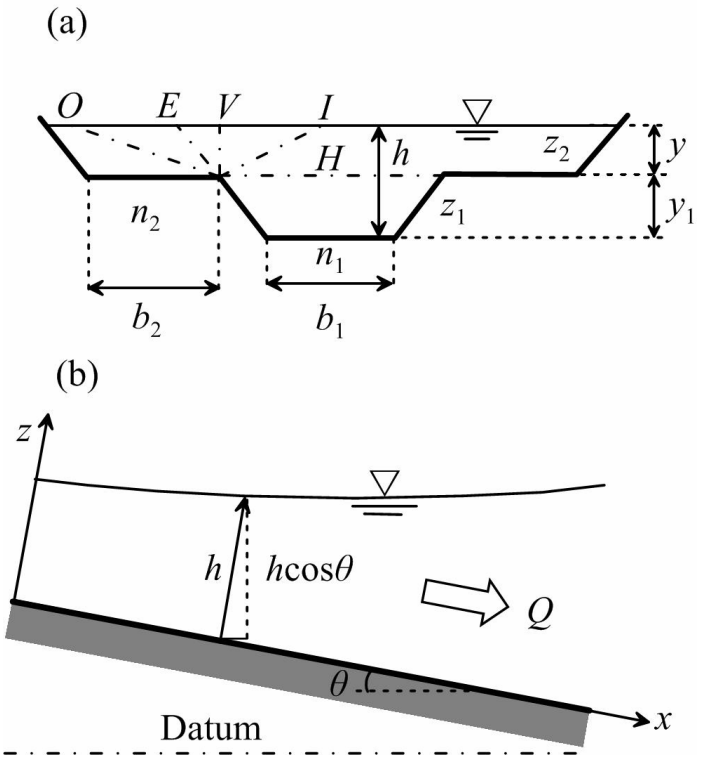

Fig. 1. Compound channel flow definition sketch (a) cross-section, (b) longitudinal profile

2.2. Velocity correction coefficients

The roughness variation in a compound channel section provokes a nonuniform lateral velocity distribution. The kinetic energy correction coefficient (or Coriolis coefficient) α is given by (Blalock and Sturm, 1981; Field et al., 1998)

$$\alpha = \frac{\int_A u^3 \mathrm{d}A}{U^3 A} = \frac{\sum_i \left(u_i^3 a_i\right)}{U^3 A} \tag{10}$$

where u_i = velocity in a subsection, a_i = area of a subsection and $U=Q/A$, that is the mean flow velocity of the whole section. The momentum correction coefficient (or Boussinesq coefficient) β coefficient is (Chaudhry and Bhallamudi, 1988; Field et al., 1998)

$$\beta = \frac{\int_A u^2 \mathrm{d}A}{U^2 A} = \frac{\sum_i \left(u_i^2 a_i\right)}{U^2 A} \tag{11}$$

For a given discharge prediction method, the discharge in each subsection u_i can be determined and therefore, α and β. The correction coefficients are needed to compute the specific energy (E) and momentum (S) functions, and thus, the flow profiles $h=h(x)$, where x = streamwise distance (Fig. 1b).

2.3. Energy equation

The specific energy (E) of gradually-varied flow in open channels is defined as (Montes, 1998; Sturm, 2001; Chaudhry, 2008; Dey, 2014)

$$E = h + \alpha \frac{Q^2}{2gA^2} \tag{12}$$

where h = maximum water depth in the main channel (= $y+y_1$) [Fig. 1(b)] and g = gravitational acceleration. In Eq. (12), the channel slope is assumed to be small, as usual for most of the river flows. For a sloping channel, the gravity term h in Eq. (12) can be simply replaced by the pressure head $h\cos\theta$, where θ = angle of channel bed with the horizontal (Chow, 1959). Introducing Eq. (12) into the one-dimensional energy balance (Montes, 1998; Sturm, 2001)

$$\frac{\mathrm{d}E}{\mathrm{d}x} = S_0 - S_e \tag{13}$$

results in (Blalock and Sturm, 1981; Sturm and Sadiq, 1996; Jain, 2001)

$$\frac{\mathrm{d}h}{\mathrm{d}x} = \frac{S_0 - S_e}{1 - \left(\dfrac{\alpha Q^2 T}{gA^3} - \dfrac{Q^2}{2gA^2} \dfrac{\mathrm{d}\alpha}{\mathrm{d}h} \right)} = \frac{S_0 - S_e}{1 - \mathsf{F}_\alpha{}^2} \tag{14}$$

where S_e = gradient of dissipated energy, T = free surface width and F_α = compound channel Froude number based on the specific energy. The latter was approximated by Blalock and Sturm (1981) as

$$\mathsf{F}_\alpha = \left(\frac{\alpha Q^2 T}{gA^3} - \frac{Q^2}{2gA^2} \frac{\mathrm{d}\alpha}{\mathrm{d}h} \right)^{1/2} = \left[\frac{Q^2}{2gK^3} \left(\frac{\sigma_2 \sigma_3}{K} - \sigma_1 \right) \right]^{1/2} \tag{15}$$

where

$$\sigma_1 = \sum_i \left[\left(\frac{k_i}{a_i} \right)^3 \left(3t_i - 2r_i \frac{\mathrm{d}p_i}{\mathrm{d}h} \right) \right] \tag{16}$$

$$\sigma_2 = \sum_i \left(\frac{k_i{}^3}{a_i{}^2} \right) \tag{17}$$

$$\sigma_3 = \sum_i \left[\left(\frac{k_i}{a_i} \right) \left(5t_i - 2r_i \frac{\mathrm{d}p_i}{\mathrm{d}h} \right) \right] \tag{18}$$

In the equations above, t_i = subsection top width, p_i = subsection wetted perimeter, r_i = subsection hydraulic radius, k_i = subsection conveyance [= $(1/n_i)a_i r_i^{2/3}$], K = total conveyance of the flow section and n_i = subsection n. Compound channels may exhibit different flow regimes in the plane of the cross-section, that is, subcritical or supercritical flow may exist in the same flow section (Lee et al., 2002; Kordi et al., 2009). However, this analysis relates to the local 2D flow conditions in a channel cross-section; whereas for one-dimensional computations, changes in flow state are mathematically described by the bulk cross-sectional Froude number given by Eq. (15), and not by a local Froude number valid for different points in a section (Blalock and Sturm, 1981, 1983; Costabile and Macchione, 2012).

2.4. Momentum equation

The specific momentum (S) of gradually-varied flow in open channels is (Montes, 1998; Sturm, 2001; Chaudhry, 2008; Dey, 2014)

$$S = \bar{z}A + \beta\frac{Q^2}{gA} \tag{19}$$

where $\bar{z}$ = distance from the free surface to the centroid of the section. The gradually-varied flow equation from the momentum approach is obtained inserting Eq. (19) into the streamwise momentum balance (Field et al., 1998)

$$\frac{\mathrm{d}S}{\mathrm{d}x} = A\left(S_0 - S_f\right) \tag{20}$$

where S_f = friction slope, resulting in

$$\frac{\mathrm{d}h}{\mathrm{d}x} = \frac{S_0 - S_f}{1-\left(\dfrac{\beta Q^2 T}{gA^3} - \dfrac{Q^2}{gA^2}\dfrac{\mathrm{d}\beta}{\mathrm{d}h}\right)} = \frac{S_0 - S_f}{1-\mathsf{F}_\beta{}^2}, \quad \mathsf{F}_\beta = \left(\frac{\beta Q^2 T}{gA^3} - \frac{Q^2}{gA^2}\frac{\mathrm{d}\beta}{\mathrm{d}h}\right)^{1/2} \tag{21}$$

where F_β = compound channel Froude number based on the momentum principle. It should be noted that the definition of F_β in Eq. (21) arises mathematically from the momentum balance equation. It can be demonstrated that $\mathrm{d}S/\mathrm{d}h = 1-\mathsf{F}_\beta^2$. Chaudhry and Bhallamudi (1988) defined a compound channel Froude number F_c based on the characteristics lines of the unsteady momentum equation (see Appendix I). The F_c defined by them has been widely accepted as the compound channel Froude number based on the momentum principle. Costabile and Macchione (2012) recently re-derived

F_c [Eq. (37), Appendix I)] and used it to produce a critical flow boundary condition to solve the unsteady, gradually-varied compound channel equations. It is found that the F_c as defined by Chaudhry and Bhallamudi (1988) is relevant to obtain an expression for critical depth computations (F_c=1), but it cannot be used to perform flow profile computations using Eq. (21) as dh/dx=(S_o−S_f)/(1−F_c^2). Instead, F_β in Eq. (21) is the general Froude number for compound channels relevant to flow profile computations (see Appendix I). Following a similar development to Blalock and Sturm (1981), F_β is estimated by the equation

$$F_\beta = \left(\frac{\beta Q^2 T}{gA^3} - \frac{Q^2}{gA^2}\frac{\mathrm{d}\beta}{\mathrm{d}h} \right)^{1/2} = \left[\frac{2Q^2}{3gAK^2}\left(\frac{\tau_2\tau_3}{K} - \tau_1 \right) \right]^{1/2} \tag{22}$$

The coefficients τ_1, τ_2 and τ_3 and the corresponding theoretical development are presented in the Appendix I.

2.5. Critical flow

Setting F_α =1 in Eq. (15), one finds the critical flow condition from the energy equation as

$$\frac{Q^2}{2gK^3}\left(\frac{\sigma_2\sigma_3}{K} - \sigma_1 \right) = 1 \tag{23}$$

that is the critical flow condition originating from the minimum specific energy (dE/dh=0) (Blalock and Sturm, 1981). Setting F_β =1 in Eq. (22) yields

$$\frac{2Q^2}{3gAK^2}\left(\frac{\tau_2\tau_3}{K} - \tau_1 \right) = 1 \tag{24}$$

Equation (24) is the critical flow condition originating from the minimum momentum function (dS/dh=0). In general, Eqs. (23) and (24) are different; so the computed critical depths differ. Both methods produce different results for each discharge predictor.

3. Rapidly-varied flow

3.1. Introduction

Gradually-varied flow computations using Eqs. (12) and (19) for E and S, respectively, are limited to portions of the flow domain, where the vertical acceleration can be neglected (Sturm, 2001; Chaudhry, 2008). This is not fulfilled at the drawdown curve of

free overfalls or at undulating wave trains, like those measured by Sturm and Sadiq (1996). To our knowledge, these flow profiles have so far not been modelled with a higher-order one-dimensional model. Higher-order free surface computations require resort to Boussinesq-type equations (Serre, 1953; Hager and Hutter, 1984a; Chaudhry, 2008; Castro-Orgaz and Hager, 2011). This mathematical technique leads Serre (1953), Hager and Hutter (1984a, b), Hosada and Tada (1994), Khan and Steffler (1996) and Bose and Dey (2007) to explain a number of flow profiles exhibiting non-hydrostatic effects in rectangular channels, in addition to standard free surface profiles. However, the Serre (1953) equations for channels of arbitrary cross-sections are not available; so a higher-order theory has so far not been presented in the literature for compound open channels. Boussinesq-type equations are relevant for river flow processes, like the development of form resistance due to sand-waves, for both subcritical and supercritical flows associated with dunes and antidunes, respectively (Bose and Dey, 2009; Dey, 2014).

3.2. Pressure

Consider a channel of arbitrary cross-section, where the origin of z is taken at the lowest point. Integrating the corresponding Euler equation along the depth, yields the pressure distribution as (Serre, 1953; Chaudhry, 2008) (Appendix II)

$$p(z) = \rho g (h - z) \cos\theta - \rho v^2 + \rho \frac{\partial}{\partial x} \int_z^h v u \mathrm{d}z \tag{25}$$

Using the depth-averaged velocity U, the continuity equations yields the vertical velocity profile as $v = -(\partial U/\partial x)z$. Inserting it into Eq. (25), yields (Appendix II)

$$\frac{p}{\gamma} = (h - z)\cos\theta + \left(U_x^2 - U U_{xx}\right)\left(\frac{h^2 - z^2}{2g}\right) \tag{26}$$

where $U_x = \partial U/\partial x$ and $U_{xx} = \partial^2 U/\partial x^2$. This pressure distribution is the basis to produce higher-order energy and momentum equations for flow in compound channels. Non-hydrostatic contributions are given by the terms U_x and U_{xx}; so for significant variations of velocity, the hydrostatic pressure approach becomes invalid.

3.3. Momentum equation

The specific momentum S in flow at a cross-sectional area A is given by (Montes, 1998; Sturm, 2001)

$$S = \int_A \left(\frac{u^2}{g} + \frac{p}{\gamma} \right) \mathrm{d}A \tag{27}$$

Inserting Eq. (26) into Eq. (27) results in

$$S = \beta \frac{Q^2}{gA} + \bar{z} A \cos\theta + \frac{U_x^2 - UU_{xx}}{2g} \left(h^2 A - \int_A z^2 \mathrm{d}A \right) \tag{28}$$

where the integral term is the moment of inertia I of the cross-sectional area A. The derivatives of $U=Q/A$ are given by

$$U_x = -\frac{Q}{A^2} A_h h_x, \quad U_{xx} = \frac{2Q}{A^3} A_h^2 h_x^2 - \frac{Q}{A^2} \left(A_h h_{xx} + A_{hh} h_x^2 \right) \tag{29}$$

where $h_x=\mathrm{d}h/\mathrm{d}x$, $h_{xx}=\mathrm{d}^2h/\mathrm{d}x^2$, $A_h=\partial A/\partial h$ and $A_{hh}=\partial^2 A/\partial h^2$. Inserting Eq. (29) into Eq. (28) results in higher-order momentum function S for flow in compound channels as

$$S = \bar{z} A \cos\theta + \frac{Q^2}{gA} \left(\beta + \frac{\left(h^2 A - I \right)}{2A^3} \left(A A_h h_{xx} + \left(A A_{hh} - A_h^2 \right) h_x^2 \right) \right) \tag{30}$$

In Eq. (30) for the developed new Boussinesq-type theory, the significant lateral velocity variation of compound channel flow is accounted for by the coefficient β; whereas non-hydrostatic pressures are approximately accounted for on the basis of Eq. (26). To the best of the authors' knowledge, this theory is the one that first accounts for both effects in flows through compound channels. Thus, this development may be regarded as a first step to model the one-dimensional rapidly-varied flow profiles in compound channels. More rigorous theories can be constructed by studying the interaction of the lateral velocity profile with the vertical non-hydrostatic pressure. Limitations of Eq. (26) are stated in Appendix II, thereby opening a new research direction on the problems of free surface flow computation in compound channels. If Eq. (30) is particularized to a flow with no-lateral velocity variation (β=1, that is, a simple channel flow), the resulting equation applies for a channel cross-sectional of general geometry. Also, this development seems to have been not given an attention, thereby indicating that the Boussinesq-type equations available in other works are only applicable to rectangular cross-sections.

3.4. Energy equation

The specific energy E in open channel flow is given by the general equation (Montes, 1998; Sturm, 2001)

$$E = \frac{1}{Q}\int_A \left(\frac{u^2 + v^2}{2g} + z\cos\theta + \frac{p}{\gamma} \right) u \mathrm{d}A \tag{31}$$

Following a similar development to that used with the momentum equation, E can be written as function of the derivatives of U, using the functions for p and v as

$$E = h\cos\theta + \alpha\frac{Q^2}{2gA^2} + \frac{U_x^2 - UU_{xx}}{2g}\frac{\left(h^2A - I\right)}{A} + \frac{U_x^2}{2gA}I \tag{32}$$

Also, after using Eqs. (29), the higher-order specific energy for flow in compound channels is

$$E = h\cos\theta + \frac{Q^2}{2gA^2}\left(\alpha + \frac{\left(h^2A - I\right)}{A^3}\left(AA_h h_{xx} + \left(AA_{hh} - A_h^2 \right) h_x^2 \right) + \frac{A_h^2}{A^3} I h_x^2 \right) \tag{33}$$

Equations (30) and (33) are the higher-order expressions for E and S in flow through compound channels, thereby generalizing Serre (1953) theory. Inserting Eqs. (33) and (30) into Eqs. (13) and (20), respectively, results in higher-order energy and momentum models for flow in compound channels. Compared to the first-order equations of gradually-varied flow [Eqs. (14) or (21)], the higher-order model results in a third-order differential equation. Comparatively, additional boundary conditions are thus required. Non-hydrostatic pressure is modelled by the terms $\mathrm{d}^2h/\mathrm{d}x^2$ and $(\mathrm{d}h/\mathrm{d}x)^2$ inside the brackets of Eqs. (30) and (33). Thus, in Eqs. (30) and (33), the lateral variation of velocity in the compound channel is accounted for by α and β; whereas the non-hydrostatic pressure is modelled by the higher-order derivative terms. These equations apply to one-dimensional flow with non-hydrostatic pressure in compound channels, that is, without lateral variation of the free surface. If the free surface in the main channel falls beyond certain limit, a lateral free surface gradient appears, and the flow in main channel and flood plain must be analyzed separately (Dey and Lambert, 2006). In this case, the flow cannot be tackled with a one-dimensional approach as presented herein.

3.5. Simplifications

For a rectangular channel, $A=b_1 h$ and Eqs. (30) and (33) reduce to

$$E = h + \frac{Q^2}{2gb_1^2 h^2}\left(1 + \frac{2hh_{xx} - h_x^2}{3}\right) \tag{34}$$

$$S = b_1 \frac{h^2}{2} + \frac{Q^2}{gb_1 h}\left(1 + \frac{hh_{xx} - h_x^2}{3}\right) \tag{35}$$

which are the higher-order E and S equations currently available (Hager and Hutter, 1984a; Montes 1998; Castro-Orgaz and Hager, 2011). However, these are not valid for other channel cross-sections, including compound channels. It highlights that a generalized result is missing so far for the flow in compound channels and in general, for open channel flow of arbitrary cross-sectional shapes.

4. Results

4.1. General

Prinos (1985) laboratory data is used to evaluate thirteen discharge prediction methods by computing errors in the prediction of discharge, velocity distribution coefficients, specific energy and momentum. Yuen (1989) data is used to evaluate the critical depth computations, and the performance of the discharge predictors in free surface computations using energy and momentum equations is evaluated using the experimental data of Sturm and Sadiq (1996).

4.2. Discharge

Prinos (1985) made experiments in a 12.2 m long flume of trapezoidal section, 0.102 m deep, with 2V:1H side slopes and base widths of 0.203, 0.305 and 0.406 m. The channel slope in the experiments was 0.0003, n_1=0.011 and n_2 varied from 0.011 to 0.022. This data is used to evaluate the discharge prediction error as

$$\Delta Q\% = 100\frac{(Q_e - Q_o)}{Q_o} \tag{36}$$

where e refers to estimation and o to observed value. The results are plotted in Fig. 2 for the experiments of Prinos' (1985) dataset corresponding to n_2/n_1=2, where the relative flood plain depth is $y_r=y/h$. Results indicate that the error is considerable and even higher than 40% for the SCMO method. Single-channel schemes are demonstrated to

perform poorly and so is the SCMV method. The analysis of Fig. 2, and that of the remaining part of Prinos dataset (1985) for n_2/n_1=1, 1.27 and 1.64, that are not presented herein for brevity, essentially indicate that the SCMASSM performs the best among all the methods.

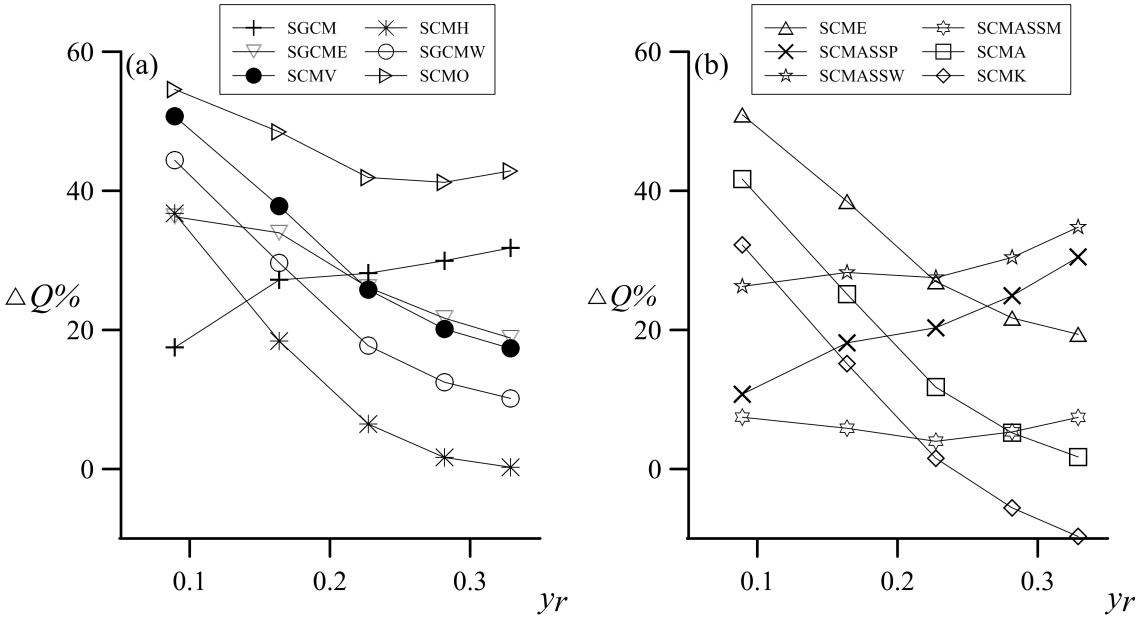

Fig. 2. Discharge errors $\Delta Q\%$ as function of y_r

4.3. Velocity correction coefficients

Equations (10) and (11) are used to compute α and β using the predicted values of discharge in the main channel and the flood plains. Both discharges are also available from the experimental measurements of Prinos (1985), permitting to estimate the values of α and β experimentally. Error indexes $\Delta\alpha\%$ and $\Delta\beta\%$ analogue to Eq. (36) are computed and the results are depicted in Figs. 3 and 4. Errors in discharge prediction are transmitted to the computation of velocity correction coefficients. The magnitude of errors is so large that it confirms that the discharge prediction method has a significant effect on the estimation of velocity correction coefficients. The SCMASSM method performs well in this test.

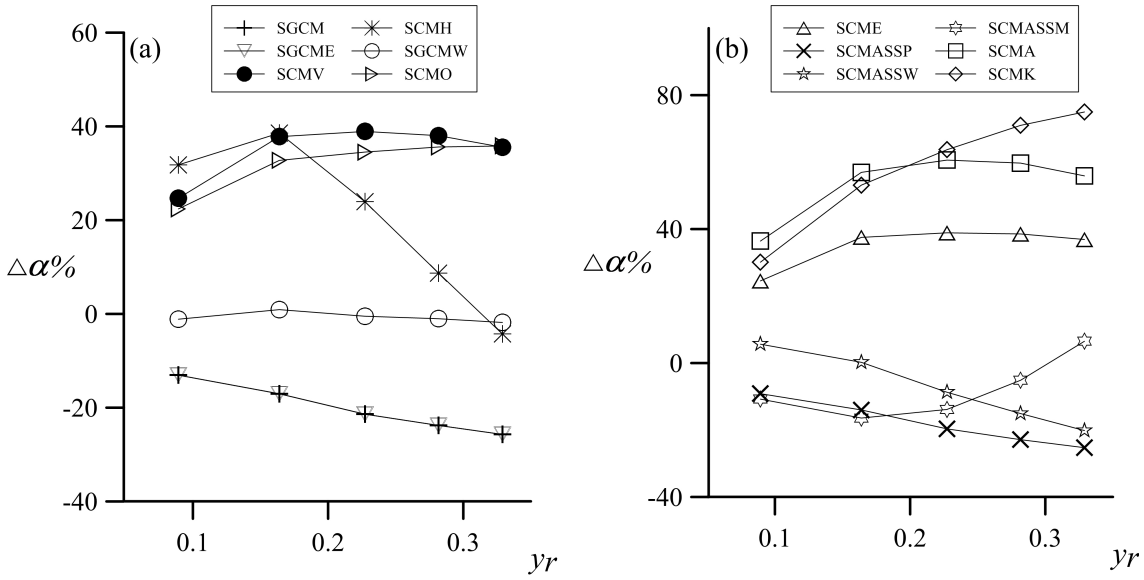

Fig. 3. Coriolis coefficient errors $\Delta\alpha\%$ as function of y_r

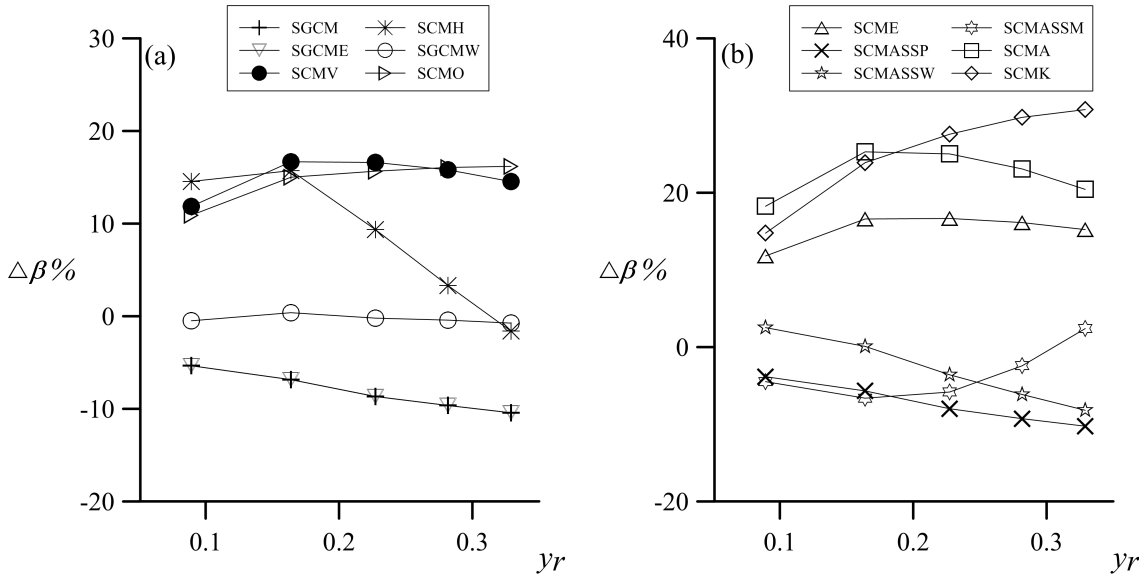

Fig. 4. Boussinesq coefficient errors $\Delta\beta\%$ as function of y_r

4.4. Specific energy and momentum

With the computed values of Q, α and β used to plot Figs. 2–4, the specific energy E and momentum S are evaluated using Eqs. (12) and (19), respectively. Experimental values of the same three variables permit the corresponding computation of E and S, from which error indexes $\Delta E\%$ and $\Delta S\%$ are computed and plotted in Figs. 5 and 6. Errors in discharge prediction and velocity correction coefficients computation are transmitted to the computation of energy and momentum fluxes. Figure 5 reveals that the error in E is generally small and that in S is higher, although both are of small

magnitude. It indicates that the flow phenomena in compound channels based on E=constant (i.e. channel transitions in subcritical flow) may not be very sensitive to the discharge prediction method. Other problems based on S=const, like the hydraulic jump, could be more sensitive. These errors are potentially transmitted to the flow profile computations, when the dynamical equations stating conservation of energy and momentum fluxes are used. Although errors in E and S are small, the free surface profile computations depend on the estimations of $S_e(Q)$ and $S_f(Q)$. The interaction of these terms [see Eqs. (13) and (20)] with $E(Q)$ and $S(Q)$ could not produce accurate free surface profile predictions. This is examined in the next section. The SCMASSM method gives errors close to zero for both E and S.

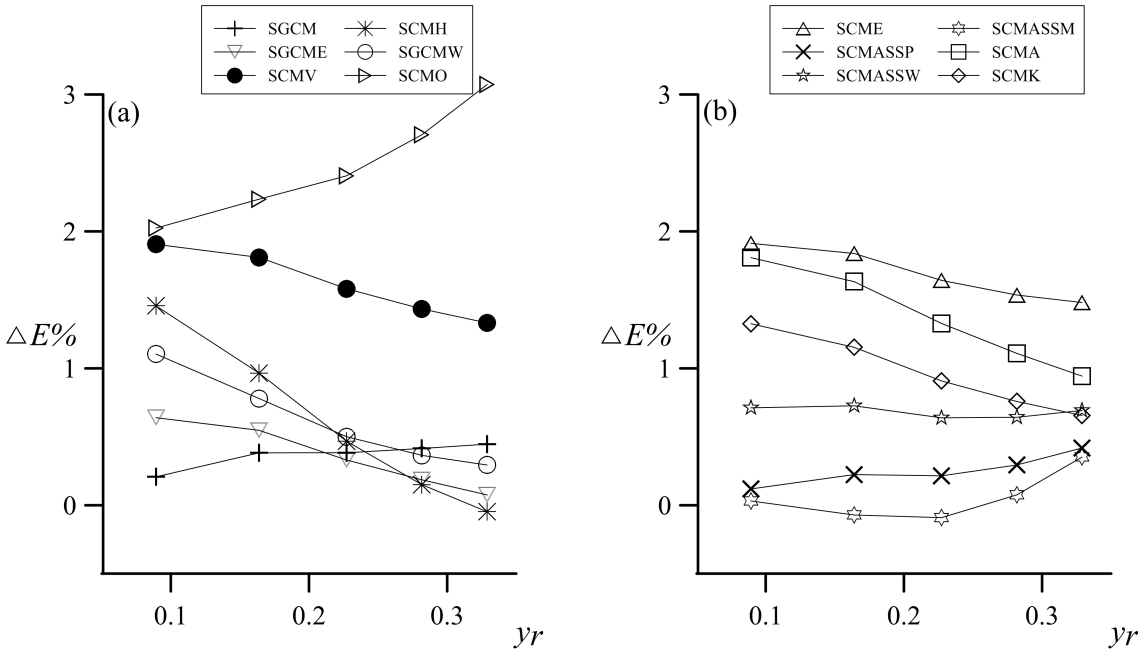

Fig. 5. Specific energy errors $\Delta E\%$ as function of y_r

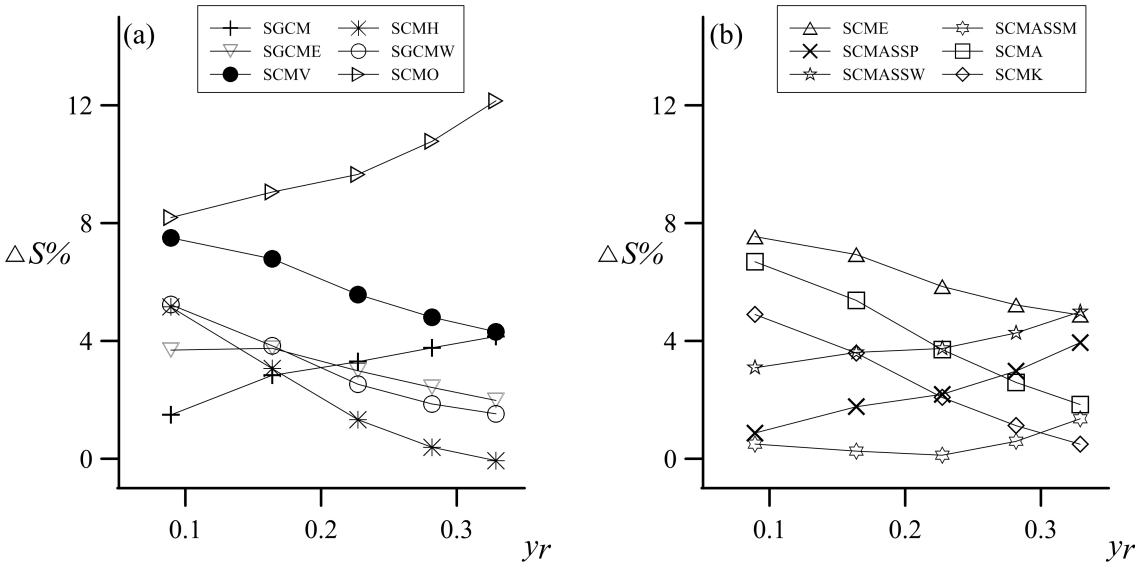

Fig. 6. Specific momentum errors $\Delta S\%$ as function of y_r

4.5. Critical depth computation

Critical depth is computed using Eqs. (23) and (24) for each discharge prediction method. Results from the energy and the momentum principles are found to differ, but the divergence is in general small. Some of the simulations performed are plotted in Fig. 6, and compared with the experimental data of Yuen (1989). Critical depth h_c and Q are scaled using y_1 and Q_u, respectively. The latter is defined as the upper discharge at which two critical depths exit (Sturm and Sadiq, 1996). The results are, in general, in agreement with the experimental data and suggest that both the energy and the momentum equations yield similar accuracy, regardless the discharge prediction methods.

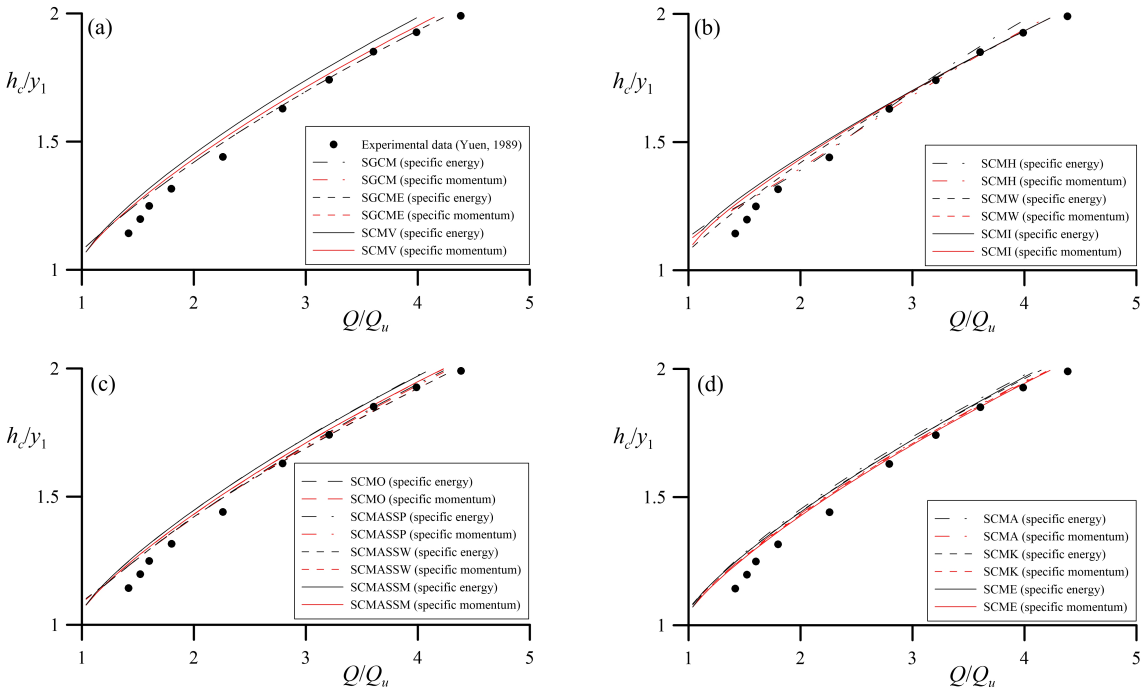

Fig. 7. Dimensionless critical depth h_c/y_1 as function of Q/Q_u calculated using the specific energy and momentum

4.6. Gradually-varied free surface profiles

An experimental time-averaged free surface profile for Q=0.113m^3/s measured by Sturm and Sadiq (1996) is considered in Fig. 8. The measurements were taken in a 17.1 m long flume with b_1=0.267m, b_2=0.934m, y_1=0.152m and S_0=0.005. The measured free surface profile in Fig. 8 corresponds to a tailwater level position of 0.243 m. Free surface profiles are simulated using the energy principle with the thirteen discharge prediction methods for the model closure of the gradient of dissipated energy $S_e(Q)$ and the velocity correction coefficient $\alpha(Q)$. Solution of Eq. (14) is done using the 4th-order Runge Kutta method (Press et al., 2007). The boundary condition to solve the first-order differential equation is taken at the experimental point in the tailwater section. The Manning coefficient n is computed for each subsection using Keulegan's equation (Sturm and Sadiq, 1996). Initial computations considering dn/dh revealed a negligible impact of this term and it is not further considered for the final analysis presented herein. Representative results for some of the methods are shown in Figs. 8(a–d). It can be observed that the interaction of main channel and flood plain is extremely important to model the flow profiles adequately. The method of Khatua et al. (2011) performs quite well. The role of the interaction of the main channel and the flood plains is clearly depicted in Fig. 8(e), where the flow profiles are computed using the standard vertical division method and then compared with same simulations using 1.19n_1 as the Manning

n in the main channel. This empirical factor in n_1 was introduced by Sturm and Sadiq (1996) to account empirically for the linear momentum transfer effects between the main channel and the flood plains in their experiments. Thus, Fig. 8(e) reveals that accounting for the momentum transfer results in very accurate simulations, or that if this interaction is not accounted for flow profile computation, predictions may be highly unrealistic.

The same computations are repeated using the momentum approach. Equation (21) is numerically integrated and the results are plotted in Figs. 8(a–d) for the different discharge prediction methods. Predicted free surface levels using the momentum equation are found to be overall in better agreement with the measured data than those using the energy equation for the same method. Energy and momentum simulations for other free surface profiles measured by Sturm and Sadiq (1996) are in conformity with this observation. The method SCMASSM gives good predictions for the free surface profile [Fig. 8(e)], but the method SCMK performs better [Fig. 8(d)]. Given the small deviations between both methods using the momentum principle and the better performance of SCMASSM in the former evaluations, it can be proposed for the flow profile computations.

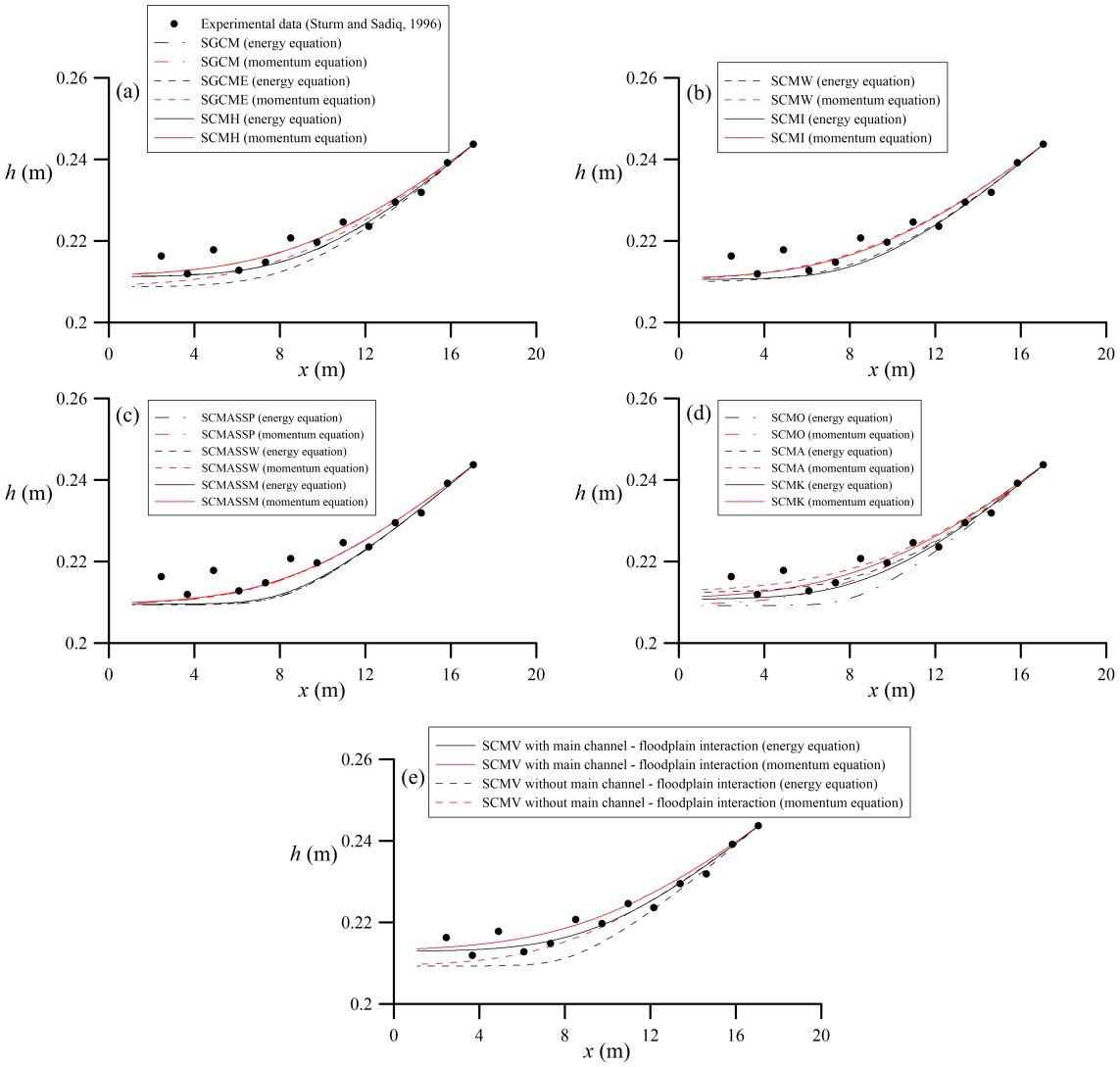

Fig. 8. Gradually-varied water surface profiles using the energy and momentum equations

4.7. Rapidly-varied free surface profiles

An experimental free surface profile for a free overfall for Q=0.113m^3/s measured by Sturm and Sadiq (1996) is presented in Fig. 9. The discharge is outside the range of multiple critical depths, and the flow profile is therefore one-dimensional. It is well known that the gradually-varied flow computations cannot tackle this kind of flow profile (Hager and Hutter, 1984a, b), where streamlines at the fall are highly curvilinear. In addition, upstream of the free overfall, a wave train around the normal depth is revealed from the experiments. This wavy free surface cannot be explained by using the gradually-varied flow theory (Hager and Hutter, 1984b). Simulations are performed using the new higher-order specific energy equation given by Eq. (33). Variation of E along the x-direction is generally given by the dynamic equation, Eq. (13). Both equations can be written as a system of three first-order ordinary differential equations

for the unknowns $h(x)$, $h_x(x)$ and $E(x)$, that can be solved using the 4th-order Runge-Kutta method (Press et al., 2007). Three boundary conditions are needed to solve the resulting system of differential equations. The flow depth at the first experimental point (x=2.47 m) is used as a boundary condition. The flow depth at the brink of the free overfall (x=17.1 m) is used as a second boundary condition. The specific energy at the boundary section upstream from the free overfall is estimated from Eq. (33), neglecting the flow curvature. At this section, however, h_x is unknown. The system of equations is then solved using a shooting approach. A value of h_x is assumed at the upstream flow section and the system of equations is then integrated up to the brink section. The flow depth computed there is, therefore, compared with the measured value; and if the results do not match, then the process is repeated with a new value of h_x. The process continues until a convergence within a prescribed tolerance is reached. Computations are done using the vertical division method without an interaction of main channel and flood plains, and also modelling the interaction effects with the main channel Manning n adjusted as $1.19n_1$. Computational results are presented in Fig. 9. The first notable aspect is that the higher-order energy model with interaction effects is capable to produce a realistic flow profile taking the upstream and brink depths as boundary conditions. Upstream of the brink, a wave train appears with oscillations around the normal depth with wave-amplitude that is dissipated as the flow approaches to the brink section. Experimental measurements indicate also an upstream wave train that is attenuated as the flow approaches to the brink. The agreement between the measured and the simulated profiles can only be regarded as fair, but the main flow features of the flow, namely, the wave train and the drawdown curve at the overfall are correctly accounted for by the new higher-order theory. Predicted wave-amplitude is also quite close to the experimental measurements. The flow profile without interaction effects is unrealistic, indicating the important interaction of the lateral momentum transfer and the streamwise energy balance when the vertical velocity is accounted for.

Following the same technique, the higher-order specific momentum, Eq. (30), is solved coupled with Eq. (20) for the variation of S in the x-direction. Results for the same test case are presented in Fig. 9 with and without interaction effects. Likewise the energy computations, the momentum approach with interaction effects provides a realistic flow profile; whereas the results without interaction effects are not in agreement with the experimental results. Given the reduced wave-amplitude, some

improvements of the momentum approach over energy formulations appear to be evident.

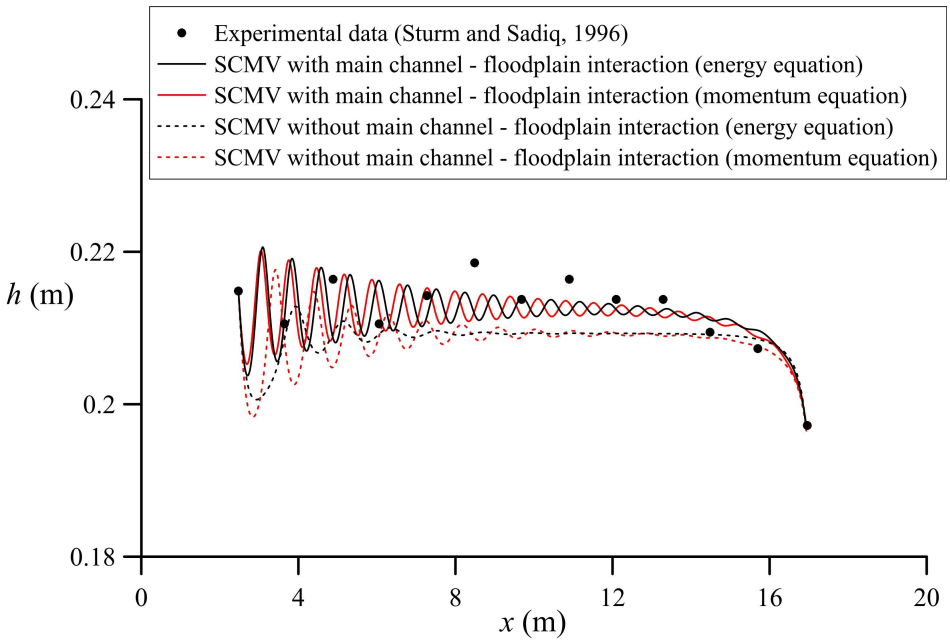

Fig. 9. Rapidly-varied water surface profiles using the energy and momentum equations for flow profile with free overfall

Another test case for the same discharge and a different tailwater level is considered in Fig. 10, where the corresponding simulations using the energy and the momentum higher-order models are plotted, respectively. In this experimental configuration, the tailgate was regulated to raise the tailwater level. No free overfall exits in this case, and the downstream boundary condition is taken as the free surface level at the tailwater section. This flow problem is presented in Fig. 8 using the gradually-varied flow theory. In the current test, the upstream wave train is attenuated in the downstream direction due to friction, but close to the tailwater section, a wavy flow profile is still evident. Wave-amplitude of the simulations is in fair agreement with experimental observations. Like the former test case (Fig. 9), the results without interaction effects between the main channel and the flood plain are unrealistic, and simulations using the momentum principle appear to be more accurate.

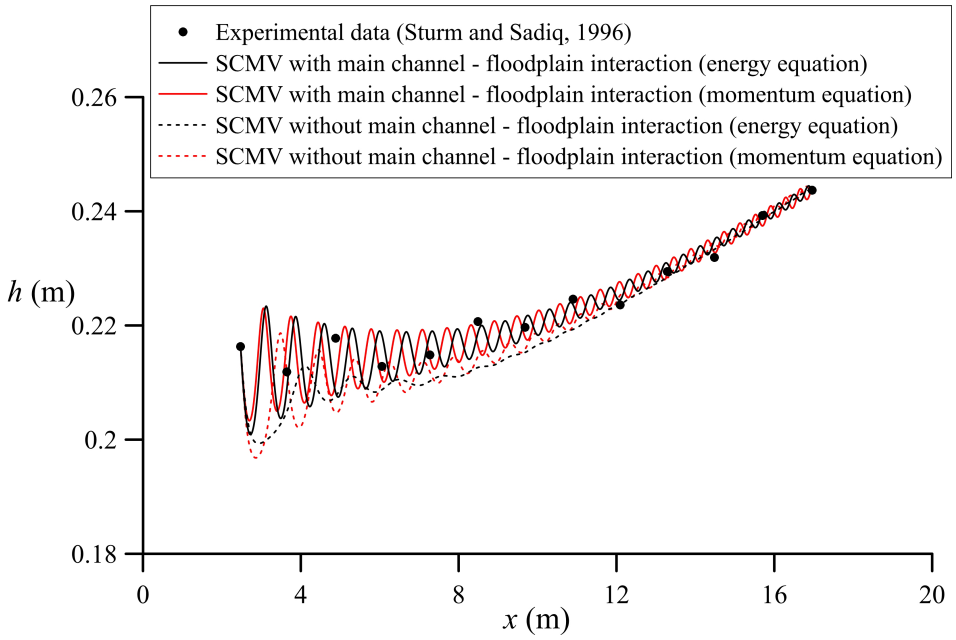

Fig. 10. Rapidly-varied water surface profiles using the energy and momentum equations for flow profile with high tailwater level

To show the improvement of higher-order energy and momentum models over gradually-varied flow theory, both models are compared in Fig. 11 for the flow profile of a free overfall. The simulated rapidly-varied flow profile using the energy equation with interaction effects is presented along with the experimental results. The gradually-varied flow equation, Eq. (14), is solved with interaction effects ($1.19n_1$) taking the critical depth as a boundary condition. Computations started in the upstream direction at a distance $4h_c$ from the free overfall (Chow, 1959). Comparison of both theories in Fig. 15 indicates that the gradually-varied flow theory simulates a monotonic increase in flow profiles in the upstream direction, being asymptotic to the uniform flow condition. Experimental observations, however, show clear oscillations around the normal depth, that in turn, is predicted theoretically by the rapidly-varied flow theory. Gradually-varied flow computations start away from the free overfall, given that this model cannot simulate the flow profiles there. In contrast, the new rapidly-varied flow theory simulates the drawdown curve near the free overfall. Overall, the gradually-varied flow theory can only be used to simulate the flow in a limited portion of the computational domain with the results that are not physically in agreement with the observations. In contrast, the rapidly-varied flow model simulates the flow in the whole computational domain and provides results that are physically in agreement with the observations. The relevant simulations using the momentum principle are presented in Fig. 11, supporting the previous discussion.

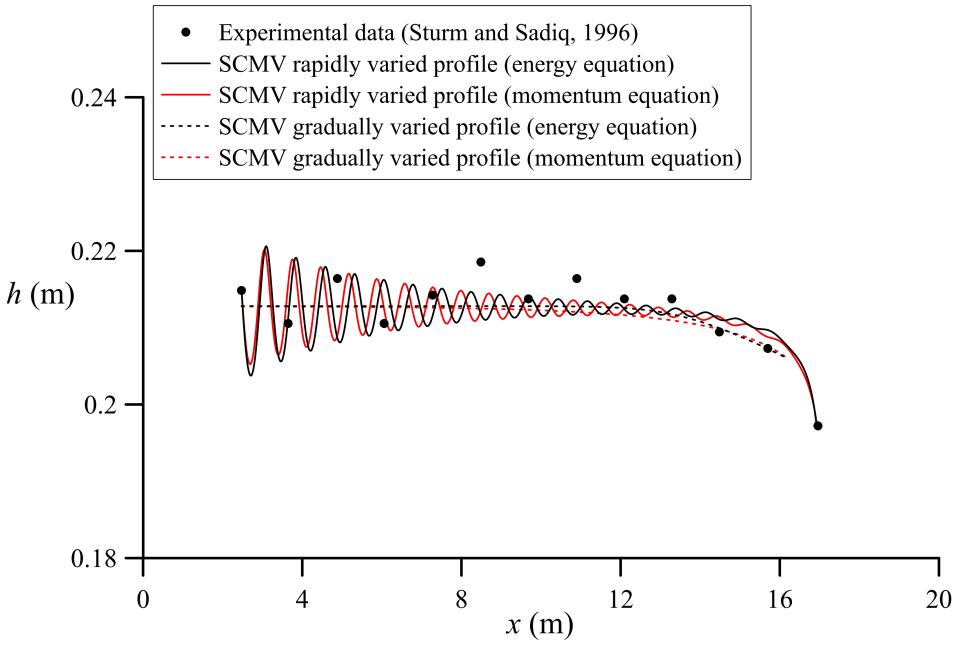

Fig. 11. Comparison of gradually-varied and rapidly-varied flow theories using the energy and momentum equations for flow profile with free overfall

In this study a spatial step size of 1mm was selected for application of the Runge-Kutta integration. A reduction of the spatial step below this value produced identical results, thereby indicating that all computations presented using gradually varied and rapidly-varied flow models are grid size independent.

5. Conclusions

In this study, thirteen discharge prediction methods are used to evaluate its impact on the computations of gradually-varied flow in compound channels. It is found that the interaction of main channel and flood plains is not only essential for discharge prediction, but also for the computation of velocity correction coefficients and free surface profiles. A method of interaction is therefore required, and the method of Wormleaton and Merrett (1990) is found to perform well. However, the impact on energy and momentum fluxes is small. In general, the dynamic computations based on momentum provide better results than the relevant simulations using the energy principle. It is suggested that the gradually-varied flow computations in natural channels should be a momentum-based computation accounting for the interaction effects. The results presented herein could assist to revise the codes used in hydrological computations, like HEC-RAS. A generalized definition of the compound channel Froude number based on the momentum equation is given for that purpose.

Gradually-varied flow computations can only be regarded as approximate mathematical solutions, not necessarily in agreement with the real physical behavior of the flow. A new higher-order theory for dynamical computations by using energy and momentum equations in flows through compound channels is presented. The new theory was found to describe the free surface profile in compound channels at the drawdown of free overfalls and at the wave train around the normal depth. These physical aspects cannot be modeled by using the gradually-varied flow computations as detailed herein. Results using a momentum approach are found to be better than using the energy equation. The new higher-order theory opens a new research direction in flows through compound channels, so far limited to the gradually-varied flow conditions only. More experimental research is needed with detailed observation of the flow profiles. The new theory then could be further expanded to more complex flow conditions, including depth-averaged two-dimensional simulations in the horizontal plane, and mobile-bed conditions with sediment transport.

Appendix A. Momentum based compound channel Froude number

Chaudhry and Bhallamudi (1988) defined the compound channel Froude number based on the characteristic directions of the unsteady momentum equation as

$$\mathsf{F}_c = \beta U \left[\frac{gA}{T} + U^2 \left(\beta^2 - \beta + \frac{A}{T} \frac{\mathrm{d}\beta}{\mathrm{d}h} \right) \right]^{-1/2} \tag{37}$$

Using $U=Q/A$, Eq. (37) can be rewritten after some manipulations as

$$\mathsf{F}_c^2 + \left(\mathsf{F}_c^2 - 1 \right) \beta^2 \frac{Q^2 T}{gA^3} - \mathsf{F}_c^2 \left(\beta \frac{Q^2 T}{gA^3} - \frac{Q^2}{gA^2} \frac{\mathrm{d}\beta}{\mathrm{d}h} \right) = 0 \tag{38}$$

The definition of F_β for flow profile computations is

$$\mathsf{F}_\beta = \left(\frac{\beta Q^2 T}{gA^3} - \frac{Q^2}{gA^2} \frac{\mathrm{d}\beta}{\mathrm{d}h} \right)^{1/2} \tag{39}$$

which is inserted into Eq. (38) to produce

$$\mathsf{F}_c^2 + \left(\mathsf{F}_c^2 - 1 \right) \beta^2 \frac{Q^2 T}{gA^3} - \mathsf{F}_c^2 \mathsf{F}_\beta^2 = 0 \tag{40}$$

For critical flow conditions given by vertical characteristic lines, that is, $\mathrm{d}x/\mathrm{d}t=0$, $\mathsf{F}_c=1$ (Chaudhry and Bhallamudi, 1988). Equation (40) then yields $\mathsf{F}_\beta=1$. It means that both the momentum based compound channel Froude numbers results in an identical critical flow condition, demonstrating the equivalence of $\mathrm{d}x/\mathrm{d}t=0$ and $\mathrm{d}S/\mathrm{d}h=0$ to define the critical flow. However, both Froude numbers are not equivalent for flow conditions different from critical. Therefore, the correct momentum based Froude number in compound channels for the flow profile computations is given by Eq. (39). Following the developments of Blalock and Sturm (1981, 1983) for the specific energy, F_β can be written as

$$\mathsf{F}_\beta{}^2 = \frac{2Q^2}{3gAK^2} \left(\frac{\tau_2 \tau_3}{K} - \tau_1 \right) \tag{41}$$

where

$$\tau_1 = \sum_i \left[\left(\frac{k_i}{a_i} \right)^2 \left(4t_i - 2r_i \frac{\mathrm{d}p_i}{\mathrm{d}h} \right) \right] \tag{42}$$

$$\tau_2 = \sum_i \left(\frac{k_i^{\,2}}{a_i} \right) \tag{43}$$

$$\tau_3 = \sum_i \left[\left(\frac{k_i}{a_i} \right) \left(5t_i - 2r_i \frac{\mathrm{d}p_i}{\mathrm{d}h} \right) \right] \tag{44}$$

Appendix B. Pressure distribution in rapidly-varied flow

The Euler equation in *z*-direction, that is normal to the channel bed, is (Serre, 1953, Montes, 1998) (Fig. 1b)

$$\frac{u}{g}\frac{\partial v}{\partial x}+\frac{v}{g}\frac{\partial v}{\partial z}+\frac{1}{\rho g}\frac{\partial p}{\partial z}=-\cos\theta \tag{45}$$

which can be integrated to obtain the pressure distribution. Using the differential identity

$$\frac{\partial}{\partial x}(uv)=v\frac{\partial u}{\partial x}+u\frac{\partial v}{\partial x} \tag{46}$$

Eq. (45) is then rewritten as

$$\frac{1}{g}\frac{\partial(uv)}{\partial x}-\frac{v}{g}\frac{\partial u}{\partial x}+\frac{v}{g}\frac{\partial v}{\partial z}=-\frac{\partial}{\partial z}\left(\frac{p}{\rho g}+\cos\theta\right) \tag{47}$$

Further, using the continuity equation

$$\frac{\partial u}{\partial x}+\frac{\partial v}{\partial z}=0 \tag{48}$$

Eq. (47) is transformed to

$$\frac{1}{g}\frac{\partial(uv)}{\partial x}+2\frac{v}{g}\frac{\partial v}{\partial z}=-\frac{\partial}{\partial z}\left(\frac{p}{\rho g}+\cos\theta\right) \tag{49}$$

which is integrated to yield

$$p(z)=\rho g(h-z)\cos\theta-\rho v^2+\rho\frac{\partial}{\partial x}\int_z^h vu\mathrm{d}z \tag{50}$$

Here, the Leibnitz rule and the bed kinematic boundary condition $v_s(z=0)=0$ are used. To integrate Eq. (50), an approximation for the velocity components (u, v) is required. In this research, the simplest basic approach for flow in compound channels is elaborated. In flow through a single channel having significant curvature in a vertical plane, it is permissible to assume that the vertical variation of flow velocity is neglected; thereby the approximation of u by its depth-averaged value U is given by

$$U=\frac{1}{h}\int_0^h u(z)\mathrm{d}z \tag{51}$$

However, the significant departure of the vertical distribution of pressure from the hydrostatic law must be accounted for. This is the usual approximation when deriving Boussinesq-type equations in open channel flows (Serre, 1953; Montes, 1998; Chaudhry, 2008). The approximation $u \approx U$ is in agreement with the gradually-varied flow computations, where the depth-averaged velocity is used in the main channel and the flood plains. Using this approach, the continuity equations yields the vertical velocity profile from Eq. (48) as

$$v = -\frac{\partial U}{\partial x} z \tag{52}$$

Inserting it into Eq. (50), yields

$$p(z) = \rho g (h - z) \cos\theta - \rho \left(U_x z\right)^2 - \rho \frac{\partial}{\partial x} \int_z^h U U_x z dz \tag{53}$$

Integrating Eq. (53), results in

$$p(z) = \rho g (h - z) \cos\theta - \rho U_x^2 z^2 - \rho \left(U_x^2 + U U_{xx}\right) \left(\frac{h^2 - z^2}{2} \right) - \rho U U_x h h_x \tag{54}$$

where $U_x = \partial U / \partial x$ and $U_{xx} = \partial^2 U / \partial x^2$. In flow through compound channels, there is a significant variation of the depth-averaged velocity U along the cross-section (from the main channel to the flood plain). In the new Boussinesq-type equations, this effect is accounted for, like in former gradually-varied flow computations, using energy (α) and momentum (β) coefficients. For the inclusion of non-hydrostatic effects in the one-dimensional model equations, the simplest approach is adopted, thereby using the cross-sectional averaged velocity as an approximation to find a mathematically closed form of the pressure distribution. Then, the depth-averaged continuity yields

$$\frac{\partial}{\partial x}(U h) = h U_x + U h_x = 0 \tag{55}$$

Inserting Eq. (55) into Eq. (54), finally yileds

$$\frac{p}{\gamma} = (h - z) \cos\theta + \left(U_x^2 - U U_{xx}\right) \left(\frac{h^2 - z^2}{2g} \right) \tag{56}$$

6. Notation

A = total flow area (m^2)

A_h = $\partial A/\partial h$ (m)

A_{hh} = $\partial^2 A/\partial h^2$ (–)

a_i = subsection flow area (m^2)

b_1 = main channel bottom width (m)

b_2 = floodplain bottom width (m)

E = specific energy (m)

F = friction factor (–)

F_α = compound channel Froude number based on specific energy (–)

F_β = compound channel Froude number based on specific momentum (–)

F_c = compound channel Froude number (–)

g = gravitational acceleration (m/s^2)

h = maximum flow depth in compound section (m)

h_c = critical depth (m)

I = moment of inertia of cross-section (m^4)

K = total conveyance (m^3/s)

k_i = subsection conveyance (m^3/s)

Q = total discharge (m^3/s)

Q_u = upper discharge for multiple critical depths (m^3/s)

n = Manning coefficient ($m^{-1/3}s$)

n_i = subsection Manning coefficient ($m^{-1/3}s$)

n_1 = main channel Manning coefficient ($m^{-1/3}s$)

n_2 = floodplain Manning coefficient ($m^{-1/3}s$)

n_e = equivalent Manning coefficient ($m^{-1/3}s$)

P = total wetted perimeter (m)

p_i = subsection wetted perimeter (m)

p =pressure (Pa)

R = hydraulic radius (m)

r_i = subsection hydraulic radius (m)

S = specific momentum (m^3)

S_0 = channel slope (-)

S_e = gradient of dissipated energy (–)

S_f = friction slope (–)

t = time (s)

T = total top width (m)

t_i = subsection top width (m/s)

U = mean flow velocity (m/s)

U_c = mean flow velocity in main channel (m/s)

U_f = mean flow velocity in flood plain (m/s)

u_i = subsection flow velocity (m/s)

u = point velocity (m/s)

v = vertical velocity (m/s)

X = wetted perimeter corrector parameter (m)

x = longitudinal coordinate along the channel bed (m)

y = floodplain depth (m)

y_1 = main channel bank-full depth (m)

y_r = relative compound channel depth (–)

z = coordinate normal to the channel bed, positive upwards (m)

α = Coriolis coefficient (–)

β = Boussinesq coefficient (–)

λ = shear force percentage for floodplain perimeter (–)

γ = specific weight of water (N/m^3)

ρ = density of water (kg/m^3)

σ_1, σ_2, σ_3 = compound channel Froude number terms in energy equation (–)

τ_1, τ_2, τ_3 = compound channel Froude number terms in momentum equation (–)

τ_a = apparent shear stress (Pa)

$\overline{z}$ = distance from the free surface to the total-section centroid (m)

θ = angle of channel bed with the horizontal (–)

7. References

Ackers, P. 1993a. Stage-Discharge functions for two-stage channel: the impact of new research. Water and Environment Journal. 7(1), 52–61.

Ackers, P. 1993b. Flow formulae for straight two-stage channels. Journal of Hydraulic Research. 31(4), 509–531.

Blalock, M.E., Sturm, T.W., 1981. Minimum specific energy in compound open channel. Journal of the Hydraulics Division. 107(6), 699–717.

Blalock, M.E., Sturm, T.W., 1983. Closure to Minimum specific energy in compound open channel. Journal of Hydraulic Engineering. 109(3), 483–487.

Bose, S.K., Dey, S., 2007. Curvilinear flow profiles based on Reynolds averaging. Journal of Hydraulic Engineering. 133(9), 1074–1079.

Bose, S.K, Dey, S., 2009. Reynolds averaged theory of turbulent shear flows over undulating beds and formation of sand waves. Physical Review E. 80(3), 036304–1/036304–9.

Bousmar, D., Zech, Y., 1999. Momentum transfer for practical flow computation in compound channels. Journal of Hydraulic Engineering. 125(7), 696–706.

Brutsaert, W., 2005. Hydrology: An Introduction. Cambridge University Press, Cambridge, UK.

Castro-Orgaz, O., Hager, W.H., 2011. Turbulent near-critical open channel flow: Serre's similarity theory. Journal of Hydraulic Engineering. 137(5), 497–503.

Chatila, J.G., 1992. Application and comparison of dynamic routing models for unsteady flow in simple and compound channels. M. A. Sc. Thesis. University of Ottawa.

Chatila, J.G. and Townsend, R.D., 1996. Discharge estimation methods for steady compound channel flows. Canadian Water Resources Journal. 21(2), 131–137.

Chaudhry, M.H., 2008. Open-channel flow, 2nd ed. Springer, New York.

Chaudhry, M. and Bhallamudi, S., 1988. Computation of critical depth in symmetrical compound channels. J. Hydraulic Research. 26(4), 377–396.

Chow, V.T., 1959. Open channel hydraulics. McGraw-Hill, New York.

Chow, V.T., Maidment, D.R., Mays, L.W., 1988. Applied Hydrology. Tata McGraw-Hill, New York.

Clemmens, A. J., Wahl, T. L., Bos, M. G., and Replogle, J. A., 2001. Water measurement with flumes and weirs. Publication #58, International Institute for Land Reclamation and Improvement, Wageningen, The Netherlands. 382 p.

Costabile, P., Macchione, F., 2012. Analysis of one-dimensional modeling for flood routing in compound channels. Water Resources Management. 26, 1065–1087.

Dey, S., 2014. Fluvial hydrodynamics: Hydrodynamic and sediment transport phenomena. Springer, Berlin.

Dey, S., Lambert, M.F., 2006. Discharge prediction in compound channels by end depth method. Journal of Hydraulic Research. 44(6), 767–776.

Dracos, T., Hardegger, P., 1987. Steady uniform flow in prismatic channels with flood plains. Journal of Hydraulic Research. 25(2), 169–185.

Field, W.G., Lambert, M.F., Williams, B.J., 1998. Energy and momentum in one dimensional open channel flow. Journal of Hydraulic Research. 36(1), 29–42.

French, R.H., 1987. Open channel hydraulics. McGraw-Hill, New York.

Hager, W.H., Hutter, K., 1984a. Approximate treatment of plane channel flow. Acta Mechanica. 51(1–2), 31–48.

Hager, W.H., Hutter, K., 1984b. On pseudo-uniform flow in open channel hydraulics. Acta Mech. 53(3–4), 183–200.

Hosoda, T., Tada, A., 1994. Free surface profile analysis on open channel flow by means of 1-D basic equations with effect of vertical acceleration. Annual Journal of Hydraulic Engineering. JSCE, 38, 457–462.

Jain, S.C., 2001. Open channel flow. John Wiley & Sons, New York.

Khan, A.A., Steffler, P.M., 1996. Vertically averaged and moment equations model for flow over curved beds. Journal of Hydraulic Engineering. 122(1), 3–9.

Khatua, K.K., Patra, K.C., Mohanty, P.K., 2011. Stage-Discharge prediction for straight and smooth compound channels with wide floodplains. Journal of Hydraulic Engineering. 138(1), 93–99.

Knight, D. W., Abril, J.B., 1996. Refined calibration of a depth-averaged model for turbulent flow in a compound channel. Proceedings of the Institution of Civil Engineers, Water, Maritime and Energy, 118(3), 151–159.

Knight, D.W., Demetriou, J.D., 1983. Floodplain and main channel flow interaction. Journal of Hydraulic Engineering. 109(8), 1073–1092.

Kordi, E., Ayyoubzadeh, S.A., Ahmadi, M.Z., Zahiri, A., 2009. Prediction of the lateral flow regime and critical depth in compound channels. Canadian Journal of Civil Engineering. 36, 1–13.

Lambert, M. F., Sellin, R.H., 1996. Discharge prediction in straight compound channels using the mixing length concept. Journal of Hydraulic Research. 34(3), 381–393.

Lee, P.J., Lambert, M.F., Simpson, A.R., 2002. Critical depth prediction in straight compound channels. Proceedings of the Institution of Civil Engineers, Water, Maritime and Energy. 154(4), 317–332.

Montes, J.S., 1998. Hydraulics of open channel flow. ASCE, Reston Va.

Myers, W.R.C., 1978. Momentum transfer in a compound channel. Journal of Hydraulic Research. 16(2), 139–150.

Petryk, S., Grant, E. U., 1978. Critical flow in rivers with flood plains. Journal of the Hydraulics Division. 104(5), 583–594.

Press, W.H., Teukolsky, S.A., Vetterling, W.T., Flannery, B.P., 2007. Numerical recipes: The art of scientific computing, 3rd ed. Cambridge Univ. Press, Cambridge.

Prinos, P., 1985. A study of momentum transfer phenomena in compound channel flows. M. A. Sc. Thesis. University of Ottawa.

Prinos, P., Townsend, R.D., 1984. Comparison of methods for predicting discharge in compound open channels. Advances in Water Resources. 7(4), 180-187.

Rajaratnam, N., Ahmadi, R.M., 1981. Hydraulics of channels with flood-plains. Journal of Hydraulic Research. 19(1), 43–59.

Schoellhamer, D. H., Peters, P.C., Larok, B.E., 1985. Subdivision Froude Number. Journal of Hydraulic Engineering. 111(7), 1099–1104.

Sellin, R. H. J., 1964. A laboratory investigation into the interaction between the flows in the channel of a river that is over its floodplain. La Houille Blanche. 7, 793–801.

Serre, F., 1953. Contribution à l'étude des écoulements permanents et variables dans les canaux (Contribution to the study of steady and unsteady channel flows). La Houille Blanche. 8(6–7), 374-388; 8(12), 830–887.

Shiono, K., Knight, D. W., 1991. Turbulent open channel flows with variable depth across the channel. Journal of Fluid Mechanics. 222, 617–646.

Sturm, T.W., Sadiq, A., 1996. Water surface profiles in compound channel with multiple critical depths. Journal of Hydraulic Engineering. 122(12), 703–709.

Sturm, T.W., 2001. Open channel hydraulics. McGraw-Hill, New York.

Wormleaton, P.R., Allen, J., Hadjipanos, P., 1982. Discharge assessment in compound channel flow. Journal of the Hydraulics Division. 108(9), 975–994.

Wormleaton, P.R., Hadjipanos, P., 1985. Flow distribution in compound channels. Journal Hydraulic Engineering. 111(2), 357–361.

Wormleaton, P.R., Merrett, D.J., 1990. An improved method of calculation for steady uniform flow in prismatic main channel/flood plain sections. Journal of Hydraulic Research. 28(2), 157–174.

Yen, C.L., Overton, D.E., 1973. Shape effects on resistance in floodplain channels. Journal of the Hydraulics Division. 99(HY1), 219–238.

Yuen, K., 1989. A study of boundary shear stress, flow resistance and momentum transfer in open channels with simple and compound trapezoidal cross section. PhD Thesis. University of Birmingham, U.K.

Yuen, K., Knight, D.W., 1990. Critical flow in a two stage channel. In Proceedings of the International Conference on River Flood Hydraulics, Wallingford, U.K., 17–20 September, John Wiley and Sons Ltd, pp. 267–276, paper G4.

Appendix II

Non-hydrostatic dam break flows I: physical equations and numerical schemes

Francisco Nicolás Cantero-Chinchilla[1]; Oscar Castro-Orgaz[2]; Subhasish Dey[3]; and Jose Luis Ayuso[4]

Accepted for publication by *Journal of Hydraulic Engineering.* Impact factor (JCR 2014): 1.621 / Q1 (28/125 Civil Engineering)

Abstract

Modeling of dam break flows is frequently required in civil and environmental engineering, given the risk associated with this catastrophic flow. Typically, model predictions are conducted using the Saint-Venant hydrostatic theory, which, however, can lead to unrealistic predictions. The prediction of the amplitude of non-hydrostatic waves generated during dam break flows is an important engineering problem, given the risk of overtopping of flow in manmade canals, or the increasing of flooding areas in natural watercourses. The weakly non-dispersive and fully non-linear Serre equations are suitable choice for modelling these flows, but there is a lack of a systematic assessment of this system of equations for dam break flow modelling reported in the literature. In this paper, the Serre equations are applied to dam break flows over horizontal rigid bottoms, whereas in the second part of this research, the non-hydrostatic dam break waves over erodible beds are considered. Here, a high resolution finite volume model is developed, where a suitable time stepping scheme is systematically investigated. The impact of the vertical pressure distribution shape, non-linear terms in the equations, and the enhancement of the linear frequency dispersion are examined in detail. The model is successfully tested against the experimental data, a solitary wave

[1]PhD student, University of Cordoba, 14071 Cordoba, Spain. E-mail: z12cachf@uco.es
[2]Professor, University of Cordoba, 14071 Cordoba, Spain. E-mail: ag2caoro@uco.es (author for correspondence)
[3]Professor, Department of Civil Engineering, Indian Institute of Technology Kharagpur, West Bengal 721302, India; and Adjunct Professor, Physics and Applied Mathematics Unit at Indian Statistical Institute Kolkata, Bengal 700108, India. E-mail: sdey@iitkgp.ac.in
[4]Professor, University of Cordoba, 14071 Cordoba, Spain. E-mail: ir1aymuj@uco.es

propagation test, and the 3D simulations. The results obtained from finite volume method are further compared with those obtained from finite element and finite difference methods available in the literature.

1. Introduction

Dam break waves originate from overtopping or foundation failure among others, thereby leading to a natural hazard that may cause huge damage. Investigation of non-hydrostatic pressure distribution effects on dam break flows is not only relevant to the real failure of dams, but also to the instantaneous gate operations in canals (Mignot and Cienfuegos 2009). Dam break flood waves are typically modelled using the Saint-Venant equations (De Almeida and Franco 1994; Chaudhry 2008). These flow equations imply a hydrostatic pressure distribution and a uniform streamwise velocity distribution. For engineering practice, this approach is routinely adopted, typically using finite difference (Chaudhry 2008) or finite volume schemes (Toro 2001) to find a numerical solution. The discontinous Galerkin method is becoming a useful tool, combining in a hybrid technique the advantages of the finite element and finite volume methods (Khan and Lai 2014). However, the hydrostatic pressure approach can lead to physically unrealistic results (Kim and Lynett 2011). Dam break waves propagate both in the upstream and the downstream directions forming a rarefaction wave and a bore front (Fig. 1) (Stoker 1958). The Saint-Venant equations predict a parabolic rarefaction fan and a sharp shock front. However, the non-hydrostatic pressure provokes undulations on the flow profile, not predicted by the Saint-Venant equations (Soares-Frazão and Zech 2002; Kim and Lynett 2011). Some of the Boussinesq-type models available in the literature suffer from two limitations, namely, the modelling of weak curvature effects (small amplitude waves) and non-breaking wave conditions. Therefore, it is necessary to consider full non-linearity (arbitrary amplitude waves) and wave breaking model in the Boussinesq-type equations. Mohapatra and Chaudhry (2004) ellaborated a higher order prediction of dam break flood waves by applying a finite-difference predictor-corrector scheme to the Serre equations. The Serre equations are a Boussinesq-type system of equations for modelling weakly dispersive and fully non-linear non-hydrostatic waves (Serre 1953; Su and Gardner 1969; Batherlemy 2004). These equations were originally derived by Serre (1953) assuming that the velocity field is represented by the depth-averaged horizontal velocity, and a linear vertical velocity profile. Later, Su and Gardner (1969) re-derived the systems based on the potential flow

assumption, and demonstrated that the horizontal velocity profile of the Serre equations is non-uniform. Using a Picard iteration method, Castro-Orgaz and Hager (2014) found that this profile is parabolic. Solving the Serre equations, Mohapatra and Chaudhry (2004) found that the position of the shock front was very close to that predicted by the Saint-Venant equations. Mignot and Cienfuegos (2009) applied a finite volume model to the Serre equations and simulated dam break flows accounting for the wave breaking based on diffusivity-like terms. They obtained good results. The frequency dispersion for a shallow flow implies that the celerity of propagation of small amplitude Serre-type waves is different from that of the shallow water (hydrostatic) waves, and close to the exact relation obtained from the Euler equations (Nwogu 1993; Batherlemy 2004). However, in shallow flow, the non-linearity implicit in the Serre equations is by far more important than the frequency dispersion. It means that finite amplitude waves are generated at the shock front, provoking higher flow depths at the wave front than those predicted by the Saint-Venant theory. Problems like overtopping of flow in canals due to sudden gate operation (Mignot and Cienfuegos 2009) or the spreading of the flood inundation area in rivers are therefore to be expected. Further, structures implanted in a natural watercourse, such as bridge piers, experiences dynamic forces as the flood wave propagates, where non-hydrostatic pressure can play a leading role. Therefore, it is preferable to compute dam break flood waves using non-hydrostatic models. If under a given flow condition the flood wave is essentially hydrostatic, then this should be an automatic result of the non-hydrostatic model rather than an external patching of the modeller between the hydrostatic and the non-hydrostatic computations. The non-hydrostatic model should therefore account for a smooth transition from non-hydrostatic to hydrostatic flow conditions. This issue was extensively investigated in coastal engineering applications for the propagation of breaking waves (Tonelli and Petti 2009; Bonneton et al. 2011; Tissier et al. 2012; Shi et al. 2012). The computational approach is based on the assumption that when the dispersive terms become less important, the results from the Boussinesq equations should collapse to those from the Saint Venant equations.

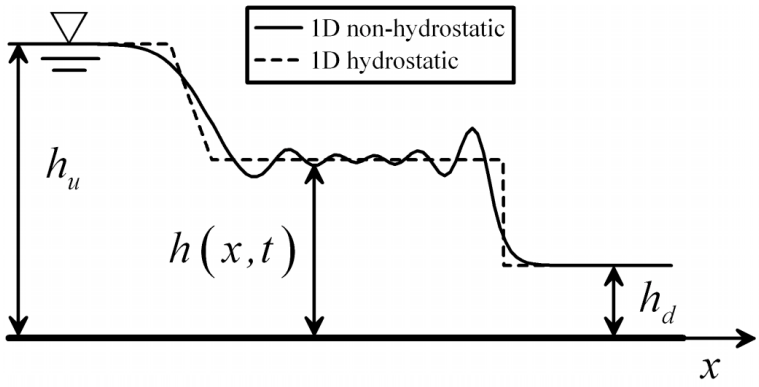

Fig. 1. Definition sketch of non-hydrostatic dam break flow

Three-dimensional (3D) numerical computations are used to account for non-hydrostatic flow simulations (Marsooli and Wu 2014). However, the depth-averaged models are also used to simulate non-hydrostatic open channel flows (Khan and Steffler 1996a,b), which are computationally less expensive. Despite the potentiality of the Serre-type models to simulate the dam break flood waves, only the isolated work of Mignot and Cienfuegos (2009) is available. However, issues such as the selection of the time-stepping scheme, enhancement of the dispersion relation, and the shape of the vertical pressure distribution are not systematically assessed in a single and structured work. Further, for the case of dam break waves over erodible beds, to the best of the authors' knowledge, there is not a single study considering the non-hydrostatic simulations with depth-averaged models. This research is organized in two companion papers. In this paper, the non-hydrostatic dam break waves over rigid bottoms are systematically investigated as described below. In Cantero-Chinchilla et al. (2016, companion paper) the physical equations and numerical schemes are extended to simulate the non-hydrostatic dam break flow waves over erodible beds.

Here, we consider the propagation of dam break flood waves over rigid and horizontal bottoms. First, the physical equations need to be assessed, given that a number of "Boussinesq-type" models can be used a priori. The following issues are therefore in need of assessment:

1. The classical Serre equations are obtained assuming that the streamwise velocity distribution is uniform with depth (Serre 1953; Castro-Orgaz et al. 2015), thereby leading to a parabolic pressure distribution along the vertical direction. The Serre equations are formulated in terms of the depth-averaged horizontal velocity, but not necessarily assuming a uniform horizontal velocity distribution (Su and Gardner 1969;

Cienfuegos et al. 2006). If second order dispersive terms are disregarded, then the vertical distribution for horizontal velocity is uniform and the vertical distribution for vertical velocity is linear (Cienfuegos et al. 2006). However, other modelling approximations are considered in the literature, as the linear, non-hydrostatic, vertical pressure distribution (Khan and Steffler 1996a,b). Castro-Orgaz et al. (2015) found that the shape of the vertical pressure distribution can lead to a significant difference in results when the depth-averaged non-hydrostatic models are used. Therefore, the impact of the vertical pressure distribution in 1D computations needs to be investigated for modelling the dam break waves.

2. For shallow water flows, the frequency dispersion is rather weak, given that the waves are long, with a wavelength typically greater than 6 times the flow depth (Steffler and Jin 1993). Thus, the wave amplitude prediction is the main engineering concern. The accurate prediction of the wave amplitude relies on the consideration of non-hydrostatic terms in the Serre equations originating from the convective acceleration term in the Euler equations, like $\partial^2 U/\partial x^2$ and $(\partial U/\partial x)^2$, where U is the depth-averaged velocity. However, various models available in the literature neglect some terms (Peregrine 1966; Nwogu 1993; Soares-Frazão and Zech 2002).

3. The dam break waves lead to undulations near the bore front and rarefaction wave for a ratio of the downstream (h_d) to upstream (h_u) flow depth greater, approximately, than 0.45 (Fig. 1) (De Almeida and Franco 1994). For smaller values, wave breaking at the shock front progressively suppresses the undulations. Inviscid simulations of non-hydrostatic waves using the Serre-type equations yield wave amplitudes that increase without bounds, given that the physical equations are unable to produce wave breaking. Therefore, a wave breaking model is needed to correctly propagate the dam break waves accounting for the change from a non-breaking to a breaking wave condition. This issue is extensively investigated in coastal engineering applications, where different wave breaking models are used (Schäffer et al. 1993; Kennedy et al. 2000; Cienfuegos et al. 2010). However, this issue appears to be not specifically addressed in the dam break literature to the best of the authors' knowledge.

Secondly, a robust numerical scheme is needed, but there is no methodical recommendation to select it:

4. The isolated works of Mohapatra and Chaudhry (2004) and Kim and Lynett (2011) suggested very different numerical schemes, but no critical comparison is available. Mohapatra and Chaudhry (2004) proposed to use a high-order finite difference scheme where the mixed space-time derivatives are included in the scheme with a fractional step approach. The scheme used artificial viscosity to suppress spurious oscillations originating from the Gibbs phenomenon. It had the disadvantage that the determination of the artificial viscosity is case dependent, and, therefore, universal results cannot be generated. Kim and Lynett (2011) used Boussinesq-type equations with enhanced frequency dispersion following Nwogu (1993). Detailed discussions on the enhancing of frequency dispersion were given by Barthélemy (2004) and Cienfuegos et al. (2006). Kim and Lynett (2011) used the finite volume method, computing the numerical fluxes with an approximate Riemann solver. The solution was reconstructed at each time level using a high-order MUSCL. The cost of enhancing the linear dispersion relation is to solve a more complex system of physical equations as compared to the standard Serre equations. However, given that both systems are fully non-linear, it is unclear if the solution of this enhanced system under shallow flow conditions is really necessary. The use of frequency dispersion enhanced models using the Nwogu-type approach should therefore be examined.

5. The performance of a Serre-type depth-averaged non-hydrostatic model heavily depends on the numerical scheme considered (Mohapatra and Chaudhry 2004; Kim et al. 2009; Kim and Lynett 2011; Mitsotakis et al. 2014). Mohapatra and Chaudhry (2004) applied the two-four finite difference scheme. In this scheme, numerical oscillations are suppressed by applying the artificial viscosity (Jameson et al. 1981). Mitsotakis et al. (2014) used the standard Galerkin finite element scheme and solved the Serre equations in dam break flows, obtaining accurate results. Higher-order finite volume schemes are reported in the literature. Kim et al. (2009) applied the fourth-order TVD monotone upstream centred scheme for conservation laws (MUSCL-TVD-4^{th}) (Yamamoto and Daiguji 1993) to get a high resolution scheme for the spatial reconstructing of the flow variables at the control volume interfaces. Following Erduran et al. (2005), a high-resolution scheme is required to ensure that the dispersive terms are not of the same order of magnitude than the truncation errors originating from the leading Saint-Venant type terms (Abbott 1979). However, these higher-order spatial reconstruction schemes are used in ocean research, but not so typically for non-

hydrostatic free surface flow problems in civil and environmental engineering. An exception is the work of Mignot and Cienfuegos (2009), who applied the finite volume model SERR-1D (Cienfuegos et al. 2006; 2010) to river flows with shocks.

6. The time stepping method is a crucial component of a numerical scheme. Gottlieb and Shu (1998) developed high-order TVD Runge-Kutta (TVD-RK) schemes for hyperbolic problems. The third-order TVD-RK scheme (TVD-RK3th) was applied to dam break flows with satisfactory results (Li et al. 2013). The fourth-order TVD-RK scheme (TVD-RK4th) can also be used for the time stepping scheme coupled with the MUSCL-TVD-4th spatial reconstruction. Nevertheless, the TVD-RK methods usually require low values of the Courant-Friedrichs-Lewy number (CFL) for stability, which is a disadvantage in terms of computational work. The higher-order Adams-Bashforth/Adams-Moulton (AB-AM) time stepping scheme (Wei and Kirby 1995; Wei et al. 1995; Kim et al. 2009; Kim and Lynett 2011) shows stability with moderate CFL values (typically greater than 0.5). It has accuracy to fourth-order. This time stepping scheme is also used in ocean research, but it is not commonly used in civil engineering. An exception is the work of Maleki and Khan (2015), where the efficiency and accuracy of several time-stepping schemes, including the Adams-Bashforth scheme, are evaluated for dam break flows using the Saint Venant equations.

In this paper, the Serre-type equations for weakly dispersive and fully non-linear non-hydrostatic waves are presented as a function of a pressure distribution coefficient. A high resolution finite volume scheme is therefore presented, which is used to evaluate several time stepping methods. Once a suitable time stepping scheme is selected, the impacts of the pressure distribution coefficient and the non-linear terms are investigated. The simulations are used further to select a suitable wave breaking model. A generalized Serre model with enhanced linear frequency dispersion is then presented based on the potential velocity distribution obtained from the Picard iteration method, and used to test, if this improvement of the governing equations is relevant in shallow open channel flows. Potential velocity and pressure fields of the Serre equations are evaluated using the 2D distributions of a solitary wave test. The 1D simulations using the finite volume scheme presented here are compared with experimental data (Stansby et al. 1998), the analytical solution of a solitary wave propagation test, 3D simulations of the Reynolds averaged Navier-Stokes (RANS) equations (Marsooli and Wu 2014),

finite element simulations (Mitsotakis et al. 2014) and finite difference simulations (Mohapatra and Chaudhry 2004).

2. Governing Equations

2.1. Depth-Averaged Conservation Laws

The depth-averaged conservation of mass and momentum equations for non-hydrostatic frictionless flow over a horizontal rigid bottom are (Castro-Orgaz et al. 2015)

$$\frac{\partial \mathbf{U}}{\partial t}+\frac{\partial \mathbf{F}}{\partial x}=\mathbf{S}\,, \tag{1}$$

$$\mathbf{U}=\begin{bmatrix} h \\ hU \end{bmatrix},\ \mathbf{F}=\begin{bmatrix} hU \\ hU^2+\frac{1}{2}gh^2+\psi \end{bmatrix},\ \mathbf{S}=\begin{bmatrix} 0 \\ 0 \end{bmatrix}, \tag{2}$$

$$\psi=\frac{h^3}{m}\left[\left(\frac{\partial U}{\partial x}\right)^2-U\frac{\partial^2 U}{\partial x^2}-\frac{\partial^2 U}{\partial x \partial t}\right], \tag{3}$$

where **U**, **F** and **S** = vector of unknowns, fluxes and source terms, respectively; h=flow depth; U=depth-averaged velocity; g=gravitational acceleration; ψ=non-hydrostatic term; m=pressure coefficient (4 for a linear pressure distribution and 3 for a parabolic pressure distribution); x=longitudinal coordinate; and t=time.

The non-hydrostatic terms in Eq. (1) are usually treated as a source term **S** (Erduran et al. 2005; Soares-Frazão and Guinot 2008). Therefore, the vectors in Eq. (1) are rewritten for numerical modelling as

$$\mathbf{U}=\begin{bmatrix} h \\ hU \end{bmatrix},\mathbf{F}=\begin{bmatrix} hU \\ hU^2+\frac{1}{2}gh^2 \end{bmatrix},\mathbf{S}=\begin{bmatrix} 0 \\ -\frac{\partial \psi}{\partial x} \end{bmatrix}. \tag{4}$$

2.2. Non-Hydrostatic Source Term

The pressure coefficient m depends on the mathematical law for the vertical pressure distribution (Castro-Orgaz et al. 2015). A parabolic pressure distribution gives m=3, whereas a linear vertical pressure distribution results in m=4. The case m=3 corresponds to the Serre equations (Serre 1953; De Almeida and Franco 1994; Mitsotakis et al. 2014; Castro-Orgaz et al. 2015). The Boussinesq-type equations by Khan and Steffler (1996a,b) are a particular case for m=4 (Castro-Orgaz et al. 2015). Soares-Frazão and Zech (2002) and Soares-Frazão and Guinot (2008) developed a Boussinesq-type model

that is regained from Eq. (4) by expanding $\partial\psi/\partial x$, neglecting the derivative products, and using m=3. The resulting source term vector is then

$$\mathbf{S} = \begin{bmatrix} 0 \\ \dfrac{h^3}{3}\left(\dfrac{\partial^3 U}{\partial x^2 \partial t} + U \dfrac{\partial^3 U}{\partial x^3} \right) \end{bmatrix}. \tag{5}$$

This is not a fully non-nonlinear model, and its ability in predicting the wave amplitudes need to be evaluated.

2.3. Wave Breaking

The main computational tool used to account for the wave breaking is based on the assumption that if the non-hydrostatic terms are not important, then the results from the Boussinesq equations should collapse to those from the Saint Venant equations. Basically, it means that if a wave breaks, then the non-hydrostatic terms are switched-off, and the Saint Venant equations are solved. Thus, the wave breaking energy dissipation is accounted for by the Rankine-Hugoniot conditions across the moving shocks modelled using the Saint Venant equations (Toro 2001).

A first approximation for wave breaking is based on the results for undular hydraulic jumps. Wave breaking initiates based on the extended energy equation if (Hager and Hutter 1984),

$$\gamma_1 = 1 + \frac{2hh_{xx} - h_x^2}{3} \le 0, \tag{6}$$

where γ_1= wave-breaking factor; $h_x = \partial h/\partial x$; and $h_{xx} = \partial^2 h/\partial x^2$. Eq. (6) states that the free surface velocity becomes zero or negative.

Serre (1953) proposed the wave breaking condition

$$\gamma_2 = 1 + \mathsf{F}^2 h h_{xx} \le 0, \tag{7}$$

where γ_2=wave breaking factor; and F= Froude number [$=U/(gh)^{1/2}$]. Eq. (7) states that the wave breaking initiates if a particle on the free surface separates due to the centripetal acceleration. If wave breaking conditions are fulfilled, based on either Eq. (6) or (7), in any node of the computational domain, the non-hydrostatic source terms are deactivated in the model. Therefore, at some nodes of the computational mesh, the full non-hydrostatic equations are solved, whereas at the breaking nodes, the Saint-

Venant equations are applied. The wave breaking condition is checked at the end of each computational step. A disadvantage of the two conditions presented above is that the transition from non-breaking to breaking flow conditions is sharp.

Hosoda and Tada (1994) proposed a continuous wave breaking factor that gradually attenuates the non-hydrostatic term ψ as follows:

$$\frac{\partial (hU)}{\partial t} + \frac{\partial}{\partial x}\left(hU^2 + \frac{1}{2} g h^2 \right) = -\frac{\partial (\gamma_3 \psi)}{\partial x}, \tag{8}$$

$$\gamma_3 = \begin{cases} 1 & , \text{ if } \quad h_x < h_{cr} \\ \exp[-\phi (h_x - h_{cr})] & , \text{ if } \quad h_x \geq h_{cr} \end{cases}, \tag{9}$$

where γ_3=wave breaking factor; in Eq. (9), ϕ=empirical factor (=2); and h_{cr}=free surface slope threshold to initiate the damping of non-hydrostatic terms. Hosoda and Tada (1994) determined this limiting slope based on the solitary wave profile. The Favre waves are considered to break, approximately, at $F_o^2 \approx 1.5625$ based on the experimental observations (Favre 1935), where F_o=Froude number of the first wave crest. This gave the maximum amplitude of the leading wave of a train of Favre waves. It is accepted that this leading wave is approximately a portion of a solitary wave profile. Hosoda and Tada (1994) pursued this idea and determined based on a solitary wave profile, the maximum free surface slope (at the inflection point) for $F_o^2 \approx 1.5625$, resulting h_{cr}=0.225. This is the maximum free surface slope under breaking conditions to be used in Eq. (9). Other wave breaking models used in coastal engineering applications are available (Schäffer et al. 1993; Kennedy et al. 2000; Cienfuegos et al. 2010).

3. Governing Equations

3.1. Finite Volume Method

The integral solution of Eq.(1) over a rectangular control volume in the *x*-*t* plane is as follows (Toro 2001, 2009):

$$\left(\frac{\partial \mathbf{U}}{\partial t} \right) \Delta t = -\frac{\Delta t}{\Delta x} (\mathbf{F}_{i+1/2} - \mathbf{F}_{i-1/2}) + \mathbf{S} \Delta t, \tag{10}$$

where **S**, **F** and $\partial \mathbf{U}/\partial t$ are cell averaged values; and Δx and Δt = dimensions of the control volume in the *x*- and *t*-directions, respectively. The index $i \pm 1/2$ refers to the control volume interfaces between nodes i and $i \pm 1$. A MUSCL-TVD-4th reconstruction of **U** gives (Yamamoto and Daiguji 1993; Kim *et al*. 2009; Kim and Lynett 2011)

$$\mathbf{U}_{i+1/2}^{L} = \mathbf{U}_i + \frac{1}{6}(\Delta^{*}\bar{\mathbf{U}}_{i-1/2} + 2\Delta^{*}\tilde{\mathbf{U}}_{i-1/2}), \tag{11}$$

$$\mathbf{U}_{i+1/2}^{R} = \mathbf{U}_{i+1} - \frac{1}{6}(2\Delta^{*}\bar{\mathbf{U}}_{i+1/2} + \Delta^{*}\tilde{\mathbf{U}}_{i+3/2}), \tag{12}$$

where

$$\Delta^{*}\bar{\mathbf{U}}_{i-1/2} = \min\mathrm{mod}[\Delta^{*}\mathbf{U}_{i-1/2}, b\Delta^{*}\mathbf{U}_{i+1/2}], \tag{13}$$

$$\Delta^{*}\tilde{\mathbf{U}}_{i+1/2} = \min\mathrm{mod}[\Delta^{*}\mathbf{U}_{i+1/2}, b\Delta^{*}\mathbf{U}_{i-1/2}], \tag{14}$$

$$\Delta^{*}\bar{\mathbf{U}}_{i+1/2} = \min\mathrm{mod}[\Delta^{*}\mathbf{U}_{i+1/2}, b\Delta^{*}\mathbf{U}_{i+3/2}], \tag{15}$$

$$\Delta^{*}\tilde{\mathbf{U}}_{i+3/2} = \min\mathrm{mod}[\Delta^{*}\mathbf{U}_{i+3/2}, b\Delta^{*}\mathbf{U}_{i+1/2}], \tag{16}$$

$$\Delta^{*}\mathbf{U}_{i+1/2} = \Delta\mathbf{U}_{i+1/2} - \frac{1}{6}\Delta^{3}\bar{\mathbf{U}}_{i+1/2}, \tag{17}$$

$$\Delta^{3}\bar{\mathbf{U}}_{i+1/2} = \Delta\bar{\mathbf{U}}_{i-1/2} - 2\Delta\bar{\mathbf{U}}_{i+1/2} + \Delta\bar{\mathbf{U}}_{i+3/2}, \tag{18}$$

$$\Delta\bar{\mathbf{U}}_{i-1/2} = \min\mathrm{mod}[\Delta\mathbf{U}_{i-1/2}, b_1\Delta\mathbf{U}_{i+1/2}, b_1\Delta\mathbf{U}_{i+3/2}], \tag{19}$$

$$\Delta\bar{\mathbf{U}}_{i+1/2} = \min\mathrm{mod}[\Delta\mathbf{U}_{i+1/2}, b_1\Delta\mathbf{U}_{i+3/2}, b_1\Delta\mathbf{U}_{i-1/2}], \tag{20}$$

$$\Delta\bar{\mathbf{U}}_{i+3/2} = \min\mathrm{mod}[\Delta\mathbf{U}_{i+3/2}, b_1\Delta\mathbf{U}_{i-1/2}, b_1\Delta\mathbf{U}_{i+1/2}], \tag{21}$$

$$\min\mathrm{mod}[i, j] = sign(i)\max\{0, \min[(i), sign(i)\, j]\}, \tag{22}$$

$$\min\mathrm{mod}[i, j, k] = sign(i)\max\{0, \min[(i), sign(i)\, j, sign(i)k]\}, \tag{23}$$

where the coefficients $b_1 = 2$ and $1<b<4$ (Yamamoto and Daiguji 1993).

3.2. Numerical Flux

The HLL approximate Riemann solver is used to compute the intercell numerical flux as follows (Toro 2001, 2009):

$$\mathbf{F}_{i+1/2} = \begin{cases} \mathbf{F}_L & , \quad \text{if} \quad S_L \geq 0 \\ \dfrac{S_R\mathbf{F}_L - S_L\mathbf{F}_R + S_R S_L(\mathbf{U}_R - \mathbf{U}_L)}{S_R - S_L} & , \quad \text{if} \quad S_L \leq 0 \leq S_R \\ \mathbf{F}_R & , \quad \text{if} \quad S_R \leq 0 \end{cases}. \tag{24}$$

where L and R=left and right subscripts for the cell interface, respectively. The signal speeds S_L and S_R are defined as

$$S_L = U_L - a_L q_L,\ S_R = U_R + a_R q_R, \tag{25}$$

where a_L and a_R=shallow water wave celerity at the corresponding side of the interface[=$(gh_{L,R})^{1/2}$].

The correction factor $q_{L,R}$ is given by

$$q_{L,R} = \begin{cases} \left\{ \frac{1}{2}\left[\frac{h_*(h_* + h_{L,R})}{h_{L,R}^{\ 2}} \right] \right\}^{1/2} & , \quad \text{if} \quad h_* > h_{L,R} \\ 1 & , \quad \text{if} \quad h_* \le h_{L,R} \end{cases}, \tag{26}$$

where h_* is defined as

$$h_* = \frac{1}{g}\left[\frac{1}{2}(a_L + a_R) + \frac{1}{4}(U_L - U_R) \right]^2. \tag{27}$$

3.3. Time Stepping

After mathematical manipulation of $\partial\psi/\partial x$ using the depth-averaged continuity equation $\partial h/\partial t = -\partial(hU)/\partial x$, the system given by Eq. (10) is rewritten in integral form as

$$\left(\frac{\partial \mathbf{W}}{\partial t} \right) \Delta t = -\frac{\Delta t}{\Delta x}(\mathbf{F}_{i+1/2} - \mathbf{F}_{i-1/2}) + \mathbf{Z}\Delta t \quad , \tag{28}$$

where

$$\mathbf{W} = \begin{bmatrix} h \\ y \end{bmatrix} = \begin{bmatrix} h \\ hU - \frac{h^3}{m}\frac{\partial^2 U}{\partial x^2} - \frac{3h^2}{m}\frac{\partial h}{\partial x}\frac{\partial U}{\partial x} \end{bmatrix},\ \mathbf{F} = \begin{bmatrix} hU \\ hU^2 + \frac{1}{2}gh^2 \end{bmatrix}, \tag{29}$$

$$\mathbf{Z} = \begin{bmatrix} 0 \\ -\frac{3h^2}{m}\frac{\partial h}{\partial x}\left[\left(\frac{\partial U}{\partial x} \right)^2 - U\frac{\partial^2 U}{\partial x^2} \right] - \frac{h^3}{m}\left(\frac{\partial U}{\partial x}\frac{\partial^2 U}{\partial x^2} - U\frac{\partial^3 U}{\partial x^3} \right) + \\ \frac{6h}{m}\frac{\partial (hU)}{\partial x}\frac{\partial h}{\partial x}\frac{\partial U}{\partial x} + \frac{3h^2}{m}\frac{\partial^2 (hU)}{\partial x^2}\frac{\partial U}{\partial x} + \frac{3h^2}{m}\frac{\partial (hU)}{\partial x}\frac{\partial^2 U}{\partial x^2} \end{bmatrix}, \tag{30}$$

Similarly, the x-momentum equation in the Boussinesq-type model of Soares-Frazão and Zech (2002) can be rewritten for numerical modelling as

$$\frac{\partial}{\partial t}\left(hU - \frac{h^3}{3}\frac{\partial^2 U}{\partial x^2} \right) + \frac{\partial}{\partial x}\left(hU^2 + \frac{1}{2}gh^2 \right) = h^2\frac{\partial (hU)}{\partial x}\frac{\partial^2 U}{\partial x^2} + U\frac{h^3}{3}\frac{\partial^3 U}{\partial x^3}. \tag{31}$$

Several time stepping schemes for Eq. (28) are investigated. The classical Euler scheme reads

$$\mathbf{W}_i^{k+1} = \mathbf{W}_i^k - \frac{\Delta t}{\Delta x}(\mathbf{F}_{i+1/2}^k - \mathbf{F}_{i-1/2}^k) + \mathbf{Z}_i^k \Delta t\,, \tag{32}$$

where Δt=time step, defined using the CFL condition; and k=time level index. Alternatively, the TVD-RK schemes are higher-order time stepping methods (Glottieb and Shu 1998). Usual high-order TVD-RK schemes are TVD-RK3th

$$\mathbf{W}_i^q = \mathbf{W}_i^k - \frac{\Delta t}{\Delta x}(\mathbf{F}_{i+1/2}^k - \mathbf{F}_{i-1/2}^k)\,, \tag{33}$$

$$\mathbf{W}_i^{(1)} = \mathbf{W}_i^q + \Delta t \mathbf{Z}(\mathbf{W}_i^q)\,, \tag{34}$$

$$\mathbf{W}_i^{(2)} = \frac{3}{4}\mathbf{W}_i^q + \frac{1}{4}\mathbf{W}_i^{(1)} + \frac{1}{4}\Delta t \mathbf{Z}(\mathbf{W}_i^{(1)})\,, \tag{35}$$

$$\mathbf{W}_i^{k+1} = \frac{1}{3}\mathbf{W}_i^q + \frac{2}{3}\mathbf{W}_i^{(2)} + \frac{2}{3}\Delta t \mathbf{Z}(\mathbf{W}_i^{(2)})\,, \tag{36}$$

and TVD-RK4th

$$\mathbf{W}_i^{(1)} = \mathbf{W}_i^q + \frac{1}{2}\Delta t \mathbf{Z}(\mathbf{W}_i^q)\,, \tag{37}$$

$$\begin{aligned}\mathbf{W}_i^{(2)} = {} & \frac{649}{1600}\mathbf{W}_i^q - \frac{10890423}{25193600}\Delta t \mathbf{Z}(\mathbf{W}_i^q) \\ & + \frac{951}{1600}\mathbf{W}_i^{(1)} + \frac{5000}{7873}\Delta t \mathbf{Z}(\mathbf{W}_i^{(1)})\end{aligned}\,, \tag{38}$$

$$\begin{aligned}\mathbf{W}_i^{(3)} = {} & \frac{53989}{2500000}\mathbf{W}_i^q - \frac{102261}{5000000}\Delta t \mathbf{Z}(\mathbf{W}_i^q) + \frac{4806213}{20000000}\mathbf{W}_i^{(1)} \\ & - \frac{5121}{20000}\Delta t \mathbf{Z}(\mathbf{W}_i^{(1)}) + \frac{23619}{32000}\mathbf{W}_i^{(2)} + \frac{7873}{10000}\Delta t \mathbf{Z}(\mathbf{W}_i^{(2)})\end{aligned}\,, \tag{39}$$

$$\begin{aligned}\mathbf{W}_i^{k+1} = {} & \frac{1}{5}\mathbf{W}_i^q + \frac{1}{10}\Delta t \mathbf{Z}(\mathbf{W}_i^q) + \frac{6127}{30000}\mathbf{W}_i^{(1)} + \frac{1}{6}\Delta t \mathbf{Z}(\mathbf{W}_i^{(1)}) \\ & + \frac{7873}{30000}\mathbf{W}_i^{(2)} + \frac{1}{3}\mathbf{W}_i^{(3)} + \frac{1}{6}\Delta t \mathbf{Z}(\mathbf{W}_i^{(3)})\end{aligned}\,, \tag{40}$$

where q, (1), (2) and (3)=auxiliary time step index; k=actual time step index; and k+1=next time step index.

The third-order Adams-Bashforth predictor and the fourth-order Adams-Moulton corrector equations can be coupled to produce a high resolution predictor-corrector scheme (Wei and Kirby 1995; Wei et al. 1995; Kim et al. 2009; Kim and Lynett 2011). The cell averaged derivative in Eq. (28) is denoted by

$$\frac{\partial \mathbf{W}}{\partial t} = \mathbf{E}(\mathbf{U}), \tag{41}$$

where **E** is

$$\mathbf{E} = -\frac{1}{\Delta x}(\mathbf{F}_{i+1/2} - \mathbf{F}_{i-1/2}) + \mathbf{Z}. \tag{42}$$

The Adams-Bashforth predictor step for Eq. (41) is given by

$$\mathbf{W}_i^{k+1} = \mathbf{W}_i^k + \frac{\Delta t}{12}(23\mathbf{E}_i^k - 16\mathbf{E}_i^{k-1} + 5\mathbf{E}_i^{k-2}). \tag{43}$$

The Adams-Moulton corrector step for Eq. (41) then reads

$$\mathbf{W}_i^{k+1} = \mathbf{W}_i^k + \frac{\Delta t}{24}(9\mathbf{E}_i^{k+1} + 19\mathbf{E}_i^k - 5\mathbf{E}_i^{k-1} + \mathbf{E}_i^{k-2}). \tag{44}$$

The predictor step results from Eq. (43) are used to calculate an initial value for $\mathbf{E}_i^{k+1}$ in Eq. (44) and in turn, to initiate the Adams-Moulton iterative process. Then, $\mathbf{W}_i^{k+1}$ from Eq. (44) is used to recompute $\mathbf{E}_i^{k+1}$ iteratively. The Adams-Moulton iterative corrector step is repeated until converges with a prescribed tolerance Δf

$$\Delta f = \frac{\sum_i \left| f_i^{k+1} - f_i^{(k+1)*} \right|}{\sum_i \left| f_i^{k+1} \right|}, \tag{45}$$

where f is any of the variables of **W**; and * denotes the previous iteration. Here, the convergence criterion $\Delta f < 10^{-4}$ is adopted, such that the iterations are continued if any of the f exceeds this value. The AB-AM scheme requires initial values for the first two time steps [$\mathbf{E}_i^{k-1}$ and $\mathbf{E}_i^{k-2}$ in Eqs. (43) and (44)]. The TVD-RK3th and TVD-RK4th schemes are considered in this study to produce the first two time steps in the AB-AM scheme. Both numerical schemes for the time stepping are denoted as TVD-RK3th AB-AM and TVD-RK4th AB-AM, respectively.

3.4. Computation of Depth-Averaged Velocity Field

After applying the corresponding time stepping scheme, the values of h and y at time level k+1 are available. To calculate U for each node at this time level, it is necessary to solve the following equation for each computational node:

$$y = hU - \frac{h^3}{m}\frac{\partial^2 U}{\partial x^2} - \frac{3h^2}{m}\frac{\partial h}{\partial x}\frac{\partial U}{\partial x}. \tag{46}$$

Eq. (46) is discretized using second order central finite differences resulting in a tridiagonal system of linear equations

$$y_i^{k+1} = h_i^{k+1}U_i^{k+1} - \frac{(h_i^{k+1})^3}{m}\frac{U_{i+1}^{k+1} - 2U_i^{k+1} + U_{i-1}^{k+1}}{\Delta x^2} - \frac{3(h_i^{k+1})^2}{m}\frac{h_{i+1}^{k+1} - h_{i-1}^{k+1}}{2\Delta x}\frac{U_{i+1}^{k+1} - U_{i-1}^{k+1}}{2\Delta x}. \tag{47}$$

Eq. (47) is rewritten as follows

$$y_i^{k+1} = A_i U_{i-1}^{k+1} + B_i U_i^{k+1} + C_i U_{i+1}^{k+1}, \tag{48}$$

where

$$A_i = \left[-\frac{(h_i^{k+1})^3}{m\Delta x^2} + \frac{3(h_i^{k+1})^2}{4m\Delta x^2}(h_{i+1}^{k+1} - h_{i-1}^{k+1}) \right], \tag{49}$$

$$B_i = \left[h_i^{k+1} + \frac{2(h_i^{k+1})^3}{m\Delta x^2} \right], \tag{50}$$

$$C_i = \left[-\frac{(h_i^{k+1})^3}{m\Delta x^2} - \frac{3(h_i^{k+1})^2}{4m\Delta x^2}(h_{i+1}^{k+1} - h_{i-1}^{k+1}) \right]. \tag{51}$$

With known values of y_i^{k+1}, A_i, B_i, and C_i, the corresponding tridiagonal matrix is solved using the Thomas algorithm to find U_i^{k+1} (Wei *et al*. 1995). For the weakly non-linear Boussinesq model of Soares-Frazão and Zech (2002), y is defined as

$$y = hU - \frac{h^3}{3}\frac{\partial^2 U}{\partial x^2}. \tag{52}$$

Using second order central finite differences, Eq. (52) is discretized as

$$y_i^{k+1} = h_i^{k+1}U_i^{k+1} - \frac{(h_i^{k+1})^3}{3}\frac{U_{i+1}^{k+1} - 2U_i^{k+1} + U_{i-1}^{k+1}}{\Delta x^2}, \tag{53}$$

Then, Eq. (53) can be written in the form of Eq. (48), where

$$A_i = \left[-\frac{(h_i^{k+1})^3}{3\Delta x^2} \right], \tag{54}$$

$$B_i = \left[h_i^{k+1} + \frac{2(h_i^{k+1})^3}{3\Delta x^2} \right], \tag{55}$$

$$C_i = \left[-\frac{(h_i^{k+1})^3}{3\Delta x^2} \right]. \tag{56}$$

3.5. Computational Sequence

The model solution encompasses the following steps:

(1) The solution **U** at time level *k* is reconstructed using MUSCL-TVD-4th.

(2) The numerical flux $\mathbf{F}_{i+1/2}$ is computed at cell interfaces with the HLL Riemann solver using the reconstructed values of *h* and *U*.

(3) Source vector **Z** [Eq. (30)] is calculated at time level *k*. The derivatives are discretized using second order central finite differences.

(4) A time stepping scheme to Eq. (28) is applied to compute **W** at time level *k*+1. Values of h_i^{k+1} and y_i^{k+1} are therefore determined.

(5) The tridiagonal matrix is solved by the Thomas algorithm to find U_i^{k+1}.

(6) For a new time level, steps 1 to 5 are repeated.

4. Serre Equations with Enhanced Frequency Dispersion

Su and Gardner (1969) derived the Serre equations based on potential flow without assuming that the velocity distribution in the *x*-direction is uniform with depth $u(x,z,t)=U(x,t)$ as originally done by Serre (1953). In fact, the second-order irrotational velocity distribution is parabolic. Castro-Orgaz and Hager (2014) determined the irrotational velocity field of unsteady water waves by systematic Picard iteration and found for the particle kinematics

$$u(x,z,t) = U + \frac{\partial^2 U}{\partial x^2}\left(\frac{h^2}{6} - \frac{z^2}{2} \right), \tag{57}$$

$$w(x,z,t) = -\frac{\partial U}{\partial x} z, \tag{58}$$

where *u* and *w* = velocity components in the *x*- and *z*-directions respectively; and

z=vertical coordinate. Using Eqs. (57) and (58), the Serre equations are obtained using the depth-averaged conservation of mass and momentum equations (Castro-Orgaz and Hager 2014). Therefore, the Serre equations are regained if the non-uniform irrotational velocity distribution is accounted for to this order of expansion. Cienfuegos et al. (2006) determined the irrotational velocity field (u,w) of unsteady water waves based on series expansions. They found that the Serre equations, formulated in terms of U, are not necessarily based on a uniform $u(z)$ profile. A limitation of the Serre equations is that the system is weakly dispersive. Nwogu (1993) presented a challenging approach where the linear dispersion relation of Boussinesq-type equations is enhanced expressing the conservation laws as a function of the velocity u_α at an undetermined elevation z_α instead of U. Castro-Orgaz and Hager (2014) indicated that Eq. (57) can be used following the Nwogu approach to produce the Serre-type equations with enhanced frequency dispersion. The resulting system is identical to that presented by Dias and Milewski (2010)

$$\frac{\partial h}{\partial t}+\frac{\partial (hu_\alpha)}{\partial x}=(1-\alpha^2)\frac{\partial}{\partial x}\left(\frac{h^3}{6}\frac{\partial^2 u_\alpha}{\partial x^2}\right), \tag{59}$$

$$\begin{aligned}\frac{\partial (hu_\alpha)}{\partial t}+\frac{\partial}{\partial x}\left(hu_\alpha^2+\frac{1}{2}gh^2\right)&=-\frac{\partial}{\partial x}\left\{\frac{h^3}{3}\left[\left(\frac{\partial u_\alpha}{\partial x}\right)^2-u_\alpha\frac{\partial^2 u_\alpha}{\partial x^2}-\frac{\partial^2 u_\alpha}{\partial x\partial t}\right]\right\}\\ &+(1-\alpha^2)\left[\frac{\partial}{\partial t}\left(\frac{h^3}{6}\frac{\partial^2 u_\alpha}{\partial x^2}\right)+\frac{\partial}{\partial x}\left(\frac{h^3}{3}u_\alpha\frac{\partial^2 u_\alpha}{\partial x^2}\right)\right]\end{aligned}. \tag{60}$$

where α=$(3)^{1/2}z_\alpha/h$. Eqs. (59) and (60) can be rewritten as Eq. (28), where

$$\mathbf{W}=\begin{bmatrix} h \\ hu_\alpha-(3-\alpha^2)\frac{h^3}{6}\frac{\partial^2 u_\alpha}{\partial x^2}-h^2\frac{\partial h}{\partial x}\frac{\partial u_\alpha}{\partial x}\end{bmatrix},\ \mathbf{F}=\begin{bmatrix} hu_\alpha \\ hu_\alpha^2+\frac{1}{2}gh^2\end{bmatrix}, \tag{61}$$

$$\mathbf{Z}=\begin{bmatrix} (1-\alpha^2)\frac{\partial}{\partial x}\left(\frac{h^3}{6}\frac{\partial^2 u_\alpha}{\partial x^2}\right) \\ (1-\alpha^2)\frac{\partial}{\partial x}\left(u_\alpha\frac{h^3}{3}\frac{\partial^2 u_\alpha}{\partial x^2}\right)-\frac{\partial}{\partial x}\left\{\frac{h^3}{3}\left[\left(\frac{\partial u_\alpha}{\partial x}\right)^2-u_\alpha\frac{\partial^2 u_\alpha}{\partial x^2}\right]\right\}- \\ \frac{\partial}{\partial x}\left[h^2\frac{\partial u_\alpha}{\partial x}\left(-\frac{\partial (hu_\alpha)}{\partial x}+(1-\alpha^2)\frac{\partial}{\partial x}\left(\frac{h^3}{6}\frac{\partial^2 u_\alpha}{\partial x^2}\right)\right)\right]\end{bmatrix}. \tag{62}$$

Therefore, the coefficients to solve the tridiagonal matrix associated to **W** are

$$A_i = \left[-(3-\alpha^2)\frac{(h_i^{k+1})^3}{6\Delta x^2} + \frac{(h_i^{k+1})^2}{4\Delta x^2}(h_{i+1}^{k+1} - h_{i-1}^{k+1}) \right], \tag{63}$$

$$B_i = \left[h_i^{k+1} + (3-\alpha^2)\frac{(h_i^{k+1})^3}{3\Delta x^2} \right], \tag{64}$$

$$C_i = \left[-(3-\alpha^2)\frac{(h_i^{k+1})^3}{6\Delta x^2} - \frac{(h_i^{k+1})^2}{4\Delta x^2}(h_{i+1}^{k+1} - h_{i-1}^{k+1}) \right]. \tag{65}$$

For α^2=1, Eqs. (59) and (60) reduce to Eqs. (1)–(3) with m=3, which is the standard Serre model. The optimized value α^2=0.66 permits to apply Eqs. (59) and (60) from shallow to intermediate flow depths (Dias and Milweski 2010).

5. Test Cases

In this section, experimental data and computational results are selected to assess the governing equations and the numerical schemes. Firstly, the Serre equations are evaluated using the experimental data of Stansby et al. (1998), focusing on the stability of the time stepping scheme and carrying out a grid dependence analysis of the models. Then, the ability of the model to reproduce a solitary wave propagation is tested. Secondly, 3D Reynolds-Averaged Navier-Stokes (RANS) simulations presented by Marsooli and Wu (2014) and the experimental data of Stansby et al. (1998) are compared with the Serre equations by using different wave breaking criteria. Thirdly, the impact of the pressure coefficient, the use of a frequency dispersion enhanced model, and consideration of all non-linear terms are highlighted. The velocity and pressure distributions of the Serre equations are tested using a highly non-linear solitary wave. Finally, the finite volume solution of the Serre equations is compared with those originating from other numerical schemes. In particular, the finite element scheme used by Mitsotakis et al. (2014) and the finite difference method proposed by Mohapatra and Chaudhry (2004) are considered. A large scale test, long term simulation, and dry bed propagation are finally conducted.

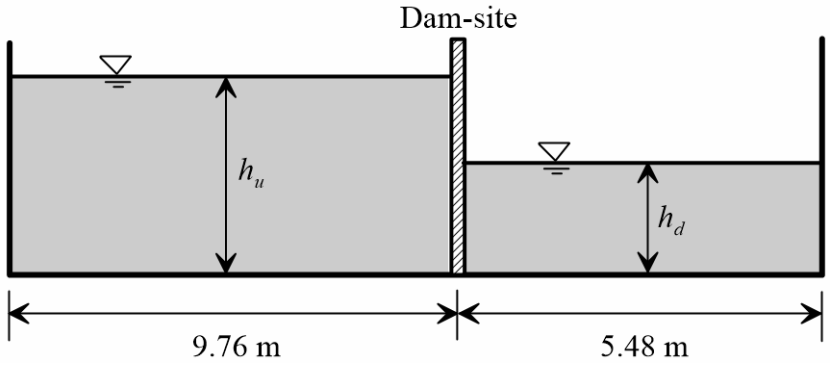

Fig. 2. Definition sketch of experimental setup used by Stansby et al. (1998)

5.1. Evaluation of Time Stepping Schemes

A sketch of the experimental setup used by Stansby et al. is shown in Fig. 2. The assessment of the different time steeping schemes is presented in Fig. 3 using the experimental data of Stansby et al. (1998). The experiment selected herein was conducted in a 15.24 m long, 0.4 m wide, and 0.4 m high laboratory flume. The initial conditions are the upstream depth h_u=0.1 m and the depth ratio $r=h_d/h_u$=0.45, where h_d=initial downstream depth. The measured flow profile (free surface) is plotted in Fig. 3 after 0.76 s of the dam break. The computations presented in Fig. 3 correspond to the solution of the Serre equations (m=3). Fig. 3(a) depicts the time stepping analysis using CFL=0.1. The results obtained by using the TVD-RK3th AB-AM and TVD-RK4th AB-AM schemes are as close to the data than those using the Euler, TVD- RK3th, and TVD-RK4th schemes. Fig. 3(b) presents the same computations using CFL=0.5. The Euler, TVD- RK3th, and TVD- RK4th schemes produce results that are dependent on the time resolution, especially in the vicinity of the shock front, where the wave amplitudes are increased. Finally, Fig. 3(c) presents the computations for CFL=0.9. The Euler scheme breaks down given the instabilities generated and therefore, the results cannot be plotted. The TVD- RK3th and TVD- RK4th schemes increase the amplitude at the bore front due to accumulated numerical errors. Nevertheless, the TVD-RK3th AB-AM and TVD-RK4th AB-AM schemes show good results that are in agreement with their previous computations [Figs. 3(a and b)]. Thus, the only time stepping scheme that was found to produce stable results for practical values of CFL is the AB-AM scheme.

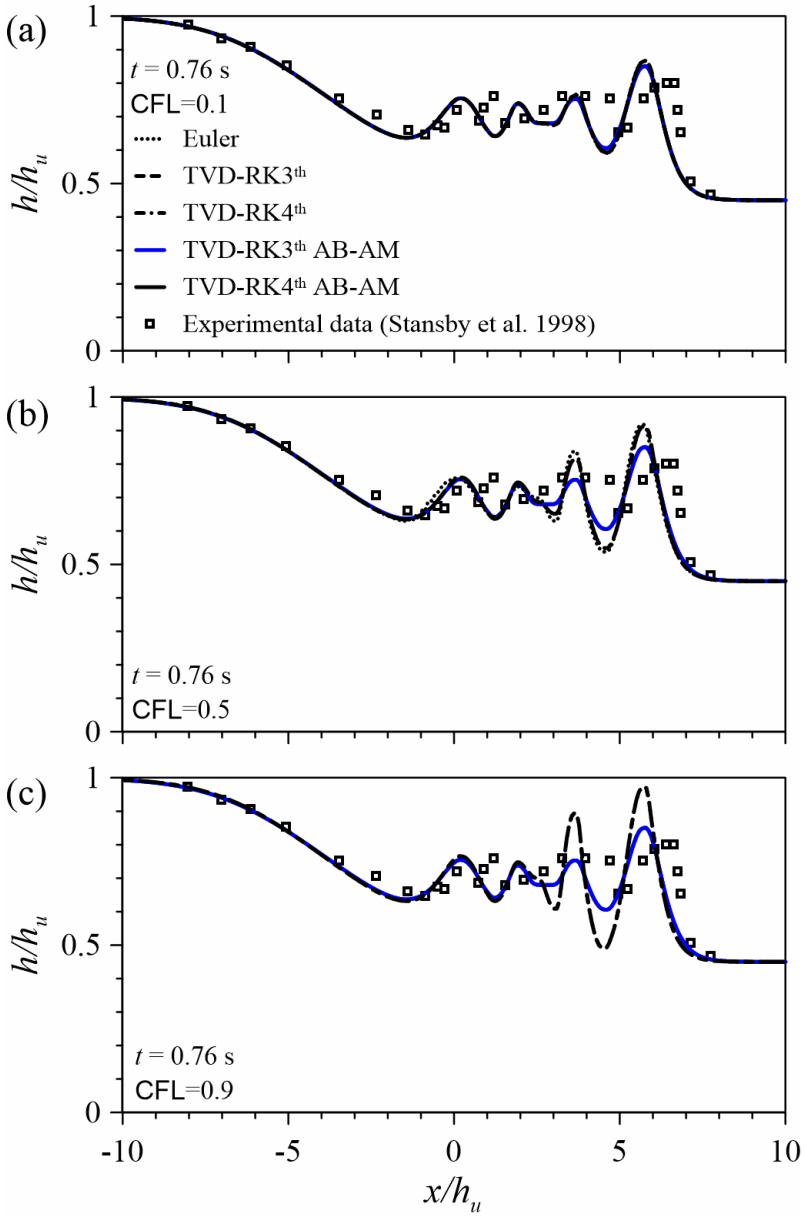

Fig. 3. Time stepping assessment for the Serre equations (m=3) using the experimental data of Stansby et al. (1998): (a) CFL=0.1; (b) CFL=0.5; (c) CFL=0.9 for Δx=0.75 cm

The grid size dependence is analyzed in Fig. 4. The TVD-RK3th AB-AM scheme is one of the best time stepping schemes; so henceforth it is selected for the computations. In Fig. 4, simulations using the Serre equations are compared with the experimental data of Stansby et al. (1998) measured at 0.2, 0.3, 0.52 and 0.76 s [Fig. 4(a–d)] after the dam break. Both the boundary and the initial conditions are the same as those considered in Fig. 3. Following Marsooli and Wu (2014), three different grid sizes Δx=2, 0.75, and 0.5 cm are tested. It is evident that the results for Δx=2 cm are grid size dependent. However, the results are unaltered for Δx values lower than 0.75 cm. The model produces convergent results reducing both Δx and CFL, thereby showing mesh size independency of results.

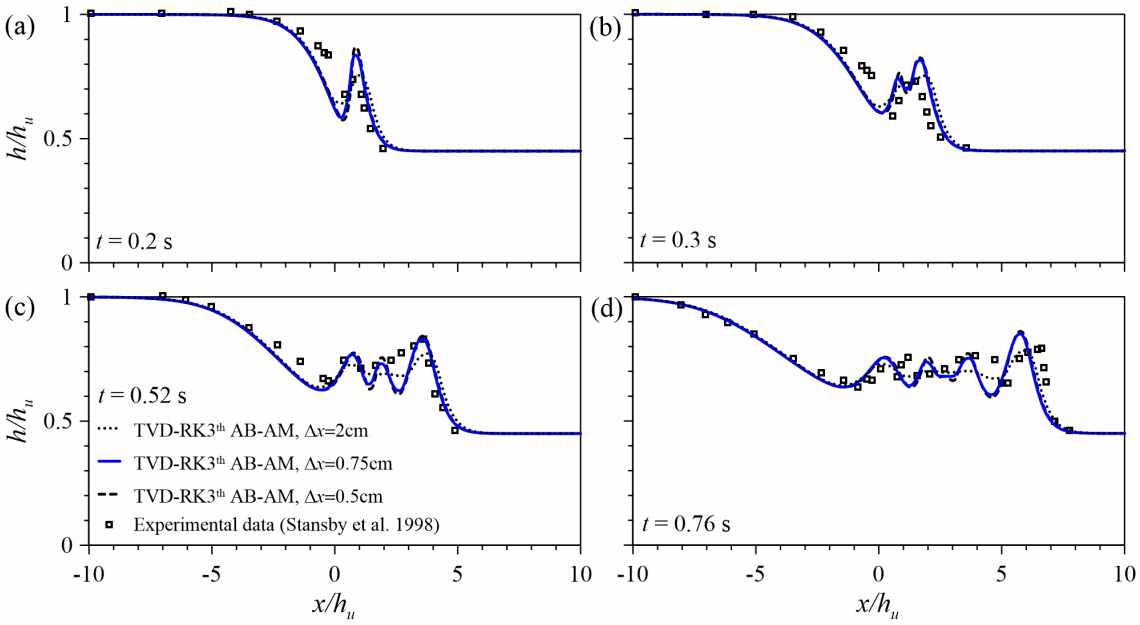

Fig. 4. Grid size dependence analysis for the Serre equations (m=3) using the experimental data of Stansby et al. (1998): (a) t=0.2 s; (b) t=0.3 s; (c) t=0.52 s; (d) t=0.76 s for CFL =0.9

5.2. Solitary Wave Propagation Test

The TVD-RK3th AB-AM scheme is evaluated in Figs. 5 and 6, using the solitary wave solution of the Serre equations (Carter and Cienfuegos 2011), which is given by

$$h(x,t) = h_o + h_o\left(\mathsf{F}_o^2 - 1\right)\mathrm{sech}^2\left[\frac{\left(3\mathsf{F}_o^2 - 3\right)^{1/2}}{\mathsf{F}_o}\frac{x - ct}{2h_o}\right], \tag{66}$$

$$U(x,t) = c\left[1 - \frac{h_o}{h(x,t)}\right], \tag{67}$$

where F_o=solitary wave Froude number=$(1+H/h_o)^{1/2}$; H=wave amplitude; h_o=still water depth; and c=solitary wave celerity=$(gh_o)^{1/2}$ F_o. A solitary wave test for h_o=1 m and H=0.5 m was used. The numerical computations are accomplished using CFL=0.1 and Δx=0.05 m. Fig. 5 shows a time-dependence analysis of the Serre equations by comparing the analytical and numerical solutions at times t=15s [Fig. 5(a) and (c)] and t=50s [Fig. 5(b) and (d)], showing that the numerical model correctly propagates the solitary wave with a satisfactory accuracy. The Root-Mean-Square Deviation (RMSD) and the square of the Pearson product-moment correlation coefficient (R) are calculated on the basis of Fig. 5 for the free surface level in the computational domain, it is $x \in$ [-10,200] m, thereby providing a quantitative model accuracy test (Table 1). As it can be inferred from Fig. 5 and Table 1, the numerical solutions of the Serre equations at both

t=15s and t=50s are in good agreement with the analytical solutions. Furthermore, Fig. 6 illustrates a grid size dependence analysis at t=50s, for testing grid sizes Δx=0.2 m, Δx=0.15 m, Δx=0.1 m, and Δx=0.05 m, with CFL=0.1. The qualitative (visual) and quantitative (RMSD and R in Table 1) assessment of the solutions the Serre equations suggest the grid independency of the numerical solutions.

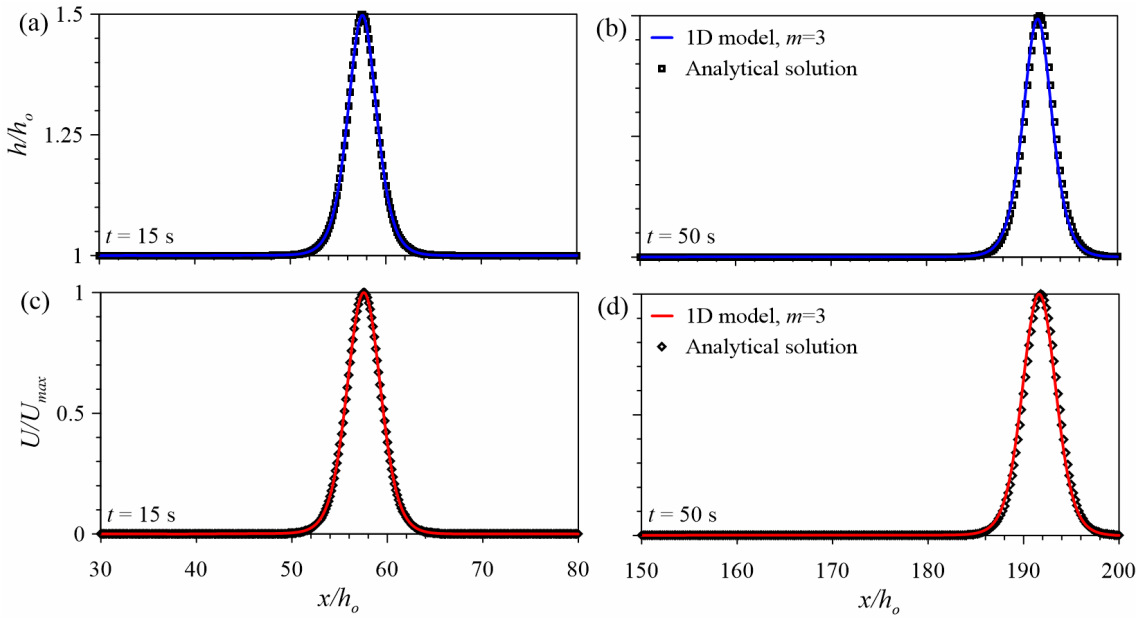

Fig. 5. Solitary wave propagation test for the Serre equations (m=3): (a) Free surface profile at t=15 s; (b) free surface profile at t=50 s; (c) depth-averaged velocity at t=15 s; (d) depth-averaged velocity at t=50 s

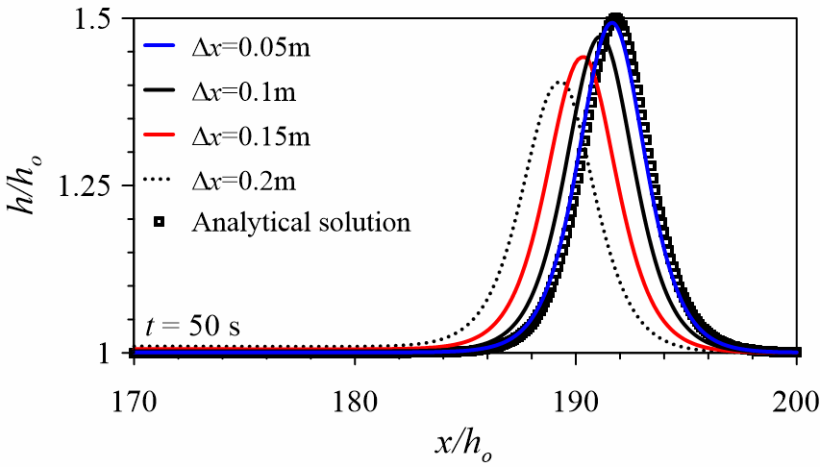

Fig. 6. Grid size independence test for the Serre equations (m=3) during solitary wave propagation at t=50 s for grid sizes: Δx=0.05 m, Δx=0.1 m, Δx=0.15 m and Δx=0.2 m

1D model, m=3	**RMSD**	**R**
t=15 s, Δx=0.05 m	3.46×10^{-4}	0.999
t=50 s, Δx=0.05 m	4.44×10^{-3}	0.994
t=50 s, Δx=0.1 m	1.73×10^{-2}	0.903
t=50 s, Δx=0.15 m	3.43×10^{-2}	0.631
t=50 s, Δx=0.2 m	4.98×10^{-2}	0.287

Table 1. RMSD and R Tests to the Serre equations (m=3) Model Using the Analytical Solution for the Free surface profile of a Solitary wave

5.3. Solitary Wave Propagation Test

Figs. 7–9 presents the 1D computations using the Serre equations with the three different wave breaking models studied here. The results are compared with the 3D simulations by Marsooli and Wu (2014) for Δx=0.75 cm and the experimental data of Stansby et al. (1998). The computational results of the present model are generated using Δx=0.75 cm and CFL=0.9. Fig. 7 shows the results generated using the first wave breaking criterion [Eq. (6)]. Fig. 8 displays the results obtained from the second wave breaking criterion [Eq. (7)]. Both factors induce wave breaking at early stages of the dam break flow, thereby damping the undulations of the flow profile. These breaking-type model computations rely on the assumption that once breaking is generated at a node, the Saint-Venant equations apply. The disadvantage is that the transition from Serre to Saint-Venant equations is sharp at every node of the computational domain, and the undulations are unrealistically suppressed. Eqs. (6) and (7) are obtained under steady, irrotational flow conditions, implying that the applications in unsteady irrotational flow models may not be guaranteed. Fig. 9 presents the result of the third wave breaking criterion [Eq. (9)]. The 1D simulation provides a good agreement with both 3D simulations by Marsooli and Wu's (2014) and the experimental data of Stansby et al. (1998), providing a smooth transition from non-breaking to breaking wave conditions.

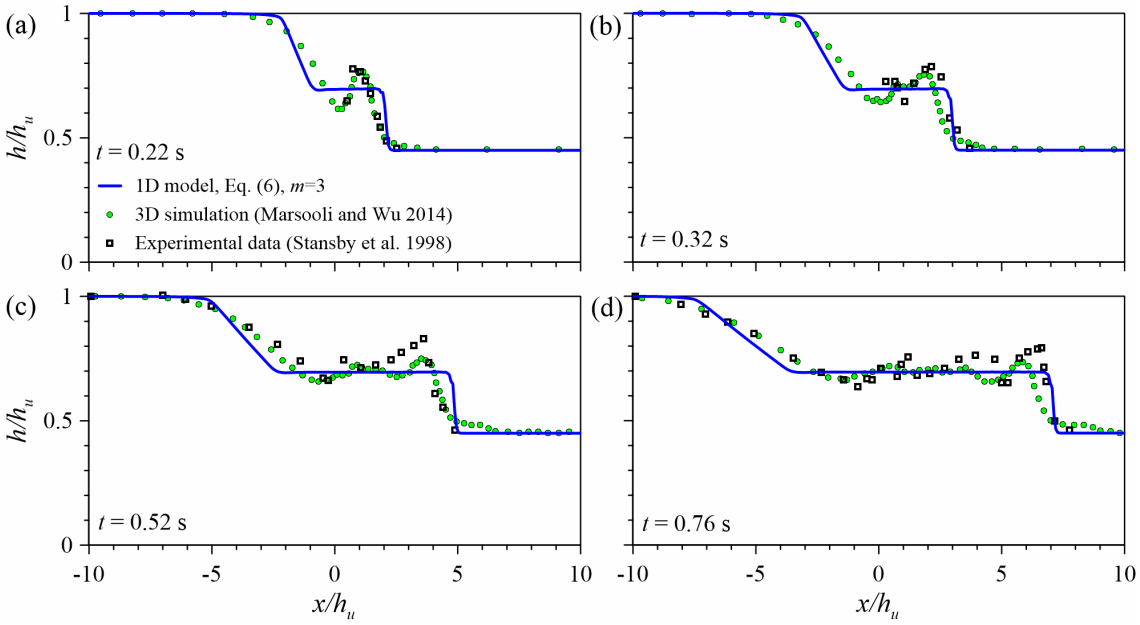

Fig. 7. Assessment of first wave breaking criterion [Eq. (6)] using the 3D simulation by Marsooli and Wu (2014) and the experimental data of Stansby et al. (1998): (a) t=0.22 s; (b) t=0.32 s; (c) t=0.52 s; (d) t=0.76 s

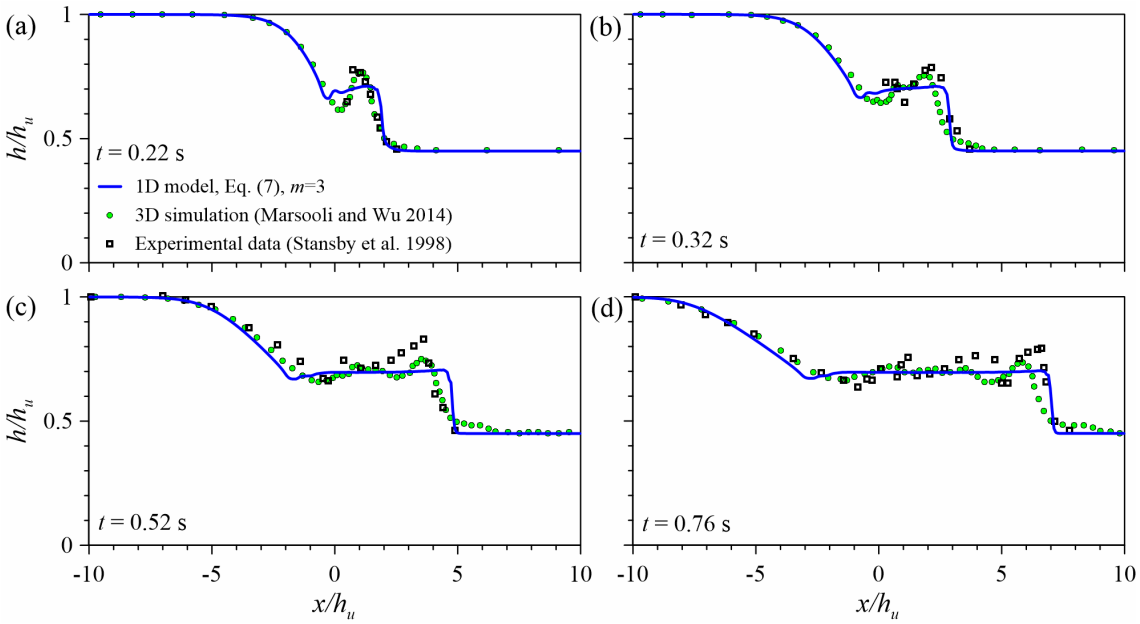

Fig. 8. Assessment of second wave breaking criterion [Eq. (7)] using the 3D simulation by Marsooli and Wu (2014) and the experimental data of Stansby et al. (1998): (a) t=0.22 s; (b) t=0.32 s; (c) t=0.52 s; (d) t=0.76 s

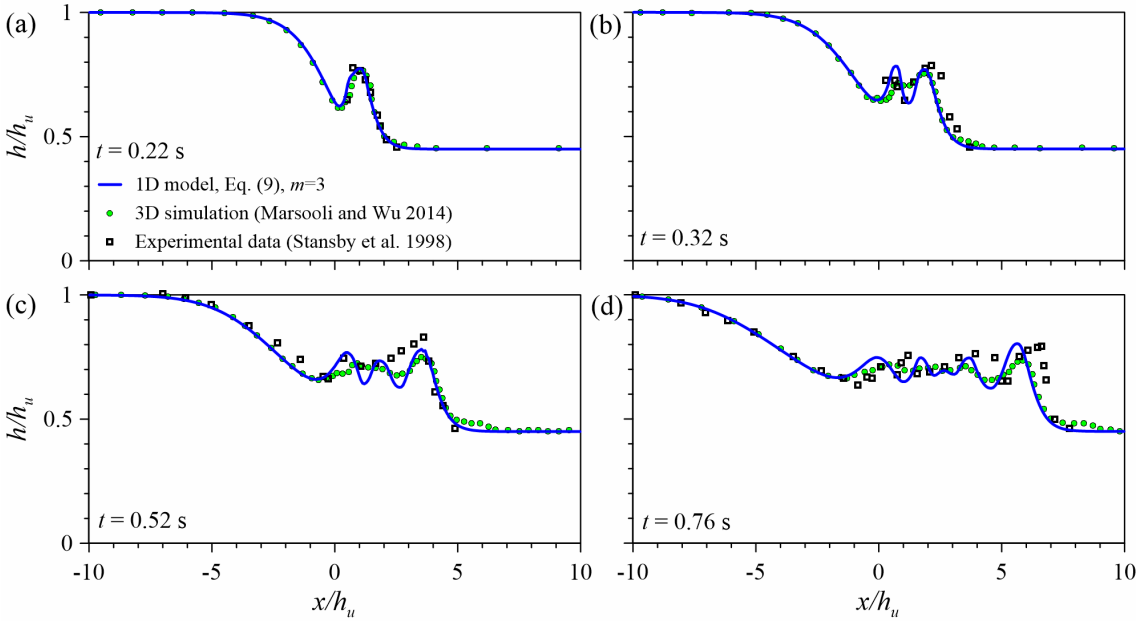

Fig. 9. Assessment of third wave breaking criterion [Eq. (9)] using the 3D simulation by Marsooli and Wu (2014) and the experimental data of Stansby et al. (1998): (a) t=0.22 s; (b) t=0.32 s; (c) t=0.52 s; (d) t=0.76 s

5.4. Evaluation of Pressure Coefficient, Frequency Dispersion and Non-Linear Terms

The impact of the pressure coefficient m is considered in Fig. 10(a), where Eq. (10) was solved without wave breaking for the typical values m=3 (Serre 1953) and m=4 (Khan and Steffler 1996a,b). It can be observed that the computed flow profiles are not greatly affected by the pressure coefficient value. In turn, the variation of the linear dispersion relation as a function of m induces a phase lag, but it is not of great importance in dam break waves. The simulation for m=4 is however closer to the experimental data. The solution of Eq. (10) using the weakly-nonlinear source term Eq. (5) is presented in the same figure. This is a simulation for m=3, where the full non-linearity is not preserved. On inspection of the simulation using the fully non-linear Serre model, it is observed that the wave amplitude predicted by the weakly non-linear Boussinesq model is significantly high and not in agreement with the experimental data. There is no significant phase lag as compared to the Serre model, given that the pressure coefficient is identical and therefore the linear dispersion relation remains unaffected. The same set of simulations is repeated using Eq. (9) to account for the wave breaking, and the results are plotted in Fig. 10(b). The agreement with the experimental data improves, especially for the weakly non-linear Boussinesq model, which significantly modifies its prediction for the wave amplitude. In general, the simulations with m=4 accounting for wave breaking produce the best results. The effects of improving the linear frequency

dispersion relation are considered in Fig. 10(c). Eqs. (59) and (60) are solved and compared with the standard Serre equations. From Fig. 10, it can be observed that the enhanced Serre equations produce a certain phase lag, but also some variation in the prediction of wave amplitude as compared to the standard Serre equations. However, the enhanced equations are not giving more accurate predictions as compared to the standard Serre equations. The use of Nwogu-type enhanced models is mandatory in ocean research, where the solution of water wave problems from deep to shallow depths is common. However, in shallow flows, the frequency dispersion that is implicit in the standard Serre equations expressed as a function of U is reasonably good. Use of the enhanced equations produces further variations in the non-linear effects, which are not desirable. Therefore, the solution of the more complex system of Nwogu-type equations is not recommended for common civil engineering applications, where the full non-linearity of the standard Serre equations gives good results. A quantitative model accuracy test was performed by calculating the RMSD and the R statistics (Table 2). The application of the wave breaking criterion, Eq. (9), allows to control the amplitude of the advancing wave train. Its application leads to less accuracy in the prediction of the rarefaction wave, thereby giving greater RMSD and lower R values (Table 2). However, despite a slight lose of accuracy in the rarefaction wave, it is physically necessary to control wave amplitude with a wave breaking model.

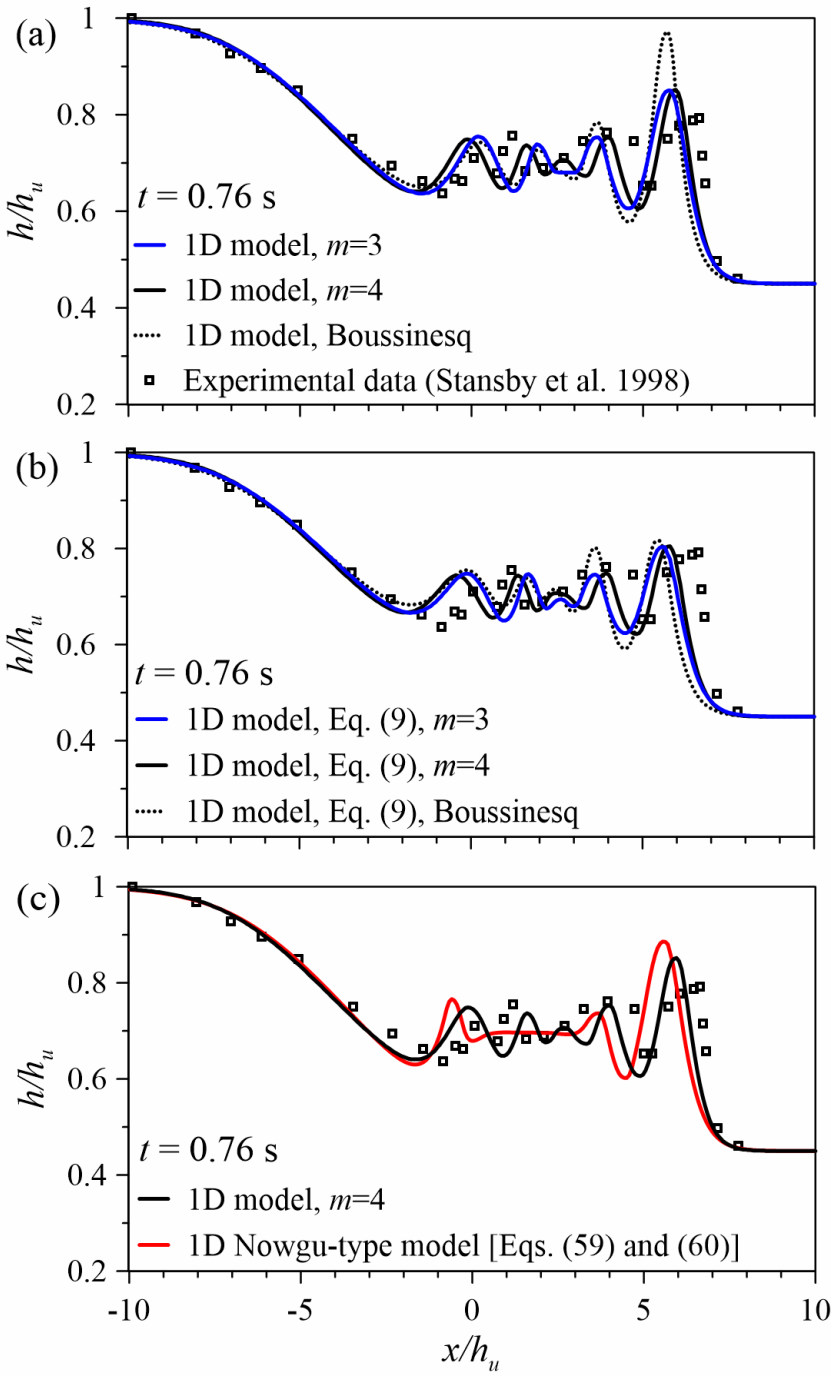

Fig. 10. Assessment of (a) pressure coefficient and non-linear terms without wave breaking; (b) idem to (a) with Eq. (9) for wave breaking; (c) standard Serre equations (m=3 and α^2=1) versus enhanced Serre equations (m=3 and α^2=0.66), and non-linear effects, without wave breaking

Model	RMSD	R
1D model, m=3	0.079	0.663
1D model, m=4	0.072	0.725
1D model, Boussinesq	0.099	0.549
1D model, Eq. (9), m=3	0.092	0.575
1D model, Eq. (9), m=4	0.085	0.638
1D model, Eq. (9), Boussinesq	0.107	0.474
1D Nowgu-type model [Eqs. (59) and (60)]	0.091	0.566

Table 2. RMSD and R Tests for Non-Hydrostatic Models Using the Experimental Data of Stansby et al. (1998) for r=0.45 at t=0.76 s

5.5. Evaluation of Non-Hydrostatic Velocity and Pressure Distributions

In this section, the accuracy of the irrotational velocity field (u,w) obtained using the Picard iteration method, Eqs. (57) and (58), is examined. To do this, an idealized test case is used. The shock front of a non-hydrostatic dam break wave is essentially a train of waves, usually called Favre waves. These waves can be considered, approximately, to be composed of a leading solitary wave-like front, followed by a train of secondary cnoidal waves (Favre 1935; Mitsotakis et al. 2014). Therefore, characteristic features of the non-hydrostatic dam break wave front can be inferred by an analogy to a solitary wave propagating over the same undisturbed water level. It may be noted that some of the wave breaking models for water wave propagation in coastal engineering are based on such an analogy. To test the accuracy of Eqs. (57) and (58), the 2D irrotational velocity field of a solitary wave is generated. In a system of reference moving with the solitary wave, it reduces to a steady flow. Therefore, the 2D irrotational, steady velocity field of a solitary wave is investigated using the x-Ψ method developed by Montes (1994). In this method, the Laplacian for the vertical coordinate z as a function of the pair of variables (Ψ,x) is solved, where Ψ=stream function. The Laplacian of this semi-inverse transformation z=z(x,Ψ) is as follows (Montes 1994):

$$\nabla^2 z = \frac{\partial^2 z}{\partial x^2}\left(\frac{\partial z}{\partial \Psi}\right)^2 + \frac{\partial^2 z}{\partial \Psi^2}\left[1+\left(\frac{\partial z}{\partial x}\right)^2\right] - 2\frac{\partial^2 z}{\partial x \partial \Psi}\frac{\partial z}{\partial x}\frac{\partial z}{\partial \Psi} = 0\,. \tag{68}$$

Montes (1994) developed a finite-difference numerical scheme to solve Eq. (68), that was applied in this test case. Details of the numerical scheme are not repeated here, given that these are extensively described by Montes (1994). The steady irrotational velocity field from Eqs. (57)–(58) is with $q=U(x)h(x)$=constant (Castro-Orgaz and Hager 2014),

$$u = \frac{q}{h}\left[1+\left(\frac{h_{xx}}{2h}-\frac{h_x^2}{h^2}\right)\left(\frac{3z^2-h^2}{3}\right)\right], \tag{69}$$

$$w = q\frac{z}{h^2}h_x . \tag{70}$$

The accuracy of Eqs. (69)–(70) is tested in Fig. 11. The full 2D solution of the irrotational velocity field (u,w) of a steady solitary wave for F_o^2=1.6 is determined using the x-Ψ method (Montes 1994). The free surface streamline (Ψ=q) is prescribed using Eq. (66); and the flow field was numerically determined solving Eq. (68). The flow was modelled using ten streamlines. The computed streamline flow pattern is plotted in Fig. 11(b). The pressure residuals at the free surface are small, so that the position of the free surface is not iterated. Experimental observations indicate the breaking of Favre waves, approximately, at $F_o^2\approx$1.5625 (Favre 1935). Therefore, the simulated solitary wave in Fig. 11 is close to breaking conditions of Favre waves, and thus, it is a limiting test case. It may be further noted that the ratio of wave amplitude to depth is 0.6, which corresponds to a highly non-linear wave. The computed 2D velocity field (u,w) at selected locations is plotted in Fig. 11(b and c), and compared with Eqs. (69)–(70), resulting in a good agreement. At the solitary wave crest (x/h_c=0), the free surface is convex, implying a u-velocity profile decreasing with the elevation. The pressure distributions for both the 2D and analytical solutions at these selected locations were determined based on the energy conservation in a potential flow. Again, the agreement is good. Naheer (1978) made the experimental observations of solitary wave propagation, from which experimental results for F_o^2=1.6 are plotted in Fig. 11(e). These experimental results are compared with Eq. (66), showing a good agreement.

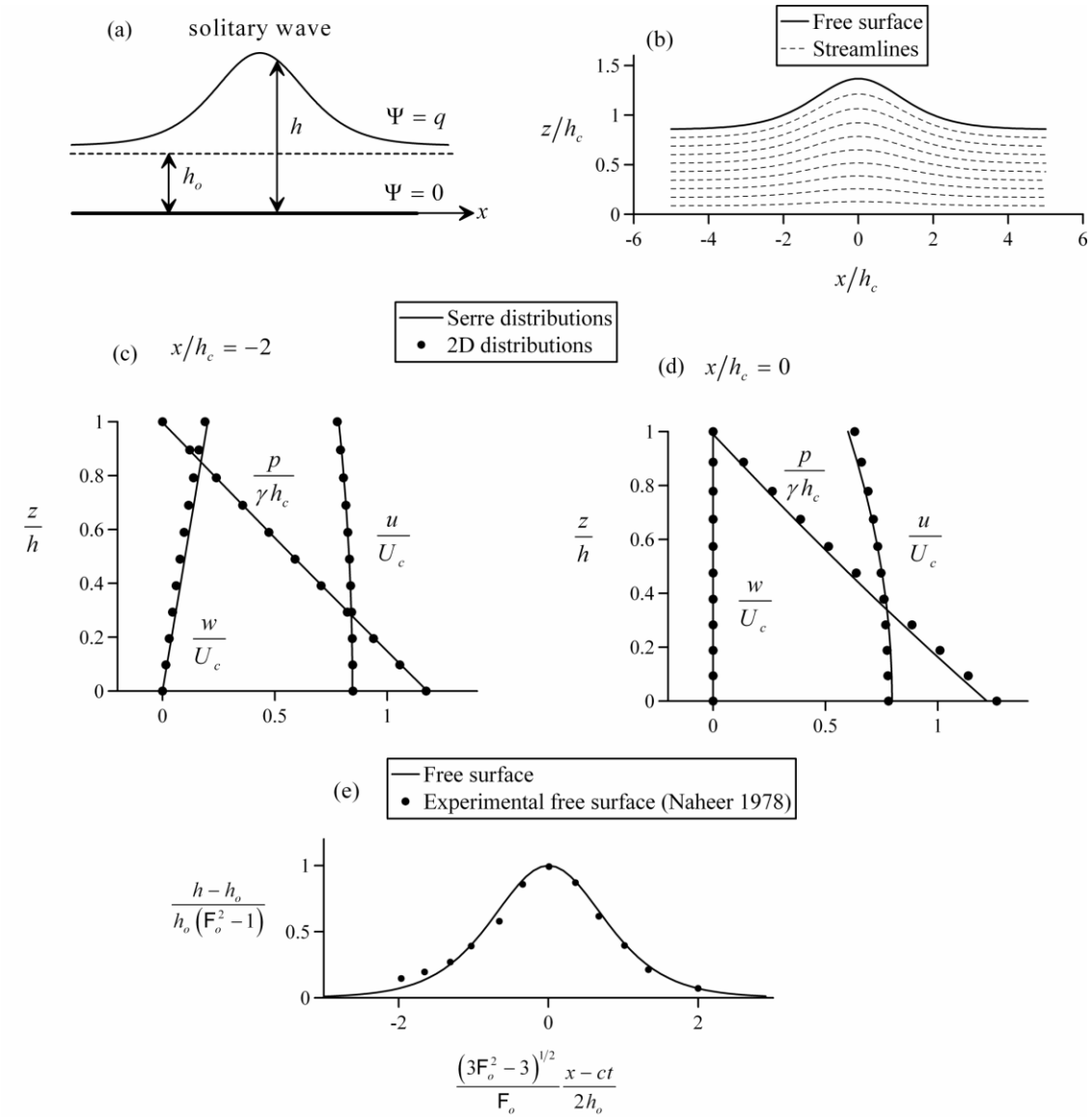

Fig. 11. Solitary wave for F_o^2=1.6: (a) Definition sketch; (b) computed streamline flow pattern, (c) velocity and pressure distributions at an approach flow section, (d) velocity and pressure distributions at crest, (d) comparison of the wave profile with experiments. Note: h_c and U_c are the critical depth and velocity, respectively

5.6. Evaluation of Non-Hydrostatic Velocity and Pressure Distributions

Mitsotakis et al. (2014) presented a solution of the Serre equations using the standard Galerkin finite-element method with smooth periodic splines and the fourth-order Runge Kutta method. A simulation presented by Mitsotakis et al. (2014) for h_u/h_d=1.4182 is plotted in Fig. 12. The results are presented in dimensionless form with $u=U/(gh_d)^{1/2}$ and $\eta=(h-h_d)/h_d$. The same simulation is conducted with the present finite volume scheme without wave breaking, and the results are plotted in Fig. 12. The results of both numerical models are similar.

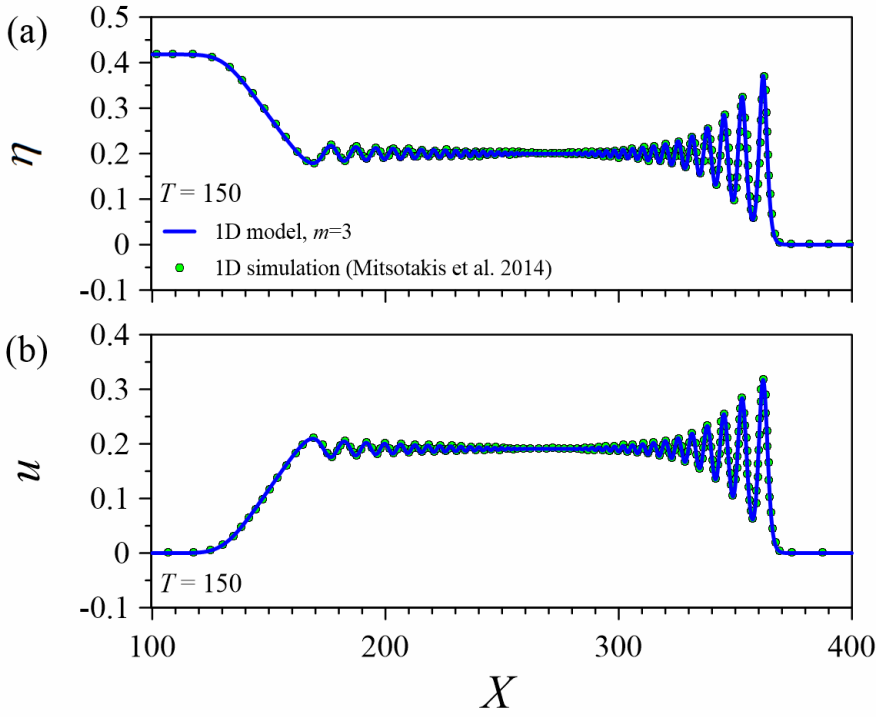

Fig. 12. Comparison of present finite volume solution and Galerkin finite element solution (Mitsotakis et al. 2014) for (a) normalized free surface elevation $\eta(X,T)$; (b) normalized depth-averaged velocity $u(X,T)$, for dimensionless time T=150

5.7. Comparison with Finite Difference Scheme

Mohapatra and Chaudhry (2004) developed the two-four finite difference predictor-corrector scheme to solve the Serre equations. This numerical scheme requires the use of artificial viscosity to suppress spurious oscillations. Otherwise, the solution becomes unstable and ultimately breaks down. The proposed finite volume numerical scheme is compared with the solution using the two-four finite difference scheme for the solution of the Serre equations (m=3) in Fig. 13, where computational results are compared with the experimental data of Stansby et al. (1998). Values of CFL=0.1 and Δx=0.05 m were used for the two-four simulations. For the finite volume model, CFL=0.1, Δx=0.05 m and Δx=0.0075 m were taken. The CFL value was reduced as much as possible in the two-four scheme to reduce truncation errors, given that it was found not possible to produce stable simulations reducing Δx below 0.05 m, during the computational work. Calibration of artificial viscosity by trial-and-error was necessary until getting a stable output. In contrast, it was possible to reduce both CFL and Δx in the finite volume scheme and then produce grid size independent results. The two-four scheme produce results that are in fair agreement with the experimental data. However, the finite volume simulation shows an overall improved performance by reducing Δx. Further, it may be

noted that the finite volume scheme lacks case-dependent parameters to be tuned for each simulation.

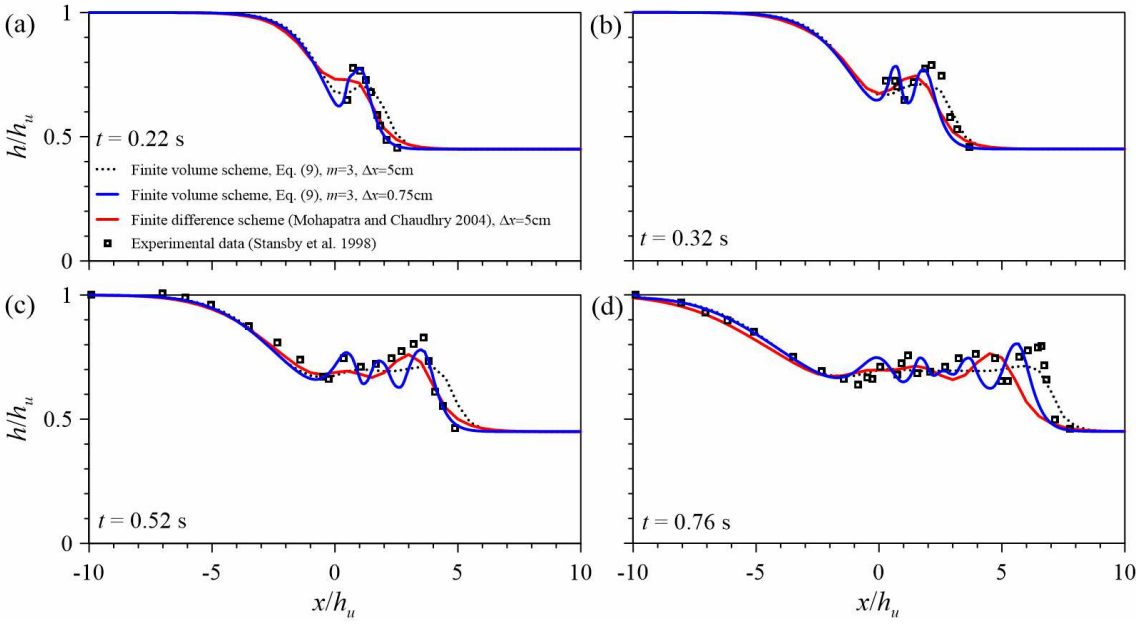

Fig. 13. Comparison of present finite volume solution and finite difference solution (Mohapatra and Chaudhry 2004) with the experimental data of Stansby et al. (1998) at times (a) t=0.22 s; (b) t=0.32 s; (c) t=0.52 s; (d) t=0.76 s.

5.8. Long-Term Simulation

To test the temporal stability of the present numerical model, Fig. 14 presents a long-term simulation. The test case by Stansby et al. (1998) for r=0.45 previously analyzed is selected. The results of the present 1D model with m=4 and using Eq. (9) are presented for t=1s [Fig. 14(a)], t=2s [Fig. 14(b)], t=5s [Fig. 14(c)], t=10s [Fig. 14(d)] and t=20s [Fig. 14(e)]. These computational results are generated using Δx=0.0075 m and CFL=0.9. It is shown that the present model results are stable. The wave breaking factor efficiently controls the wave amplitude of the shock front, which would grow without limits if wave breaking is not accounted for.

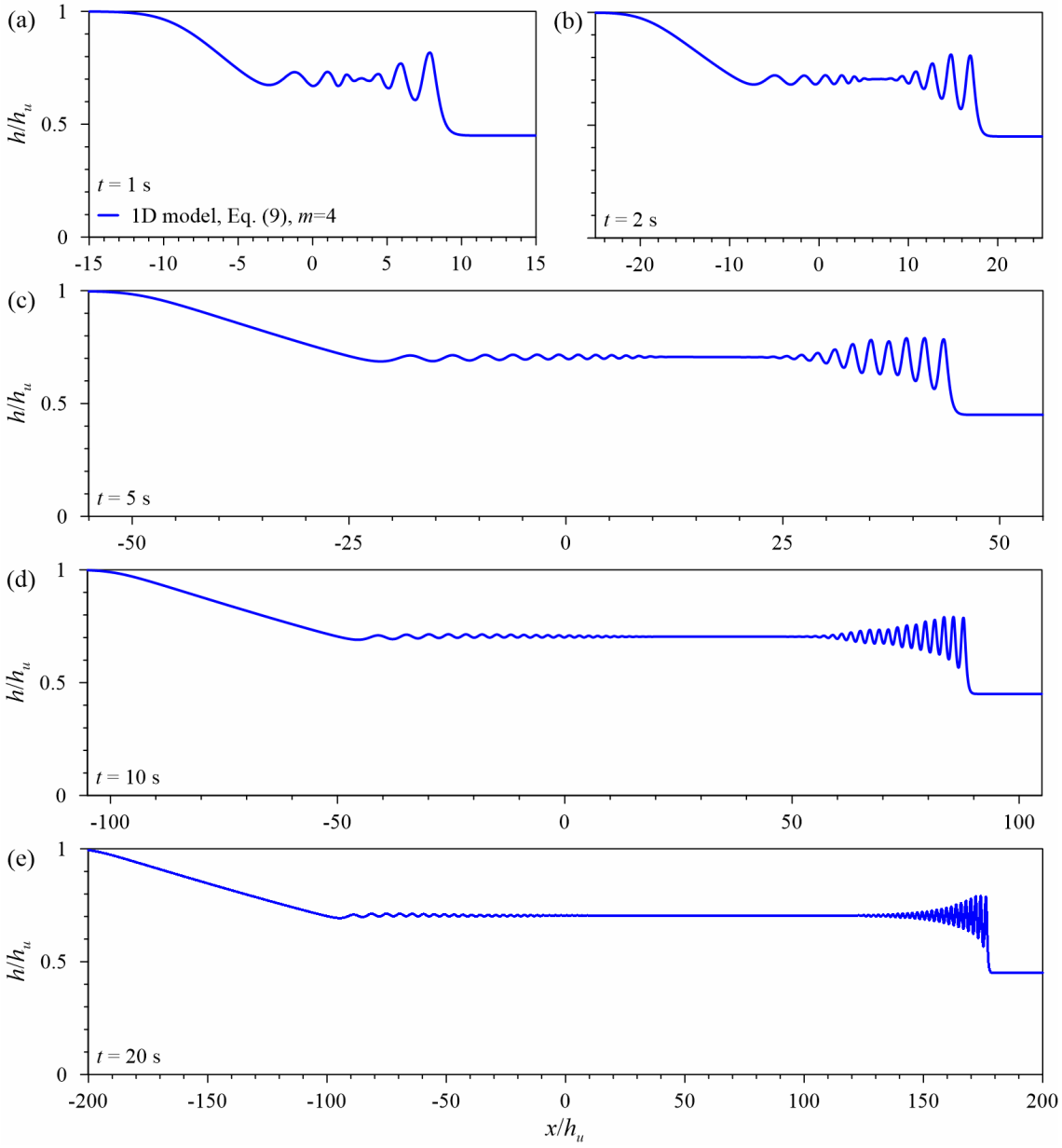

Fig. 14. Long-term simulation for the present model accounting for Eq. (9) and m=4 at: (a) t=1 s; (b) t=2 s; (c) t=5 s; (d) t=10 s; (d) t=20 s

5.9. Large Scale Test

A large scale test case is conducted in Fig. 15 to check the stability of the numerical scheme in a real life configuration. The upstream condition used in the numerical model is h_u=20m with depth ratio as r=0.45. The computational results are generated using CFL=0.9 and Δx=1 m. The results are presented for t=10s. Fig. 15 shows that the model results are stable.

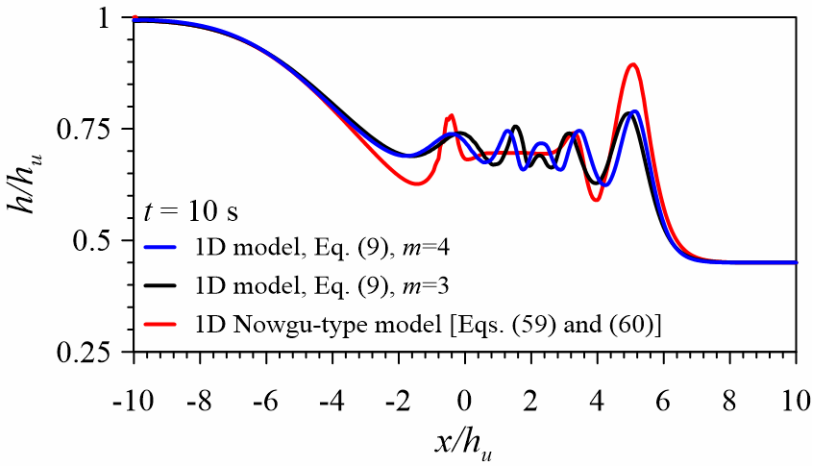

Fig. 15. Assessment of the present model accounting for Eq. (9) for a large scale test-case

5.10. Dry Downstream Bed

Dam break wave propagation over a dry downstream bed is a challenging test for a numerical model. Non-hydrostatic effects are significant for h_u/h_d>0.45, which is a threshold value and above which physical undulations appear both in the shock front and the rarefaction wave. However, the model was applied to a dry bed condition to test its stability. Fig. 16 depicts the comparison of the present model using Eq. (9) as damping factor, and m=4 (linear, non-hydrostatic, vertical pressure distribution) with the experimental data of Ozmen-Cagatay and Kocaman (2010). Computational results are compared with the experimental measurements at t=0.44 s [Fig. 16(a)], t=0.62 s [Fig. 16(b)], t=0.8 s [Fig. 16(c)] and t=1.06 s [Fig. 16(d)]. The computational results are generated using Δx=0.05 m, and CFL=0.4. The downstream reach is artificially wetted to produce a stable wet-dry front computation (Wu and Wang 2007, 2008). The downstream flow depth used in the model is h_d=0.00001 m, whilst the initial upstream flow depth is h_u=0.25m. In this test case, the high free surface slopes and curvatures numerically computed during the initial stages of the dam break generated small numerical ripples in the vicinity of the dam axis. The accuracy and the stability of the solution are however not affected. To remove these ripples, rather than introducing any numerical manipulation, the dam break flow is initiated using the Saint Venant equations up to t=0.1 s. The correct solution corresponding to the Serre equations was quickly set only after a few time steps, and it was verified that the initial run of the model had no impact on the solution but to reduce the numerical ripples near the dam axis. It can be observed that the non-hydrostatic simulations are in good agreement with

the experimental data. The analytical solution of the Saint Venant equations for the instantaneous free surface profile given by Ritter (Toro 2001)

Q
$$h = \frac{h_u}{9}\left[2 - \frac{x}{t\left(gh_u\right)^{1/2}}\right]^2, \tag{71}$$

is plotted for the same test case in Fig. 16. The rarefaction wave was accurately predicted by the Serre equations, showing an improved result as compared to Ritter's solution. For the positive wave, both models gave almost identical results.

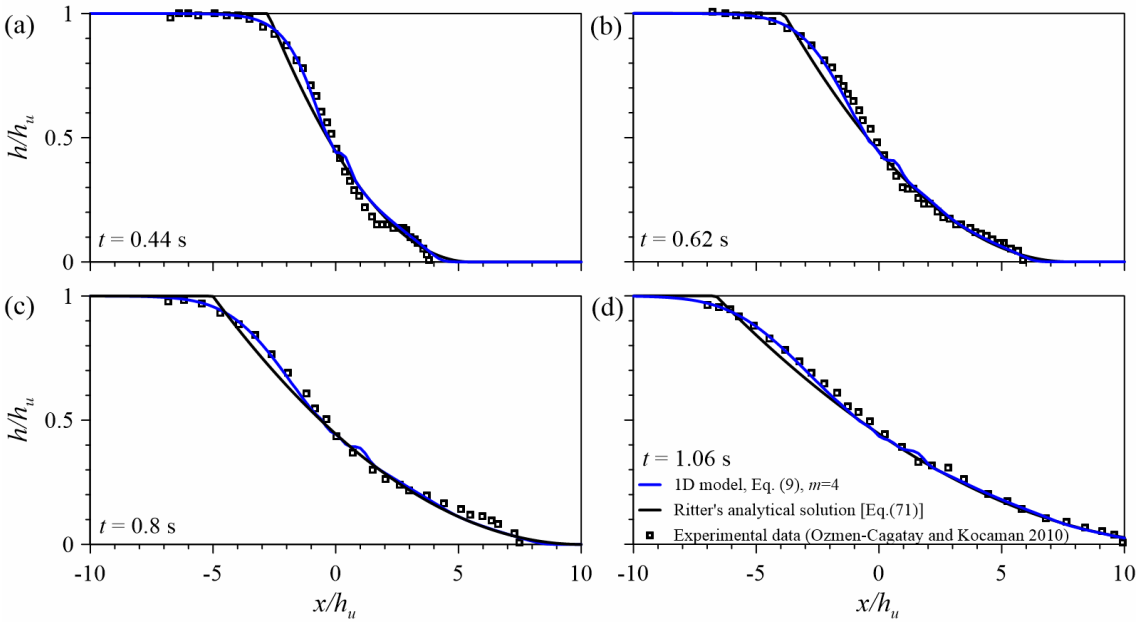

Fig. 16. Dry bed propagation test using Eq. (9) and m=4 at: (a) t=0.44 s; (b) t=0.62 s; (c) t=0.8 s; (d) t=1.06 s

6. Conclusions

The following conclusions are drawn from this study:

• Evaluation of several time stepping schemes, including the Euler and the Runge-Kutta TVD methods, shows that the third-order Adams-Bashforth predictor and the fourth-order Adams-Moulton corrector scheme produce stable results solving the Serre equations with a value of CFL close to 1, for instance, 0.9. The other schemes produce unstable results and require a significant reduction of CFL, increasing the computational cost.

• Wave breaking models based on steady irrotational flow considerations produce computational results that are in disagreement with the experimental data. In contrast, the damping factor proposed by Hosoda and Tada (1994) produces a smooth transition

from non-breaking to breaking wave condition, providing results in good agreement with the experimental data. This is in agreement with former results in the coastal engineering field since the pioneering work of Schäffer et al. (1993) (Tonelli and Petti 2009; Bonneton et al. 2011; Tissier et al. 2012; Shi et al. 2012).

• The impact of the vertical pressure distribution coefficient is not significant, and the results of the Serre equations (Serre 1953) and Khan and Steffler's (1996a,b) depth-averaged equations are similar. The latter model produces results slightly in better agreement with the experimental data; so the use of a linear pressure distribution for dam break wave modelling is recommended.

• The consideration of the full non-linearity in the Serre-type equations is found to be important for predicting the wave amplitudes of dam break waves. The weakly non-linear Boussinesq-type model produces exaggerated wave amplitudes, although this effect diminished when wave breaking is included. In general, the consideration of the full non-linearity is preferable.

• The use of the Serre equations with enhanced linear frequency dispersion is found to not giving an improvement of computational predictions as compared to the experimental data. Therefore, use of this more complex system of equations is not needed in shallow open channel flows.

• The proposed finite volume scheme for solving the Serre equations with wave breaking produces results in agreement with the experimental data (Stansby et al. 1998) and the 3D solution of the RANS equations (Marsooli and Wu 2014). The accuracy of the solution without wave breaking is found to be similar to that developed by Mitsotakis et al. (2014) with the standard Galerkin finite element solution. The present finite volume results are better than those generated by using the finite difference methods (Mohapatra and Chaudhry 2004).

7. Acknowledgements

This study, which is part of the PhD thesis of the first author, was supported by the Spanish project CTM2013-45666-R, Ministerio de Economía y Competitividad.

8. Notation

The following symbols are used in this paper:

a = shallow water wave celerity (m/s);

b = MUSCL-TVD-4th coefficient;

b_1 = MUSCL-TVD-4th coefficient;

c = solitary wave celerity (m/s);

CFL = Courant-Friedrichs-Lewy number;

$\mathbf{E}$ = auxiliary vector (m/s, m^2/s^2);

F = Froude number;

F_o = Froude number of solitary wave;

$\mathbf{F}$ = vector of fluxes in x-direction (m^2/s, m^3/s^2);

g = gravitational acceleration (m/s^2);

H = solitary wave amplitude (m);

h = flow depth (m);

h_c = critical flow depth (m);

h_* = flow depth in star region of Riemann problem (m);

h_{cr} = critical free surface slope;

h_d = initial downstream flow depth (m);

h_o = still water depth (m);

h_u = initial upstream flow depth (m);

h_x = free surface slope, $\partial h/\partial x$;

h_{xx} = free surface curvature, $\partial^2 h/\partial x^2$ (1/m);

i = cell index in x-direction;

k = time step index;

m = pressure distribution coefficient;

q = non-dimensional correction factor to shallow water wave celerity in HLL

solver;

q = discharge (m^2/s);

r = depth ratio;

S = signal speed (m/s);

S, **Z** = source terms vectors (m/s, m^2/s^2);

T = normalized time;

t = time (s);

U = depth-averaged velocity (m/s);

U_c = critical velocity (m/s);

U, **W** = vectors of unknowns (m, m^2/s);

u = velocity in x-direction (m/s);

u = non-dimensional depth-averaged velocity;

u_α = velocity at a reference level (m/s);

w = velocity in z-direction (m/s);

X = normalized horizontal coordinate (m);

x = horizontal coordinate (m);

y = auxiliary variable (m^2/s);

z = vertical coordinate (m);

z_α = reference elevation (m);

α = normalized reference elevation;

Δt = time step (s);

Δx = grid size (m);

ϕ = wave-breaking empirical factor;

γ_1, γ_1, γ_3= wave breaking factors;

η = normalized free surface elevation;

ψ = non-hydrostatic term (m^3/s^2); and

Ψ = stream function (m^2/s).

Subscripts

* = previous iteration;

L, *R* = left and right control volume interface; and

q, (1), (2), (3)= time stepping intermediate levels.

9. References

Abbott, M. B. (1979). *Computational hydraulics: Elements of the theory of free surface flows*. Pitman, London, United Kingdom.

Barthelemy, E. (2004). "Nonlinear shallow water theories for coastal waters." *Surveys in Geophysics*, 25(3), 315–337.

Bonneton, P., Chazel, F., Lannes, D., Marche, F., and Tissier, M. (2011). "A splitting approach for the fully nonlinear and weakly dispersive Green-Naghdi model." *J. Computational Phys.*, 230(4), 1479–1498.

Cantero-Chinchilla, F., Castro-Orgaz, O., Dey, S., and Ayuso, J. L. (2016). "Non-hydrostatic dam break flows II: One-dimensional depth-averaged modeling for movable bed flows." *J. Hydraul. Eng*. (under review).

Carter, J. D., and Cienfuegos, R. (2011). "The kinematics and stability of solitary and cnoidal wave solutions of the Serre equations."*European J. Mech. B/Fluids*,30(3), 259–268.

Castro-Orgaz, O., and Hager, W. H. (2014). "1D modelling of curvilinear free surface flow: Generalized Matthew theory." *J. Hydraul. Res*., 52(1), 14–23.

Castro-Orgaz, O., Hutter, K., Giraldez, J. V., and Hager, W. H. (2015). "Non-hydrostatic granular flow over 3D terrain: New Boussinesq-type gravity waves?" *J. Geophys. Res. Earth Surface*, 120(1), 1–28, 10.1002/2014JF003279.

Chaudhry, M. H. (2008). *Open-channel flow*. Springer, Berlin, Germany.

Cienfuegos, R., Barthélemy, E., and Bonneton, P. (2006). "A fourth-order compact finite volume scheme for fully nonlinear and weakly dispersive Boussinesq-type equations. Part I: model development and analysis." *Int. J. Numer. Meth. Fluids*, 51(11), 1217–1253.

Cienfuegos, R., Barthélemy, E., and Bonneton, P. (2010). "Wave-breaking model for Boussinesq-type equations including roller effects in the mass conservation equation." *J. Waterw., Port, Coastal, Ocean Eng.*, 136(1), 10–26.

De Almeida, A. B., and Franco, A. B. (1994). *Modeling of dam-break flow*. Springer, Berlin, Germany.

Dias, F., and Milewski, P. (2010). “On the fully non-linear shallow-water generalized Serre equations.” *Physics Letters* A, 374(8), 1049–1053.

Erduran, K. S., Ilic, S., and Kutija, V. (2005). “Hybrid finite-volume finite-difference scheme for the solution of Boussinesq equations.” *Int. J. Num. Meth. Fluids*, 49(11), 1213–1232.

Favre, H. (1935). *Étude théorique et expérimentale des ondes de translation dans les canaux découverts* (Theoretical and experimental study of translation waves in open channels). Dunod, Paris, France (in French).

Gottlieb, S., and Shu, C. W. (1998). “Total variation diminishing Runge-Kutta schemes.” *Math. Computation*, 67(221), 73–85.

Hager, W. H., and Hutter, K. (1984). “On pseudo-uniform flow in open channel hydraulics.” *Acta Mech*., 53(3-4), 183–200.

Hosoda, T., and Tada, A. (1994). “Free surface profile analysis on open channel flow by means of 1-D basic equations with effect of vertical acceleration.” *JSCE Annual J. Hydraul. Eng*., 38, 457-462 (in Japanese).

Jameson, A., Schmidt, W., and Turkel, E. (1981). “Numerical solutions of the Euler equations by finite volume methods using Runge-Kutta time-stepping schemes.” *AIAA* paper 81-1259, 315–333.

Kennedy, A., Chen, Q., Kirby, J., and Dalrymple, R. (2000). “Boussinesq modeling of wave transformation, breaking, and runup. I: 1D.” *J. Waterw., Port, Coastal, Ocean Eng.*, 126(1), 39–47.

Khan, A. A., and Steffler, P. M. (1996a). “Vertically averaged and moment equations model for flow over curved beds.” *J. Hydraul. Eng*., 122(1), 3–9.

Khan, A. A., and Steffler, P. M. (1996b). “Modelling overfalls using vertically averaged and moment equations.” *J. Hydraul. Eng*., 122(7), 397–402.

Khan, A. A., and Lai, W. (2014). *Modeling shallow water flows using the discontinuous Galerkin method*. CRC Press, Taylor and Francis, New York.

Kim, D. -H., and Lynett, P. J. (2011). “Dispersive and nonhydrostatic pressure effects at the front of surge.” *J. Hydraul. Eng*., 137(7), 754–765.

Kim, D. -H., Lynett, P. J., and Socolofsky, S. (2009). “A depth-integrated model for weakly dispersive, turbulent, and rotational fluid flows.” *Ocean Modelling* 27(3), 198–214.

Li, J., Cao, Z., Pender, G., and Liu, Q. (2013). “A double layer-averaged model for dam-break flows over mobile bed.” *J. Hydraul. Res*., 51(5), 518–534.

Maleki, S., and Khan, A. A. (2015). “Effect of channel shape on selection of time Marching scheme in the discontinuous Galerkin method for 1D open channel flow.” *J. Hydrodynamics Ser. B*, 27(3), 413–426.

Marsooli, R., and Wu, W. (2014). “3-D finite-volume model of dam-break flow over uneven beds based on VOF method.” *Adv. Water Resour.*, 70, 104–117.

Mignot, E., and Cienfuegos, R. (2009). “On the application of a Boussinesq model to river flows including shocks.” *Coastal Eng.*, 56(1), 23–31.

Mitsotakis, D., Ilan, B., and Dutykh, D. (2014). “On the Galerkin/finite-element method for the Serre equations.” *J. Scientific Computing*, 61(1), 166–195.

Mohapatra, P. K., and Chaudhry, M. H. (2004). “Numerical solution of Boussinesq equations to simulate dam-break flows.” *J. Hydraul. Eng*., 130(2), 156–159.

Montes, J. S. (1994). “Potential flow solution to the 2D transition form mild to steep slope.” *J. Hydraul. Eng*., 120(5), 601–621.

Naheer, E. (1978). “Laboratory experiments with solitary wave.” *J. Waterw., Port, Coastal, Ocean Eng.*, 104(4), 421–436.

Nwogu, O. (1993). “Alternative form of Boussinesq equations for nearshore wave propagation.” *J. Waterw., Port, Coastal, Ocean Eng.*, 119(6), 618–638.

Ozmen-Cagatay, H., and Kocaman, S. (2010). “Dam-break flows during initial stage using SWE and RANS approaches.” *J. Hydraul. Res.*, 48(5), 603–611.

Peregrine, D. H. (1966). “Calculations of the development of an undular bore.” *J. Fluid Mech*., 25(2), 321–330.

Schäffer, H. A., Madsen, P. A., Deigaard, R. (1993). “A Boussinesq model for waves breaking in shallow water.” *Coastal Eng.*, 20(3–4), 185–202.

Serre, F. (1953). “Contribution à l'étude des écoulements permanents et variables dans les canaux (Contribution to the study of steady and unsteady channel flows).” *La Houille Blanche*, 8(6-7), 374–388; 8(12), 830–887 (in French).

Shi, F., Kirby, J. T., Harris, J. C., Geiman, J. D., and Grilli, S. T. (2012). “A high-order adaptive time-stepping TVD solver for Boussinesq modeling of breaking waves and coastal inundation.” *Ocean Modelling*, 43–44, 36–51.

Soares-Frazão, S., and Guinot, V. (2008). “A second-order semi-implicit hybrid scheme for one-dimensional Boussinesq-type waves in rectangular channels.” *Int. J. Num. Meth. Fluids*, 58(3), 237–261.

Soares-Frazão, S., and Zech, Y. (2002). “Undular bores and secondary waves: Experiments and hybrid finite-volume modelling.” *J. Hydraul. Res*., 40(1), 33–43.

Stansby, P. K., Chegini, A., and Barnes, T. C. D. (1998). “The initial stages of dam-break flow.” *J. Fluid Mech*., 374, 407–424.

Steffler, P.M.., and Jin, Y.C. (1993). “Depth-averaged and moment equations for moderately shallow free surface flow.” *J. Hydraul. Res*., 31(1), 5–17.

Stoker, J. J. (1958). *Water waves: The mathematical theories with applications*. John Wiley and Sons, New York.

Su, C. H., and Gardner, C. S. (1969). “KDV equation and generalizations. Part III. Derivation of Korteweg-de Vries equation and Burgers equation.” *J. Math. Phys*., 10(3), 536–539.

Tonelli, M., and Petti, M. (2009). “Hybrid finite volume - finite difference scheme for 2DH improved Boussinesq equations.” *Coastal Eng.*, 56(5–6), 609–620.

Tissier, M., Bonneton, P., Marche, F., Chazel, F., and Lannes, D. (2012). “A new approach to handle wave breaking in fully non-linear Boussinesq models.” *Coastal Eng.*, 67(September), 54–66.

Toro, E .F. (2001). *Shock-capturing methods for free-surface shallow flows*. John Wiley and Sons, Singapore.

Toro, E. F. (2009). *Riemann solvers and numerical methods for fluid dynamics: A practical introduction*. Springer, Berlin, Germany.

Wei, G., and Kirby, J. T. (1995). “Time-dependent numerical code for extended Boussinesq equations.” *J. Waterw., Port, Coastal, Ocean Eng.*, 121(5), 251–261.

Wei, G., Kirby, J. T., Grilli, S. T., and Subramanya, R. (1995). “A fully nonlinear Boussinesq model for surface waves. Part 1. Highly nonlinear unsteady waves.” *J. Fluid Mech.*, 294, 71–92.

Wu, W., and Wang, S. S. Y. (2007). “One-dimensional modeling of dam-break flow over movable beds.” *J. Hydraul. Eng.*, 133(48), 48–58.

Wu, W., and Wang, S. S. Y. (2008). “One-dimensional explicit finite-volume model for sediment transport.” *J. Hydraul. Res.*, 46(1), 87–98.

Yamamoto, S., and Daiguji, H. (1993). “Higher-order-accurate upwind schemes for solving the compressible Euler and Navier-Stokes equations.” *Comp. Fluids*, 22(2), 259–270.

Appendix III

Non-hydrostatic dam break flows II: one-dimensional depth-averaged modeling for movable bed flows

Francisco Nicolás Cantero-Chinchilla[1]; Oscar Castro-Orgaz[2]; Subhasish Dey[3]; and Jose Luis Ayuso-Muñoz[4]

Accepted for publication by *Journal of Hydraulic Engineering*. Impact factor (JCR 2014): 1.621 / Q1 (28/125 Civil Engineering)

Abstract

The dam break flow over a movable bed is an important problem in fluvial flow processes. These flows are usually predicted by a one-dimensional (1D) approach based on a hydrostatic pressure distribution. Recent 3D non-hydrostatic simulations of dam break waves over movable beds based on the Reynolds-averaged Navier-Stokes (RANS) equations revealed that Saint Venant theory is not accurate predicting the flow dynamics within the scour hole developed. In this work, a generalized 1D non-hydrostatic model for flow over movable beds is proposed assuming a linear, non-hydrostatic, pressure distribution. The new set of 1D equations account for the vertical acceleration, which is important in dam break waves over movable beds, given the instantaneous curved beds generated over the erodible terrain. These equations account for both the bed- and suspended-load transport modes. A high-resolution finite volume numerical scheme with a semi-implicit treatment of non-hydrostatic terms is developed to solve the governing equations, producing solutions that are in good agreement with 3D computational results and experimental data. The free surface profiles predicted by the new model show a significant improvement as compared to those obtained from the existing hydrostatic simulations. The unsteady non-hydrostatic simulations are shown to be convergent to steady flow solutions with non-hydrostatic pressure.

[1]PhD student, University of Cordoba, 14071 Cordoba, Spain. E-mail: z12cachf@uco.es
[2]Professor, University of Cordoba, 14071 Cordoba, Spain. E-mail: ag2caoro@uco.es (author for correspondence)
[3]Professor, Department of Civil Engineering, Indian Institute of Technology Kharagpur, West Bengal 721302, India. E-mail: sdey@iitkgp.ac.in
[4]Professor, University of Cordoba, 14071 Cordoba, Spain. E-mail: ir1aymuj@uco.es

1. Introduction

Dam break flow is a topic of continued research interest given its tremendous detrimental effects. The usual engineering approach to predict these flows relies on the use of depth-averaged shallow water wave models based on a hydrostatic pressure distribution (Wu 2008). In recent years, hydrostatic shallow-water flow models were extensively investigated. Wu and Wang (1999, 2007, 2008) developed Saint Venant-type mixture flow equations for dam break flows over erodible beds. Fraccarollo and Capart (2002) proposed a two-layer movable bed dam break flow model with separate simulations of clear water and mixture sediment-water layers. Li et al. (2013) developed a double-layer averaged model. Capart and Young (1998, 2002), Cao et al. (2004) and Zhang et al. (2013) developed models for dam break waves over erodible bed considering non-equilibrium sediment transport conditions. Wu et al. (2000, 2004) studied non-uniform sediment transport using 3D and depth-averaged models. Wu et al. (2012) treated the non-cohesive embankment breaching. Geomorphic shallow water flows, as the dam break waves over an erodible bed, requires consideration of fluid motion and erosion/deposition of particles. It is widely accepted that the shallow water flow approximation with hydrostatic pressure produces a reasonable balance between computational efforts and accuracy of results (Greco et al. 2012). An alternative to the two-layer formulation follows the two-phase flow approach pursued by Greco et al. (2012). Therefore, the development of a model for fast geomorphic flows require the study of a number of components, including the type of formulation to simulate sediment transport processes (mixture model, two-layer model or two-phase flow model), and the hypothesis to close the momentum equations for the fluid flow above the erodible beds. While huge efforts were made to produce physically accurate sediment transport components, the fluid flow above the erodible bed is routinely assumed to be governed by a hydrostatic pressure distribution. This limitation is important, given that the models based on the hydrostatic pressure distribution ignore the vertical flow acceleration. Marsooli and Wu (2015) conducted a detailed and accurate assessment of the importance of non-hydrostatic simulations over movable beds using three-dimensional (3D) computations. Non-hydrostatic pressures are generated by local and convective accelerations in a variety of flow problems. Examples are the initial stages of the dam break flow over rigid beds, the flow above the scour hole formed in the dam break wave over an erodible bed, or the flow at obstacles embedded in the natural streambed downstream of the dam, such as a bridge pier

(Marsooli and Wu 2015). However, to the best of the authors' knowledge, no attempt has so far been made to develop a depth-averaged model considering the non-hydrostatic pressure distribution and the sediment transport for dam break waves over movable beds. Thus, it remains untested to what extent the non-hydrostatic pressure distribution closure law to the 1D momentum equations of the fluid flow above an erodible bed produces results in conformity with nature.

The literature on depth-averaged non-hydrostatic open channel flow is extensive. It is well known that Boussinesq-type equations can simulate undular bores and the formation of dunes and anti-dunes in erodible beds (Wu 1987; Onda and Hosoda 2004; Onda et al. 2010; Bashiri et al. 2015). Castro-Orgaz et al. (2015) presented a recent review of the topic of Boussinesq equations, and detailed applications in geophysical contexts, including avalanche dynamics. The process to produce vertically integrated systems for unsteady non-hydrostatic flows is described in detail therein. One of the most accurate models developed for unsteady non-hydrostatic flow over rigid beds was presented by Khan and Steffler (1996a,b). It is a finite element numerical model based on the momentum and moment of momentum equations developed by Steffler and Jin (1993). In this method, each degree of freedown assigned to velocity and pressure fields in the form of a perturbation-type function was handled by a closure transport equation derived by using a weighted residual method. Khan and Steffler (1996a,b) showed that this system may be simplified to a Boussinesq-type model, and physically good results were still feasible. Both the original momentum and moment equations model, and its simplified Boussinesq-type version, were developed, however, for clear water flow over rigid beds. Khan and Steffler (1996a,b) demonstrated that the consideration of non-hydrostatic pressures in flows over curved beds was of great importance. Given the scour hole generated in dam break flows over erodible beds, where the bed is curved (Wu 2008), some influence on the computation of flow profiles in dam break waves over erodible beds is expected. The free surface profile in the vicinity of this scour hole shows, experimentally, an undulating free surface, which suggests the influence of a non-hydrostatic pressure on the flow dynamics (Onda et al. 2004, 2010). Based on these observations, the main motivation of this study is to investigate the impact of non-hydrostatic pressures on dam break flows over erodible beds. For this task, a new 1D-depth-averaged, unsteady, non-hydrostatic model for flow over curved, erodible beds, is developed. Formulation of such a model requires the integration of the RANS equations

in a vertical plane considering that the bed is deforming in space and time due to erosion/deposition processes, whilst the fluid flow is composed of a mixture of water and sediment with an average density, which is also a function of time and space variables. The developed equations are shown to be a generalization of the Boussinesq-type equations by Khan and Steffler (1996a,b). A non-equilibrium sediment transport model is used based on Wu and Wang (2007) with some modifications (Wu 2015). A robust and accurate high-resolution finite volume scheme was developed for the new set of physical equations, and the solutions are tested against the experimental data of Fraccarollo and Capart (2002) and the results of the 3D numerical solution by Marsooli and Wu (2015).

2. Governing Equations

We consider 1D unsteady non-hydrostatic free surface flow over an erodible bed in a vertical plane (Fig. 1). The elevation of the static erodible bed of sediment is $z_b(x,t)$, and the fluid flow above is composed of a mixture of water and sediments. The dynamic flow above the bed is composed of a bed-load layer, where the flux per unit width is q_b, and a suspended-load layer. The flow depth is $h(x,t)$, the discharge is $q(x,t)$ and the depth-averaged velocity in the x-direction is $U(x,t)=q/h$. The depth-averaged mass conservation equation for the mixture flow layer integrating the RANS mass conservation equation in a vertical plane is

$$\frac{\partial(\rho h)}{\partial t}+\frac{\partial(\rho hU)}{\partial x}+\frac{\partial(\rho_b z_b)}{\partial t}=0\,, \tag{1}$$

where $\rho(x,t)$=mass density of water-sediment mixture, given by $\rho=\rho_w(1-C_t)+\rho_s C_t$; ρ_w=clear water mass density; ρ_s=sediment mass density; $C_t(x,t)$=depth-averaged total sediment concentration in the fluid layer of thickness h (suspended plus bed-load layers); ρ_b=mass density of static bed layer, defined as $\rho_b=\rho_w p_m+\rho_s(1-p_m)$; p_m=sediment porosity; t=time; and x=streamwise coordinate. Integrating the RANS x- and z-momentum equations for a mixture flow in a vertical plane yields, respectively,

$$\frac{\partial(\rho hU)}{\partial t}+\frac{\partial}{\partial x}\left(\rho hU^2+\frac{1}{2}\rho gh^2\right)=-\rho gh\frac{\partial z_b}{\partial x}-\tau_b-p_1\frac{\partial z_b}{\partial x}-\frac{\partial}{\partial x}\left(\frac{hp_1}{2}\right), \tag{2}$$

$$\frac{\partial(\rho hW)}{\partial t}+\frac{\partial(\rho hUW)}{\partial x}=p_1-\tau_b\frac{\partial z_b}{\partial x}\,. \tag{3}$$

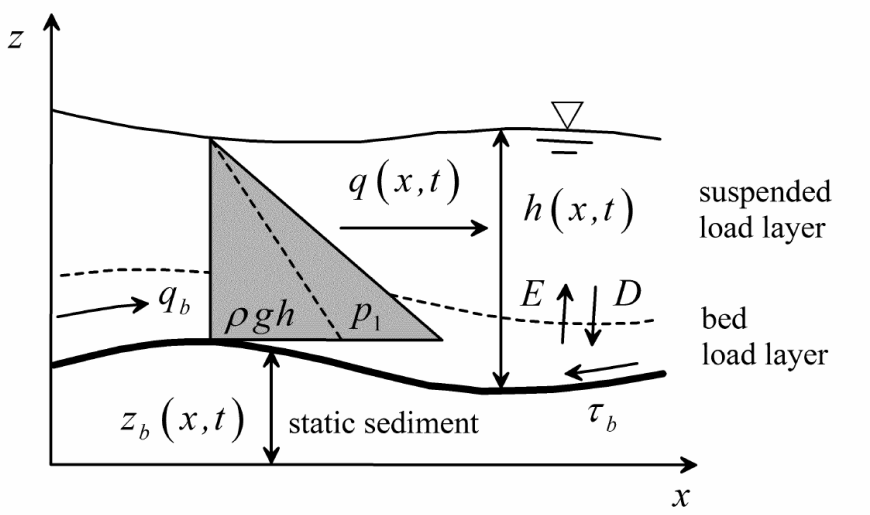

Fig. 1. Definition sketch of 1D non-hydrostatic flow over an erodible bed

To obtain Eqs. (2)–(3), it was assumed that the velocity in the x-direction is uniform and equal to its depth-averaged value U, that the vertical velocity and non-hydrostatic pressure distributions are linear, and the stress state at the bed is of pure shear. Mathematical details of the vertically-integration process are given in Steffler and Jin (1993) and Castro-Orgaz et al. (2015). In the above, g=gravitational acceleration; $\tau_b(x,t)$=bed shear stress; $p_1(x,t)$= pressure at bed in excess of hydrostatic; and $W(x,t)$=depth-averaged vertical velocity component. The depth-averaged vertical velocity W can be expressed in terms of the depth-averaged streamwise velocity U using the kinematic boundary conditions at the bed and the free surface levels. The resulting equation is (Castro-Orgaz et al. 2015)

$$W = \frac{1}{2}(w_b + w_s) = \frac{1}{2}\left(\frac{\partial z_s}{\partial t} + U\frac{\partial z_s}{\partial x} + \frac{\partial z_b}{\partial t} + U\frac{\partial z_b}{\partial x} \right), \tag{4}$$

where w_s and w_b=vertical velocity at the free surface and the bed sediment surfaces, respectively; and z_s=free surface level ($=h+z_b$). Eqs. (1)–(4) are generalized equations for unsteady non-hydrostatic flow with bed- and suspended-load transport over erodible beds. Note the presence of $\partial z_b/\partial t$ allowing for a movable bed, and the C_t concentration of the sediment mixture. These terms are absent in Khan and Steffler (1996a,b) model. Further, in the original model solved by Khan and Steffler (1996a,b), the horizontal velocity profile was set using a linear function as a perturbation from uniformity, whilst the vertical velocity and pressure varied quadratically. Letting the streamwise velocity profile be uniform and equal to its depth-averaged value U, and assuming linear variations for the vertical velocity and pressure, they obtained a Boussinesq-type model.

For clear water flow over rigid beds, Eqs.(2)–(4) simplify to the Boussinesq model by Khan and Steffler (1996a,b), that was verified to be a significant improvement over Saint Venant equations for flow over curved beds. Therefore, in Eqs. (2) and (3), the non-hydrostatic pressure distribution is prescribed using a linear function (Fig. 1) (Castro-Orgaz et al. 2015), following Khan and Steffler (1996a,b) Boussinesq-type version of their momentum and moment of momentum model. The rigorous mathematical formulation for Boussinesq-type equations, however, relies on a hydrostatic pressure component corrected by a quadratic variation due to non-hydrostatic terms (Iwasa 1956; Onda et al. 2010; Castro-Orgaz et al. 2015). Castro-Orgaz et al. (2015) compared "exact" Boussinesq-type equations based on the quadratic pressure distribution with Khan and Steffler (1996a,b) Boussinesq-type equations based on the linear pressure distribution. They found that the non-hydrostatic terms accounted for in both formulations were similar, with an identical bottom pressure head function. However, a different correction factor emerged in the dispersion part of the differential equation describing cnoidal and solitary wave solutions. For steady flow solutions (or travelling waves), the momentum is conserved, leading to the differential momentum equation describing cnoidal and solitary waves

$$\frac{h^2}{2}+\frac{q^2}{gh}\left(1+\frac{hh_{xx}-h_x^2}{4}\right)=\text{const}\,, \tag{5}$$

where h_x=dh/dx; and h_{xx}=d^2h/dx^2. Eq. (5) is derived from Eqs. (2)–(4) assuming steady, clear water, frictionless flow over a rigid and horizontal bed. For the "exact" Boussinesq equations, the non-hydrostatic term in Eq. (5) is divided by a factor equal to 3, rather than by 4, as it is based on the linear pressure distribution. Therefore, Eqs. (2)–(4) are a Boussinesq-type model where cnoidal and solitary wave solutions are embedded, with a particular averaging factor affecting the dispersion part of the model. The linear, non-hydrostatic pressure law gave good results for dam break flow over rigid beds (Cantero-Chinchilla et al. 2016), and it is therefore adopted here.

The bed shear stress is computed from

$$\tau_b=\rho g\frac{n_w^2U\left|U\right|}{R^{1/3}}, \tag{6}$$

where n_w=roughness coefficient including sidewalls effects; and R=hydraulic radius. The value of n_w is estimated from the following expression (Wu 2015):

$$n_w = \left(\frac{2hf_w^{3/2} + bn^{3/2}}{2h + b} \right)^{2/3}, \tag{7}$$

where f_w and n=Manning roughness coefficients for sidewalls and bed, respectively; and b=channel width.

The sediment transport phenomenon is included in the vertically-integrated flow equations with non-hydrostatic pressure [Eqs. (1)–(3)] as highlighted by the presence of the functions $\rho(x,t)$ and $z_b(x,t)$. These flow variables are related to the bed- and suspended-load fluxes, thereby implying that additional transport equations are needed. Here, the sediment transport model of Wu and Wang (2007) is used to complete the system of governing equations. The 1D depth-averaged mass conservation equation for the suspended sediment, neglecting the thickness of bed-load layer, is (Wu and Wang 2007; Wu 2008):

$$\frac{\partial (hC_s)}{\partial t} + \frac{\partial (hUC_s)}{\partial x} = E - D, \tag{8}$$

where $C_s(x,t)$=depth-averaged suspended sediment concentration; and $E(x,t)$ and $D(x,t)$=entrainment and depositional rates of sediment, respectively. The mass balance in the bed-load layer is (Wu and Wang 2007; Wu 2008)

$$\frac{\partial (h_b C_b)}{\partial t} + \frac{\partial q_b}{\partial x} + (1 - p_m) \frac{\partial z_b}{\partial t} = D - E, \tag{9}$$

where $h_b(x,t)$=thickness of the bed-load layer; $C_b(x,t)$= depth-averaged bed-load sediment concentration; and $q_b(x,t)$=bed-load flux. Following Wu (2004), the evolution of the static bed of sediment can be determined from

$$\frac{\partial z_b}{\partial t} = \frac{1}{1 - p_m} \left(D - E + \frac{q_b - q_{b*}}{L} \right), \tag{10}$$

where L=non-equilibrium adaptation length of total-load transport; and $q_{b*}(x,t)$ = equilibrium bed-load flux. Nakagawa and Tsujimoto (1980) developed an alternative 1D non-equilibrium sediment transport model, extended to 2D flows by Nagata et al. (2000, 2005). Inserting Eq. (10) into Eq. (9), and using $q_b = h_b U_b C_b$, the bed-load mass balance equation is rewritten as

$$\frac{\partial}{\partial t} \left(\frac{q_b}{U_b} \right) + \frac{\partial q_b}{\partial x} = \frac{q_{b*} - q_b}{L}, \tag{11}$$

where U_b=bed-load velocity, approximated here as U (Wu and Wang 2007). Inserting the definitions $\rho=\rho_w(1-C_t)+\rho_s C_t$ and $C_t=C_s+q_b/(hU)$ into Eqs. (1)–(3), the complete system of conservation laws is rewritten as

$$\frac{\partial h}{\partial t}+\frac{\partial (hU)}{\partial x}=\frac{1}{1-p_m}\left(E-D+\frac{q_{b*}-q_b}{L}\right), \tag{12}$$

$$\begin{aligned}\frac{\partial (hU)}{\partial t}+\frac{\partial}{\partial x}\left(hU^2+\frac{1}{2}gh^2\right)=&-gh\frac{\partial z_b}{\partial x}-\frac{\tau_b}{\rho}-\frac{p_1}{\rho}\frac{\partial z_b}{\partial x}-\frac{1}{\rho}\frac{\partial}{\partial x}\left(\frac{hp_1}{2}\right)\\&-\frac{1}{2}gh^2\frac{\partial \rho}{\partial x}-\frac{\rho_s-\rho_w}{\rho}U\left(1-\frac{C_t}{1-p_m}\right)\left(E-D+\frac{q_{b*}-q_b}{L}\right)\end{aligned}, \tag{13}$$

$$\frac{\partial (hW)}{\partial t}+\frac{\partial (hUW)}{\partial x}=\frac{p_1}{\rho}-\frac{\tau_b}{\rho}\frac{\partial z_b}{\partial x}-\frac{\rho_s-\rho_w}{\rho}W\left(1-\frac{C_t}{1-p_m}\right)\left(E-D+\frac{q_{b*}-q_b}{L}\right). \tag{14}$$

Inserting Eqs. (10) and (12) into Eq. (4) permits to rewrite W as

$$W=\frac{1}{2}\left[-\frac{1}{1-p_m}\left(E-D+\frac{q_{b*}-q_b}{L}\right)-\frac{\partial (hU)}{\partial x}+U\frac{\partial z_s}{\partial x}+U\frac{\partial z_b}{\partial x}\right], \tag{15}$$

which is the form used in the numerical model.

3. Governing Equations

To close the depth-averaged non-hydrostatic erosion model presented in the preceding section, it is required to determine the sediment transport functions D, E, q_{b*}, and L. The bed sediment fluxes are defined as $D=\omega_s C_a$ and $E=\omega_s C_{a*}$, where ω_s=settling velocity of a sediment particle; and C_a and C_{a*}=actual and equilibrium near-bed suspended sediment concentrations, respectively. These are computed following the work of Wu and Wang (2007). To compute the equilibrium bed-load flux q_{b*}, several empirical formulations are considered for comparative purposes, including the classical equations by Meyer-Peter and Müller, Yalin and van Rijn's (Dey 2014), and also the recent one by Wu et al. (2000). In unsteady flows, a certain distance is required to reach the equilibrium condition of the sediment transport. This length L is defined as the non-equilibrium adaptation length, and it is computed here following Wu (2008). Non-equilibrium adaptation lengths can be defined for the total sediment load (L), suspended load (L_s) and bed-load (L_b).

4. Numerical Scheme

4.1. Finite volume Method

The governing equations for non-hydrostatic unsteady open channel flow over an erodible bed can be written in conservative form as follows:

$$\frac{\partial \mathbf{U}}{\partial t}+\frac{\partial \mathbf{F}}{\partial x}=\mathbf{S}\,, \tag{16}$$

$$\mathbf{U}=\begin{bmatrix} h \\ hU \\ hW \\ hC_s \\ q_b/U \\ z_b \end{bmatrix},\ \mathbf{F}=\begin{bmatrix} hU \\ hU^2+\frac{1}{2}gh^2 \\ hUW \\ hUC_s \\ q_b \\ 0 \end{bmatrix}, \tag{17}$$

$$\mathbf{S}=\begin{bmatrix} \frac{1}{1-p_m}\left(E-D+\frac{q_{b*}-q_b}{L}\right) \\ \left\{\begin{matrix} -gh\frac{\partial z_b}{\partial x}-\frac{\tau_b}{\rho}-\frac{p_1}{\rho}\frac{\partial z_b}{\partial x}-\frac{1}{\rho}\frac{\partial}{\partial x}\left(\frac{hp_1}{2}\right)-\frac{1}{2}g\frac{h^2}{\rho}\frac{\partial \rho}{\partial x} \\ -\frac{\rho_s-\rho_w}{\rho}U\left(1-\frac{C_t}{1-p_m}\right)\left(E-D+\frac{q_{b*}-q_b}{L}\right) \end{matrix}\right\} \\ \frac{p_1}{\rho}-\frac{\tau_b}{\rho}\frac{\partial z_b}{\partial x}-\frac{\rho_s-\rho_w}{\rho}W\left(1-\frac{C_t}{1-p_m}\right)\left(E-D+\frac{q_{b*}-q_b}{L}\right) \\ E-D \\ \frac{q_{b*}-q_b}{L} \\ \frac{1}{1-p_m}\left(D-E+\frac{q_b-q_{b*}}{L}\right) \end{bmatrix}, \tag{18}$$

where **U**, **F,** and **S** = vector of unknowns, fluxes, and source terms, respectively.

According to Toro (2001, 2009), the integral solution of Eq. (16) over a rectangular control volume in the *x*-*t* plane is

$$\left(\frac{\partial \mathbf{U}}{\partial t}\right)_i=-\frac{1}{\Delta x}(\mathbf{F}_{i+1/2}-\mathbf{F}_{i-1/2})+\mathbf{S}_i\,, \tag{19}$$

where **F, S**, and $\partial\mathbf{U}/\partial t$=cell-averaged vectors within the control volume ($\Delta x\cdot\Delta t$) in the *x*-*t* plane, of fluxes, source terms and time-derivatives of unknown variables, respectively.

Here, Δx and Δt=dimensions of the control volume in x- and t-directions, respectively. The index $i \pm 1/2$ refers to the control volume interfaces between nodes i and $i \pm 1$.

A finite volume numerical scheme is developed based on Eq. (19). To solve Boussinesq-type equations, a high-resolution scheme in both time and space is required (Abbott 1979; Wei et al. 1995; Kim et al. 2009). If second-order accuracy is used for the discretization of both Saint-Venant and dispersive terms, then the truncation errors originating from the Saint-Venant terms have, mathematically, the same form as the physical dispersive terms introduced into the governing equations by the Boussinesq approximation. Form a practical side, if such a system is numerically solved, the dispersion features are a combination of the true frequency dispersion originating from the Boussinesq terms, plus a "numerical" frequency dispersion introduced by the truncation errors. To avoid such an undesirable phenomenon, discretization of the Saint-Venant terms on Boussinesq-type equations is conducted using a high-resolution scheme, while the discretization itself of the non-hydrostatic (dispersive) source terms is conducted using second-order accuracy formulae (Abbott 1979; Wei et al. 1995; Kim et al. 2009). Therefore, the fourth-order monotone upstream centred scheme for conservation laws (MUSCL-TVD-4th) is used to reconstruct the conservative variables at the interfaces of the finite volumes. The Surface Gradient Method (SGM) (Zhou et al. 2001) is applied to reconstruct z_s to avoid unphysical flow over variable topography under static conditions. Then, the flow depth is computed as $h=z_s-z_b$. The intercell numerical fluxes are determined by applying the HLLC approximate Riemann solver (Toro 2001, 2009) to the reconstructed variables.

4.2. Time Stepping

To reduce truncation errors and produce non-hydrostatic simulations free of any numerical influence, a high-resolution time-stepping method is advisable for Boussinesq-type equations (Wei et al. 1995; Kim et al. 2009). Thus, the high-order Adams-Bashforth/ Adams-Moulton (AB-AM) time stepping scheme is selected to compute non-hydrostatic dam break flows over erodible beds. Simulation of these flows is, however, complex. The presence of source terms originating from the non-hydrostatic pressure distribution provokes instabilities if these terms are explicitly evaluated at time level k. Therefore, an implicit treatment of the source terms is necessary to produce a stable numerical solution of the system of equations. The AB-AM scheme requires the solution for $\mathbf{U}$ at 3 previous time levels (k, $k-1$ and $k-2$), given

that it is not a self-starting scheme. Thus, the first two time steps must be computed by an alternative time-stepping scheme.

For the first time step, the Euler time stepping formula is used to explicitly solve h, U, w, C_s, q_b, and z_b at time level k+1, because p_1 is zero at the initial static condition before the dam break. From Eq. (19), one gets

$$\mathbf{U}_i^{k+1} = \mathbf{U}_i^k - \frac{\Delta t}{\Delta x}(\mathbf{F}_{i+1/2}^k - \mathbf{F}_{i-1/2}^k) + \mathbf{S}_i^k \Delta t \,. \tag{20}$$

For the second time step, the Euler time stepping formula is used again. However, the momentum equations, Eqs. (13) and (14), require an accurate treatment. Inserting Eq. (15) into Eq. (14), the dependence on W in the vertical momentum balance is eliminated. Given that U at time level k+1 appears also in Eq. (14) after using Eq. (15), p_1 cannot be solved explicitly from the z-momentum equation. Therefore, the system defined by Eqs. (13)–(14) is implicit. Attempts to solve the system by explicit approximations failed, given that strong numerical instabilities were generated, even using very small time steps to initiate the computations. Values of p_1 and W determined by explicit computations using a fractional step approach generated unstable results that ultimately crashed the numerical computations. Therefore, an implicit numerical scheme is developed as follows. Eqs. (13) and (14) produce an implicit system of two equations (x- and z-momentum equations) and two unknown variables (U and p_1). Using the Euler time stepping, the integral form of Eqs. (13) and (14) reads

$$h_i^{k+1}U_i^{k+1} - C_1^k - \Delta t\left(-\frac{p_{1i}^{\,k}}{\rho_i^k}\frac{z_{bi+1}^{\,k} - z_{bi-1}^{\,k}}{2\Delta x} - \frac{1}{\rho_i^k}\frac{h_{i+1}^k p_{1i+1}^{\,k} - h_{i-1}^k p_{1i-1}^{\,k}}{2\Delta x}\right) = 0\,, \tag{21}$$

$$\begin{aligned} h_i^{k+1}\frac{1}{2}\Bigg[& -\frac{1}{1-p_m}\left(E_i^k - D_i^k + \frac{q_{b*i}^{\,k} - q_{bi}^{\,k}}{L_i^k}\right) - \frac{h_{i+1}^{k+1}U_{i+1}^{k+1} - h_{i-1}^{k+1}U_{i-1}^{k+1}}{2\Delta x} \\ & + U_i^{k+1}\frac{z_{si+1}^{\,k+1} - z_{si-1}^{\,k+1}}{2\Delta x} + U_i^{k+1}\frac{z_{bi+1}^{\,k+1} - z_{bi-1}^{\,k+1}}{2\Delta x}\Bigg] - C_2^k - \Delta t\frac{p_{1i}^{\,k}}{\rho_i^k} = 0, \end{aligned} \tag{22}$$

where

$$C_1^k = h_i^k U_i^k - \frac{\Delta t}{\Delta x}\left[(hU^2)_{i+1/2}^k + \frac{1}{2} g \left(h_{i+1/2}^k\right)^2 - (hU^2)_{i-1/2}^k - \frac{1}{2} g \left(h_{i-1/2}^k\right)^2 \right] + \Delta t \left[-g h_i^k \frac{z_{bi+1}^k - z_{bi-1}^k}{2\Delta x} - \frac{\tau_{bi}^k}{\rho_i^k} - \frac{1}{2} g \frac{(h_i^k)^2}{\rho_i^k} \frac{\rho_{i+1}^k - \rho_{i-1}^k}{2\Delta x} - \frac{\rho_s - \rho_w}{\rho_i^k} U_i^k \left(1 - \frac{C_{ti}^k}{1-p_m}\right)\left(E_i^k - D_i^k + \frac{q_{b*i}^k - q_{bi}^k}{L_i^k}\right)\right], \quad (23)$$

$$C_2^k = h_i^k W_i^k - \frac{\Delta t}{\Delta x}\left[(hUW)_{i+1/2}^k - (hUW)_{i-1/2}^k \right] + \Delta t \left[-\frac{\tau_{bi}^k}{\rho_i^k} \frac{z_{bi+1}^k - z_{bi-1}^k}{2\Delta x} - \frac{\rho_s - \rho_w}{\rho_i^k} W_i^k \left(1 - \frac{C_{ti}^k}{1-p_m}\right)\left(E_i^k - D_i^k + \frac{q_{b*i}^k - q_{bi}^k}{L_i^k}\right)\right]. \quad (24)$$

Second order central finite differences are used for the spatial derivatives in Eqs. (21)–(24), simplifying the implicit scheme. Therefore, the unknown flow variables in Eqs. (21) and (22) are U_{i-1}^{k+1}, U_i^{k+1}, U_{i+1}^{k+1}, and p_{1i-1}^k, p_{1i}^k, p_{1i+1}^k. The implicit system is solved iteratively using the Newton-Rapshon method with an analytical Jacobian matrix. At the end of each iteration stage, the values of U and p_1 are used to initiate the next cycle. The C_1^k and C_2^k are invariants during the iteration process. After convergence of the numerical solution, the W_i at k+1 is given by

$$W_i^{k+1} = -\frac{1}{1-p_m}\left(E_i^k - D_i^k + \frac{q_{b*i}^k - q_{bi}^k}{L_i^k}\right) - \frac{h_{i+1}^{k+1} U_{i+1}^{k+1} - h_{i-1}^{k+1} U_{i-1}^{k+1}}{2\Delta x} + U_i^{k+1} \frac{z_{si+1}^{k+1} - z_{si-1}^{k+1}}{2\Delta x} + U_i^{k+1} \frac{z_{bi+1}^{k+1} - z_{bi-1}^{k+1}}{2\Delta x}. \quad (25)$$

Once the first two time steps are computed by using the Euler scheme, the AB-AM time stepping scheme is initiated and used onwards.

The cell averaged derivative in Eq. (19) is written as

$$\frac{\partial \mathbf{U}}{\partial t} = \mathbf{E}, \quad (26)$$

where **E** is

$$\mathbf{E} = -\frac{1}{\Delta x}(\mathbf{F}_{i+1/2} - \mathbf{F}_{i-1/2}) + \mathbf{S}. \quad (27)$$

The Adams-Bashforth predictor step for Eq. (26) is given by

$$\mathbf{U}_i^p = \mathbf{U}_i^k + \frac{\Delta t}{12}(23\mathbf{E}_i^k - 16\mathbf{E}_i^{k-1} + 5\mathbf{E}_i^{k-2}), \quad (28)$$

where *p*=predictor step index. In this step, the implicit integral form of Eqs. (13) and (14) is discretized as follows

$$h_i^{\,p}U_i^{\,p} - C_1^{\,k} - \frac{23}{12}\Delta t\left(-\frac{p_{1i}^{\,k}}{\rho_i^{\,k}}\frac{z_{bi+1}^{\,k} - z_{bi-1}^{\,k}}{2\Delta x} - \frac{1}{\rho_i^{\,k}}\frac{h_{i+1}^{\,k}p_{1i+1}^{\,k} - h_{i-1}^{\,k}p_{1i-1}^{\,k}}{2\Delta x}\right) = 0\,, \tag{29}$$

$$\begin{aligned} h_i^{\,p}\frac{1}{2}\Bigg[&-\frac{1}{1-p_m}\left(E_i^{\,k} - D_i^{\,k} + \frac{q_{b^*i}^{\,k} - q_{bi}^{\,k}}{L_i^{\,k}}\right) - \frac{h_{i+1}^{\,p}U_{i+1}^{\,p} - h_{i-1}^{\,p}U_{i-1}^{\,p}}{2\Delta x} \\ &+ U_i^{\,k+1}\frac{z_{si+1}^{\,p} - z_{si-1}^{\,p}}{2\Delta x} + U_i^{\,k+1}\frac{z_{bi+1}^{\,p} - z_{bi-1}^{\,p}}{2\Delta x}\Bigg] - C_2^{\,k} - \frac{23}{12}\Delta t\frac{p_{1i}^{\,k}}{\rho_i^{\,k}} = 0, \end{aligned} \tag{30}$$

where

$$\begin{aligned} C_1^{\,k} = {} & h_i^{\,k}U_i^{\,k} + \frac{\Delta t}{12}(-16\mathbf{E}_i^{\,k-1} + 5\mathbf{E}_i^{\,k-2}) \\ & - \frac{23}{12}\frac{\Delta t}{\Delta x}\left[(hU^2)_{i+1/2}^{k} + \frac{1}{2}g\left(h_{i+1/2}^{k}\right)^2 - (hU^2)_{i-1/2}^{k} - \frac{1}{2}g\left(h_{i-1/2}^{k}\right)^2\right] \\ & + \frac{23}{12}\Delta t\Bigg[-gh_i^{\,k}\frac{z_{bi+1}^{\,k} - z_{bi-1}^{\,k}}{2\Delta x} - \frac{\tau_{bi}^{\,k}}{\rho_i^{\,k}} - \frac{1}{2}g\frac{(h_i^{\,k})^2}{\rho_i^{\,k}}\frac{\rho_{i+1}^{\,k} - \rho_{i-1}^{\,k}}{2\Delta x} \\ & - \frac{\rho_s - \rho_w}{\rho_i^{\,k}}U_i^{\,k}\left(1 - \frac{C_{ti}^{\,k}}{1-p_m}\right)\left(E_i^{\,k} - D_i^{\,k} + \frac{q_{b^*i}^{\,k} - q_{bi}^{\,k}}{L_i^{\,k}}\right)\Bigg], \end{aligned} \tag{31}$$

$$\begin{aligned} C_2^{\,k} = {} & h_i^{\,k}W_i^{\,k} + \frac{\Delta t}{12}(-16\mathbf{E}_i^{\,k-1} + 5\mathbf{E}_i^{\,k-2}) - \frac{23}{12}\frac{\Delta t}{\Delta x}\left[(hUW)_{i+1/2}^{k} - (hUW)_{i-1/2}^{k}\right] \\ & + \frac{23}{12}\Delta t\Bigg[-\frac{\tau_{bi}^{\,k}}{\rho_i^{\,k}}\frac{z_{bi+1}^{\,k} - z_{bi-1}^{\,k}}{2\Delta x} - \frac{\rho_s - \rho_w}{\rho_i^{\,k}}W_i^{\,k}\left(1 - \frac{C_{ti}^{\,k}}{1-p_m}\right)\left(E_i^{\,k} - D_i^{\,k} + \frac{q_{b^*i}^{\,k} - q_{bi}^{\,k}}{L_i^{\,k}}\right)\Bigg]. \end{aligned} \tag{32}$$

The implicit system for the Adams-Bashforth predictor scheme is solved iteratively using the Newton-Rapshon method with an analytical Jacobian matrix to compute U and p_1. After the iterations, the W_i at p is given by

$$\begin{aligned} W_i^{\,p} = {} & -\frac{1}{1-p_m}\left(E_i^{\,k} - D_i^{\,k} + \frac{q_{b^*i}^{\,k} - q_{bi}^{\,k}}{L_i^{\,k}}\right) \\ & - \frac{h_{i+1}^{\,p}U_{i+1}^{\,p} - h_{i-1}^{\,p}U_{i-1}^{\,p}}{2\Delta x} + U_i^{\,k+1}\frac{z_{si+1}^{\,p} - z_{si-1}^{\,p}}{2\Delta x} + U_i^{\,k+1}\frac{z_{bi+1}^{\,p} - z_{bi-1}^{\,p}}{2\Delta x} \end{aligned}\,. \tag{33}$$

From Eq. (28), once the iterative numerical solution converges, the h, U, W, C_s, q_b, and z_b at p and p_1 at k are determined and used to initiate the corrector step.

The iterative Adams-Moulton corrector step for Eq. (26) reads

$$\mathbf{U}_i^{k+1} = \mathbf{U}_i^k + \frac{\Delta t}{24}(9\mathbf{E}_i^p + 19\mathbf{E}_i^k - 5\mathbf{E}_i^{k-1} + \mathbf{E}_i^{k-2}). \tag{34}$$

The implicit system formed by the *x*- and *z*-momentum equations is solved iteratively using the Newton-Raphson method with analytical Jacobian matrix for each time step during the iterative Adams-Moulton time stepping scheme. The integral, discrete version of Eqs. (13) and (14) for the Adams-Moulton corrector step, gives

$$h_i^{k+1}U_i^{k+1} - C_1^p - \frac{9}{24}\Delta t\left(-\frac{p_{1i}^{\ p}}{\rho_i^p}\frac{z_{bi+1}^{\ p} - z_{bi-1}^{\ p}}{2\Delta x} - \frac{1}{\rho_i^p}\frac{h_{i+1}^p p_{1i+1}^{\ p} - h_{i-1}^p p_{1i-1}^{\ p}}{2\Delta x}\right) = 0, \tag{35}$$

$$\begin{aligned} h_i^{k+1}\frac{1}{2}\Bigg[& -\frac{1}{1-p_m}\left(E_i^p - D_i^p + \frac{q_{b*i}^{\ p} - q_{bi}^{\ p}}{L_i^p}\right) - \frac{h_{i+1}^{k+1}U_{i+1}^{k+1} - h_{i-1}^{k+1}U_{i-1}^{k+1}}{2\Delta x} \\ & + U_i^{k+1}\frac{z_{si+1}^{\ k+1} - z_{si-1}^{\ k+1}}{2\Delta x} + U_i^{k+1}\frac{z_{bi+1}^{\ k+1} - z_{bi-1}^{\ k+1}}{2\Delta x}\Bigg] - C_2^p - \frac{9}{24}\Delta t\frac{p_{1i}^{\ p}}{\rho_i^p} = 0, \end{aligned} \tag{36}$$

where

$$\begin{aligned} C_1^p = {} & h_i^k U_i^k + \frac{\Delta t}{12}(-16\mathbf{E}_i^{k-1} + 5\mathbf{E}_i^{k-2}) \\ & - \frac{23}{12}\frac{\Delta t}{\Delta x}\left[(hU^2)_{i+1/2}^p + \frac{1}{2}g\left(h_{i+1/2}^p\right)^2 - (hU^2)_{i-1/2}^p - \frac{1}{2}g\left(h_{i-1/2}^p\right)^2\right] \\ & + \frac{23}{12}\Delta t\Bigg[-gh_i^p\frac{z_{bi+1}^{\ p} - z_{bi-1}^{\ p}}{2\Delta x} - \frac{\tau_{bi}^{\ p}}{\rho_i^k} - \frac{1}{2}g\frac{(h_i^p)^2}{\rho_i^k}\frac{\rho_{i+1}^p - \rho_{i-1}^p}{2\Delta x} \\ & - \frac{\rho_s - \rho_w}{\rho_i^p}U_i^p\left(1 - \frac{C_{ti}^{\ p}}{1-p_m}\right)\left(E_i^p - D_i^p + \frac{q_{b*i}^{\ p} - q_{bi}^{\ p}}{L_i^p}\right)\Bigg] \end{aligned}, \tag{37}$$

$$\begin{aligned} C_2^p = {} & h_i^k W_i^k + \frac{\Delta t}{12}(-16\mathbf{E}_i^{k-1} + 5\mathbf{E}_i^{k-2}) - \frac{23}{12}\frac{\Delta t}{\Delta x}\left[(hUW)_{i+1/2}^p - (hUW)_{i-1/2}^p\right] \\ & + \frac{23}{12}\Delta t\left[-\frac{\tau_{bi}^{\ p}}{\rho_i^p}\frac{z_{bi+1}^{\ p} - z_{bi-1}^{\ p}}{2\Delta x} - \frac{\rho_s - \rho_w}{\rho_i^p}W_i^p\left(1 - \frac{C_{ti}^{\ p}}{1-p_m}\right)\left(E_i^p - D_i^p + \frac{q_{b*i}^{\ p} - q_{bi}^{\ p}}{L_i^p}\right)\right]. \end{aligned} \tag{38}$$

After the iteration, one gets W_i at k+1 as given by

$$\begin{aligned} W_i^{k+1} = {} & -\frac{1}{1-p_m}\left(E_i^p - D_i^p + \frac{q_{b*i}^{\ p} - q_{bi}^{\ p}}{L_i^p}\right) - \frac{h_{i+1}^{k+1}U_{i+1}^{k+1} - h_{i-1}^{k+1}U_{i-1}^{k+1}}{2\Delta x} \\ & + U_i^{k+1}\frac{z_{si+1}^{\ k+1} - z_{si-1}^{\ k+1}}{2\Delta x} + U_i^{k+1}\frac{z_{bi+1}^{\ k+1} - z_{bi-1}^{\ k+1}}{2\Delta x} \end{aligned} \tag{39}$$

4.3. Computational Sequence

The numerical solution at each time step is obtained by the following sequence:

(1) The solution **U** at time level k is reconstructed using MUSCL-TVD-4th.

(2) The numerical flux $\mathbf{F}_{i+1/2}$ is computed at cell interfaces with the HLLC Riemann solver using the reconstructed values of h, U, w, C_s, and q_b. The surface gradient method is applied.

(3) The solution **U** at time level k+1 is computed applying the hybrid time stepping sequence:

   (a) The first time level is computed applying the Euler time stepping scheme with explicit evaluation of the source terms.

   (b) The second time level is computed applying the Euler time stepping scheme with implicit evaluation of the source terms originating from the momentum balance in x- and z-directions. The U at k+1 and the p_1 at k are calculated by solving the x- and z-momentum implicit system using the Newton-Rapshon method with analytical Jacobian matrix until a convergence is obtained. The variables h, C_s, q_b, and z_b are explicitly determined at k+1.

   (c) The third time level onwards is accomplished by computing the AB-AM scheme. Firstly, the Adams-Bashforth predictor scheme is applied, solving an implicit system of equations to obtain U at p and p_1 at time level k. Hence, using h, U, C_s, q_b, and z_b at p and p_1 at k, the iterative Adams-Moulton corrector scheme is initiated to calculate h, U, C_s, q_b, and z_b at k+1 and p_1 at p. Besides, U at k+1 and p_1 at p are also solved by using the implicit Newton-Rapshon method. The loop is repeated until a convergence is obtained. Two Jacobian matrixes are computed at each iteration in the AB-AM scheme for using in the implicit Newton-Raphson method until a convergence is obtained.

(4) The cell-averaged variables h, U, C_s, q_b, and z_b at time level k+1 and p_1 at time level k are accepted.

(5) The ρ and C_t are computed at time level k+1 using the functions $\rho=\rho_w(1-C_t)+\rho_s C_t$ and $C_t=C_s+q_b/(hU)$.

(6) The W and the sediment transport functions D, E, q_{b*}, and L, are computed at k+1.

(7) For a new time level, steps 1 to 6 are repeated.

The numerical scheme developed here encompasses an accurate predictor-corrector time stepping scheme where an implicit solution of the *x*- and *z*-momentum equations at each time step is required to get a stable contribution of the non-hydrostatic terms in the numerical solution. Use of other time stepping schemes like the Euler scheme or consideration of an explicit evaluation of the source terms, resulted in highly unstable schemes. The application of the Euler time scheme for the first two steps requires use of a low CFL number. To reduce errors and instabilities, a value of the Courant-Friedrichs-Lewy number CFL<0.1 is used in the first 10 time steps and a value of CFL<0.5 thereafter. The need of using these values of CFL is a disadvantage as compared to Godunov-type finite-volume numerical models to solve Saint Venant equations, where a value of CFL=0.9 is typical (Toro 2001). Even for the solution of Saint Venant equations, it is advisable to use a smaller time step size at the initial stages of the motion, to compensate the approximate estimation of the maximum signal speed to compute CFL (Toro 2000, code "HW_MUSH.F"). In "HW_MUSH.F", the time step size is reduced to $0.2\Delta t$ during the first 5 steps. Other methods to solve Saint Venant equations require values of CFL below unity. The discontinuous method of Galerkin (Khan and Lai 2014) is usually implemented based on TVD Runge-Kutta schemes for the time-stepping, with a typical value for stability CFL<1/3 using a linear polynomial for space discretization. Solution of Saint Venant equations using the discontinuous method of Galerkin based on CFL=0.1 are not unusual. Solution of Boussinesq-type equations in coastal engineering problems are typically done based on CFL=0.5 (Kim et al. 2009).

Given the complex system of equations to be modelled, a rigorous analysis of the stability was not found possible. By numerical experimentation, we determined that the scheme is stable for CFL<0.5. It is pertinent to mention that to initiate the implicit system calculations, the information of U at k is used. However, p_1 does not need to be initiated; so that a zero vector is assumed. The numerical scheme was found to be robust as fast converging to the solution. It is more complex than the classical finite volume solutions of the hydrostatic Saint-Venant equations. However, by extensive numerical experimentation, it was not found possible to implement a fully explicit scheme. Bashiri et al. (2015) developed a Bousisnesq-type model for free surface flow in conduits, where the dispersion terms were treated implicitly. A possible alternative to the hybrid scheme developed in this work is to produce a fully implicit scheme. The convergence

criterion $\varepsilon<10^{-4}$ was adopted for both the implicit Newton-Raphson method and the AB-AM scheme.

5. Test Cases

Non-hydrostatic movable bed computations are compared with experimental data for Taipei (Capart and Young 1998) and Louvain (Spinewine 2005) tests cases, following the former analysis by Fraccarollo and Capart (2002) using hydrostatic computations. The mesh independency of the model is then examined, and several equilibrium bed-load formulas are assessed. The experimentally-adjustable parameters are determined based on experimental observations (Fraccarollo and Capart 2002). Simulations conducted with the 1D non-hydrostatic model are compared to the results from the 3D simulations by Marsooli and Wu (2015). The convergence of the present model results to steady non-hydrostatic flow solutions is finally investigated.

5.1. Dam Break waves over Movable Beds

Figs. 2 and 3 present the computational results for dam break waves over erodible beds based on the present 1D non-hydrostatic model, and those when non-hydrostatic terms are suppressed. The 1D hydrostatic model is obtained neglecting p_1 in Eq. (2), and removing the z-momentum equation [Eq. (3)] from the system. The resulting physical model is then coincident with the 1D hydrostatic model presented by Wu and Wang (2007), with differences in the model closure relationships and the numerical scheme. The experimental data of Figs. 2 and 3 are selected from the Taipei and Louvain test cases (Capart and Young 1998; Fraccarollo and Capart 2002). Both sets of experiments correspond to laboratory observations, where the flow depth upstream of the dam was h_u=0.1 m and the tailwater portion of the flume was dry. The q_{b*} formula proposed by Wu et al. (2000) was selected; values of Δx=0.75 cm, CFL=0.01 for the 10 first time steps and CFL=0.4 for the rest of the computational steps are set in the numerical model. According to Wu and Wang (2007), C_b=0.6, L_b=0.25 m, α_0=2, f_w=0.01, and n=0.025 are used as simulation data for both test cases. The bed sediment layer porosities p_m are 0.28 and 0.3 for the Taipei and Louvain tests, respectively. The dry downstream bed is simulated by adopting a very small flow depth h_d=0.0005 m. This technique is accepted for dam break flow simulations (Wu 2008), although this is not conceptually correct (Toro 2001). Alternatively, a zero tailwater depth can be prescribed if an algorithm to preserve positivity in the computed water depths near the wet-dry

front is implemented (Wu 2008).

In Fig. 2, the Taipei test experiment (Capart and Young 1998) is simulated by using both non-hydrostatic and hydrostatic models at times $t=3t_0$, $4t_0$ and $5t_0$ after the dam failure, where the time scaling is $t_0=(h_u/g)^{1/2}=0.1$ s. The sediment particles used in the Taipei test were artificial pearls covered with a shiny white coating, having $d=6.1$ mm, $\rho_s=1048$ kg/m^3, and $\omega_{s0}=7.6$ cm/s. The flume was sufficiently long and deep with $b=0.2$ m to satisfactorily carry the experiment. The results obtained from the hydrostatic simulation are in agreement with those obtained by Wu and Wang (2007) model. The model accurately reproduces the bed profile eroded by the dam break flow at $t=3t_0$ and $4t_0$ [Figs. 2(a and b)], whilst the bed profile data at $t=5t_0$ is somewhat overestimated in the lowest zone [Fig. 2(c)]. The free surface profile is composed of a negative smooth wave (monotone wave with propagation in negative x-direction), followed by a train of undulations above the scour hole, ending in a positive wave where its edge is a wet-dry front propagating in the positive x-direction. This free surface profile is not accurately reproduced by means of the hydrostatic pressure-based model. Note that the experimental data shows free surface undulations at the vicinity of the positive wave portion, not predicted by hydrostatic computations. Further, the shape of the smooth negative wave is also not precisely reproduced by the hydrostatic model. However, the position of the wet-dry front predicted by the hydrostatic model is in agreement with the experimental data. The non-hydrostatic results for the eroded bed profile at $t=3t_0$ and $4t_0$ reasonably reproduce the upward bed slope. The backward bed slope and the trough of the bed profile are shifted to the right in the simulations of Figs. 2(a and b) with respect to the experimental data. This behaviour is highlighted in the bed profile prediction at $t=5t_0$ [Fig. 2(c)]. The present 1D non-hydrostatic model gives improved predictions for the free surface profile. The overall trend of the free surface oscillations near the positive wave at $t=3t_0$, $4t_0$ and $t=5t_0$ is reproduced. The smooth negative wave is predicted with good accuracy by the non-hydrostatic model. Note that the free surface undulations propagate in the upstream direction. The flow profile is somewhat underestimated at the early dam break stages [Figs. 2(a and b)]. However, the inclusion of non-hydrostatic modelling for the free surface profile results in physically improved results as compared to hydrostatic approximations, due to the inclusion of p_1 in the x-momentum balance and W via the z-momentum balance. Non-hydrostatic modelling permits to mimic the undulations near the positive wave portion and determine with

accuracy the shape of the negative smooth wave.

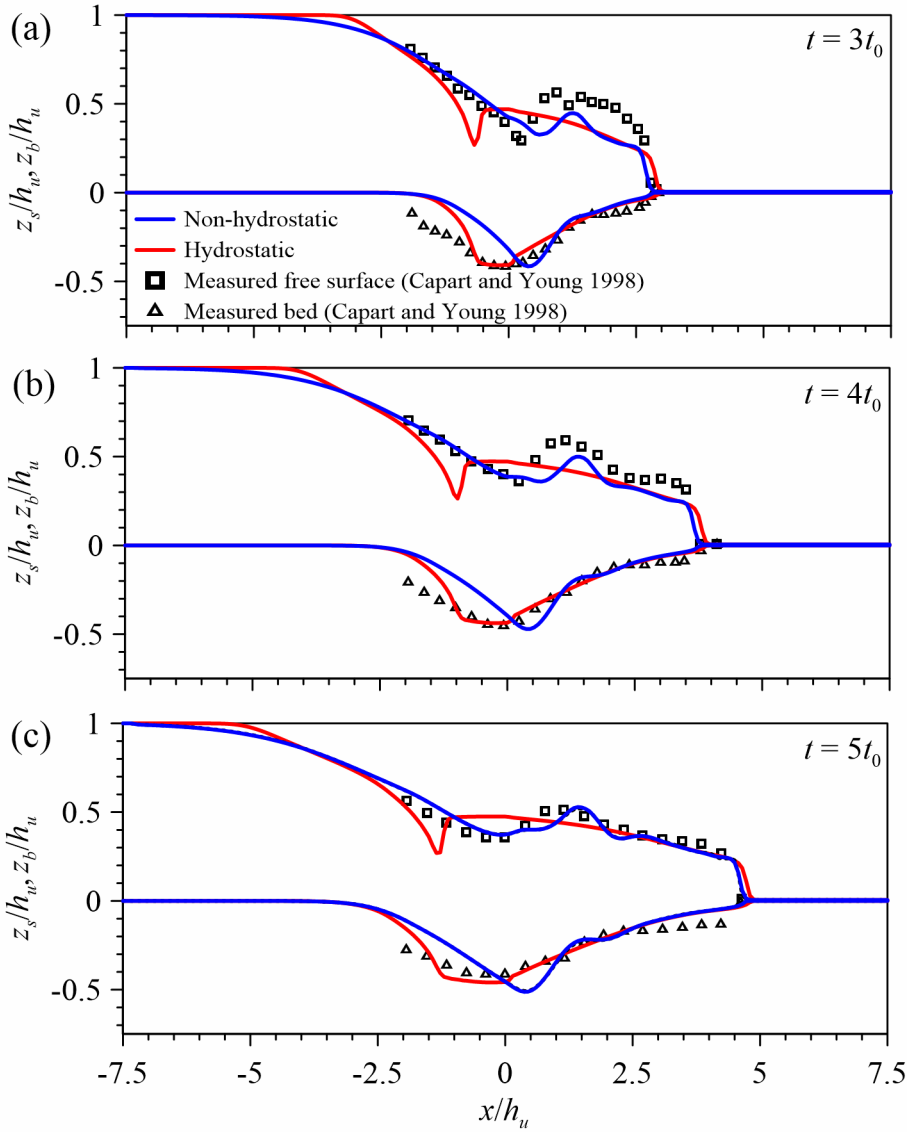

Fig. 2. Comparison of the present non-hydrostatic and hydrostatic models with the Taipei test experimental data of Capart and Young (1998): (a) at $t = 3t_0$; (b) at $t = 4t_0$; (c) at $t = 5t_0$

The study of the Louvain test experiment at times t=5t_0, 7.5t_0 and 10t_0 after the dam break is presented in Fig. 3. In this experiment, Fraccarollo and Capart (2002) used cylindrical PVC pellets as sediment particles, having d=3.5 mm, ρ_s=1540 kg/m^3, and ω_{s0}=18 cm/s. The flume had a width b=0.1 m. The hydrostatic model produces simulations of the eroded bed profiles with some divergence from the experimental results, but in overall agreement with the hydrostatic simulations of Wu and Wang (2008). The depth of bed scour is overestimated by the hydrostatic model at the three dam break stages. The non-hydrostatic simulations give similar eroded bed profiles. The free surface profile predicted by the non-hydrostatic model is however better than that predicted by the hydrostatic model. The improved predictions of the negative wave and

the undulations near the positive wave portion are evident. It may be noted that the flow profile undulations observed in the experimental data are fairly well simulated by the non-hydrostatic model.

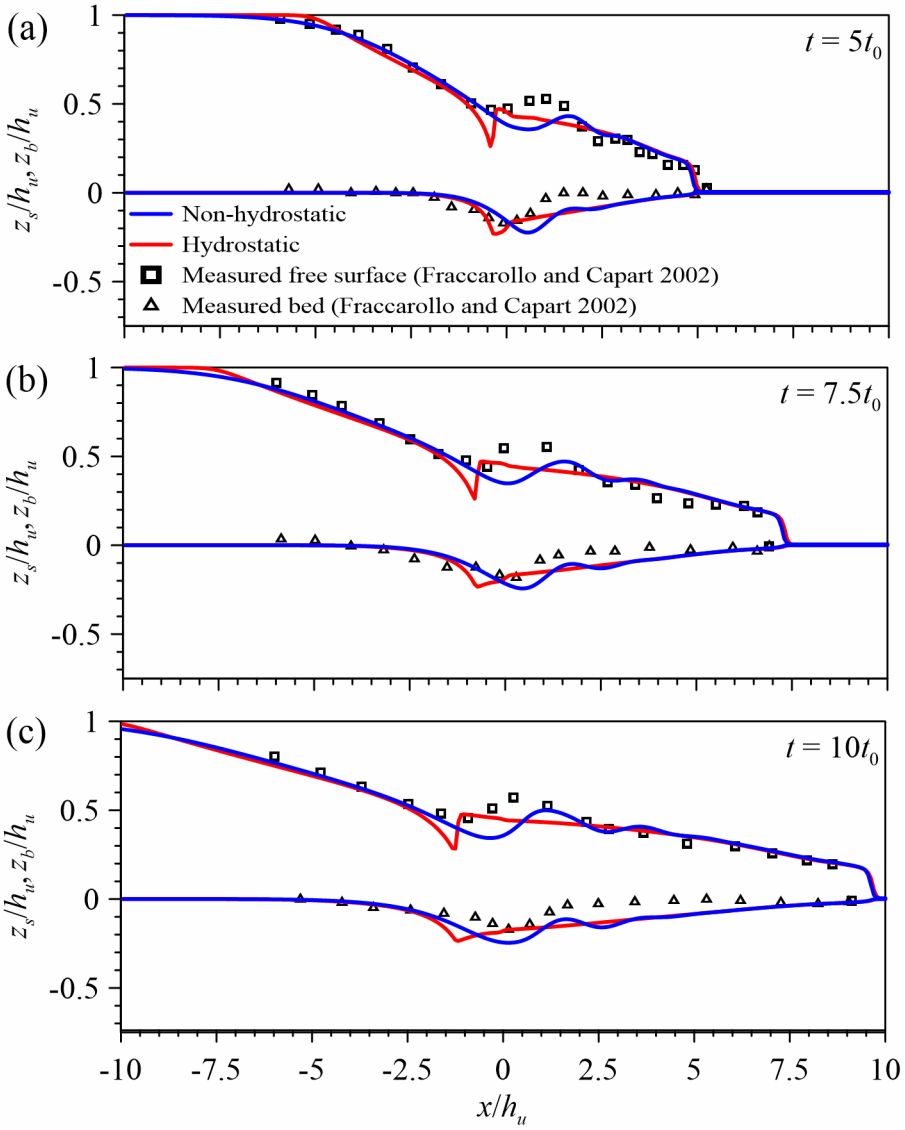

Fig. 3. Comparison of the present non-hydrostatic and hydrostatic models with the Louvain test experimental data of Fraccarollo and Capart (2002): (a) at $t = 5t_0$; (b) at $t = 7.5t_0$; (c) at $t = 10t_0$

5.2. Grid Size Dependency Test

The grid dependency test is accomplished by the following analysis, presented in Fig. 4. Accordingly, the Taipei test at $t=4t_0$ [Fig. 4(a)] and the Louvain test at $t=7.5t_0$ [Fig. 4(b)] are simulated by using Δx=2, 0.75, and 0.5 cm grid sizes. In the Taipei case, use of Δx=2 cm gave poor results. For Δx=0.75 cm and Δx=0.5 cm grid sizes, the results are identical, thereby giving mesh-independent results.

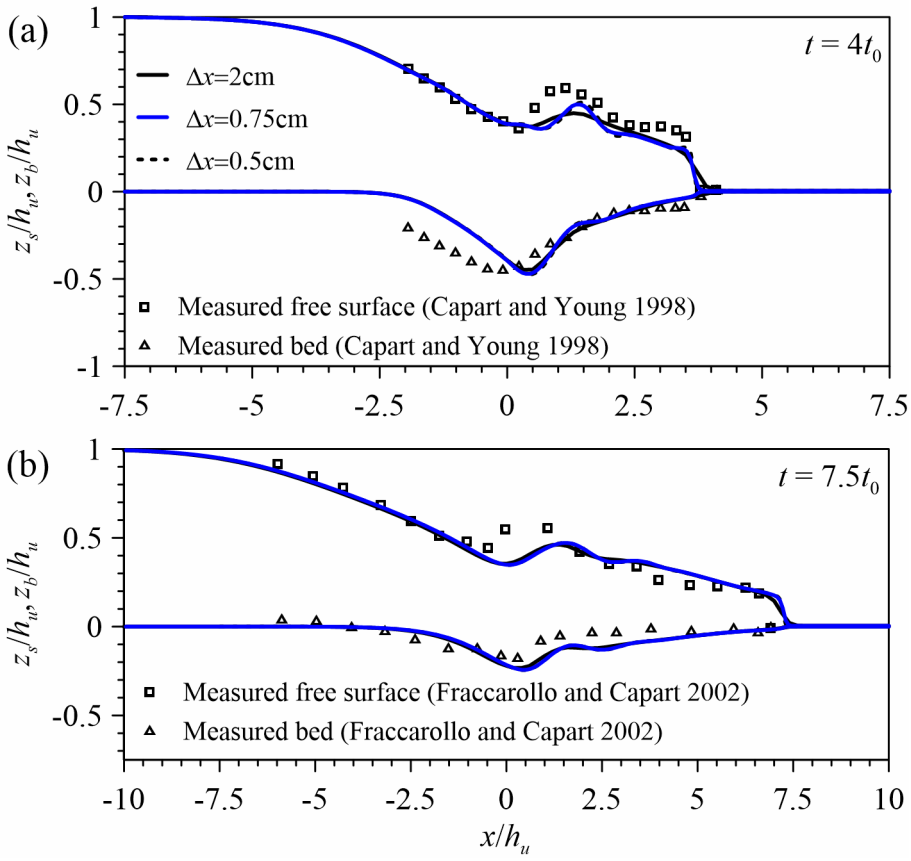

Fig. 4. Grid size dependency analysis for the present 1D non-hydrostatic model using experimental data of Capart and Young (1998) and Fraccarollo and Capart (2002): (a) Taipei test at t=4t_0; (b) Louvain test at t=7.5t_0

5.4. Sensitivity Analysis

The sensitivity of the 1D non-hydrostatic model to L_b and n is investigated by testing different L_b and n values in Figs. 5 and 6. Since the less accurate bed profile prediction was obtained for the Louvain case (Fig. 3), it is selected for the current analysis. The parameter L_b can be approximated for sand dunes as 5 to 10 times the maximum initial flow depth h_u, which correspond to 0.5 and 1 m in the Louvain test. Values of L_b=0.25, 0.5 and 1 m are considered for the simulations as shown in Fig. 5 for the Louvain case at times t=5t_0, 7.5t_0 and 10t_0. By increasing L_b, the results are slightly improved for both the flow profile and the eroded bed profile predictions. A sensitivity analysis to α_0 provides the same conclusions, and the results are therefore not presented here. A sensitivity analysis of the model with respect to n is shown in the new Fig. 6, using the values of n = 0.01, 0.025 and 0.05. It can be observed that an increase in n increases the free surface wave heights and the scour hole depths.

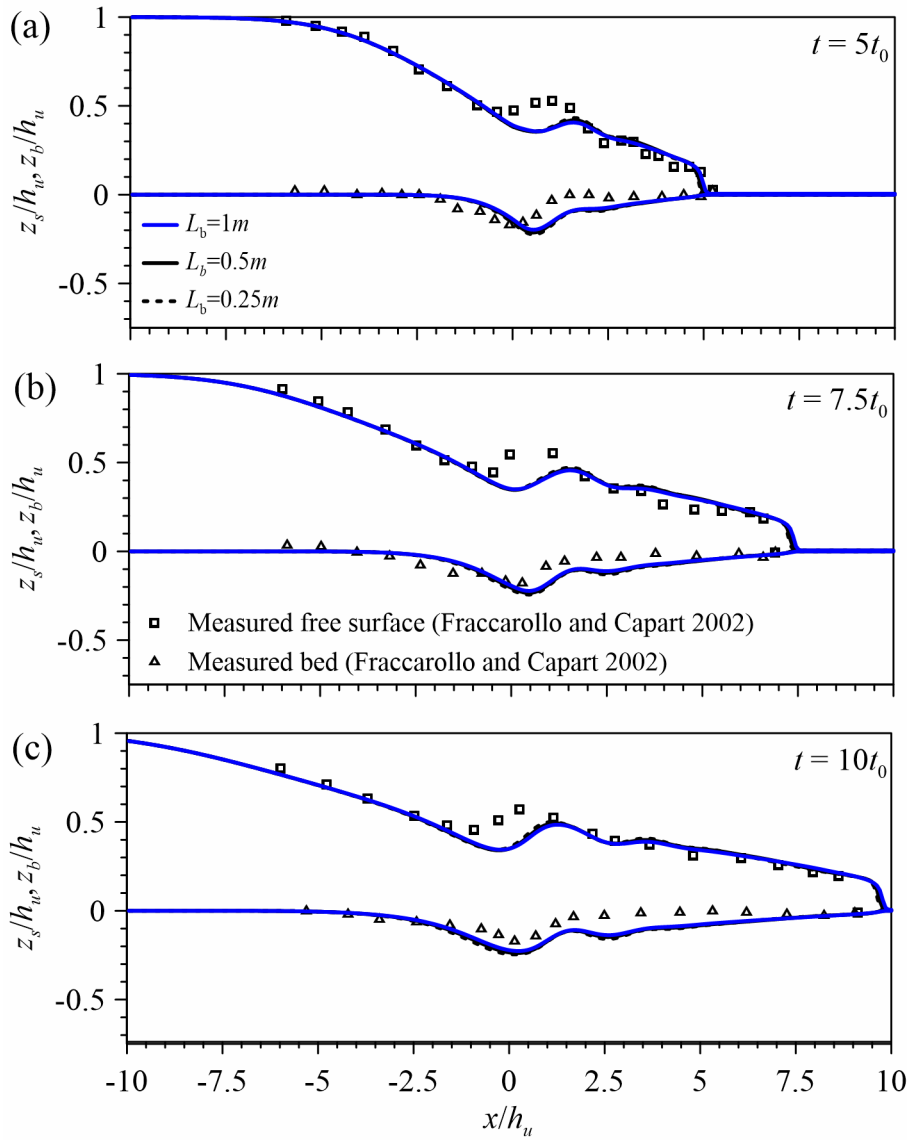

Fig. 5. The L_b sensitivity analysis for the present 1D non-hydrostatic model using the Louvain test experimental data of Fraccarollo and Capart (2002): (a) at t=5t_0; (b) at t=7.5t_0; (c) at t=10t_0

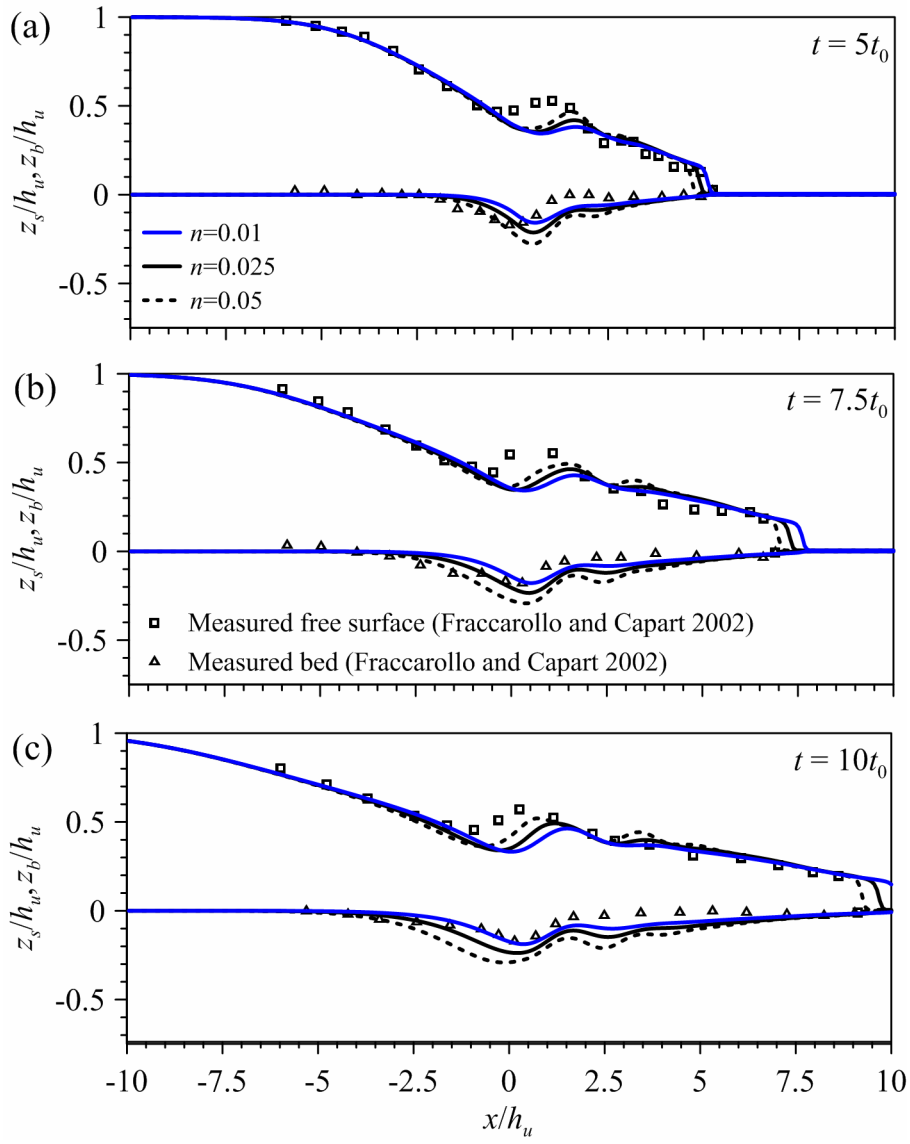

Fig. 6. The n sensitivity analysis for the present 1D non-hydrostatic model using the Louvain test experimental data of Fraccarollo and Capart (2002): (a) at t=5t_0; (b) at t=7.5t_0; (c) at t=10t_0

5.5. Assessment of Equilibrium Bed-Load Formulas

The comparison of different q_{b*} formulas is shown in Fig. 7. The Taipei test at t=4t_0 is considered in the simulations is shown in Figs. 7(a and c) as well as the Louvain test at t=7.5t_0 in Figs. 7(b and d). The results using the q_{b*} formulas in the non-hydrostatic simulations are presented as follows: Results from Meyer-Peter and Müller (1948) and Yalin (1963) are presented in Figs. 7(a and b), whereas those from van Rijn (1984) and Wu et al. (2000) are shown in Figs. 7(c and d). Although the results from Meyer-Peter and Müller's bed-load formula are in agreement with the experimental free surface profile, it produces a poor prediction for the eroded bed profile [Fig. 7(b)]. The Yalin's formula gives better results, but the prediction of the eroded bed profile is still not good

[Fig. 7(b)]. The Wu et al.(2000) formula is an improvement of van Rijn (1984) equation, which in fact provides the best computational results.

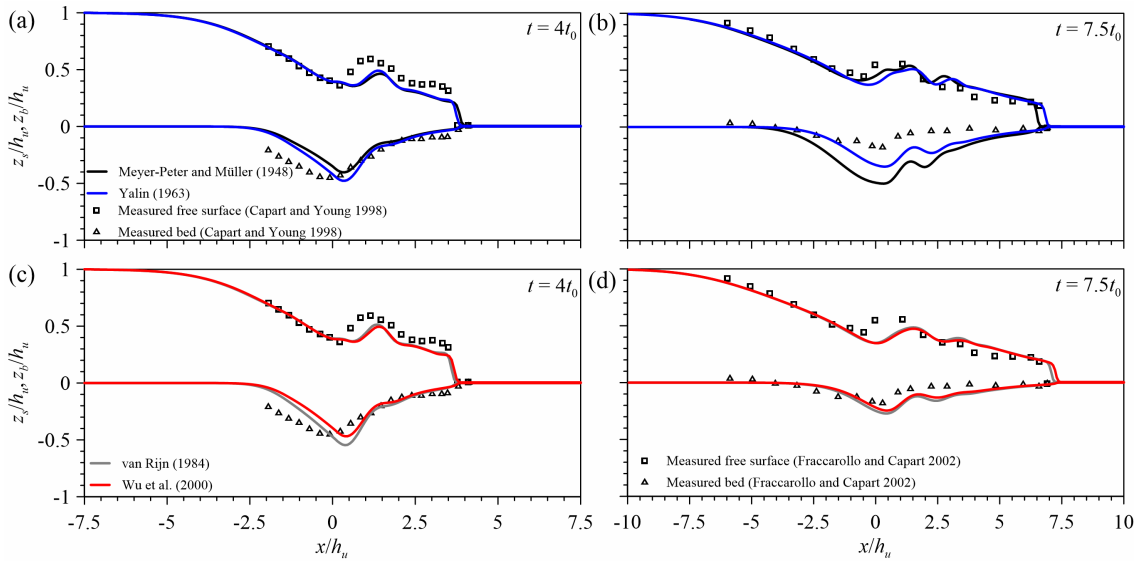

Fig. 7. Assessment of different non-equilibrium bed-load flux formulas applied to the present 1D non-hydrostatic model using the experimental data of Capart and Young (1998) Fraccarollo and Capart (2002): (a) Yalin (1963) and Meyer-Peter and Müller (1948) formulas (see Dey 2014) for Taipei test at t=4t_0; (b) Yalin (1963) and Meyer-Peter and Müller (1948) formulas for Louvain test at t=7.5t_0; (c) van Rijn (1984) and Wu et al. (2000) formulas for Taipei test at t = 4t_0; (d) van Rijn (1984) and Wu et al. (2000) formulas Louvain test at t=7.5t_0

5.6. Comparison with 3D non-Hydrostatic RANS Model Simulations

The results obtained from the present 1D non-hydrostatic model are compared with those obtained from a 3D non-hydrostatic RANS model by Marsooli and Wu (2015), as shown in Fig. 8. The experimental data of the Louvain case at t=5t_0, 7.5t_0 and 10t_0 are considered for the assessment. It is pertinent to mention that in Fig. 8(b), the simulation by the present model is skilful at t=7t_0 to match with the 3D simulation shown in Fig. 3 from Marsooli and Wu (2015). At t=5t_0, the 3D simulation data accurately predicts the bed profile experimental data, whereas the present model overestimate them [Fig. 8(a)]. The present 1D computation predicts a free surface profile that is in good agreement with the experimental data (Fraccarollo and Capart 2002) and 3D simulations (Marsooli and Wu 2015). Note that in Fig. 8, the free surface undulations predicted by the 3D simulations are successfully reproduced by the 1D non-hydrostatic simulation. The 1D theoretical simulations are conducted assuming that the dam release is instantaneous, whilst the real conditions in experiments diverge to some extent. Thus, simulations and experiments are out of phase in Fig. 8. However, this 1D non-hydrostatic simulations are reasonably in phase with the 3D simulations in Fig. 8.

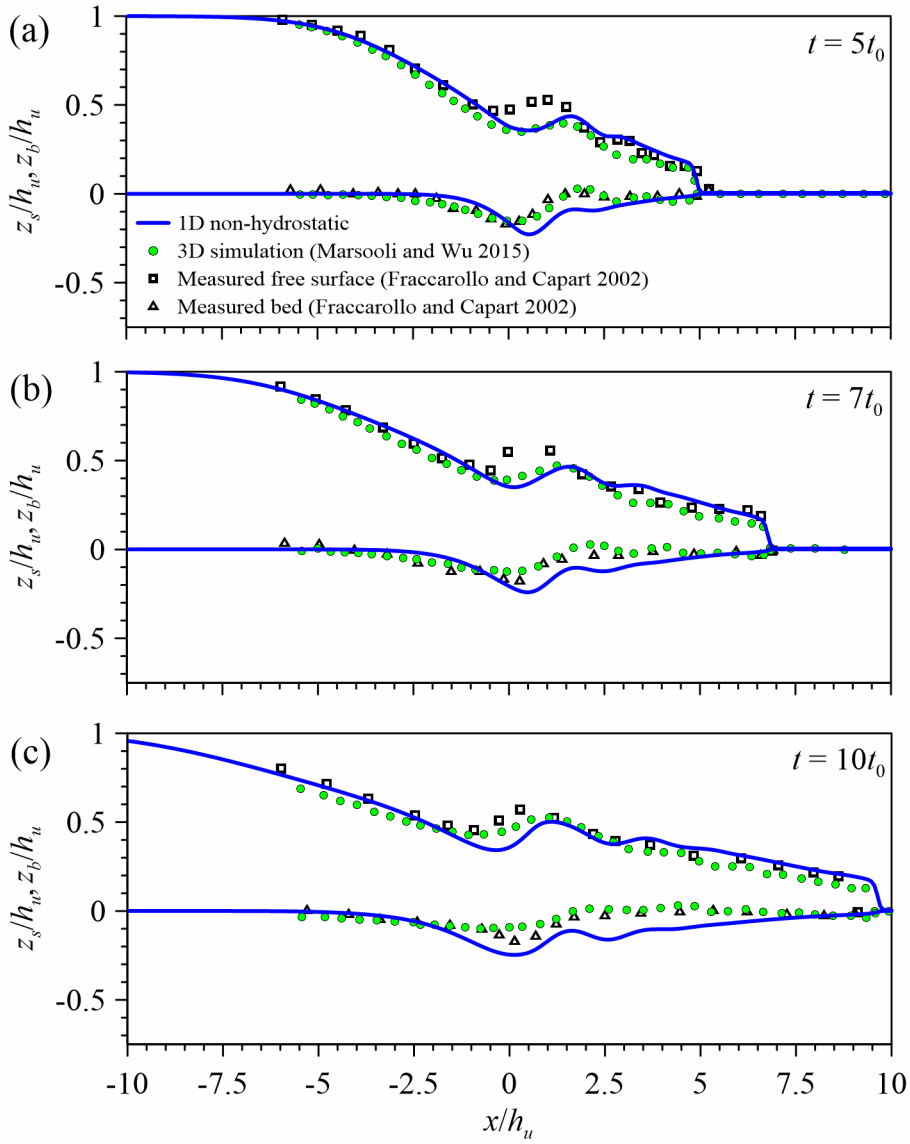

Fig. 8. Comparison between the present 1D non-hydrostatic model and 3D RANS model of Marsooli and Wu (2015) with the Louvain test experimental data of Fraccarollo and Capart (2002): (a) at t=5t_0; (b) experimental data at t=7.5t_0 and present model computed at t=7t_0; (c) at t=10t_0

The scour hole profiles are in agreement with the results of the 3D model, showing wavelike profiles. However, the scour depths predicted by the 1D non-hydrostatic model are larger than those shown by experiments and 3D simulations, indicating that this specific aspect needs to be resolved with further research.

5.7. Convergence to Steady Flow Solutions

Convergence of the present 1D non-hydrostatic model to a non-hydrostatic steady flow solution is tested in Fig. 9. This test is important to check the accuracy of the numerical model. The experimental data obtained by Sivakumaran et al. (1983) for the free surface profile and bed pressure in transcritical flow over a Gaussian hump are plotted in Figs. 9(a and b). The experimental discharge q=1119.7 cm^2/s and Δx=2 cm were set in the

numerical model. The computational results are shown after 50 s. The results of the bed pressure $p_b=\rho gh+p_1$ are plotted in Fig. 9(b). The results obtained from the present 1D non-hydrostatic model show good agreement with the experimental data for both the free surface profile [Fig. 9(a)] and bed pressure [Fig. 9(b)], demonstrating converge to a steady flow. The predicted unit discharge is seen to be constant and stable and is in excellent agreement with the experimental data [Fig. 9(c)]. The present finite volume results are compared with the simulations presented by Khan and Steffler (1996a) using the dissipative Galerkin finite element scheme, showing a good agreement.

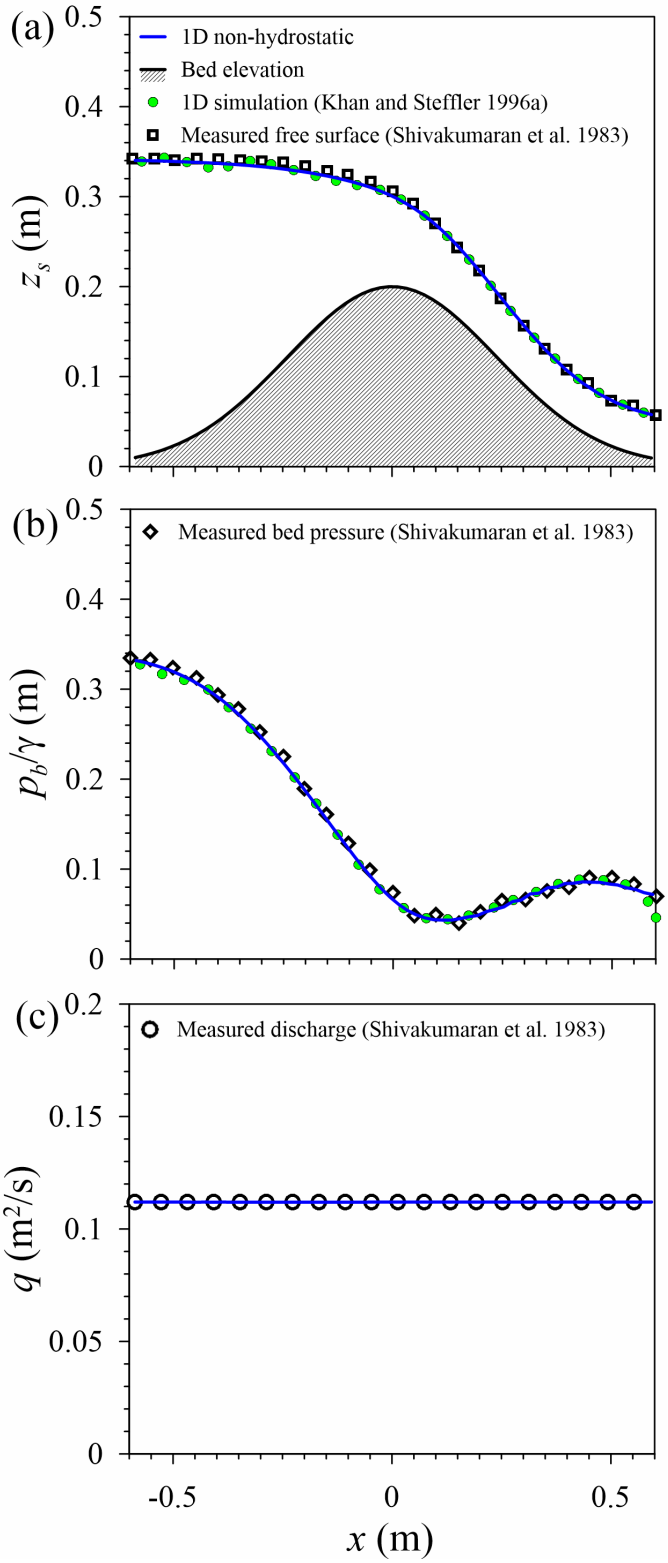

Fig. 9. Steady 1D non-hydrostatic flow over a symmetric hump: Comparison of present 1D results with experimental data (Sivakumaran et al. 1983) and the 1D simulation by Khan and Steffler (1996a) for: (a) free surface profile; (b) bed pressure; (c) unit discharge

6. Conclusions

The following conclusions are drawn from this study:

• A new depth-averaged 1D non-hydrostatic model for shallow free surface flow over movable beds was developed. To the best of the authors' knowledge, this is the first 1D modelling approach presented in the literature for non-hydrostatic dam break waves over erodible beds. The model couples a generalization for sediment transport of the non-hydrostatic momentum equations of Khan and Steffler (1996a,b) with the sediment transport model of Wu and Wang (2007).

• The physical equations are solved using a high-resolution finite volume scheme, needed to accurately solve Boussinesq-type equations. The time stepping scheme that produces an accurate, robust and stable solution is the Adams-Bashforth/Adam Moulton predictor-corrector scheme, where the non-hydrostatic contributions in the *x*- and *z*-momentum equations are treated implicitly, and solved by the Newton-Rapshon method. Schemes used for the solution of hydrostatic dam break waves over movable beds were tested, and it was found that all crashed within a few time steps.

• The predicted free surface profiles using the new set of physical equations are found to be in good agreement with results of the 3D non-hydrostatic RANS simulations by Marsooli and Wu (2015) and the experimental data of Fraccarollo and Capart (2002). The 1D non-hydrostatic model gives a significant improvement in free surface profile predictions as compared to the simulations using a hydrostatic model. It produces undulations at the vicinity of the positive wave portion, also shown experimentally and in the 3D simulations, and yields a good prediction of the smooth negative wave portion. The bed scour profiles predicted by the non-hydrostatic model are similar to those given by the hydrostatic model, indicating that more research is needed to improve the sediment transport model for the non-hydrostatic simulations.

• The model produces results convergent to steady flow profiles with non-hydrostatic pressure. The finite volume scheme gave steady flow results in good agreement with the finite element solution by Khan and Steffler (1996a).

7. Acknowledgements

This study is supported by the Spanish project CTM2013-45666-R, Ministerio de Economía y Competitividad. The authors thank Professor W. Wu for personal communications which allowed us to improve the sediment transport module used in this study.

Appendix: Derivation of Vertically-Integrated Equations for Non-Hydrostatic Mixture Flows

The RANS mass and momentum conservation equations in the *x*- and *z*-directions for a mixture of water and sediments are (Wu 2008, pages 42-43)

$$\frac{\partial \rho}{\partial t}+\frac{\partial(\rho u)}{\partial x}+\frac{\partial(\rho w)}{\partial z}=0, \tag{A1}$$

$$\frac{\partial(\rho u)}{\partial t}+\frac{\partial}{\partial x}\left(\rho u^2+p-\tau_{xx}\right)+\frac{\partial(\rho u w)}{\partial z}=\frac{\partial \tau_{xz}}{\partial z}, \tag{A2}$$

$$\frac{\partial(\rho w)}{\partial t}+\frac{\partial(\rho u w)}{\partial x}+\frac{\partial}{\partial z}\left(\rho w^2+p-\tau_{zz}\right)=\frac{\partial \tau_{zx}}{\partial x}-\rho g, \tag{A3}$$

To obtain a 1D system of equations, the equations are first vertically integrated, then Leibnitz's rule is used and finally the kinematic boundary conditions are applied (Steffler and Jin 1993, Castro-Orgaz et al. 2015). The terms on the mass conservation Eq. (A1) then produce

$$\int_{z_b}^{z_s}\frac{\partial \rho}{\partial t}\mathrm{d}z=\frac{\partial}{\partial t}\int_{z_b}^{z_s}\rho \mathrm{d}z-\rho_s\frac{\partial z_s}{\partial t}+\rho_b\frac{\partial z_b}{\partial t}, \tag{A4}$$

$$\int_{z_b}^{z_s}\frac{\partial(\rho u)}{\partial x}\mathrm{d}z=\frac{\partial}{\partial x}\int_{z_b}^{z_s}\rho u \mathrm{d}z-\rho_s u_s\frac{\partial z_s}{\partial x}+\rho_b u_b\frac{\partial z_b}{\partial x}, \tag{A5}$$

$$\int_{z_b}^{z_s}\rho w \mathrm{d}z=\rho_s w_s-\rho_b w_b. \tag{A6}$$

Coupling Eqs. (A4)-(A5) produces the depth-averaged continuity equation as

$$\frac{\partial}{\partial t}\int_{z_b}^{z_s}\rho \mathrm{d}z+\frac{\partial}{\partial x}\int_{z_b}^{z_s}\rho u \mathrm{d}z-\rho_s\left(\frac{\partial z_s}{\partial t}+u_s\frac{\partial z_s}{\partial x}-w_s\right)+\rho_b\left(\frac{\partial z_b}{\partial t}+u_b\frac{\partial z_b}{\partial x}-w_b\right)=0, \tag{A7}$$

The free surface kinematic boundary conditions is

$$\frac{\partial z_s}{\partial t}+u_s\frac{\partial z_s}{\partial x}-w_s=0, \tag{A8}$$

and, at the bed, the no-slip condition is

$$u_b=w_b=0, \tag{A9}$$

Inserting Eqs. (A8)-(A9) into Eq.(A7), considering depth-averaged values of density ρ and velocity U, finally yields the depth-averaged mass conservation equation as

$$\frac{\partial(\rho h)}{\partial t}+\frac{\partial(\rho U h)}{\partial x}+\rho_b\frac{\partial z_b}{\partial t}=0\,. \tag{A10}$$

Vertical integration of each term of the *x*-momentum Eq. (A2) yields

$$\int_{z_b}^{z_s}\frac{\partial(\rho u)}{\partial t}\mathrm{d}z=\frac{\partial}{\partial t}\int_{z_b}^{z_s}\rho u\mathrm{d}z-\rho_s u_s\frac{\partial z_s}{\partial t}+\rho_b u_b\frac{\partial z_b}{\partial t}\,, \tag{A11}$$

$$\int_{z_b}^{z_s}\frac{\partial(\rho u^2)}{\partial x}\mathrm{d}z=\frac{\partial}{\partial x}\int_{z_b}^{z_s}\rho u^2\mathrm{d}z-\rho_s u_s^2\frac{\partial z_s}{\partial x}+\rho_b u_b^2\frac{\partial z_b}{\partial x}\,, \tag{A12}$$

$$\int_{z_b}^{z_s}\frac{\partial p}{\partial x}\mathrm{d}z=\frac{\partial}{\partial x}\int_{z_b}^{z_s}p\mathrm{d}z-p_s\frac{\partial z_s}{\partial x}+p_b\frac{\partial z_b}{\partial x}\,, \tag{A13}$$

$$\int_{z_b}^{z_s}\frac{\partial\tau_{xx}}{\partial x}\mathrm{d}z=\frac{\partial}{\partial x}\int_{z_b}^{z_s}\tau_{xx}\mathrm{d}z-\tau_{xxs}\frac{\partial z_s}{\partial x}+\tau_{xxb}\frac{\partial z_b}{\partial x}\,, \tag{A14}$$

$$\int_{z_b}^{z_s}\frac{\partial(\rho uw)}{\partial z}\mathrm{d}z=\rho_s u_s w_s-\rho_b u_b w_b\,, \tag{A15}$$

$$\int_{z_b}^{z_s}\frac{\partial\tau_{xz}}{\partial z}\mathrm{d}z=\tau_{xs}-\tau_{xb}\,, \tag{A16}$$

Collecting Eqs. (A11)-(A16) the depth-averaged *x*-momentum equation reads

$$\begin{aligned}&\frac{\partial}{\partial t}\int_{z_b}^{z_s}\rho u\mathrm{d}z+\frac{\partial}{\partial x}\left(\int_{z_b}^{z_s}\rho u^2\mathrm{d}z+\int_{z_b}^{z_s}p\mathrm{d}z+\int_{z_b}^{z_s}\tau_{xx}\mathrm{d}z\right)\\&-\rho_s u_s\frac{\partial z_s}{\partial t}+\rho_b u_b\frac{\partial z_b}{\partial t}-\rho_s u_s^2\frac{\partial z_s}{\partial x}+\rho_b u_b^2\frac{\partial z_b}{\partial x}-p_s\frac{\partial z_s}{\partial x}+p_b\frac{\partial z_b}{\partial x}\\&-\tau_{xxs}\frac{\partial z_s}{\partial x}+\tau_{xxb}\frac{\partial z_b}{\partial x}+\rho_s u_s w_s-\rho_b u_b w_b=\tau_{xs}-\tau_{xb}.\end{aligned} \tag{A17}$$

Grouping terms yields

$$\begin{aligned}&\frac{\partial}{\partial t}\int_{z_b}^{z_s}\rho u\mathrm{d}z+\frac{\partial}{\partial x}\left(\int_{z_b}^{z_s}\rho u^2\mathrm{d}z+\int_{z_b}^{z_s}p\mathrm{d}z+\int_{z_b}^{z_s}\tau_{xx}\mathrm{d}z\right)\\&-\rho_s u_s\left(\frac{\partial z_s}{\partial t}+u_s\frac{\partial z_s}{\partial x}-w_s\right)+\rho_b u_b\left(\frac{\partial z_b}{\partial t}+u_b\frac{\partial z_b}{\partial x}-w_b\right)\\&+\left(p_b+\tau_{xxb}\right)\frac{\partial z_b}{\partial x}-\left(p_s+\tau_{xxs}\right)\frac{\partial z_s}{\partial x}=\tau_{xs}-\tau_{xb}.\end{aligned} \tag{A18}$$

Inserting Eqs. (A8)-(A9) into Eq.(A18), and considering zero pressure and stresses at the free surface, yield

$$\frac{\partial}{\partial t}\int_{z_b}^{z_s}\rho u\mathrm{d}z+\frac{\partial}{\partial x}\left(\int_{z_b}^{z_s}\rho u^2\mathrm{d}z+\int_{z_b}^{z_s}p\mathrm{d}z+\int_{z_b}^{z_s}\tau_{xx}\mathrm{d}z\right)+\left(p_b+\tau_{xxb}\right)\frac{\partial z_b}{\partial x}=-\tau_{xb}. \tag{A19}$$

Neglecting the integral of the normal Reynolds stresses τ_{xx}, and considering depth-averaged values of density ρ and velocity U, Eq. (A19) reduces to

$$\frac{\partial}{\partial t}(\rho hU)+\frac{\partial}{\partial x}\left(\rho hU^2\right)+\frac{\partial}{\partial x}\int_{z_b}^{z_s} p\mathrm{d}z+\left(p_b+\tau_{xxb}\right)\frac{\partial z_b}{\partial x}=-\tau_{xb}. \tag{A20}$$

The pressure distribution is at this stage assumed to be non-hydrostatic and linearly distributed with depth, e.g.

$$p=p_b\left(1-\frac{z}{h}\right), \tag{A21}$$

where the bottom pressure p_b can be rewritten as

$$p_b=\rho gh+p_1. \tag{A22}$$

Inserting Eq. (A21) into Eq. (A20), performing the pressure integral, and using Eq. (A22) yield

$$\frac{\partial}{\partial t}(\rho hU)+\frac{\partial}{\partial x}\left(\rho hU^2\right)+\frac{\partial}{\partial x}\left(\frac{1}{2}\rho gh^2+\frac{hp_1}{2}\right)+\left(\rho gh+p_1+\tau_{xxb}\right)\frac{\partial z_b}{\partial x}=-\tau_{xb}. \tag{A23}$$

Assuming that the stress state at the bed is of pure shear, rotation of the stress tensor an angle equal to the bed slope angle permits to express Cartesian stresses as function of the shear stress τ_b locally tangential to the bed (Steffler and Jin 1993; Castro-Orgaz et al. 2015). The x-momentum equation is then written as

$$\frac{\partial}{\partial t}(\rho hU)+\frac{\partial}{\partial x}\left(\rho hU^2+\frac{1}{2}\rho gh^2\right)=-\left(\rho gh+p_1\right)\frac{\partial z_b}{\partial x}-\tau_b-\frac{\partial}{\partial x}\left(\frac{hp_1}{2}\right). \tag{A24}$$

Vertical integration of each term of the z-momentum Eq. (A3) yields

$$\int_{z_b}^{z_s}\frac{\partial(\rho w)}{\partial t}\mathrm{d}z=\frac{\partial}{\partial t}\int_{z_b}^{z_s}\rho w\mathrm{d}z-\rho_s w_s\frac{\partial z_s}{\partial t}+\rho_b w_b\frac{\partial z_b}{\partial t}, \tag{A25}$$

$$\int_{z_b}^{z_s}\frac{\partial(\rho uw)}{\partial x}\mathrm{d}z=\frac{\partial}{\partial x}\int_{z_b}^{z_s}\rho uw\mathrm{d}z-\rho_s u_s w_s\frac{\partial z_s}{\partial x}+\rho_b u_b w_b\frac{\partial z_b}{\partial x}, \tag{A26}$$

$$\int_{z_b}^{z_s}\frac{\partial}{\partial z}\left(\rho w^2+p-\tau_{zz}\right)\mathrm{d}z=\rho_s w_s^2+p_s-\tau_{zzs}-\rho_b w_b^2-p_b+\tau_{zzb}, \tag{A27}$$

$$\int_{z_b}^{z_s}\frac{\partial\tau_{zx}}{\partial x}\mathrm{d}z=\frac{\partial}{\partial x}\int_{z_b}^{z_s}\tau_{zx}\mathrm{d}z-\tau_{zxs}\frac{\partial z_s}{\partial x}+\tau_{zxb}\frac{\partial z_b}{\partial x}, \tag{A28}$$

$$\int_{z_b}^{z_s} -\rho g \, \mathrm{d}z = -g \int_{z_b}^{z_s} \rho \, \mathrm{d}z \,, \tag{A29}$$

Therefore, collecting Eqs. (A25)-(A29) yield

$$\begin{aligned} &\frac{\partial}{\partial t}\int_{z_b}^{z_s} \rho w \mathrm{d}z + \frac{\partial}{\partial x}\left(\int_{z_b}^{z_s} \rho u w \mathrm{d}z + \int_{z_b}^{z_s} \tau_{zx} \mathrm{d}z\right) \\ &-\rho_s w_s \frac{\partial z_s}{\partial t} + \rho_b w_b \frac{\partial z_b}{\partial t} - \rho_s u_s w_s \frac{\partial z_s}{\partial x} + \rho_b u_b w_b \frac{\partial z_b}{\partial x} \\ &+\rho_s w_s^2 + p_s - \tau_{zzs} - \rho_b w_b^2 - p_b + \tau_{zzb} = -\tau_{zxs} \frac{\partial z_s}{\partial x} + \tau_{zxb} \frac{\partial z_b}{\partial x} - g \int_{z_b}^{z_s} \rho \, \mathrm{d}z. \end{aligned} \tag{A30}$$

Neglecting the integral of the tangential Reynolds stresses τ_{zx}, applying Eqs. (A8)-(A9), and considering depth-averaged values of density ρ and velocity U, Eq. (A30) reduces to

$$p_b = \rho g h + \tau_{zzb} - \tau_{zxb} \frac{\partial z_b}{\partial x} + \frac{\partial}{\partial t}\int_{z_b}^{z_s} \rho w \mathrm{d}z + \frac{\partial}{\partial x}\left[\int_{z_b}^{z_s} \rho u w \mathrm{d}z\right]. \tag{A31}$$

Defining the depth-averaged vertical velocity W by

$$W = \frac{1}{h}\int_{z_b}^{z_s} w \mathrm{d}z, \tag{A32}$$

Eq. (A31) is rewritten, assuming that the stress state at the bed is of pure shear

$$p_b = \rho g h + \tau_b \frac{\partial z_b}{\partial x} + \frac{\partial(\rho h W)}{\partial t} + \frac{\partial(\rho h U W)}{\partial x}, \tag{A33}$$

or

$$\frac{\partial(\rho h W)}{\partial t} + \frac{\partial(\rho h U W)}{\partial x} = p_1 - \tau_b \frac{\partial z_b}{\partial x}. \tag{A34}$$

Now, the flow density ρ is eliminated from Eq. (A10). The depth-averaged mass conservation Eq. (A10) is rewritten as

$$\frac{\partial(\rho h)}{\partial t} + \frac{\partial(\rho h U)}{\partial x} + \frac{\partial(\rho_b z_b)}{\partial t} = 0. \tag{A35}$$

With the definitions $\rho=\rho_w(1-C_t)+\rho_s C_t$ and $\rho_b=\rho_w p_m+\rho_s(1-p_m)$, Eq. (A35) is transformed to

$$\rho_w \frac{\partial h}{\partial t} - \rho_w \frac{\partial (hC_t)}{\partial t} + \rho_s \frac{\partial (hC_t)}{\partial t} + \rho_w \frac{\partial (hU)}{\partial x} - \rho_w \frac{\partial (hUC_t)}{\partial x} + \rho_s \frac{\partial (hUC_t)}{\partial x} + \rho_w p_m \frac{\partial z_b}{\partial t} + \rho_s (1 - p_m) \frac{\partial z_b}{\partial t} = 0. \tag{A36}$$

With the definition $C_t = C_s + q_b/(hU)$, Eq. (A36) is further written as

$$\rho_w \left[\frac{\partial h}{\partial t} + \frac{\partial (hU)}{\partial x} \right] - \rho_w \left[\frac{\partial (hC)}{\partial t} + \frac{\partial}{\partial t}\left(\frac{q_b}{u_b} \right) + \frac{\partial (hUC)}{\partial x} + \frac{\partial q_b}{\partial x} \right] + \rho_s \left[\frac{\partial (hC)}{\partial t} + \frac{\partial}{\partial t}\left(\frac{q_b}{u_b} \right) + \frac{\partial (hUC)}{\partial x} + \frac{\partial q_b}{\partial x} \right] + \rho_w p_m \frac{\partial z_b}{\partial t} + + \rho_s (1 - p_m) \frac{\partial z_b}{\partial t} = 0. \tag{A37}$$

The mass balance equation in the bed-load layer is

$$\frac{\partial}{\partial t}\left(\frac{q_b}{U_b} \right) + \frac{\partial q_b}{\partial x} = \frac{q_{b*} - q_b}{L}, \tag{A38}$$

and the suspended sediment mass conservation equation is

$$\frac{\partial (hC_s)}{\partial t} + \frac{\partial (hUC_s)}{\partial x} = E - D, \tag{A39}$$

Summing up Eqs. (A38) and (A39) yields the conservation equation for the total mass of sediments as

$$\frac{\partial (hC)}{\partial t} + \frac{\partial}{\partial t}\left(\frac{q_b}{u_b} \right) + \frac{\partial (hUC)}{\partial x} + \frac{\partial q_b}{\partial x} = E - D + \frac{q_{b*} - q_b}{L}, \tag{A40}$$

and inserting Eq. (A40) into Eq. (A37) yields

$$\rho_w \left[\frac{\partial h}{\partial t} + \frac{\partial (hU)}{\partial x} \right] + (\rho_s - \rho_w) \left(E - D + \frac{q_{b*} - q_b}{L} \right) + \frac{\rho_w p_m}{1 - p_m} \left(D - E + \frac{q_b - q_{b*}}{L} \right) + \rho_s \left(D - E + \frac{q_b - q_{b*}}{L} \right) = 0, \tag{A41}$$

or

$$\boxed{\frac{\partial h}{\partial t} + \frac{\partial (hU)}{\partial x} = \frac{1}{1 - p_m} \left(E - D + \frac{q_{b*} - q_b}{L} \right)}. \tag{A42}$$

With the definition $\rho = \rho_w (1 - C_t) + \rho_s C_t$, Eq. (A23) for the x-momentum balance reads

$$\begin{aligned}
&\rho_w\left[\frac{\partial(hU)}{\partial t}-\frac{\partial(hUC_t)}{\partial t}\right]+\rho_s\frac{\partial(hUC_t)}{\partial t}\\
&+\rho_w\left[\frac{\partial}{\partial x}\left(hU^2+\frac{1}{2}gh^2\right)-\frac{\partial}{\partial x}\left(C_thU^2+\frac{1}{2}C_tgh^2\right)\right]\\
&-\rho_s\frac{\partial}{\partial x}\left(C_thU^2+\frac{1}{2}C_tgh^2\right)=-\rho gh\frac{\partial z_b}{\partial x}-\tau_b-p_1\frac{\partial z_b}{\partial x}-\frac{\partial}{\partial x}\left(\frac{hp_1}{2}\right).
\end{aligned}\tag{A43}$$

The left hand side (LHS) of Eq. (A43) is

$$\rho_w\left[\frac{\partial(hU)}{\partial t}+\frac{\partial}{\partial x}\left(hU^2+\frac{1}{2}gh^2\right)\right]+(\rho_s-\rho_w)\underbrace{\left[\frac{\partial(hUC_t)}{\partial t}+\frac{\partial}{\partial x}\left(hU^2C_t+\frac{1}{2}gh^2C_t\right)\right]}_{\text{Term I}},\tag{A44}$$

where term I can be expressed as follows

$$\begin{aligned}
&\frac{\partial(hUC_t)}{\partial t}+\frac{\partial}{\partial x}\left(hU^2C_t+\frac{1}{2}gh^2C_t\right)=U\left(E-D+\frac{q_{b*}-q_b}{L}\right)\\
&+C_t\left[\frac{\partial(hU)}{\partial t}+\frac{\partial}{\partial x}\left(hU^2+\frac{1}{2}gh^2\right)\right]-C_tU\left[\frac{\partial h}{\partial t}+\frac{\partial(hU)}{\partial x}\right]+\frac{1}{2}gh^2\frac{\partial C_t}{\partial x},
\end{aligned}\tag{A45}$$

and applying the continuity Eq. (A42) yields

$$\begin{aligned}
&\rho_w\left[\frac{\partial(hU)}{\partial t}+\frac{\partial}{\partial x}\left(hU^2+\frac{1}{2}gh^2\right)\right]\\
&+(\rho_s-\rho_w)\left[U\left(1-\frac{C_t}{1-p_m}\right)\left(E-D+\frac{q_{b*}-q_b}{L}\right)\right.\\
&\left.+C_t\left[\frac{\partial(hU)}{\partial t}+\frac{\partial}{\partial x}\left(hU^2\frac{1}{2}gh^2\right)\right]+\frac{1}{2}gh^2\frac{\partial C_t}{\partial x}\right]=-\rho gh\frac{\partial z_b}{\partial x}\\
&-\tau_b-p_1\frac{\partial z_b}{\partial x}-\frac{\partial}{\partial x}\left(\frac{hp_1}{2}\right),
\end{aligned}\tag{A46}$$

Finally, after some algebraical manipulations and using the definition $\rho=\rho_w(1-C_t)+\rho_sC_t$ yield

$$\boxed{\begin{aligned}
&\frac{\partial(hU)}{\partial t}+\frac{\partial}{\partial x}\left(hU^2+\frac{1}{2}gh^2\right)=-gh\frac{\partial z_b}{\partial x}-\frac{\tau_b}{\rho}-\frac{p_1}{\rho}\frac{\partial z_b}{\partial x}-\frac{1}{\rho}\frac{\partial}{\partial x}\left(\frac{hp_1}{2}\right)\\
&-\frac{1}{2}gh^2\frac{\partial\rho}{\partial x}-\frac{\rho_s-\rho_w}{\rho}U\left(1-\frac{C_t}{1-p_m}\right)\left(E-D+\frac{q_{b*}-q_b}{L}\right).
\end{aligned}}\tag{A47}$$

Likewise, with the definition $\rho=\rho_w(1-C_t)+\rho_sC_t$, Eq. (A34) for the z-momentum balance reads

$$\rho_w\left[\frac{\partial(hW)}{\partial t}+\frac{\partial(hUW)}{\partial x}\right]+(\rho_s-\rho_w)\underbrace{\left[\frac{\partial(hWC_t)}{\partial t}+\frac{\partial(hUWC_t)}{\partial x}\right]}_{\text{Term II}}=p_1-\tau_b\frac{\partial z_b}{\partial x}, \quad \text{(A48)}$$

where term II is expressed as follows,

$$\begin{aligned}\frac{\partial(hWC_t)}{\partial t}+\frac{\partial(hUWC_t)}{\partial x}&=W\frac{\partial(hC_t)}{\partial t}+hC_t\frac{\partial W}{\partial t}+W\frac{\partial(hUC_t)}{\partial x}+hUC_t\frac{\partial W}{\partial x}\\&=W\left[\frac{\partial(hC_t)}{\partial t}+\frac{\partial(hUC_t)}{\partial x}\right]+hC_t\left(\frac{\partial W}{\partial t}+U\frac{\partial W}{\partial x}\right).\end{aligned} \quad \text{(A49)}$$

Eq. (A40) is written as

$$\frac{\partial}{\partial t}\left(hC+\frac{q_b}{u_b}\right)+\frac{\partial}{\partial x}(hUC+q_b)=E-D+\frac{q_{b*}-q_b}{L}, \quad \text{(A50)}$$

or as function of the total load using $C_t=C_s+q_b/(hU)$ as

$$\frac{\partial(hC_t)}{\partial t}+\frac{\partial(hUC_t)}{\partial x}=E-D+\frac{q_{b*}-q_b}{L}. \quad \text{(A51)}$$

Using this result, Eq. (A49) yields

$$\frac{\partial(hWC_t)}{\partial t}+\frac{\partial(hUWC_t)}{\partial x}=W\left(E-D+\frac{q_{b*}-q_b}{L}\right)+hC_t\left(\frac{\partial W}{\partial t}+U\frac{\partial W}{\partial x}\right). \quad \text{(A52)}$$

Further, the last term in Eq. (A52) can be written as

$$hC_t\left(\frac{\partial W}{\partial t}+U\frac{\partial W}{\partial x}\right)=C_t\left[\frac{\partial(hW)}{\partial t}+\frac{\partial(hUW)}{\partial x}\right]-WC_t\left[\frac{\partial h}{\partial t}+\frac{\partial(hU)}{\partial x}\right]. \quad \text{(A53)}$$

and inserting Eq.(A42) into Eq.(A53) results

$$hC_t\left(\frac{\partial W}{\partial t}+U\frac{\partial W}{\partial x}\right)=C_t\left[\frac{\partial(hW)}{\partial t}+\frac{\partial(hUW)}{\partial x}\right]-\frac{WC_t}{1-p_m}\left(E-D+\frac{q_{b*}-q_b}{L}\right). \quad \text{(A54)}$$

Inserting Eqs. (A52) and (A54) into Eq. (A48) and using the definition $\rho=\rho_w(1-C_t)+\rho_sC_t$ yield

$$\boxed{\frac{\partial(hW)}{\partial t}+\frac{\partial(hUW)}{\partial x}=\frac{p_1}{\rho}-\frac{\tau_b}{\rho}\frac{\partial z_b}{\partial x}-\frac{\rho_s-\rho_w}{\rho}W\left(1-\frac{C_t}{1-p_m}\right)\left(E-D+\frac{q_{b*}-q_b}{L}\right)}. \quad \text{(A55)}$$

8. Notation

The following symbols are used in this paper:

b = channel width (m);

C_a = actual near-bed suspended-load sediment concentration;

C_{a*} = equilibrium near-bed suspended sediment concentration;

C_b = depth-averaged bed-load sediment concentration;

CFL = Courant-Friedrichs-Lewy number;

C_s = depth-averaged suspended sediment concentration;

C_t = total-load depth-averaged sediment concentration;

D = sediment depositional rate (m/s);

d = sediment particle diameter (m)

E = sediment entrainment rate (m/s);

$\mathbf{E}$ = auxiliary vector (m/s, m^2/s^2);

$\mathbf{F}$ = vector of fluxes in x-direction (m^2/s, m^3/s^2);

f_w = roughness coefficient for sidewalls ($m^{-1/3}s$);

g = gravitational acceleration (m/s^2);

h = flow depth (m);

h_x = dh/dx;

h_{xx} = d^2h/dx^2 (m^{-1});

h_b = thickness of bed-load layer (m);

h_d = initial downstream flow depth (m);

h_u = initial upstream flow depth (m);

L = non-equilibrium adaptation length of total-load transport (m);

L_b = non-equilibrium adaptation length for bed-load transport (m);

L_s = non-equilibrium adaptation length for suspended-load transport (m),

n = Manning roughness coefficient for bed ($m^{-1/3}s$);

n_w = Manning roughness coefficient for wall ($m^{-1/3}s$);

p_1 = pressure at bed in excess from hydrostatic (Pa);

p_b = pressure at bed (Pa);

p_m = sediment porosity;

q = flow discharge per unit width (m^2/s);

q_b = bed-load flux (m^2/s);

q_{b*} = equilibrium bed-load flux (m^2/s);

R = hydraulic radius (m);

$\mathbf{S}$ = source terms vectors (m/s, m^2/s^2);

t = time (s);

t_0 = $(h_u/g)^{1/2}$ (s);

U = depth-averaged streamwise velocity (m/s);

U_b = bed-load velocity (m/s);

$\mathbf{U}$ = vectors of unknowns (m, m^2/s);

W = depth-averaged vertical velocity (m/s);

w_b = vertical velocity at bed (m/s);

w_s = vertical velocity at free surface (m/s);

x = horizontal coordinate (m);

z_b = erodible bed elevation (m);

z_s = free surface level (m);

α = nonequilibrium adaptation coefficient of suspended-load;

α_0 = empirical coefficient;

Δt = time step (s);

Δx = grid size (m);

ε = tolerance;

ω = settling velocity of a particle (m/s);

ρ = mass density of water-sediment mixture (kg/m^3);

ρ_b = bed layer mass density (kg/m^3);

ρ_s = sediment mass density (kg/m^3);

ρ_w = clear water mass density (kg/m^3);

τ_b = bed shear stress (kg/m/s^2);

Subscripts and Superscripts

i = cell index in x-direction;

k = time step index;

p = predictor index.

9. References

Abbott, M. B. (1979). *Computational hydraulics: Elements of the theory of free surface flows*. Pitman, London, United Kingdom.

Bashiri, A. H., Hosoda, T., and Tada, A. (2015). "Simulation of air cavity advancing into a straight duct." *J. Hydraul. Eng.*, 141(1), 04014068.

Cantero-Chinchilla, F., Castro-Orgaz, O., Dey, S., and Ayuso, J. L. (2016). "Non-hydrostatic dam break flows I: Physical equations and numerical schemes." *J. Hydraul. Eng*. (submitted).

Cao, Z., Pender, G., Wallis, S., and Carling, P. (2004). "Computational dam-break hydraulics over erodible sediment bed." *J. Hydraul. Eng.*, 130(7), 689–703.

Capart, H., and Young, D. L. (1998). "Formation of a jump by the dam-break wave over a granular bed." *J. Fluid Mech*., 372, 165–187.

Capart, H., and Young, D. L. (2002). "Two-layer shallow water computations of torrential flows." *Proc. River Flow*, Balkema, Lisse, The Netherlands, Vol. 2, 1003–1012.

Castro-Orgaz, O., Hutter, K., Giraldez, J. V., and Hager, W. H. (2015). "Non-hydrostatic granular flow over 3-D terrain: New Boussinesq-type gravity waves?" *J. Geophys. Res. Earth Surface*, 120(1), 1–28.

Dey, S. (2014). *Fluvial hydrodynamics: Hydrodynamic and sediment transport phenomena*. Springer, Berlin.

Fraccarollo, L., and Capart, H. (2002). "Riemann wave description of erosional dam break flows." *J. Fluid Mech*., 461, 183–228.

Greco, M., Iervolino, M., Leopardi, A., and Vacca, A. (2012). "A two-phase model for fast geomorphic shallow flows." *Int. J. Sed. Res.*, 27(4), 409–425.

Iwasa, Y. (1956). "Analytical considerations on cnoidal and solitary waves." *Memoires Faculty of Engineering*, Kyoto University 17(4), 264–276.

Khan, A. A., and Steffler, P. M. (1996a). "Vertically averaged and moment equations model for flow over curved beds." *J. Hydraul. Eng*., 122(1), 3–9.

Khan, A. A., and Steffler, P. M. (1996b). “Modelling overfalls using vertically averaged and moment equations.” *J. Hydraul. Eng*., 122(7), 397–402.

Khan, A. A., and Lai, W. (2014). *Modeling shallow water flows using the discontinuous Galerkin method*. CRC Press, Taylor and Francis, New York.

Kim, D. -H., Lynett, P. J., and Socolofsky, S. (2009). “A depth-integrated model for weakly dispersive, turbulent, and rotational fluid flows.” *Ocean Modelling*, 27(3), 198–214.

Li, J., Cao, Z., Pender, G., and Liu, Q. (2013). “A double layer-averaged model for dam-break flows over mobile bed.” *J. Hydraul. Res.*, 51(5), 518–534.

Marsooli, R., and Wu, W. (2015).“Three-dimensional numerical modeling of dam-break flows with sediment transport over movable beds.”*J. Hydraul. Eng.*, 141(1), 04014066.

Nakagawa, H., and Tsujimoto, T. (1980). “Sand bed instability due to bed load motion.” *J. Hydraul. Div*., 106(HYI2), 2029–2051.

Nagata, N., Hosoda, T., and Muramoto, Y. (2000). “Numerical analysis of river channel processes with bank erosion.”*J. Hydraul. Eng*., 126(4), 243–252.

Nagata, N., Hosoda T., Nakato, T., and Muramoto, Y. (2005). “Three-dimensional numerical model for flow and bed deformation around river hydraulic structures.” *J. Hydraul. Eng*, 131(12), 1074–1087.

Onda, S., and Hosoda, T. (2004). “Numerical simulation on development process of dunes and flow resistance.” Proc. River Flow, Vol. 1, 245–252.

Onda, S., Hosoda, T., and Ishibashi, Y. (2010). “Numerical simulation of transition processes of dunes under unsteady flow conditions using a depth averaged flow model”. River, Coastal and Estuarine Morphodynamics, RCEM2009, 719–726.

Sivakumaran N. S., Tingsanchali T., and Hosking R. J. (1983). “Steady shallow flow over curved beds.” *J. Fluid Mech.,* 128, 469–487.

Spinewine, B. (2005). “Two-layer flow behaviour and the effects of granular dilatancy in dam-break induced sheet-flow.” Ph.D. thesis, Univerisité Catholique de Louvain, Louvain-la-Neuve, Belgium.

Steffler, P. M., and Jin, Y. -C. (1993). “Depth averaged and moment equations for moderately shallow free surface flow.” *J. Hydraul. Res.*, 31(1), 5–17.

Toro, E. F. (2000). HYPER_WAT: Library of 13 source codes for solving the non-linear time-dependent shallow water equations in one and two space dimensions.

Toro, E. F. (2001). *Shock-capturing methods for free-surface shallow flows*. John Wiley and Sons, Singapore.

Toro, E. F. (2009). *Riemann solvers and numerical methods for fluid dynamics: A practical introduction*. Springer, Berlin, Germany.

Wei, G., Kirby, J. T., Grilli, S. T., and Subramanya, R. (1995). “A fully nonlinear Boussinesq model for surface waves. Part 1. Highly nonlinear unsteady waves.” *J. Fluid Mech.*, 294, 71–92.

Wu, T. Y. -T. (1987). “Generation of upstream advancing solitons by moving disturbances.” *J. Fluid Mech*., 184, 75–99.

Wu, W. (2004). “Depth-averaged two-dimensional numerical modeling of unsteady flow and nonuniform sediment transport in open channels.” *J. Hydraul. Eng.*, 130(10), 1013–1024. doi: 10.1061/(ASCE)0733-9429(2004)130:10(1013)

Wu, W. (2008). *Computational river dynamics*. Taylor and Francis, London, U.K.

Wu, W. (2015). Personal communication.

Wu, W., and Wang, S. S. Y. (1999). “Movable bed roughness in alluvial rivers.” *J. Hydraul. Eng.*, 125(12), 1309–1312.

Wu, W., and Wang, S. S. Y. (2007). “One-dimensional modeling of dam-break flow over movable beds.” *J. Hydraul. Eng.*, 133(48), 48–58.

Wu, W., and Wang, S. S. Y. (2008). “One-dimensional explicit finite-volume model for sediment transport.” *J. Hydraul. Res.*, 46(1), 87–98.

Wu, W., Rodi, W., and Wenka, T. (2000). “3D numerical modeling of flow and sediment transport in open channels.” *J. Hydraul. Eng.*, 126(4), 4–15.

Wu, W., Vieira, D. A., and Wang, S. S. Y. (2004). “One-dimensional numerical model for nonuniform sediment transport under unsteady flows in channel networks.” *J. Hydraul. Eng.*, 130(9), 914–923.

Wu, W., Marsooli, R., and He, Z. (2012). “A depth-averaged two-dimensional model of unsteady flow and sediment transport due to non-cohesive embankment break/breaching.” *J. Hydraul. Eng.*, 138(6), 503–516.

Zhang, S., Duan, J. G., and Strelkoff, T. S. (2013). “Grain-scale nonequilibrium sediment-transport model for unsteady flow.” *J. Hydraul. Eng.*, 139(1), 22–36.

Zhou, J. G., Causon, D. M., Mingham, C. G., and Ingram, D. M. (2001). “The surface gradient method for the treatment of source terms in the shallow-water equations.” *J. Comput. Phys.*, 168(1), 1–25.

Appendix IV

Distribution of suspended sediment concentration in wide sediment-laden streams: a novel power-law theory

Francisco Nicolás Cantero-Chinchilla[1], Oscar Castro-Orgaz[1], Subhasish Dey[2]

Journal of Sedimentology, "Early View" doi:10.1111/sed.12276. Impact factor (JCR 2014): 2.948 / Q1 (6/46 Geology)

Abstract

The diffusion equation of suspended sediment concentration in a wide sediment-laden stream flow is dependent on the vertical gradient of streamwise velocity and the sediment diffusivity. This study aims at investigating the influence of the streamwise velocity laws on the suspended sediment concentration distributions, resulting from the solution of the diffusion equation. Firstly, the sediment concentration distributions are obtained numerically from the solution of the diffusion equation using different velocity laws, and compared with the experimental data. It is found that the power-law approximation produces good computational results for the concentration distributions. The accuracy of using a power law velocity model is comparable with the results obtained from other classical velocity laws, namely, log-, log wake-, and stratified log-law. Secondly, a novel analytical solution is proposed for the determination of sediment concentration distribution, where a power-law, wall-concentration profile, is coupled with a concentration wake function. The power-law model (for velocity and concentration) is calibrated using the experimental data, and then a generalised wake function is obtained by choosing a suitable law. The developed power-law model involving the wake function adjusted by an exponent predicts the sediment concentration distributions quite satisfactorily. Finally, a new explicit formula for the suspended-load transport rate is derived from the proposed theory, where numerical computation of integrals, as needed in the Einstein theory, is avoided.

[1] Dept. of Agronomy, Univ. of Cordoba, Campus Rabanales, Edif. Da Vinci, Cra Madrid Km 396, 14071 Cordoba, Spain
[2] Dept. of Civil Engineering, Indian Institute of Technology, Kharagpur 721302, West Bengal, India

1. Introduction

Sediment transport as suspended-load is important in most of the fluvial streams, thereby resulting in a number of significant studies over the last eight decades. Dey (2014) gave a summary of the important studies on suspended-load. In fluvial streams, sediment transport is classified as bed-load, suspended-load, and wash-load. The suspended-load is generally the major contributing fraction to the total-load transport (van Rijn, 1984; Mateos & Giráldez, 2005; Dey, 2014). It is well known that important fluvial processes, like bed stability and bed-form development, are consistently influenced by the suspended-load (Bose & Dey, 2009; Dey, 2014). Urban drainage flows are good examples containing suspended-load, in which a variation of sediment concentration with depth is prevalent (Carnacina & Larrarte, 2014; Larrarte, 2015). Thus, the study of suspended-load is still a topic of continued research interest, due to its practical importance.

Suspended-load transport is a complex phenomenon, given the interaction between the turbulent flow and the sediment particle motion, resulting in an alteration of the bed morphology. Several models were proposed to simulate the sediment suspension in a fluvial stream and thus, to compute the suspended-load transport rate. These mainly originate from three major theoretical concepts: (i) The diffusion concept (Rouse, 1937), (ii) the energy concept (Velikanov, 1954, 1958; Bagnold, 1966; Leeder, 1983; Wu *et al.*, 2000), and (iii) the stochastic concept (Cheng & Chiew, 1999; Bose & Dey, 2013). Besides these, Boogerd *et al*. (2001) pointed out the significance of applying the turbulence spectrum, together with an energy approach, as an alternative to the classical theoretical concepts. Among these, the methods based on the diffusion concept are widely accepted and used to produce the models in fluvial hydraulics related to suspended-load. In these methods, the advection-diffusion mechanism constitutes the basis involving the turbulent diffusivity (and in turn, sediment diffusivity), which is a function of the velocity distribution (Dey, 2014).

The three-dimensional (3D) continuity equation for suspended sediment motion is used in 3D numerical models. However, 3D computations of sediment-laden flows at a hydrological catchment scale are still time-consuming and challenging. For this reason, most of the practical models for sediment transport in fluvial streams are still based on a cross-sectional averaged one-dimensional (1D) flow approximation. To this degree of resolution, the vertical distribution of suspended sediment at a section is given by a

diffusion equation involving only the gradient of sediment concentration in the vertical direction (Dey, 2014).

The diffusion equation can be integrated in terms of the reference concentration, reference elevation, terminal fall velocity of sediment particles, and sediment diffusivity. It is pertinent to mention that Hunter Rouse (1906–1966) (Rouse, 1937) was the first to derive the analytical solution for the concentration distribution based on the velocity log-law. The resulting equation is commonly called the Rouse equation. However, the equation was simultaneously derived by Arthur Thomas Ippen (1907–1974). For this reason, the equation should be formally called the Ippen-Rouse equation, as stated by Montes (1973), the last PhD student of Arthur Ippen (personal communication of Montes to the second Author). The Ippen-Rouse equation is a common approach to model the suspended sediment concentration distribution in sediment transport.

Lane & Kalinske (1941) proposed another concentration distribution equation by using a depth-averaged value of the diffusivity. Their concentration distribution is of exponential type. Hunt (1954) considered mass balance for solid (suspended sediment) and fluid phases, separately. He introduced the concept of vertical velocity of a suspended sediment particle into the governing equation as a sum of the flow velocity and the terminal fall velocity of sediment in still water. Hunt's concentration distribution differs from the Ippen-Rouse equation in terms of free parameters. The Ippen-Rouse equation involves only the Rouse number Z as a free parameter, while the Hunt equation possesses two. Further, coupling of the Ippen-Rouse sediment distribution equation with the log-law of velocity for computing the suspended sediment-load produces the Einstein's integrals (Guo & Julien, 2004). A numerical computation is required to solve these integrals. Following Hunt's analysis, van Rijn (1984) also replaced the terminal fall velocity of sediment in still water by that in sediment-laden water flow, thereby correlating both in terms of sediment concentration (Richardson & Zaki, 1954). The determination of terminal fall velocity of sediment is an essential prerequisite and plays a key role in predicting sedimentation of suspended sediment particles (Lucas-Aigier *et al.*, 1998; Camenen *et al.*, 2011; Chauchat *et al.*, 2013). Despite the progressive developments since the Ippen-Rouse equation, it is extensively used (Cao *et al.*, 2003; Lamb *et al.*, 2008).

It is pertinent to state that the Ippen-Rouse equation produces vanishing sediment concentration at the free surface of flow. However, the concentration at the free surface may not be zero in natural stream flows. Zagustin (1968) investigated this limitation assuming a velocity defect-law mathematically given by a hyperbolic tangent function. He derived a concentration distribution equation accounting for a nonzero value at the free surface. Importantly, the velocity gradient along the vertical affects the turbulent diffusivity. Typically, in urban drainage and open-channel flows, the secondary currents induced due to confinement of the flow by the side-walls result in a dip-phenomenon (Knight & Sterling, 2000; Yoon *et al*., 2012; Lassabatere *et al*., 2013; Guo *et al*., 2015). Therefore, the variations in the velocity laws would provoke variations in the computed sediment diffusivity and thus, in the concentration distributions. Accordingly, a family of solutions for the concentration distribution is obtained from various velocity laws. Thus, it suggests to revisit the solutions for the diffusion equation for different velocity laws to explore the viability of the resulting sediment concentration distributions.

The main objective of this study is therefore to find different solutions for the diffusion equation by using some classical velocity laws for the wall-bounded turbulent shear flows. After obtaining the concentration distributions by using these velocity laws, a new analytical theory for the sediment concentration distribution is developed by applying the power-law approximation for the turbulent velocity distribution developed by Castro-Orgaz & Dey (2011). Numerical and analytical results of the study are compared with the experimental results on the sediment concentration (Coleman, 1986; Lyn, 1986; Montes, 1973). Finally, an analytical formula to calculate the suspended-load transport rate is presented, where the numerical computation of integrals is avoided. Thus, it could be a practical tool for the estimation of suspended-load transport rate.

2. Diffusion model

In sediment-laden flows, the suspended sediment motion is defined by the generalised advection-diffusion equation (Dey, 2014)

$$\frac{\partial C}{\partial t}+u\frac{\partial C}{\partial x}+v\frac{\partial C}{\partial y}+w\frac{\partial C}{\partial z}+C\left(\frac{\partial u}{\partial x}+\frac{\partial v}{\partial y}+\frac{\partial w}{\partial z}\right)$$

$$=\frac{\partial}{\partial x}\left[\left(\varepsilon_m+\varepsilon_{sx}\right)\frac{\partial C}{\partial x}\right]+\frac{\partial}{\partial y}\left[\left(\varepsilon_m+\varepsilon_{sy}\right)\frac{\partial C}{\partial y}\right]+\frac{\partial}{\partial z}\left[\left(\varepsilon_m+\varepsilon_{sz}\right)\frac{\partial C}{\partial z}\right] \qquad (68)$$

where C is the time-averaged sediment concentration at (x, y, z), t is the time, ε_m is the molecular diffusivity, ε_{si} is the solid diffusivity in i-direction ($i = x, y, z$), and u, v, and w are the time-averaged velocity components in x-, y-, and z-direction, respectively. Under a steady-uniform flow condition, the dynamic equilibrium of suspended sediment motion is maintained by balancing the sediment diffusion flux in the vertical direction with the sediment flux due to settling velocity. Thus, the problem reduces to a 1D ordinary differential equation (ODE) in z-direction. The schematic distributions of concentration C, streamwise velocity u, and Reynolds shear stress τ in uniform sediment-laden flow are shown in Fig. 1. Equation 1 therefore reduces to (Dey 2014)

$$\varepsilon_s \frac{dC}{dz} + w_s C = 0 \tag{69}$$

where ε_s is the sediment diffusivity, and w_s is the terminal fall velocity of sediment particles. The solution for concentration $C(z)$ is obtained from Eq. 2 once the appropriate functions for the sediment diffusivity and the terminal fall velocity of sediment particles are introduced.

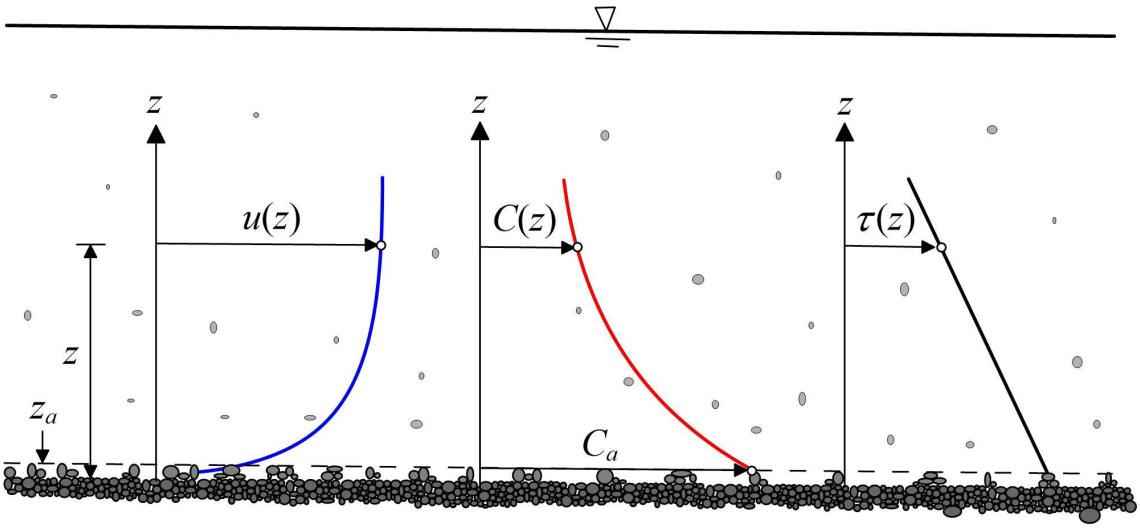

Fig. 1. Schematic of concentration C, streamwise velocity u, and Reynolds shear stress τ distributions in uniform sediment-laden flow over a streambed.

According to the Boussinesq hypothesis (Dey, 2014),

$$\tau \approx \rho \varepsilon_t \frac{du}{dz} \tag{70}$$

where ε_t is the eddy viscosity or turbulent diffusivity, and ρ is the mass density of fluid.

In a two-dimensional (2D) steady-uniform flow, the momentum balance provides the linear Reynolds shear stress distribution (Fig. 1) (Dey, 2014)

$$\tau \approx \tau_0 \left(1 - \frac{z}{h}\right) \tag{71}$$

where τ_0 is the bed shear stress (= ρghS), g is the gravitational acceleration, h is the flow depth, and S is the friction slope.

Equating Eqs 3 and 4 yields

$$\varepsilon_t = u_* h \frac{1-\eta}{du^+/d\eta} = \frac{\varepsilon_s}{\beta} \tag{72}$$

where u_* is the shear velocity [=$(\tau_0/\rho)^{1/2}$], u^+ = u/u_*, and η = z/h. The sediment and turbulent diffusivities are related as $\varepsilon_s = \beta\varepsilon_t$, where β is a proportionality factor.

Inserting ε_s from Eq. 5 into Eq. 2 and integrating it between a reference level z_a and an arbitrary level z yield

$$c^+ = \exp\left(-\kappa Z \int_{\eta_a}^{\eta} \frac{du^+/d\eta}{1-\eta} d\eta\right) \tag{73}$$

where κ is the von Kármán constant for clear-water flows (= 0.41), c^+ is the nondimensional sediment concentration (= C/C_a), C_a is the reference concentration at reference level z_a, η_a is the nondimensional reference level (= z_a/h), and Z is the Rouse number (Rouse, 1937). The Rouse number is given by

$$Z = \frac{w_s}{\beta\kappa u_*} \tag{74}$$

The proportionality factor β in the Rouse number may be considered to be unity as an approximation.

3. The laws of streamwise velocity distribution

As previously discussed, different laws for the streamwise velocity distribution produce varied sediment concentration distributions. An examination of Eq. 6 suggests that it depends on the Rouse number Z and the velocity gradient $du^+/d\eta$. Therefore, in order to investigate the impact of the velocity distributions on the c^+-distribution, various well-established velocity laws are considered.

Firstly, the logarithmic-law (henceforth called log-law) is considered (Rouse, 1937; Dey, 2014). It is expressed in the defect form as

$$U^+ - u^+ = -\frac{1}{\kappa}\ln\eta \tag{75}$$

where U^+ is the nondimensional maximum streamwise velocity occurring at the free surface devoid of any dip (= U_{max}/u_*), and U_{max} is the maximum streamwise velocity. It is pertinent to mention that the dip-phenomenon prevails in the flows through narrow channels due to the presence of secondary currents. For example, urban drainage flows exhibit the dip-phenomenon significantly in laboratory experimental and field studies (Knight & Sterling, 2000; Larrarte, 2015). It may be noted that using Eq. 8 into Eq. 7, results in the classical Ippen-Rouse equation for the concentration distributions.

The log-law is only applicable in the wall-shear layer of turbulent flow. Roughly, it limits to about the 20% of the flow depth close to the bed in most practical problems (ASCE Task Force, 1963). To generalise the log-law to the entire turbulent boundary layer, Coles (1956) proposed the so-called log wake-law. It is

$$U^+ - u^+ = -\frac{1}{\kappa}\ln\eta + \frac{2\Pi}{\kappa}\cos^2\left(\frac{\pi}{2}\eta\right) \tag{76}$$

where Π is the Cole's wake parameter. It is clear that Eq. 9 differs from Eq. 8 in terms of the additional second term in the right hand side of Eq. 9, which is known as wake function.

In sediment-laden flows excluding urban drainage flows (Larrarte, 2015), most of the sediment particles are transported in the inner-layer of flow close to the bed (Coleman, 1986), whereas the outer-layer is characterised by a lower sediment concentration, thus creating a stratification. The particle size distributions of sediment suspension also reveal the concept of stratification (Sengupta, 1975, 1979; Mazumder, 1994). This stratification modifies the turbulent momentum transfer, thereby affecting the velocity distribution (Wright & Parker, 2004; García, 2008; Dutta *et al.*, 2014). Wright & Parker (2004) stated that the sediment concentration gradient along the vertical affects the momentum flux through the change of turbulent diffusivity. Thus, they proposed a modified expression for turbulent diffusivity ε_t involving the flux Richardson number. Assuming a constant Richardson number over the entire flow depth, the turbulent diffusivity is expressed as

$$\varepsilon_t = \alpha \kappa u_* z(1-\eta) \tag{77}$$

where α is the stratification parameter. Generally, α needs to be determined empirically.

From Eqs 5 and 10, the velocity gradient is

$$\frac{du}{dz} = \frac{u_*}{\alpha \kappa z} \tag{78}$$

Integrating Eq. 11, the streamwise velocity distribution is

$$U^+ - u^+ = -\frac{1}{\alpha \kappa} \ln \eta \tag{79}$$

Equation 12 is defined as the stratified log-law in velocity defect form.

Finally, the power-law model for streamwise velocity distribution developed by Castro-Orgaz & Dey (2011) is considered. It is

$$u^+ = U^+ \left(\frac{z}{\delta} \right)^{1/n} \tag{80}$$

where δ is the boundary layer thickness, and $n = \kappa U^+[(11 + 12\Pi)/12]^{-1} - 1$. For a fully developed flow in a wide channel (with no-dip), that is $\delta \approx h$, Eq. 13 is rewritten as

$$u^+ = U^+ \eta^{1/n} \tag{81}$$

4. Power-law concentration model

The power-law model, given by Eq. 14, is used to determine the new sediment concentration distribution. Lyn (1986) was the first to point out that the c^+-distribution can be represented by an inner-layer concentration component plus a wake function to adjust the concentration distribution in the outer-layer of flow. Later, Lyn (2000) developed this concept for the Ippen-Rouse c^+-distribution, which was affected by a wake parameter. This isolated work is the only appearance of a wake function for the c^+-distribution. This challenging approach is here considered in combination with the power-law model given by Eq. 14.

Introducing Eq. 14 into Eq. 6 results

$$c^+ = \exp\left(-\kappa Z \int_{\eta_a}^{\eta} \frac{U^+}{n} \cdot \frac{\eta^{(1-n)/n}}{1-\eta} d\eta \right) \tag{82}$$

A primitive function of Eq. 15 is not known; so a numerical integration is required. However, assuming $\eta << 1$, the integral in Eq. 15 can be approximated as

$$\int_{\eta_a}^{\eta} \frac{U^+}{n} \cdot \frac{\eta^{(1-n)/n}}{1-\eta} d\eta \approx \int_{\eta_a}^{\eta} \frac{U^+}{n} \eta^{(1-n)/n} (1+\eta) d\eta \tag{83}$$

Using Eq. 16 into Eq. 15 yields

$$c^+ = \exp\left[-\kappa Z U^+ \left(\eta^{1/n} - \eta_a^{1/n} + \frac{\eta^{(1+n)/n} - \eta_a^{(1+n)/n}}{n+1} \right) \right] \tag{84}$$

Further, neglecting the last term inside the parenthesis of right hand side of Eq. 17 given its small magnitude, Eq. 17 reduces to

$$c^+ = \exp\left[-\kappa Z U^+ \left(\eta^{1/n} - \eta_a^{1/n} \right) \right] \tag{85}$$

Considering the wall-layer $\eta << 1$, the equivalence between a log-law and a power-law is given by $\eta^{1/n} \approx 1 + [(\ln \eta)/(1+n)]$. Therefore, Eq. 18 is solved as

$$c^+ = \Psi \exp\left(-\frac{\kappa Z U^+}{1+n} \ln \eta \right) = \Psi \eta^{-\Gamma} \tag{86}$$

where $\Psi = \eta_a^{\Gamma}$, and $\Gamma = \kappa Z U^+/(1+n)$. It may be noted that Eq. 19 is only applicable to the inner-layer of flow. To generalise Eq. 19 for the entire flow depth, a wake function for the concentration distribution is assumed (Lyn, 1986)

$$c^+ = \Psi \eta^{-\Gamma} W(\eta, \Pi_c) \tag{87}$$

where $W(\eta, \Pi_c)$ is the wake function that must preserve the asymptotic conditions as follows:

$$\begin{aligned} \eta &\to 0 \quad W \to 1 \\ \eta &\to 1 \quad W \to 0 \end{aligned} \tag{88}$$

The second condition is based on the fact that the concentration distribution in Eq. 19 is valid for the inner-layer of flow, but should vanish at the free surface. Notwithstanding, there is no evidence of the form of the wake function, which has to be plausibly proposed in the light of the experimental data. As a first approach, the wake function is assumed in this study as

$$W(\eta, \Pi_c) = 1 - \eta^{\Pi_c} \tag{89}$$

where Π_c is an exponent of wake parameter that needs to be determined empirically.

Thus, the power-law model for sediment concentration distribution is finally given by

$$c^+ = \Psi \eta^{-\Gamma}(1-\eta^{\Pi_c}) \tag{90}$$

5. Suspended-load transport rate

The suspended-load transport rate q_s is calculated from the depth integration of the product of the sediment concentration and the streamwise velocity distribution of the flow. It is

$$q_s = \int_{z_a}^{h} Cudz \tag{91}$$

Using nondimensinal forms of the sediment concentration and the streamwise velocity distributions, Eq. 24 is given by

$$q_s = C_a u_* h \int_{\eta_a}^{1} c^+ u^+ d\eta \tag{92}$$

Inserting Eqs 14 and 23 into Eq. 25, the suspended-load transport rate is modified in terms of the power-law model as

$$q_s = C_a u_* h \Psi U^+ \int_{\eta_a}^{1} (1-\eta^{\Pi_c})\eta^{\frac{1}{n}-\Gamma} d\eta \tag{93}$$

The integral in Eq. 26 is performed as

$$\int_{\eta_a}^{1} (1-\eta^{\Pi_c})\eta^{\frac{1}{n}-\Gamma} d\eta = \frac{1-\eta_a^{1+\frac{1}{n}-\Gamma}}{1+\frac{1}{n}-\Gamma} - \frac{1-\eta_a^{1+\frac{1}{n}-\Gamma+\Pi_c}}{1+\frac{1}{n}-\Gamma+\Pi_c} = \frac{1-\eta_a^{A}}{A} - \frac{1-\eta_a^{A+\Pi_c}}{A+\Pi_c} \tag{94}$$

where $A = 1 + [(1 - n\Gamma)/n]$.

The nondimensional form of the suspended-load transport rate, called the suspended-load transport intensity Φ_s, is expressed as

$$\Phi_s = \frac{q_s}{\left(\Delta g d_{50}^3\right)^{0.5}} \tag{95}$$

where Δ is the submerged relative density.

Inserting Eq. 27 into Eq. 26 and then using Eq. 28, the suspended-load transport intensity Φ_s for the power-law model is analytically formulated as

$$\Phi_s = \frac{C_a u_* h \Psi U^+}{\left(\Delta g d_{50}^3\right)^{0.5}} \left(\frac{1-\eta_a^A}{A} - \frac{1-\eta_a^{A+\Pi_c}}{A+\Pi_c} \right) \tag{96}$$

It may be noted that this function is analytical, and thus numerical computations are avoided. In contrast, use of the Ippen-Rouse equation coupled with the log-law of velocity distribution produces the well-known Einstein's integrals to compute Φ_s, where a numerical solution is required. Therefore, Eq. 29 is a new and simple analytical tool for the estimation of suspended-load transport rate.

6. Methodology

One of the main objectives of this study is to compare the new analytical power-law model for concentration (Eq. 23) involving the power-law velocity distribution (Eq. 14) with the computational results for the concentration distribution based on Eq. 6. Equation 6 needs a mathematical closure in terms of the velocity gradient. Therefore, the log-, log wake-, power- and stratified log-law are used to produce c^+-distributions. Firstly, a critical comparison between the analytical and the numerical c^+-distributions for all the four velocity laws, discussed in preceding sections, is carried out. Then, Eq. 23 is compared with Eq. 6 coupled with Eq. 14 for the velocity gradient closure.

The experimental data sets selected for the comparisons are from Coleman (1986), Lyn (1986), and Montes (1973).

The computational procedure is furnished as follows:

1. For a given experimental data set (including streamwise velocity and sediment concentration distributions), determine U^+ from the data near the free surface and η_a from the data at the lowest level z_a.
2. Adjust Π and α coefficients in Eqs 9, 12, and 14 by evaluating the lowest level of the velocity from the data set.
3. Calculate the vertical distributions of streamwise velocity u^+ inserting computations from Steps 1 and 2 into Eqs 8, 9, 12, and 14.
4. Substituting nondimensional velocity gradients $du^+/d\eta$ into Eq. 6, numerically compute the distribution of nondimensional sediment concentration c^+ by using the

Simpson's rule. Try with different values of Rouse number Z until a best fit for the computed $c^+(\eta)$ with the experimental data is obtained. Note that fitting Z, w_s is not computed.

5. Use Eq. 20 along with the results obtained from Step 4 to determine the wake function distributions $W(\eta)$.

The suspended-load transport intensity Φ_s can be calculated from Eq. 29.

7. Results

The experimental data set of Coleman (1986) has been extensively used for the validation purposes of sediment concentration models (Bose & Dey, 2009; Ghoshal & Kundu, 2013; Kundu & Ghoshal, 2014) and also streamwise velocity laws (Guo & Julien, 2008; Absi, 2011). In this study, Runs 12, 27, and 34 from the experimental data set of Coleman are selected, representing each one with different bed roughness values. In brief, Coleman conducted experiments in a 0.356 m wide and 15 m long rectangular flume. The flow depth was approximately 0.17 m in all the selected runs having an aspect ratio (flume width to flow depth ratio) of about 2. The shear velocity was 0.041 m s^{-1}; and the von Kármán constant was assumed to be equal to its universal value as 0.41. With these, Fig. 2 shows the velocity and the sediment concentration distributions obtained from the computations using different velocity laws and the experimental data used for the calibration of free parameters. The values of Z shown in Fig. 2 are the ones which ensured a satisfactory fitting between the computed c^+-distribution and the experimental data for a given experimental run.

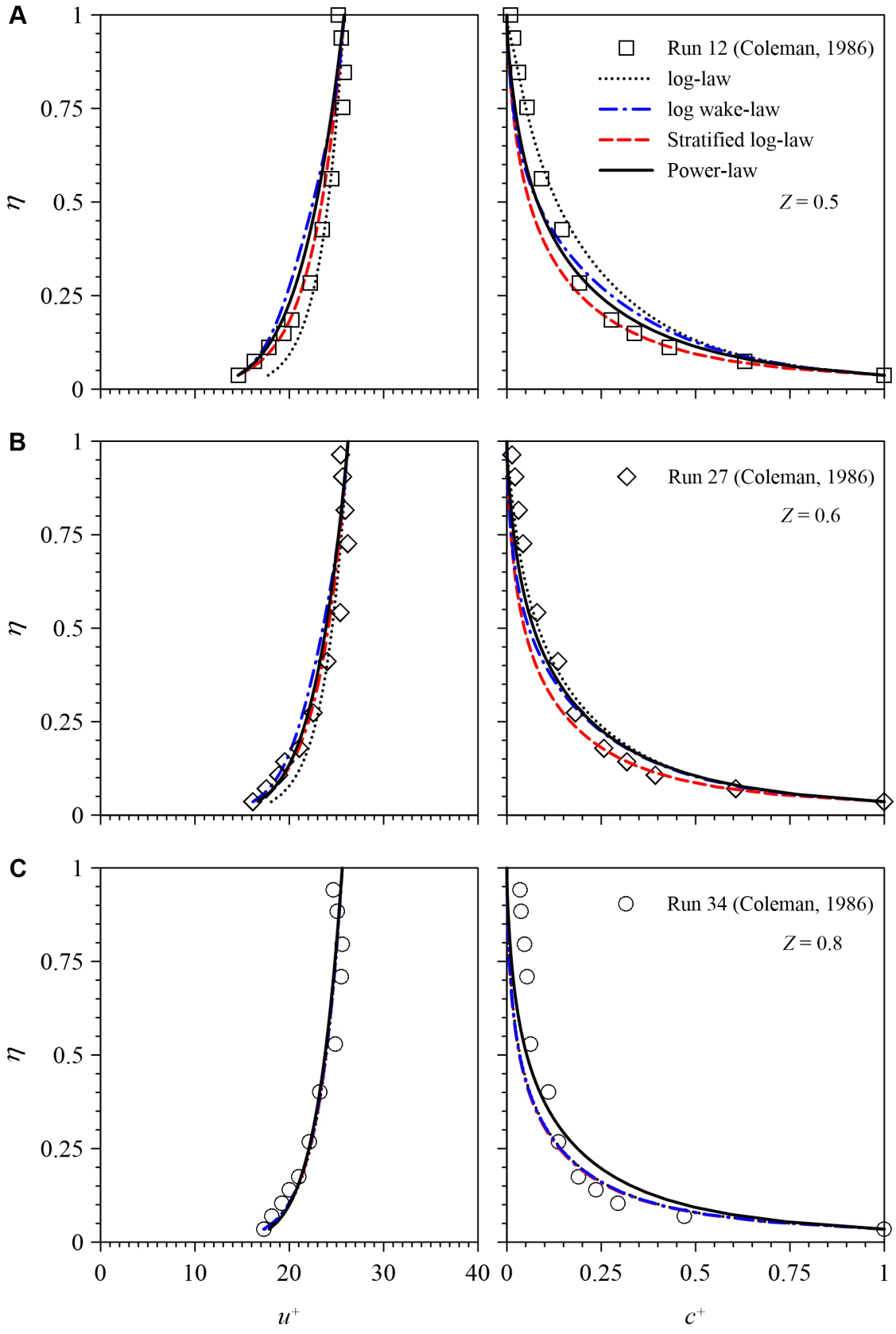

Fig. 2. Nondimensional velocity $u^+(\eta)$ and concentration $c^+(\eta)$ distributions obtained using Coleman's (1986) experimental data: (A) Run 12, (B) Run 27 and (C) Run 34.

Figures 3 and 4 likewise exhibit velocity and concentration distributions using different velocity laws and experimental data of Lyn (1986) and Montes (1973) used for the calibration of free parameters. From Lyn's experimental data, Runs 1957ST2A and 1957ST2B, characterised as a starved-bed flow, are considered. The Rouse numbers are also shown in Figs 3 and 4. In this case, no equilibrium of sediment transport in the flow was established. In brief, Lyn's experiments were conducted in a rectangular flume of approximately 0.267 m wide and 13 m long. The main difference between Runs 1957ST2A and 1957ST2B was the quantity of sediment load in the experiments, where Run 1957ST2A corresponded to a larger suspended sediment load than Run 1957ST2B. The shear velocity, flow depth, and bed slope of the flume remained same for both the runs, being approximately 0.043 m s^{-1}, 0.058 m, and 0.004, respectively. Regarding the experimental data of Montes (1973), two experimental data sets (Runs 22 and 44) are taken into consideration based on the more number of available data points. Briefly, Montes conducted experiments in a rectangular flume of 0.487 m wide and 19.5 m long. For Run 22, the shear velocity and flow depth were 0.077 m s^{-1} and 0.074 m, respectively. On the other hand, for Run 44, they were 0.061 m s^{-1} and 0.077 m. Further, Run 44 was performed with a lower sediment load than Run 22.

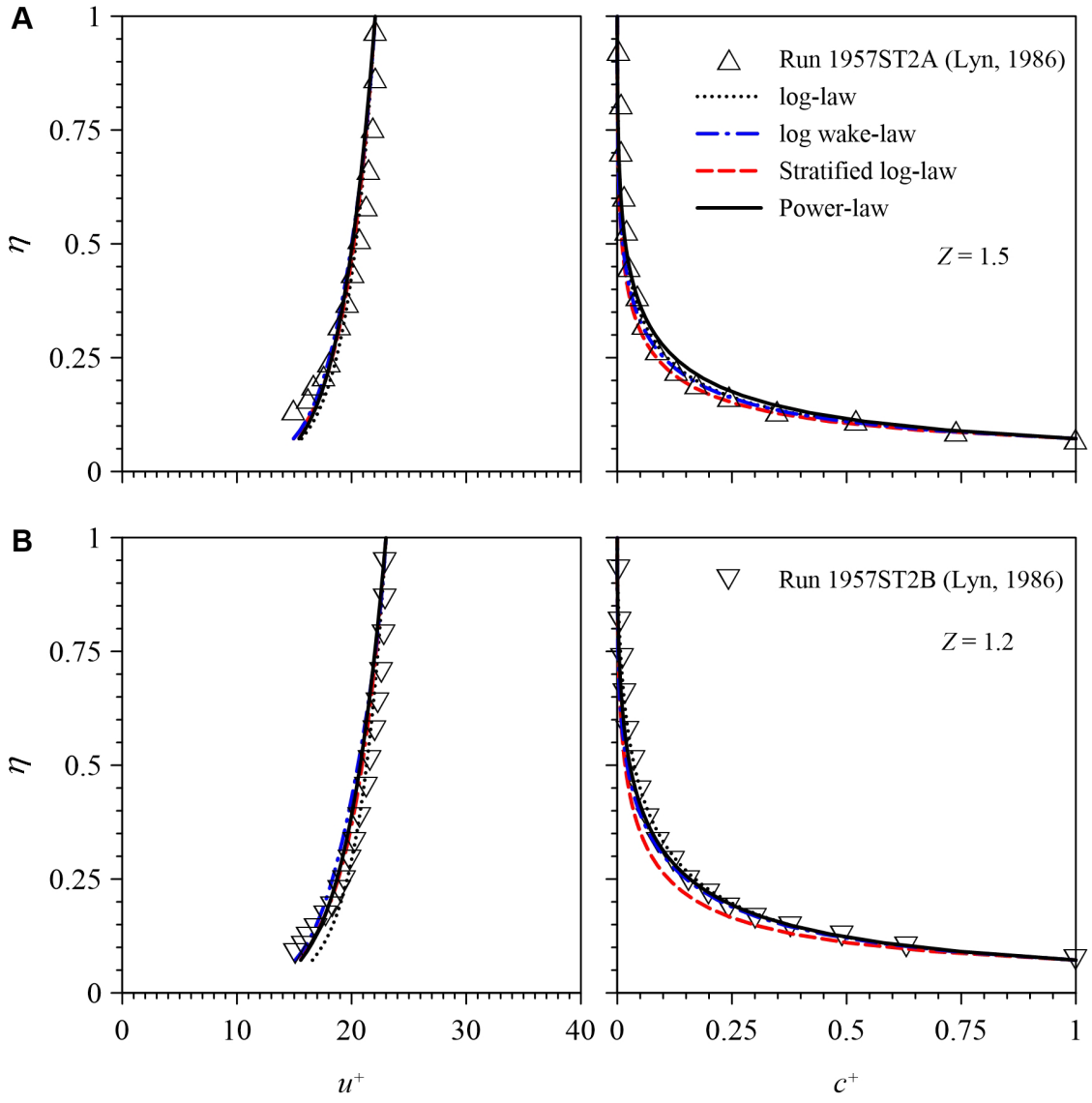

Fig. 3. Nondimensional velocity $u^+(\eta)$ and concentration $c^+(\eta)$ distributions obtained using Lyn's (1986) experimental data: (A) Run 1957ST2A and (B) Run 1957ST2B.

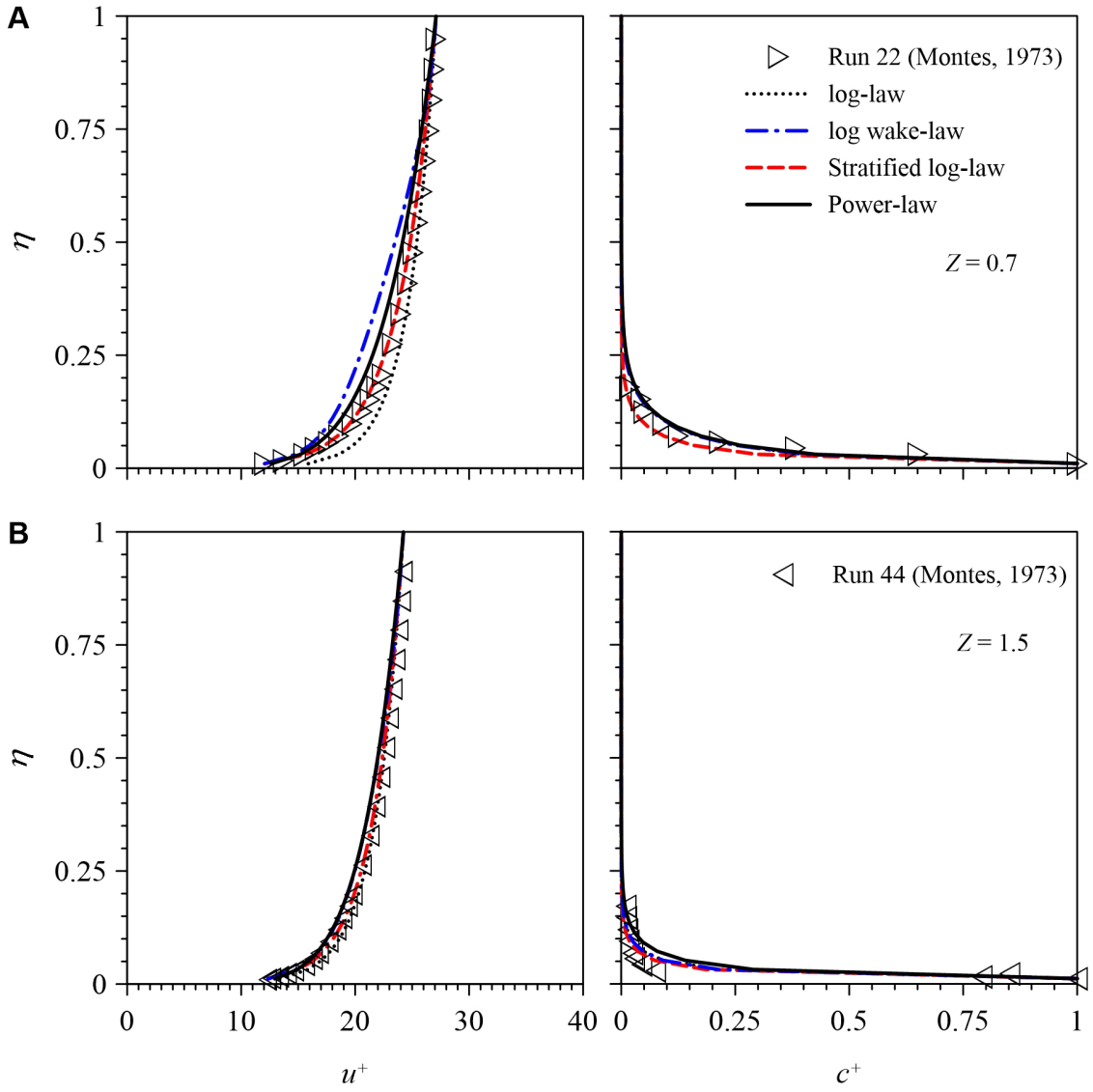

Fig. 4. Nondimensional velocity $u^+(\eta)$ and concentration $c^+(\eta)$ distributions obtained using Montes' (1973) experimental data: (A) Run 22 and (B) Run 44.

Using the relationship between the sediment concentration c^+ and the wake function W given by Eq. 20, the wake function over the entire flow depth are obtained with the aid of the experimental data sets. Figures 5–7 (left side) depict the $W(\eta)$-curves obtained numerically and analytically for Eqs 20 and 22, respectively. On the other hand, Figs 5–7 (right side) display the $c^+(\eta)$-curves obtained numerically from Eq. 6, analytically from Eq. 19, and using the power-law model from Eq. 23. Further, Figs 5–7 (both left and right sides) show the experimental data plots. The wake function data are the cause of the resulting computed c^+-curves from Eq. 19 having a departure from the experimental data. In this case, the experimental data plots of wake function for $W < 1$ in the outer-layer of flow are to produce the overestimated c^+-curves from Eq. 19, whereas c^+-curves corresponding to $W > 1$ in the inner-layer are to produce

underestimated c^+-curves. An appropriate wake function therefore was sought that could fit most of the experimental data over the entire flow depth. The exponent of wake functions Π_c and Rouse numbers Z were adjusted by the trial-and-error method until the best fitted curves for the computed $W(\eta)$- and $c^+(\eta)$-distributions with the experimental data were obtained. To conclude the overall variation of the wake function $W(\eta)$, Fig. 8 presents the wake function $Z(\eta)$ for different values of Π_c. However, a scatter of Montes' experimental data in the inner-layer of flow is apparent.

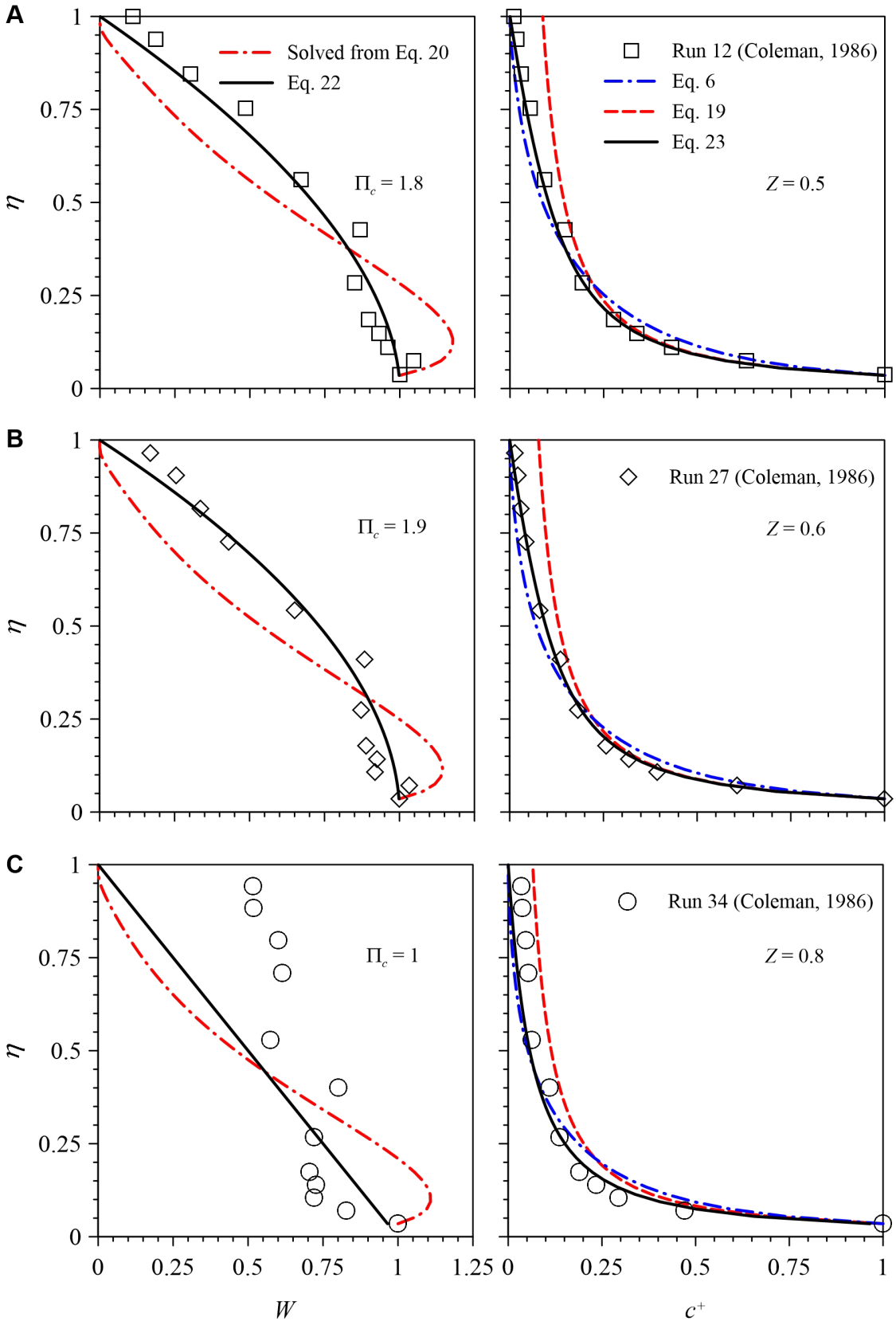

Fig. 5. Wake function $W(\eta)$ and concentration $c^{+}(\eta)$ distributions obtained using Coleman's (1986) experimental data: (A) Run 12, (B) Run 27 and (C) Run 34.

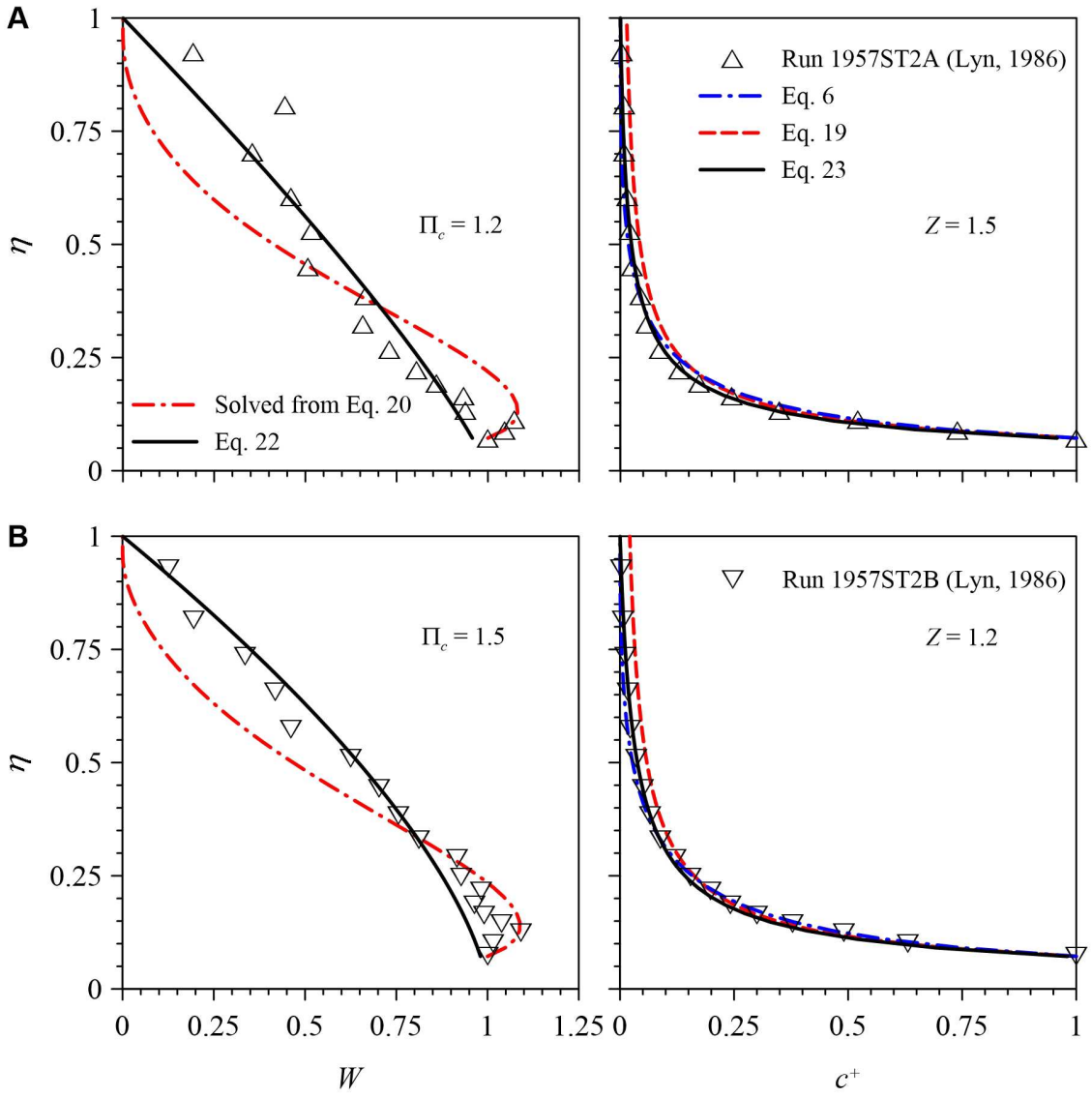

Fig. 6. Wake function $W(\eta)$ and concentration $c^{+}(\eta)$ distributions obtained using Lyn's (1986) experimental data: (A) Run 1957ST2A and (B) Run 1957ST2B.

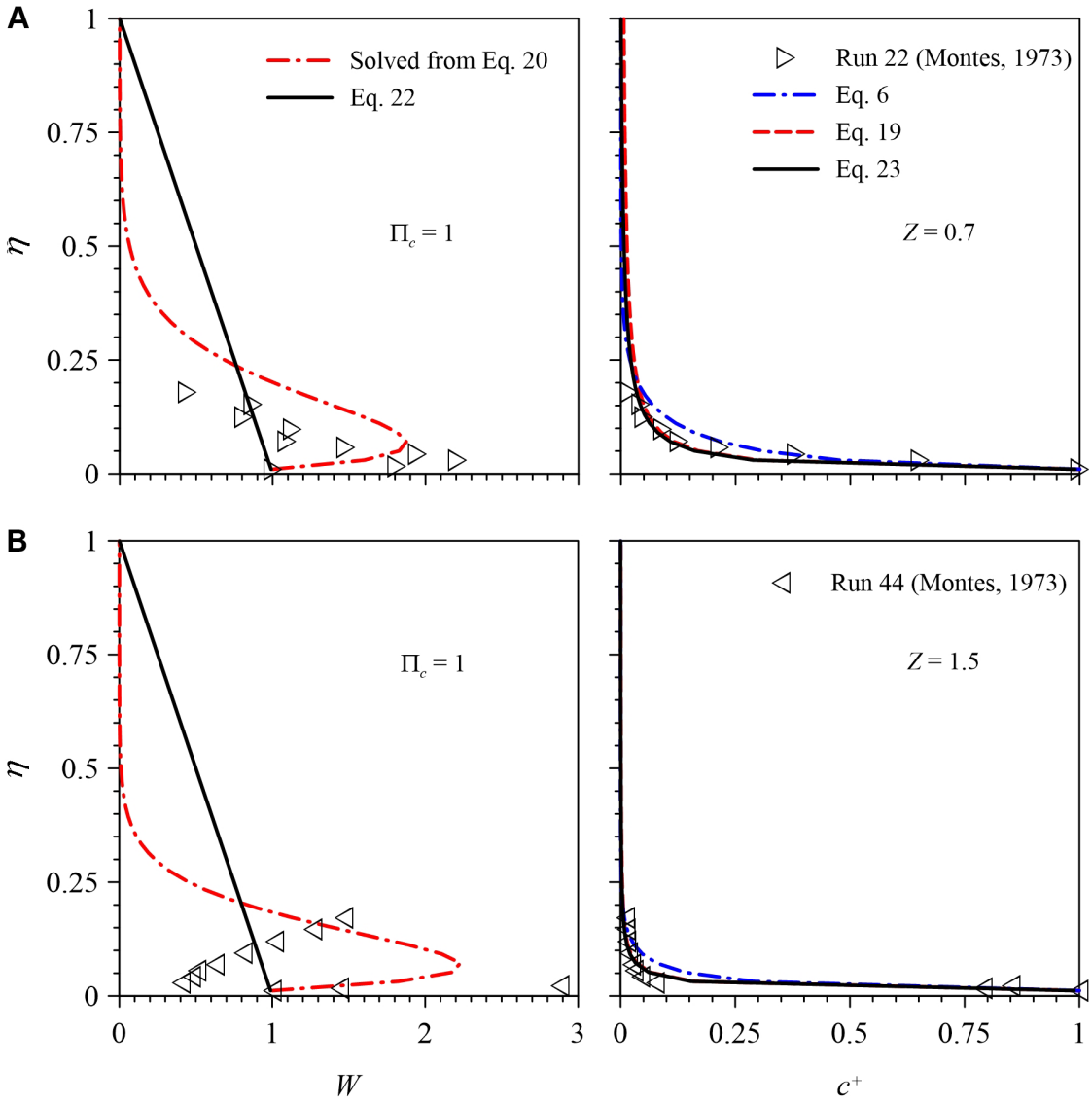

Fig. 7. Wake function $W(\eta)$ and concentration $c^{+}(\eta)$ distributions obtained using Montes' (1973) experimental data: (A) Run 22 and (B) Run 44.

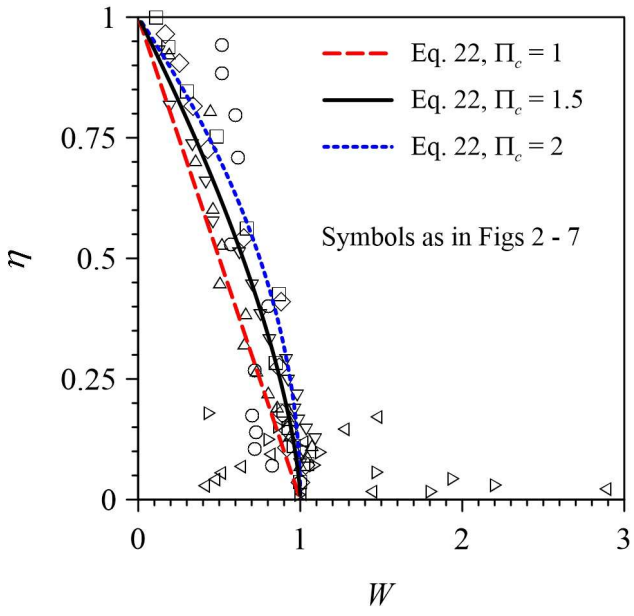

Fig. 8. Wake function $W(\eta)$ for different values of Π_c obtained from Eq. 22 using all experimental data.

8. Discussion

The velocity laws are considered here to compare with the experimental data. Figures 2–4 (left side) show that the log-law corresponds less to the experimental data, whilst the log wake-law underestimates the experimental data. This discrepancy is partially attributed to the lack of adjustable parameters. Thus, the log-law provides a poor prediction. On the other hand, the power- and the stratified log-law compare quite well with the experimental data and thus produce satisfactory results. An improved fitting could also be achieved by considering the dip phenomenon modification terms in the velocity laws (Yang *et al.*, 2004; Guo & Julien, 2008). However, the differences in velocity distributions obtained from different velocity laws are somewhat not significant. Regarding the concentration distributions in Figs 2–4 (right part), a similar observation is inferred. For the given values of Z, as shown in Figs 2–4, the experimental data almost collapse on the computed concentration distributions. The stratified log-law, which is theoretically sound from the viewpoint of sediment-water mixture and agrees well with velocity data, tends to underestimate the experimental data of concentration. In contrast, the log-law overestimates the experimental data. The power-law produces good results simultaneously for velocity and sediment concentration distributions.

It is pertinent to mention that the wake function distribution $W(\eta)$ depends on the estimation of the Rouse number Z. As shown in Figs 5–7 (right side), Eq. 19 produces concentration distributions that in general overestimate the experimental data, yielding wake function data from Eq. 20 lower than unity. Nevertheless, the computed concentration distributions still overestimate some experimental data in the inner-layer of flow. Experimental data of wake function greater than unity in the inner-layer of flow are not achievable to be fitted by the proposed wake function in Eq. 22, whilst the numerical results of Eq. 20 show that trend in the inner-layer. However, Eq. 23, which involves Eq. 22, gives concentration distributions that agree well with the experimental data. These computed distributions are better than the distributions obtained numerically from Eq. 6. The proposed concentration model, based on the power-law, performs satisfactorily with the same value of Rouse number that was used in the numerical computation. So, it is not required to perform a double adjustment for the Rouse number.

In determining the wake function distributions for different values of exponent Π_c as shown in Fig. 8, the exponent of wake function Π_c is set for all the experimental data for *W*-distributions complying with certain values of Π_c. To do this, it was convenient to adjust the values of Π_c for different experimental data. However, in view of the average values and the standard deviations, the values of Π_c are typically in between 1 and 2, with Π_c = 1.5 to give the best overall agreement between the fitted $W(\eta)$-curve and the experimental data.

In view of the results, it is evident that the power-law velocity model and the resulting wall-wake concentration distribution can be used as predictors. Besides the novelty of proposing a concentration distribution model based on wall-wake components, the analytical developments based on the power law functions are simple. Actually, the proposed $c^+(\eta)$-distribution in Eq. 23 needs to be understood as a semi-empirical approximation of Eq. 15, which is firstly solved as a wall function (Eq. 19) and later expanded across the whole water depth using the wake function (Eq. 22). Therefore, it is justified to use Eq. 29 to calculate the suspended-load transport rate, which is analytically modelled here. In fact, it also facilitates the calculation avoiding the numerical computation of integrals (Guo & Julien, 2004).

9. Conclusions

A critical analysis involving different velocity laws, namely, log-, log wake-, stratified log-, and power-law, has been carried out. The log-law tends to overestimate both the velocity and the sediment concentration data, while log wake-law underestimates. In contrast, the log-wake law produces somewhat better results. The log- and stratified log-law make the upper and lower bounds of the concentration data for a given value of Rouse number. On the other hand, as far as the agreement with the experimental data is concerned, it is found that the power-law is a good choice for predicting velocity and suspended sediment concentration. A new power-law model for concentration distributions is therefore proposed here, based on the power-law for velocity distribution given by Castro-Orgaz & Dey (2011).

Subsequently, the proposed power-law model for concentration has been tested using the same experimental data. Following a trial-and-error method, the distributions of wake function have been calculated. The proposed wake function performs quite well in the outer-layer of flow, but it is somewhat not highly satisfactory in the inner-layer of

flow. Nonetheless, it is important to point out that this discrepancy has a little effect on the computation of sediment concentration distributions. The exponent of wake function varies in between 1 and 2, with a typical average value of 1.5. Subsequently, an analytical tool to perform the suspended-load transport rate is presented, which facilitates the calculation in comparison to the classical approximations involving the Einstein's integrals. Therefore, the strength of the new formula lies in the fact that, in contrast to classical approaches, it leads to analytical form for suspended-load transport.

The wake function can be further improved as a future scope, especially for the suspended sediment load with low concentrations, in which the wake function for the proposed model shows some departure from the experimental data. In addition, the inclusion of the nonuniversal von Kármán constant in sediment-laden flows remains unexplored (Gaudio *et al.*, 2010; Gaudio & Dey, 2012).

10. Notation

c^+ = nondimensional sediment concentration (= C/C_a);

C = time-averaged sediment concentration;

C_a = sediment concentration at reference level;

d_{50} = median size of sediment;

g = gravitational acceleration;

h = flow depth;

q_s = suspended-load transport rate;

S = friction slope;

t = time;

u = time-averaged streamwise velocity along x-direction;

u_* = shear velocity;

u^+ = nondimensional streamwise velocity (= u/u_*);

U^+ = nondimensional maximum streamwise velocity (= U_{max}/u_*);

U_{max} = maximum time-averaged streamwise velocity;

v = time-averaged transverse velocity along y-direction;

w = time-averaged vertical velocity along z-direction;

w_s = terminal fall velocity of sediment particles;

W = wake function;

x, y, z = Cartesian coordinates or streamwise, transverse, and vertical distances, respectively;

z_a = reference level;

Z = Rouse number;

α = stratification parameter;

β = proportionality factor;

δ = boundary layer thickness;

Δ = submerged relative density;

ε_m = molecular diffusivity;

ε_s = solid or sediment diffusivity;

ε_t = turbulent diffusivity;

Φ_s = suspended-load transport intensity;

Γ = exponent;

η = nondimensional vertical distance (= z/h);

η_a = nondimensional reference level (= z_a/h);

κ = von Kármán constant;

Π = Cole's wake parameter;

Π_c = exponent of wake function;

ρ = mass density of fluid;

τ = Reynolds shear stress;

τ_0 = bed shear stress;

υ = kinematic viscosity of fluid;

Ψ = η_a^{Γ}.

11. References

Absi, R. (2011) An ordinary differential equation for velocity distribution and dip-phenomenon in open channel flows. *J. Hydraul. Res.*, 49 (1), 82–89.

ASCE Task Force. (1963) Friction factor in open channels. *J. Hydraul. Div.*, 89 (2), 97–143.

Bagnold, R.A. (1966) An approach to the sediment transport problem from general physics. *Geological Survey Professional Paper 422-I*, pp. 231–291. United States Geological Survey, Washington, DC, The United States of America.

Boogerd, P., Scarlett, B. and Brouwer, R. (2001) Recent modelling of sedimentation of suspended particles: a survey. *Irrig. Drain.*, 50 (2), 109–128.

Bose, S.K. and Dey, S. (2009) Suspended load in flows on erodible bed. *Int. J. Sediment Res.*, 24 (3), 315–324.

Bose, S.K. and Dey, S. (2013) Sediment entrainment probability and threshold of sediment suspension: Exponential-based approach. *J. Hydraul. Eng.*, 139 (10), 1099–1106.

Camenen, B. and van Bang, D.P. (2011) Modelling the settling of suspended sediments for concentrations close to the gelling concentration. *Continental Shelf Res.*, 31 (10), S106–S116.

Cao, Z., Egashira, S. and Carling, P.A. (2003) Role of suspended-sediment particle size in modifying velocity profiles in open channel flows. *Water Resour. Res.*, 39 (2), DOI: 10.1029/2001WR000934.

Carnacina, I. and Larrarte, F. (2014) Coupling acoustic devices for monitoring combined sewer network sediment deposits. *Water Sci. Technol.*, 69 (8), 1653–1660.

Castro-Orgaz, O. and Dey, S. (2011) Power-law velocity profile in turbulent boundary layers: An integral Reynolds-number dependent solution. *Acta Geophysica*, 59 (5), 993–1012.

Chauchat, J., Guillou, S., Van Bang, D.P. and Nguyen, K.D. (2013) Modelling sedimentation-consolidation in the framework of a one-dimensional two-phase flow model. *J. Hydraul. Res.*, 51 (3), 293–305.

Cheng, N.-S. and Chiew, Y.-M. (1999) Analysis of initiation of sediment suspension from bed load. *J. Hydraul. Eng.*, 125 (8), 855–861.

Coleman, N.L. (1986) Effects of suspended sediment on the open-channel velocity distribution. *Water Resour. Res.*, 22 (10), 1377–1384.

Dey, S. (2014) *Fluvial Hydrodynamics: Hydrodynamic and Sediment Transport Phenomena.* Springer, Berlin, Germany.

Dutta, S., Cantero, M.I. and García, M.H. (2014) Effect of self-stratification on sediment diffusivity in channel flows and boundary layers: a study using direct numerical simulations. *Earth Surface Dynamics*, 2 (2), 419–431.

García, M.H. (2008) Sediment transport and morphodynamics. In: *Sedimentation Engineering: Processes, Measurements, Modeling, and Practice* (Ed. M.H. García), pp. 21–163. Manuals and Reports on Engineering Practice Number 110, American Society of Civil Engineers, Reston, VA, The United States of America.

Gaudio, R. and Dey, S. (2012) Evidence of non-universality of von Kármán's κ. In: *Experimental and Computational Solutions of Hydraulic Problems* (Ed. P. Rowinski), pp. 71–83. Springer, Heidelberg, Germany.

Gaudio, R., Miglio, A. and Dey, S. (2010) Non-universality of von Kármán's κ in fluvial streams. *J. Hydraul. Res.*, 48 (5), 658–663.

Ghoshal, K. and Kundu, S. (2013) Influence of secondary current on vertical concentration distribution in an open channel flow. *ISH J. Hydraul. Eng.*, 19 (2), 88–96.

Guo, J. and Julien, P.Y. (2004) Efficient algorithm for computing Einstein integrals. *J. Hydraul. Eng.*, 130 (12), 1198–1201.

Guo, J. and Julien, P.Y. (2008) Application of the modified log-wake law in open-channels. *J. Appl. Fluid Mech.*, 1 (2), 17–23.

Guo, J., Mohebbi, A., Zhai, Y. and Clark, S.P. (2015) Turbulent velocity distribution with dip phenomenon in conic open channels. *J. Hydraul. Res.*, 53 (1), 73–82.

Hunt, J.N. (1954) The turbulent transport of suspended sediment in open channels. *Proc. Roy. Soc. London A*, 224 (1158), 322–335.

Kundu, S. and Ghoshal, K. (2014) Effects of secondary current and stratification on suspension concentration in an open channel flow. *Environ. Fluid Mech.*, 14 (6), 1357–1380.

Lamb, M.P., Dietrich, W.E. and Sklar, L.S. (2008) A model for fluvial bedrock incision by impacting suspended and bed load sediment. *J. Geophys. Res. Earth Surface*, 113 (F3), DOI: 10.1029/2007JF000915.

Lane, E.W. and Kalinske, A.A. (1941) Engineering calculations of suspended sediment. *Trans. Am. Geophys. Union*, 20 (3), 603–607.

Larrarte, F. (2015) Velocity and suspended solids distributions in an oval-shaped channel with a side bank. *Urban Water J.*, 12 (2), 165–173.

Lassabatere, L., Pu, J.H., Bonakdari, H., Joannis, C. and Larrarte, F. (2012) Velocity distribution in open channel flows: Analytical approach for the outer region. *J. Hydraul. Eng.*, 139 (1), 37–43.

Leeder, M.R. (1983) On the dynamics of sediment suspension by residual Reynolds stresses-confirmation of Bagnold's theory. *Sedimentology*, 30 (4), 485–491.

Lucas-Aiguier, E., Chebbo, G., Bertrand-Krajewski, J.-L., Gagné, B. and Hedges, P. (1998) Analysis of the methods for determining the settling characteristics of sewage and stormwater solids. *Water Sci. Tech.*, 37 (1), 53–60.

Lyn, D.A. (1986) Turbulence and turbulent transport in sediment-laden open-channel flows. PhD Thesis, California Institute of Technology, Padsadena, California, The United States of America.

Lyn, D.A. (2000) Regression residuals and mean profiles in uniform open-channel flows. *J. Hydraul. Eng.*, 126 (1), 24–32.

Mateos, L. and Giráldez, J.V. (2005) Suspended load and bed load in irrigation furrows. *Catena*, 64 (2–3), 232–246.

Mazumder, B.S. (1994) Grain size distribution in suspension from bed materials. *Sedimentology*, 41 (2), 271–277.

Montes, J.S. (1973) *Interaction of two-dimensional turbulent flow with suspended particles*. PhD Thesis, Massachusetts Institute of Technology, Cambridge, The United States of America.

Richardson, J.F. and Zaki, W.N. (1954) Sedimentation and fluidization: Part I. *Trans. Inst. Chem. Eng.*, 32 (1), S82–S100.

Rouse, H. (1937) Modern conceptions of the mechanics or fluid turbulence. *Trans. Am. Soc. Civ. Eng.*, 102 (1), 463–505.

Sengupta, S. (1975) Size-sorting during suspension transportation - lognormality and other characteristics. *Sedimentology*, 22 (2), 257–273.

Sengupta, S. (1979) Grain-size distribution of suspended load in relation to bed materials and flow velocity. *Sedimentology*, 26 (1), 63–82.

van Rijn, L.C. (1984) Sediment transport, part II: suspended load transport. *J. Hydraul. Eng.*, 110 (11), 1613–1641.

Velikanov, M.A. (1954) *Principle of the Gravitational Theory of the Movement of Sediments*. Academy of Sciences Bulletin, Number 4, Geophysical Series, Russia.

Velikanov, M.A. (1955) *Dynamics of Alluvial Stream*. State Publishing House of Theoretical and Technical Literature, Volume 2, Russia.

Wright, S. and Parker, G. (2004) Flow resistance and suspended load in sand-bed rivers: Simplified stratification model. *J. Hydraul. Eng.*, 130 (8), 796–805.

Wu, W., Wang, S.S.Y. and Jia, Y. (2000) Nonuniform sediment transport in alluvial rivers. *J. Hydraul. Res.*, 38 (6), 427–434.

Yang, S.-Q., Tan, S.-K. and Lim, S.-Y. (2004) Velocity distribution and dip-phenomenon in smooth uniform open channel flows. *J. Hydraul. Eng.*, 130 (12), 1179–1186.

Yoon, J.-I., Sung, J. and Lee, M.H. (2012) Velocity profiles and friction coefficients in circular open channels. *J. Hydraul. Res.*, 50 (3), 304–311.

Appendix V

Hydrodynamic analysis of fully-developed turbidity currents over plane beds based on self-preserving velocity and concentration distributions

Francisco Nicolás Cantero-Chinchilla[1], Subhasish Dey[2], Oscar Castro-Orgaz[1], Sk Zeeshan Ali[2]

Journal of Geophysical Research – Earth Surface, 120(10), 2176–2199. doi: 10.1002/2015JF003685. Impact factor (JCR 2014): 3.426 / Q1 (19/175 Geosciences, Multidisciplinary)

Abstract

This paper presents a hydrodynamic analysis for the fully developed turbidity currents over a plane bed stemming from the classical three-equation model (depth-averaged fluid continuity, sediment continuity, and fluid momentum equations). The streamwise velocity and the concentration distributions preserve self-similarity characteristics and are expressed as single functions of vertical distance over the turbidity current layer. Using the experimental data of turbidity and salinity currents, the undetermined coefficients and exponents are approximated. The proposed relationships for velocity and concentration distributions exhibit self-preserving characteristic for turbidity currents. The depth-averaged velocity, momentum, and energy coefficients are thus obtained using the proposed expression for velocity law. Also, from the expressions for velocity and concentration, the turbulent diffusivity and the Reynolds shear stress distributions are deduced with the aid of the diffusion equation of sediment concentration and the Boussinesq hypothesis. The generalized equation of unsteady-nonuniform turbidity current is developed by using the velocity and concentration distributions in the moments of the integral scales over the turbidity current layer. Then, the equation is applied to analyze the gradually-varied turbidity currents considering closure relationships for boundary interaction and shear velocity. The streamwise variations of current depth, velocity, concentration, reduced sediment flux, and

[1] Dept. of Agronomy, Univ. of Cordoba, Campus Rabanales, Edif. Da Vinci, Cra Madrid Km 396, 14071 Cordoba, Spain
[2] Dept. of Civil Engineering, Indian Institute of Technology, Kharagpur 721302, West Bengal, India

Richardson number are presented. Further, the self-accelerating and depositional characteristics of turbidity currents including the transitional feature from erosional to depositional modes are addressed. The effects of the streamwise bed slope are also accounted for in the mathematical derivations. The results obtained from the present model are compared with those from the classical model.

1. Introduction

Turbidity currents are gravity currents, which are often referred to as inclined plumes or underflows, consisting of a water-sediment mixture flowing over a sloping bed. In nature, high density turbidity currents are able to carry such amount of suspended sediment that their erosive power usually produces remarkable geological reforms, e.g., submarine canyons [*Inman et al.*, 1976; *Fukushima et al.*, 1985; *Mastbergen and Van Den Berg*, 2003; *Sumner and Paull*, 2014]. Inland, man-made mining tailings, earthquakes or heavy storms, among others, can often originate turbidity currents with huge sediment mass, such as, rocks or debris as underwater landslide to produce sediment-laden flows [*Normark and Dickson*, 1976; *Piper et al.*, 1999]. It is conceptually helpful to contemplate turbidity currents as a flow constituted by two separate parts, current-head (that is the current front) and current-body [*Stacey and Bowen*, 1988]. High suspended sediment concentration in turbidity currents produces a pressure gradient downslope arising from the density difference between the current-head and the ambient water just in front of it and thus providing a driving force. The water-sediment mixture forming turbidity current, as a layer, is driven by the downslope gravitational component acting on the denser water-sediment mixture. Although it is in principle the same hydrodynamics as that driving the head, the buoyancy contrast between the turbidity current and the ambient water leads to a system where the downslope gradients of flow and sediment transport parameters may be small. The sediment laden flow however generates adequate turbulence to hold the sediment particles in suspension. Uniform or gradually-varied turbidity currents containing very fine sediments over a rigid bed were investigated by several investigators [*Bonnefille and Goddet*, 1959; *Stefan*, 1973; *Ashida and Egashira*, 1975].

Depending on the flow conditions, turbidity currents are distinguished as erosional or depositional underwater sediment-laden flows [*Akiyama and Stefan*, 1985]. The interaction of the turbidity current with the ambient flow can be envisaged as an entrainment of water from the ambient flow to the turbidity current through the interface

between them. In addition, in erodible beds, the sediment entrainment and deposition occur at the same time due to the interaction of the turbidity current with the bed-layer. Under high erodible conditions, the sediment entrainment rate from the bed toward the turbidity current becomes sufficiently intense so that an inrushing of ambient water toward the turbidity current layer takes place to balance the mass and momentum fluxes. On the other hand, the entrainment of ambient water into the turbidity current gets reduced if sediment deposition occurs at the bed. In turn, the turbidity current becomes stagnant when there is no sediment transport. In other words, the thickness of the turbidity current layer is dependent on the ability of the flow to carry the suspended sediment particles. However, turbidity currents can be considered as a self-generated current in which sediment particles are suspended by the turbulence.

Less erosive gravity currents can be simulated in the laboratory environment by creating a salinity or temperature gradient. *Stacey and Bowen* [1988] stated that the competence of the flow to transport and suspend the sediment depends on the terminal fall velocity of sediment particles. In the limit, it is believed that for larger sediment particles, steady flow is not practically feasible. Salinity currents are good examples of containing sediments with a low terminal fall velocity. *Sequeiros et al.* [2010] conducted a large number of experiments on the velocity and the excess density distributions of saline and turbidity underflows. They observed the development of bedforms with time depending on the flow conditions. They also identified an upward shift of the reference level (that is, the demarcation level between bed- and suspended-load [*Dey*, 2014]) due to the change in bed roughness, as the bedforms grow with time. As a result, the velocity and concentration distributions are modified. *Nourmohammadi et al*. [2011] reported a study on the vertical distribution of gravity currents over a non-erodible bed. They observed a similarity in velocity and concentration distributions. Although the vertical distribution of velocity in turbidity currents seems not to be significantly affected by the suspended particle size [*Parker et al.*, 1987; *Altinakar et al.*, 1996], it is somehow interesting to analyze the effects of the terminal fall velocity on suspended sediment concentration.

In fact, the governing equations of turbidity current are similar to those used in sediment-laden flows. By applying the conservation laws of sediment-laden flows, the governing equations of turbidity current are obtained. *Akiyama and Stefan* [1985] introduced an analytical model based on the governing equations of turbidity current

along with the entrainment and the depositional fluxes. The model, which was depth-averaged into the one-dimensional form, constituted an extension of the formulation earlier reported by *Ellison and Turner* [1959]. Besides, the turbulent energy equation was accounted for reducing the formula to Bagnold's auto-suspension concept [*Bagnold*, 1962]. However, their model was not verified due to non-availability of the experimental data. *Parker et al*. [1986] presented a four-equation model, in which the mean turbulent kinetic energy (TKE) was considered. By considering the classical three-equation model (depth-averaged fluid continuity, sediment continuity, and fluid momentum equations [*Lai et al*., 2015]), as an extension from *Ellison and Turner*'s [1959] formulation, *Parker et al*. [1986] pointed out the importance of accurately predicting the bed sediment entrainment. *Stacey and Bowen* [1988] developed a simple numerical model (three-equation) that matched well with the experimental data of velocity and concentration, although they initially failed to obtain the adequate solutions for the analytical model. Further, *Pratson et al.* [2000] solved the four-equation model developed by *Parker et al.* [1986] using numerical techniques. However, *Hu et al*. [2015] found that the three-equation model does not fail to simulate self-accelerating turbidity currents, rendering unclear the need of using the four-equation model. *Felix* [2001] proposed a two-dimensional turbulence model to address the development of turbidity current. In the same line, the large eddy simulation along with direct numerical simulation was also applied to simulate the turbidity currents [*Mahdinia et al*., 2010; *Dutta et al*., 2012]. On the other hand, as a new trend in simulation of gravity currents, the application of the thermal lattice Boltzmann method was also reported [*Lizhong et al*., 2011; *Prestininzi et al*., 2013]. However, in derivation of the full depth-averaged models, similarity solutions were sought for the convenience [*Parker et al.*, 1986], assuming the velocity, concentration, and TKE distributions to preserve similarity.

Similarity approximation for the vertical distributions of the main flow characteristics are likely well justified in turbidity currents. Besides *Parker et al.* [1986] and *Stacey and Bowen* [1988], *Altinakar et al.* [1996] highlighted the self-similarity in velocity and concentration distributions. In this regard, *Stacey and Bowen* [1988] previously argued that the decoupling of the concentration from the temporal evolution of velocity is an inappropriate concept. Interestingly, their results suggested the self-preserving characteristic distributions for the flow characteristics. A turbidity current, as stated by *Altinakar et al.* [1996], can be viewed, as far as the flow structure is

concerned, analogous to a wall-jet flow. Accordingly, *Altinakar et al.* [1996] assumed a power-law for the velocity distribution and a linear-law for the concentration distribution for the inner-layer of flow (wall shear layer). For the outer-layer of flow, they assumed the near-Gaussian relationships for the velocity and concentration distributions. These scaling laws gave a satisfactory agreement with their experimental data. It means that they considered different scaling laws for the inner- and outer-layer of flow. However, little attention has so far been paid to obtain the generalized scaling laws (represented by single functions) for the velocity and concentration distributions over the entire turbidity current layer. These generalized scaling laws, which should comply with the wide range of experimental data, are therefore a long due.

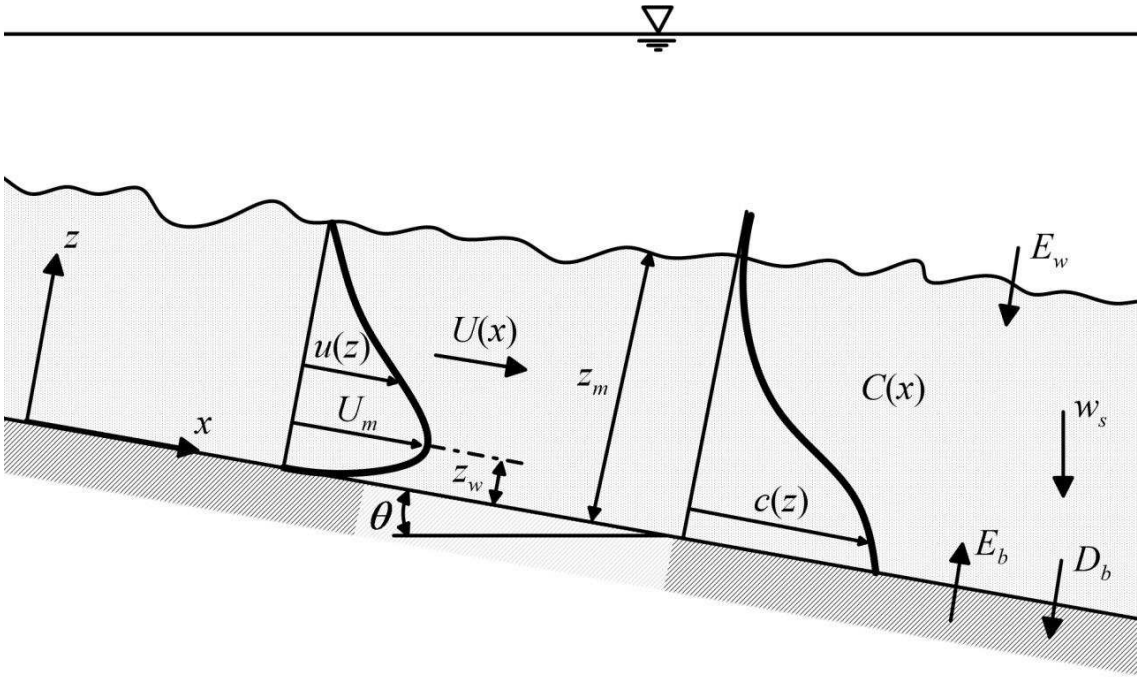

Fig. 1. Definition sketch of a turbidity current on a sloping bed.

The objective of this study is to initially revisit the vertical distributions of velocity and concentration in turbidity currents to obtain single similarity functions (continuous over the entire layer) for them. Appropriate scaling for the similarity functions could bring the available experimental data of velocity and suspended sediment concentration for turbidity and salinity currents to single bands. This analysis thus provides us the self-preserving type relationships for the velocity and concentration distributions in turbidity currents. Using the developed similarity functions for the velocity and concentration, the Reynolds shear stress and turbulent diffusivity distributions are derived. Further, to enhance the mathematical model of the turbidity current according to the velocity and concentration distributions, three-equation model (depth-averaged

fluid continuity, sediment continuity, and fluid momentum equations) is analyzed for gradually-varied flow formulations using appropriate closure relationships.

2. Introduction

The problem of turbidity current is usually treated as a problem of incompressible turbulent flow [*Graf and Altinakar*, 1998]. When the fluid mass is sufficiently wide, the width has a minimal influence on the flow, and thus the motion of the turbidity current can be approximated as a two-dimensional problem (x- and z-direction) (Figure 1) [*Parker et al.*, 1986; *Akiyama and Stefan*, 1985]. Subsequently, the general depth-averaged equations of the fluid mass, sediment mass, and turbidity current momentum are as follows [*Parker et al.*, 1986]:

$$\frac{\partial z_m}{\partial t} + \frac{\partial}{\partial x}\int_0^\infty u\,\mathrm{d}z = -w_h\,, \tag{97}$$

$$\frac{\partial}{\partial t}\int_0^\infty c\,\mathrm{d}z + \frac{\partial}{\partial x}\int_0^\infty uc\,\mathrm{d}z = -w_s c\big|_b + \overline{c'w'}\big|_b\,, \tag{98}$$

$$\frac{\partial}{\partial t}\int_0^\infty u\,\mathrm{d}z + \frac{\partial}{\partial x}\int_0^\infty u^2\,\mathrm{d}z = -\frac{1}{2}\Delta_s g\frac{\partial}{\partial x}\int_0^\infty\int_z^\infty c\,\mathrm{d}z\mathrm{d}z\cos\theta + \Delta_s g\int_0^\infty c\,\mathrm{d}z\sin\theta - u_{*b}^2\,, \tag{99}$$

where z_m is the vertical distance where velocity vanishes (u = 0) into the turbidity current, considered to be the turbidity current depth, $u(z)$ is the streamwise velocity at a vertical distance z, w_h is the vertical velocity component at the top edge of the current, w_s is the terminal fall velocity of suspended sediment particles, $c(z)$ is the suspended sediment concentration velocity at z, $\overline{c'w'}$ is the Reynolds flux of suspended particles, Δ_s is the submerged relative density [= $(\rho_s - \rho_a)/\rho_a$], ρ_s is the mass density of sediment particles, ρ_a is the mass density of ambient fluid, g is the gravitational acceleration, θ is the streamwise bed slope, u_{*b} is the shear velocity, and subscript b refers to bed. In Figure 1, the depth-averaged sediment concentration in turbidity current is given by $C(x)$. It may be noted that in four-equation model [*Parker et al.*, 1986], the TKE budget is included as the fourth equation, which is briefly discussed in Appendix A.

In equations (1)–(3), the boundary-layer approximations for a two-dimensional turbidity current are considered. Henceforth the turbidity current is considered as a fully turbulent flow. Thereby, only the viscous dissipation due to turbulence remains, neglecting other viscous terms. Also, the vertical-flux terms appearing in the right hand

side of the equation (2) are evaluated somewhat above the lower boundary to avoid singular solutions related to the vanishing molecular diffusivity. Equation (3) accounts for the non-hydrostatic treatment of turbidity currents, decomposing the actual pressure into a component due to the ambient fluid and an additional component due to the presence of sediment particles. Thus, the terms in the right hand side of equation (3) are regarded as the pressure force of the turbidity current.

The integrals in equations (1)–(3), which define the depth-averaged quantities of the flow, are known as the moments of the integral scales [*Ellison and Turner*, 1959; *Turner*, 1973]. They are

$$I_1 = \int_0^\infty u\mathrm{d}z\ ,\ I_2 = \int_0^\infty u^2\mathrm{d}z\ , \tag{100}$$

$$I_3 = \int_0^\infty c\mathrm{d}z\ ,\ I_4 = \int_0^\infty uc\mathrm{d}z\ ,\ I_5 = \int_0^\infty \int_z^\infty c\mathrm{d}z\mathrm{d}z\ . \tag{101}$$

Equations (1)–(3) can be expressed by means of interaction processes that occur at the interface of the layers (turbidity current and ambient fluid layers). The static pressure in the ambient still fluid is greater than the actual pressure in the turbidity current. According to the Bernoulli equation, a negative pressure gradient in the upper-layer (ambient fluid layer) results in an inward movement of ambient fluid into the turbidity current through the interface. Therefore, the entrainment velocity is assumed to be proportional to the velocity of the turbidity current [*Turner*, 1973], $-w_h = E_w U$, where E_w is the entrainment coefficient of ambient fluid, and $U(x)$ is the depth-averaged velocity of the turbidity current. Besides, according to *Parker et al.* [1987], the first and second terms in the right hand side of equation (2) can be identified as the erosion rate E_b and deposition D_b rate of sediment at the bed (Figure 1). Therefore,

$$w_s c\big|_b = D_b\ , \tag{102}$$

$$\overline{c'w'}\Big|_b = E_b\ . \tag{103}$$

Thus, the three-equation model is finally written as follows:

$$\frac{\partial z_m}{\partial t} + \frac{\partial I_1}{\partial x} = E_w U\ , \tag{104}$$

$$\frac{\partial I_3}{\partial t} + \frac{\partial I_4}{\partial x} = E_b - D_b \,, \tag{105}$$

$$\frac{\partial I_1}{\partial t} + \frac{\partial I_2}{\partial x} = -\frac{1}{2}\Delta_s g \frac{\partial I_5}{\partial x}\cos\theta + \Delta_s g I_3 \sin\theta - u_{*b}^2 \,. \tag{106}$$

The streamwise bed slope $\sin\theta$ cannot be ignored, since a turbidity current is, by nature, a sloping flow inside a greater mass of fluid [*Graf and Altinakar*, 1998], as shown in Figure 1. Accordingly, $\cos\theta$ cannot be simplified as unity.

Note that following *Graf* [1976] and *Parker et al*. [1986] the erosion and deposition rates E_b and D_b appear in the mass conservation for the suspended sediment phase, equation (9), whereas the mass conservation equation for the water phase is free from exchange terms. These terms appear as well in the mixture mass conservation equation of a turbidity current [*Hu et al*., 2012].

3. Velocity Distribution

In a fully developed state, the velocity distribution in turbidity current is almost similar to that in submerged plane wall-jet. A submerged plane wall-jet is described as a jet of fluid that impinges tangentially (or at an angle) on a solid wall surrounded by the same fluid (stationary or moving) progressing along the wall [*Dey et al*., 2010]. For a turbidity current, on one side (in the inner-layer), the current is confined to the bed, while on the other side (in the outer-layer), it is bounded by the stationary ambient fluid (Figure 1). The boundary conditions for the velocity distribution in turbidity current are such that the velocity vanishes at the bed and at the interface between the turbidity current and the ambient fluid. Thus, the velocity distribution attains a maximum (peak velocity) at the extremity of the inner-layer, that is, the junction of the inner- and outer-layer of the current. Below the maximum velocity level (in the inner-layer), the flow is featured by a boundary layer flow, while above the maximum velocity level (in the outer-layer), the flow is structurally similar to a free jet. Therefore, the turbidity currents are characterized by an inner shear layer influenced by the bed and an outer-layer of the self-similar type of a shear flow [*Parker et al*., 1987; *Stacey and Bowen*, 1988; *Altinakar et al.*, 1996; *Shringarpure et al.*, 2012]. For the similarity in velocity distributions, the nondimensional variables introduced are $\hat{u} = u/U_m$ and $\eta = z/z_m$, where U_m is the maximum velocity. Previous studies primarily assumed two separate velocity distributions for the inner- and outer-layer of turbidity currents. However, in

this study, a single velocity distribution over the entire range of the inner- and outer-layer is assumed in the following form:

$$\hat{u}(\eta) = \sigma \eta^{\xi} (1-\eta)^{\chi}, \tag{107}$$

where σ is a coefficient and ξ and χ are the exponents. They are the unknown parameters to be determined from the experimental data. It is pertinent to mention that the nondimensional velocity distribution in equation (11) is considered as a combination of a power function η^{ξ} and a wake function $(1 - \eta)^{\chi}$ in order to preserve the boundary conditions, namely, $\hat{u}(\eta = 0) = 0$ and $\hat{u}(\eta = 1) = 0$. Besides, the product of those functions in equation (11) corresponds to the study of *Islam and Imran* [2010]. Equation (11) shows that the velocity distribution in the inner-layer is analogous to a boundary layer flow, while that in the outer-layer is similar to a free jet. The maximum velocity U_m occurs at a location $z = z_w$. Introducing $\eta_w = z_w/z_m$ at the occurrence of the maximum velocity, another boundary condition $_{u^*}(\eta = \eta_w) = 1$ is satisfied at the extremity of the inner-layer. Therefore, from equation (11), one obtains

$$\sigma = \eta_w^{-\xi} (1-\eta_w)^{-\chi}. \tag{108}$$

The velocity gradient at $z = z_w$ vanishes due to the occurrence of maximum velocity at that level, that is $\mathrm{d}\hat{u}/\mathrm{d}\eta\ (\eta = \eta_w) = 0$. Applying this boundary condition, equation (11) produces

$$\eta_w = \frac{\xi}{\xi + \chi}. \tag{109}$$

Substituting equation (13) into equation (12) yields

$$\sigma = \frac{(\xi + \chi)^{\xi+\chi}}{\xi^{\xi} \chi^{\chi}}. \tag{110}$$

Equation (14) shows the dependency of the coefficient σ on the exponents ξ and χ. The exponents ξ and χ are to be determined using the experimental data.

Figure 2 displays the computed velocity distributions obtained from equation (11) and using two equations given by *Altinakar et al.* [1996]. The experimental data plots of turbidity and salinity currents obtained from *Parker et al.* [1987], *García* [1993], *Altinakar et al.* [1996], *Sequeiros et al.* [2010], *Islam and Imran* [2010], and *Nourmohammadi et al.* [2011] are overlapped on the computed curves in Figure 2 for

comparison. It is found that the values ξ = 0.6 and χ = 2.2 ensure a satisfactory agreement of equation (11) with the experimental data. Therefore, from equations (14), one obtains σ = 4.28. The standard deviation, standard error, and correlation coefficient for Figure 2 are 0.333, 0.011, and 0.930, respectively, which provide a quantitative understanding on the data scatter from equation (11). The occurrence of the maximum velocity determined from equation (13) is η_w = 0.214. In Figure 2, the experimental data of runs 6–10, 12, 13, 17, 20, 23, and 24 from *Parker et al*. [1987] are shown. From *García* [1993], run DAPER6 is also selected for the peak velocity data in subcritical and supercritical flow conditions. Three sets of experimental data are taken from *Altinakar et al.* [1996]. Among them, two sets belong to the turbidity currents with sediment sizes d = 0.047 and 0.026 mm, where d is the median size of sediment particles, and the third set belongs to the salinity current. From *Sequeiros et al.* [2010], the experimental data for runs 2, 10, 16, 23, 31, 36–38, 40, and 41, in which no bedforms occurred, are considered. The experimental velocity data of sections 1-12 for salinity and turbidity currents reported by *Islam and Imran* [2010] are extracted. Besides, from *Nourmohammadi et al.* [2011], the experimental data for run 3 at streamwise distances of 2.5 and 3.5 m, run 10 at 4.5 m and runs 7 and 8 at 3.5 and 4.5 m, respectively, from the flume inlet are used. Finally, the computed velocity distribution of *Altinakar et al.* [1996] over predicts most of the experimental data (Figure 2).

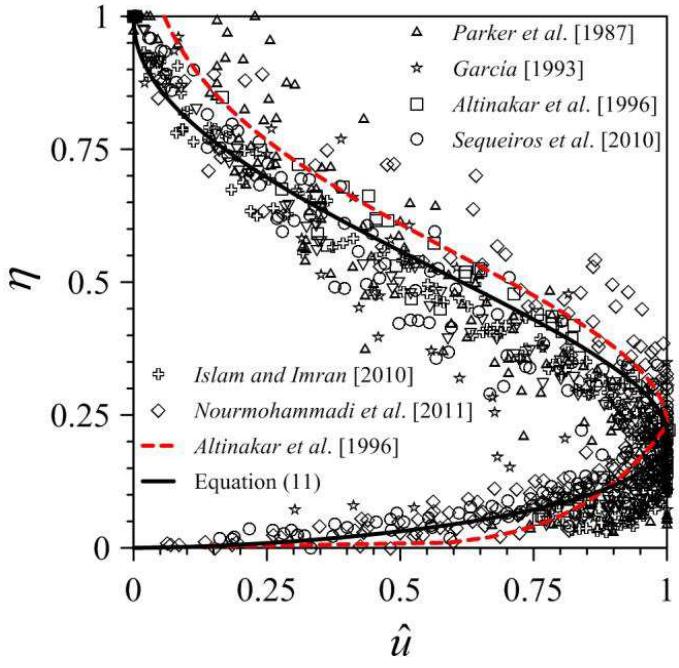

Fig. 2. Computed velocity distribution $\hat{u}$ (η) obtained from equation (11) showing the comparison with the velocity distribution obtained using two equations given by *Altinakar et al.* [1996] and the experimental data of different investigations.

From Figure 2, it is observed that the following empirical relationship between ξ and χ shows a good agreement between the fitted velocity distribution and the experimental data:

$$\chi \approx 1+2\xi\,. \tag{111}$$

Therefore, using equations (14) and (15), equation (11) takes the following form:

$$\hat{u} = \frac{(1+3\xi)^{1+3\xi}}{\xi^{\xi}(1+2\xi)^{1+2\xi}}\eta^{\xi}(1-\eta)^{1+2\xi}\,. \tag{112}$$

Equation (16) thus provides the velocity distribution in turbidity currents with a single free parameter ξ, which was empirically determined as 0.6. This relationship for the velocity distribution is in fact of self-preserving type for turbidity currents.

The depth-averaged velocity U in nondimensional form is

$$\hat{U} = \int_0^1 \hat{u}\,\mathrm{d}\eta\,, \tag{113}$$

where $\hat{U} = U/U_m$. Inserting equation (16) into equation (17) yields

$$\hat{U} = \frac{(1+3\xi)^{1+3\xi}}{\xi^{\xi}(1+2\xi)^{1+3\xi}}\cdot\frac{\Gamma(1+\xi)\Gamma(2+2\xi)}{\Gamma(3+3\xi)}\,, \tag{114}$$

where $\Gamma(s)$ is the Euler gamma function defined as

$$\Gamma(s) = \int_0^{\infty} y^{s-1}\exp(-y)\mathrm{d}y\,. \tag{115}$$

Since the velocity distribution is obtained from equation (16), typically the flow parameters of interest, such as momentum (Boussinesq) coefficient, energy (Coriolis) coefficient, and the moments of the integral scales defined in equation (4), are determined.

The momentum (Boussinesq) coefficient β is defined as

$$\beta = \frac{\int_0^{z_m} u^2\mathrm{d}z}{U^2 z_m} = \frac{\int_0^1 \hat{u}^2\mathrm{d}\eta}{\hat{U}^2}\,. \tag{116}$$

Inserting equations (16) and (18) into Eq. (20) yields

$$\beta = \frac{1}{\hat{U}^2} \cdot \frac{(1+3\xi)^{2+6\xi}}{\xi^{2\xi}(1+2\xi)^{2+4\xi}} \cdot \frac{\Gamma(1+2\xi)\Gamma(3+4\xi)}{\Gamma(4+6\xi)}. \tag{117}$$

The energy (Coriolis) coefficient α is defined as

$$\alpha = \frac{\int_0^{z_m} u^3 \mathrm{d}z}{U^3 z_m} = \frac{\int_0^1 \hat{u}^3 \mathrm{d}\eta}{\hat{U}^3}. \tag{118}$$

Inserting equations (16) and (18) into equation (22) yields

$$\alpha = \frac{1}{\hat{U}^3} \cdot \frac{(1+3\xi)^{3+9\xi}}{\xi^{3\xi}(1+2\xi)^{3+6\xi}} \cdot \frac{\Gamma(1+3\xi)\Gamma(4+6\xi)}{\Gamma(5+9\xi)}. \tag{119}$$

With ξ = 0.6, the following parameters are obtained from equations (18), (21), and (23):

$$\hat{U} = 0.52\,,\ \beta = 1.465\,,\ \alpha = 2.366\,. \tag{120}$$

The moments of the integral scales in equation (4) are determined as

$$I_1 = \int_0^{\infty} u \mathrm{d}z = \int_0^{z_m} u \mathrm{d}z = 0.52 U_m z_m, \tag{121}$$

$$I_2 = \int_0^{\infty} u^2 \mathrm{d}z = \int_0^{z_m} u^2 \mathrm{d}z = 0.396 U_m^2 z_m\,. \tag{122}$$

For details of integral equations (25) and (26), see Appendix B.

4. Concentration Distribution

In accordance with the mechanism of suspended sediment motion, the turbidity current can be considered as a self-generated current in which sediment particles are suspended by the turbulence. The transport of suspended sediment particles in turbulent flow takes place due to the advection and diffusion processes in the ambient fluid. The governing equation of the diffusion of suspended sediment concentration shows a remarkable dependency of the concentration distribution on the velocity distribution [*Dey*, 2014]. The concentration distribution in turbidity current is therefore affected by the velocity distribution, allowing two distinctive zones. Above the maximum velocity level ($z > z_w$), the concentration distribution asymptotically vanishes ($c \rightarrow 0$) just above z_m, and beneath the maximum velocity level ($z \leq z_w$), the concentration distribution follows a

classical boundary layer approximation. For the similarity in concentration distributions, the nondimensional variable is introduced as $\hat{c} = c/C_m$, where C_m is the concentration at $\eta = \eta_w$. Unlike the previous studies which considered two separate expressions for concentration distributions in the inner- and outer-layer of turbidity currents [*Altinakar et al.*, 1996], a single concentration distribution over the entire range of the inner- and outer-layer is assumed here in the following form:

$$\hat{c}(\eta) = \lambda \exp(-\phi \eta^{\zeta}), \tag{123}$$

where λ, ϕ, and ζ are the unknown parameters. Equation (27) shows that the concentration has a decreasing trend with the vertical distance. It also provides a finite value of concentration c_0 at the bed (η = 0). Importantly, equation (27) does not consider any reference level for the concentration distribution in particular. Applying the boundary condition, $\hat{c}(\eta = \eta_w) = 1$ to equation (27) yields

$$\lambda = \exp(\phi \eta_w^{\zeta}). \tag{124}$$

Substituting equation (28) into equation (27) yields

$$\hat{c}(\eta) = \exp\left[-\phi(\eta^{\zeta} - \eta_w^{\zeta})\right]. \tag{125}$$

Figure 3 presents the computed concentration distributions obtained from equation (29) and using two equations proposed by *Altinakar et al.* [1996]. The experimental data of *Parker et al*. [1987], *García* [1993], *Altinakar et al.* [1996], and *Nourmohammadi et al.* [2011] for gravity currents are shown in Figure 3 for comparison. In addition, the values ϕ = 4 and ζ = 1.5 provide a best fitting of the computed curve with the experimental data. Therefore, with η_w = 0.214 in equation (28), the λ is obtained as 1.486. The standard deviation, standard error, and coefficient of correlation for Figure 3 are 0.526, 0.029, and 0.949, respectively, which provide an insight of the data scatter from equation (29). In Figure 3, the experimental data for runs 6–10, 12, 13, 17, 20, 23, and 24 from *Parker et al*. [1987], and runs DAPER6 in subcritical and supercritical conditions from *García* [1993] are shown. From *Altinakar et al.* [1996], three sets of experimental data used in the velocity distributions as mentioned before are considered for the concentration distribution, whereas from *Nourmohammadi et al.* [2011], the experimental data for runs 5 and 6 at 2.5 and 5.5 m, respectively, and run 3 at 2.5 and 3.5 m from the flume inlet are considered. Finally, the computed concentration

distribution of *Altinakar et al.* [1996] corresponds to the curve obtained from the present study (Figure 3).

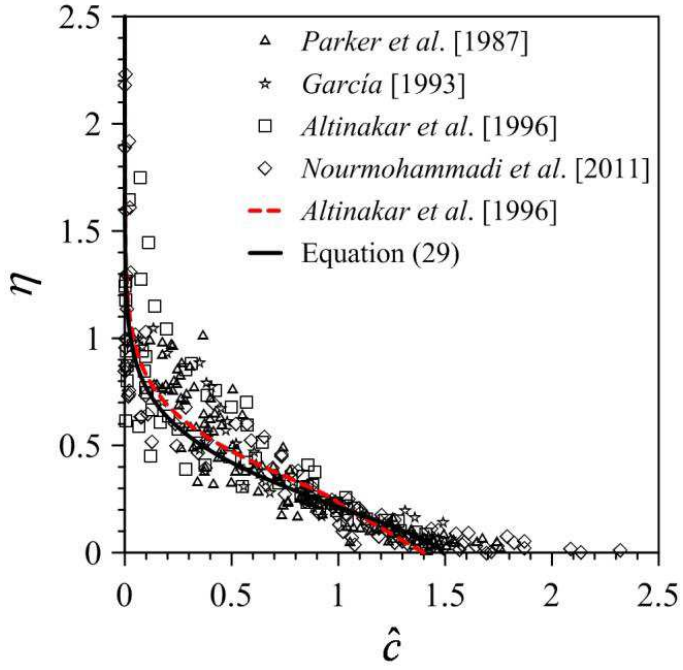

Fig. 3. Computed concentration distribution $\hat{c}\,(\eta)$ obtained from equation (29) showing the comparison with the concentration distribution obtained using two equations given by *Altinakar et al.* [1996] and the experimental data of different investigations.

From the data plots in Figure 3, an empirical relationship between the parameters ϕ and ζ are obtained as

$$\phi = 5\zeta - 3.5\,. \tag{126}$$

Substituting equation (30) into equation (29), the concentration distribution is

$$\hat{c}(\eta) = \exp[-(5\zeta - 3.5)(\eta^{\zeta} - \eta_w^{\zeta})]\,. \tag{127}$$

This relationship for the concentration distribution is indeed self-preserving type for turbidity currents.

From equation (31), the sediment concentration c_0 at the bed (η = 0) in nondimensional form is

$$\hat{c}_0 = \exp[(5\zeta - 3.5)\eta_w^{\zeta}]\,, \tag{128}$$

where $\hat{c}_0 = c_0/C_m$. The depth-averaged concentration C in nondimensional form is

$$\hat{C} = \int_0^1 \hat{c}\,\mathrm{d}\eta\,, \tag{129}$$

where $\hat{C} = C/C_m$. Inserting equation (31) into equation (33) yields

$$\hat{C} = \frac{1}{\zeta}(5\zeta - 3.5)^{-1/\zeta} \exp[5(\zeta - 0.7)\eta_w^{\zeta}]\left[\Gamma\left(\frac{1}{\zeta}\right) - \Gamma\left(\frac{1}{\zeta}, 5\zeta - 3.5\right)\right], \qquad (130)$$

where $\Gamma(a, s)$ is the incomplete gamma function defined as

$$\Gamma(a, s) = \int_s^{\infty} y^{a-1} \exp(-y)\mathrm{d}y\,. \qquad (131)$$

For $\zeta = 1.5$ and $\eta_w = 0.214$, equation (34) yields $\hat{C} = 0.528$.

Equation (31) suggests that the concentration distribution has a finite value at $z = z_m$ ($\eta = 1$), although it is feeble. For $\eta > 1$, the asymptotic trend of $\hat{c}(\eta)$ toward the ordinate is evident (Figure 3). The area under the curve $\hat{c}(\eta)$ bounded by $\eta = 0$ and $\hat{c} = 0$ for the two cases when the limits of integration are $\eta = 0$ to 1 and $\eta = 0$ to 2.5 shows an approximate relative error of 0.7%. Thus, the upper limit of the moments of the integral scales defined in equation (5) is considered at $z = z_m$ ($\eta = 1$). Hence, the integral scales in equation (5) are given by

$$I_3 = \int_0^{\infty} c\mathrm{d}z = \int_0^{z_m} c\mathrm{d}z = 0.528 C_m z_m\,, \qquad (132)$$

$$I_4 = \int_0^{\infty} uc\mathrm{d}z = \int_0^{z_m} uc\mathrm{d}z = 0.396 U_m C_m z_m\,, \qquad (133)$$

$$I_5 = \int_0^{\infty}\int_z^{\infty} c\mathrm{d}z\mathrm{d}z = \int_0^{z_m}\int_z^{z_m} c\mathrm{d}z\mathrm{d}z = 0.743 C_m z_m^2\,. \qquad (134)$$

For details of the moments of the integral equations (36)–(38), see Appendix B.

5. Reynolds Shear Stress and Turbulent Diffusivity Distributions

In a fully developed turbulent flow, the Reynolds shear stress is much greater than the viscous shear stress except in the vicinity of the bed, where the flow is laminar within a thin viscous sublayer. It may be noted that the Reynolds shear stress nearly composes the total shear stress (Reynolds shear stress and viscous shear stress) in absence of viscous shear stress. Since the turbidity current is characterized by the turbulent flow, the molecular diffusivity is negligible as compared to the turbulent diffusivity. Moreover, the solid diffusivity is considered approximately equalling the turbulent

diffusivity [*Rouse*, 1937; *Dey*, 2014]. Hence, the Reynolds shear stress and the turbulent diffusivity distributions are determined from the proposed velocity and concentration distributions [equations (16) and (31)].

The suspended sediment stratification due to turbidity affects the structure of the turbulent diffusivity in turbidity currents [*Stacey and Bowen*, 1988]. From the diffusion equation of suspended sediment concentration, the turbulent diffusivity ε_t is defined as

$$\varepsilon_t = -w_s c \left(\frac{\mathrm{d}c}{\mathrm{d}z} \right)^{-1}. \tag{135}$$

The nondimensional turbulent diffusivity $\hat{\varepsilon}_t$ is then expressed as

$$\hat{\varepsilon}_t = -Z\hat{c} \left(\frac{\mathrm{d}\hat{c}}{\mathrm{d}\eta} \right)^{-1}, \tag{136}$$

where $\hat{\varepsilon}_t = \varepsilon_t/(\kappa u_{*b} z_m)$, κ is the von Kármán constant, and Z is the Rouse number [$= w_s/(\kappa u_{*b})$]. Using equation (31), equation (40) reduces to

$$\hat{\varepsilon}_t = Z \frac{\eta^{1-\zeta}}{(5\zeta - 3.5)\zeta}. \tag{137}$$

According to the Boussinesq hypothesis, the Reynolds shear stress τ in turbulent flow is expressed as

$$\tau = \rho \varepsilon_t \frac{\mathrm{d}u}{\mathrm{d}z}, \tag{138}$$

where ρ is the mass density of the fluid-sediment mixture. In nondimensional form, the Reynolds shear stress is

$$\hat{\tau} = \hat{\varepsilon}_t \frac{U_m}{u_{*b}} \cdot \frac{\mathrm{d}\hat{u}}{\mathrm{d}\eta}, \tag{139}$$

where $\hat{\tau} = \tau/\rho u_{*b}^2$. Substituting equations (16) and (41) into equation (43) yields

$$\tilde{\tau} = Z \frac{\eta^{1-\zeta}}{(5\zeta - 3.5)\zeta} (1-\eta)^{2\xi} \eta^{-1+\xi} \xi^{-\xi} (1+2\xi)^{-1-2\xi} (1+3\xi)^{1+3\xi} [\xi - \eta(1+3\xi)], \tag{140}$$

where $\tilde{\tau} = \hat{\tau}\,(u_{*b}/U_m)$.

The turbulent diffusivity and the Reynolds shear stress are computed from equations (41) and (44), respectively, using ξ = 0.6 and ζ = 1.5. Figures 4a and 4b show the

variations of computed nondimensional turbulent diffusivity $\hat{\varepsilon}_t$ and Reynolds shear stress $\tilde{\tau}$ with nondimensional vertical distance η for Rouse numbers Z = 0.3, 0.5, and 1. The nondimensional reference level considered at η = 0.05, according to *Graf and Altinakar* [1998], is also shown.

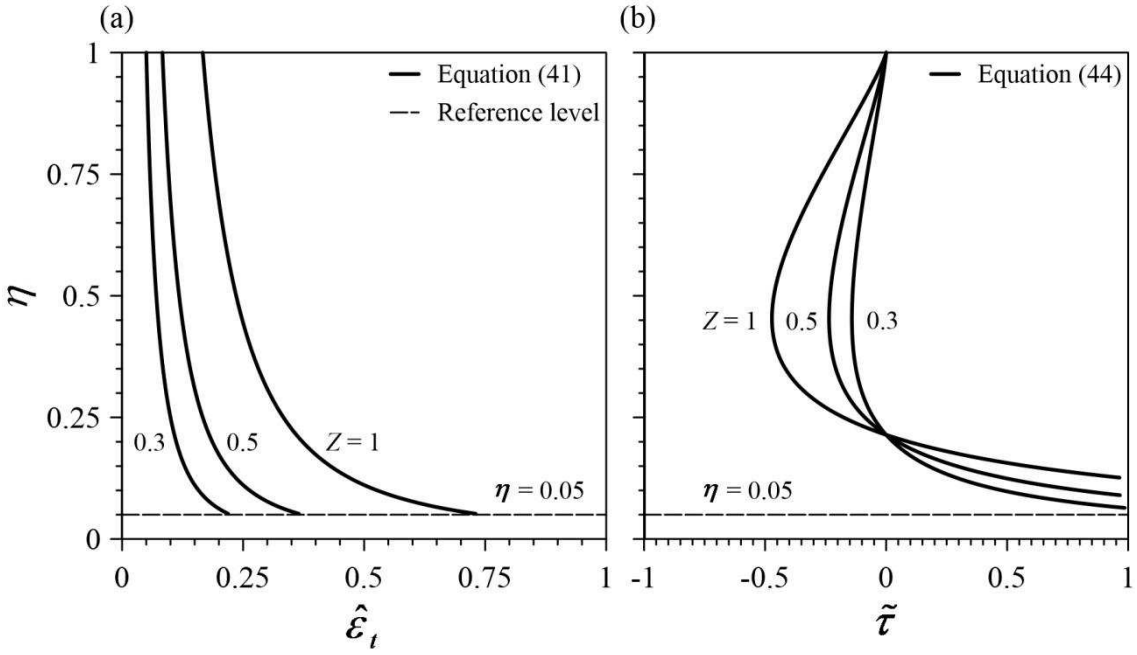

Fig. 4. Distributions of computed turbulent diffusivity $\hat{\varepsilon}_t$ (η) and Reynolds shear stress $\tilde{\tau}$ (η) for different Rouse numbers Z (= 0.3, 0.5, and 1) obtained from the present model.

At the reference level (η = 0.05), the $\hat{\varepsilon}_t$ is maximum. Then, the $\hat{\varepsilon}_t$ decreases with an increase in η approaching a constant value for η > 1. It implies that $\hat{\varepsilon}_t$ has a finite value at the upper boundary of the turbidity current (η = 1). This feature can be explained from the viewpoint of the applicability of the governing equation of suspended sediment concentration [equation (39)]. Strictly, equation (39) is only applicable to steady-uniform flows. However, as an approximation, the present study assumes that equation (39) is applicable to nonuniform flows. On the other hand, the entrainment of ambient fluid into the turbidity current induces a significant mixing at the interface between the turbidity current and the ambient fluid. Hence, a finite value of $\hat{\varepsilon}_t$ at the upper boundary of the turbidity current is meaningful. Another important feature is that for a given η, $\hat{\varepsilon}_t$ increases with an increase in Z.

In case of Reynolds shear stress, in the immediate vicinity above the reference level (η = 0.05), the $\tilde{\tau}$ is positive. It diminishes with an increase in η within the inner-layer

following a similar trend of $\tilde{\tau}$ -distribution in a boundary layer flow due to the reduction in velocity gradient with η and becomes zero at the point of occurrence of maximum velocity. With a further increase in η (within the outer-layer), the $\tilde{\tau}$ becomes negative forming a protuberance (maximum negative value of $\tilde{\tau}$ in $\tilde{\tau}$ -distribution) at the point of inflection of the $\hat{u}$ -distribution, and then it gradually approaches to zero. It is relevant to mention that a similar trend of $\tilde{\tau}$ -distribution was observed by *Dey et al.* [2010] in a submerged wall-jet. For a given η, $\tilde{\tau}$ decreases with an increase in *Z* in the outer layer, while in the inner layer, $\tilde{\tau}$ increases with *Z*.

6. Turbidity Current Model and Gradually-Varied Flow Formulations

Since velocity and the concentration distributions are known, the three-equation model for the turbidity currents is obtained by inserting $\hat{U}$ = 0.52, β = 1.465, α = 2.366, and the moments of the integral scales of equations (25), (26), (36)–(38) into equations (8)–(10). Therefore, the three-equation model is

$$\frac{\partial z_m}{\partial t} + 0.52\frac{\partial (U_m z_m)}{\partial x} = 0.52 E_w U_m , \tag{141}$$

$$0.528\frac{\partial (C_m z_m)}{\partial t} + 0.396\frac{\partial (U_m C_m z_m)}{\partial x} = E_b - D_b , \tag{142}$$

$$0.52\frac{\partial (U_m z_m)}{\partial t} + 0.396\frac{\partial (U_m^2 z_m)}{\partial x} = -0.372\Delta_s g\frac{\partial (C_m z_m^2)}{\partial x}\cos\theta + 0.528\Delta_s g C_m z_m \sin\theta - u_{*b}^2 . \tag{143}$$

For a steady flow, time derivatives in equations (45)–(47) disappear. Therefore, using equations (45)–(47) under the steady flow condition yields the gradually-varied flow formulations for z_m and C_m as

$$\frac{\mathrm{d}z_m}{\mathrm{d}x} = \frac{1}{1-0.961\mathrm{Ri}}\left[1.213\mathrm{Ri}\frac{E_b - D_b}{U_m C_m} + \frac{1}{2}(4-0.961\mathrm{Ri})E_w - 0.683\mathrm{Ri}\tan\theta + 2.525\left(\frac{u_{*b}}{U_m}\right)^2\right], \tag{144}$$

$$\frac{\mathrm{d}C_m}{\mathrm{d}x} = \frac{1}{U_m z_m}\left(\frac{E_b - D_b}{0.396} - E_w U_m C_m\right), \tag{145}$$

where Ri is the Richardson number given by

$$\mathrm{Ri} = \frac{\Delta_s g C z_m \cos\theta}{U^2} = 1.952\frac{\Delta_s g C_m z_m \cos\theta}{U_m^2} . \tag{146}$$

The streamwise variation of Ri is obtained as

$$\frac{\mathrm{d}\mathsf{Ri}}{\mathrm{d}x}=\frac{3\mathsf{Ri}}{z_m(1-0.961\mathsf{Ri})}\left[\begin{array}{l}\frac{1}{2}(2+0.961\mathsf{Ri})\left(E_w+\frac{1}{3}\cdot\frac{E_b-D_b}{0.396U_mC_m}\right)\\ -0.683\mathsf{Ri}\tan\theta+2.525\left(\frac{u_{*b}}{U_m}\right)^2\end{array}\right]. \tag{147}$$

Further, Ri is expressed in terms of the reduced sediment flux B as

$$\mathsf{Ri}=1.952\frac{\Delta_s gC_m z_m U_m\cos\theta}{U_m^3}=7.098\frac{B\cos\theta}{U_m^3}, \tag{148}$$

where $B = \Delta_s gCUz_m = 0.275\Delta_s gC_m U_m z_m$. The B can be interpreted as the sediment transport rate CUz_m affected by the gravitational acceleration reduced by the buoyancy effect $\Delta_s g$ [*Graf and Altinakar*, 1998; *Wang et al.*, 2010]. Differentiating equation (52), the streamwise gradient of B is expressed as

$$\frac{\mathrm{d}B}{\mathrm{d}x}=\frac{U_m^3}{7.098\cos\theta}\cdot\frac{\mathrm{d}\mathsf{Ri}}{\mathrm{d}x}+3\frac{B}{z_m}\left(E_w-\frac{\mathrm{d}z_m}{\mathrm{d}x}\right). \tag{149}$$

Substituting equations (48) and (51) into equation (53) yields

$$\frac{\mathrm{d}B}{\mathrm{d}x}=\frac{B}{z_m}\cdot\frac{E_b-D_b}{0.396U_mC_m}. \tag{150}$$

7. Closure Relationships

Closure relations are required to evaluate the boundary interaction functions and the bed shear stress involved in the formulations in the preceding sections. The parameters involved with them are often specified by empirical relationships reported in literature.

The empirical relationship for the entrainment coefficient of ambient fluid E_w was proposed by *Parker et al*. [1987] and was extended to gravity currents by *Altinakar et al.* [1993] using the experimental data of turbidity currents and density currents [*Graf and Altinakar*, 1998]. It is

$$E_w=0.075(1+718\mathsf{Ri}^{2.4})^{-0.5}. \tag{151}$$

The net sediment rate $(E_b - D_b)$ is then expressed as

$$E_b-D_b=w_s(E_s-c_b), \tag{152}$$

where E_s is the entrainment coefficient of sediment particles from the bed, and c_b is the reference suspended sediment concentration. The empirical relationship for E_s given by

Parker et al. [1987], which was used by *Altinakar et al*. [1996] and *Graf and Altinakar* [1998], is considered here. It is

$$E_s = 3\times10^{-11}\left(\frac{u_{*b}}{w_s}\mathrm{Re}_p^{0.75}\right)^7\left[1+10^{-10}\left(\frac{u_{*b}}{w_s}\mathrm{Re}_p^{0.75}\right)^7\right]^{-1}, \tag{153}$$

where Re_p is the particle Reynolds number [= $(\Delta_s g d^3/\upsilon^2)^{0.5}$], and υ is the kinematic viscosity of fluid.

The c_b is usually evaluated in the vicinity of the bed at η = 0.05 as indicated in Figure 4. According to *Graf* [1971], c_b is expressed as

$$\frac{c_b}{C} = f\left(\frac{u_{*b}}{w_s}\right). \tag{154}$$

From the experimental observation concerning turbidity currents, it was found that $c_b/C \approx 2$ for $1 < u_{*b}/w_s < 50$. [*Parker et al.*, 1987; *Altinakar et al.*, 1993], However, this relationship can be revised and extended to salinity currents as well using the concentration distribution proposed in this study. Evaluating equation (31) at the nondimensional reference level (η = 0.05), equation (58) is expressed as

$$\frac{c_b}{C_m} = 1.421,\ \frac{c_b}{C} = 2.691. \tag{155}$$

Equations (56) and (57) show the dependency of ($E_b - D_b$) and E_s on terminal fall velocity w_s. Hence, the determination of w_s for a given sediment size is an essential prerequisite. For natural sediment particles, different formulas are available to evaluate w_s in turbid fluid [*Hallermeier*, 1981; *Chang and Liou*, 2001; *Guo*, 2002] and still fluid [*Dietrich*, 1982; *Ahrens*, 2000; *Wu and Wang*, 2006]. A summary of the formulas of w_s is available in *Dey* [2014]. *Zhang and Xie*'s [1993] empirical formula, which agreed well with the experimental data over a wide range of sediment sizes from laminar to turbulent flow [*Wu*, 2008], is considered here. It is

$$w_s = \left[1.09\Delta_s g d + \left(\frac{13.95\upsilon}{d}\right)^2\right]^{0.5} - \frac{13.95\upsilon}{d}. \tag{156}$$

The u_{*b} is determined as follows:

$$u_{*b} = U\left(\frac{\lambda_D}{8}\right)^{0.5} = 0.52U_m\left(\frac{\lambda_D}{8}\right)^{0.5}, \qquad (157)$$

where λ_D is the Darcy-Weisbach friction factor.

8. Numerical Experiment

A numerical example is selected from *Graf and Altinakar*'s [1998] book (7.7.1, page 491), where the initial values of z_{m0} = 1 m, U_0 = 1 m s^{-1}, and C_0 = 0.0212 are considered for the computation. The initial reduced sediment flux B_0 is calculated from $B_0 = 0.275\Delta_s g C_0 U_0 z_0$. The streamwise bed slope $\theta = 5^o$, mass density of sediment particles ρ_s = 2650 kg m^{-3}, mass density of water ρ = 1000 kg m^{-3}, and friction factor λ_D = 0.032 are assumed. The total length of the channel reach is taken as 4000 m. The gradually-varied flow formulations [equations (48), (49), (51), and (54)] derived in Section 6 are solved numerically using the fourth-order Runge-Kutta method along with a first-order forward difference scheme. The numerical scheme is proved to be independent of the grid size. Here, $\Delta\hat{x}$ (= $\Delta x/z_{m0}$) is considered as 0.5 to ensure a smooth variation of parametric variables. The parametric variables for turbidity currents are specified as

$$\tilde{z}_m = \frac{z_m}{z_{m0}},\ \tilde{U} = \frac{U}{U_0},\ \tilde{C} = \frac{C}{C_0},\ \tilde{\mathrm{Ri}} = \frac{\mathrm{Ri}}{\mathrm{Ri}_0},\ \tilde{B} = \frac{B}{B_0}, \qquad (158)$$

where z_m is the nondimensional turbidity current depth, $\tilde{U}$ is the nondimensional depth-averaged velocity, $\tilde{C}$ is the nondimensional depth-averaged concentration, $\tilde{\mathrm{Ri}}$ is the relative Richardson number, and $\tilde{B}$ is the nondimensional reduced sediment flux. In Figures (5)–(12), the computational results obtained from the present model are shown and compared with those obtained from the formulations (henceforth classical model) of *Graf and Altinakar* [1998].

Figures 5a–5c exhibit the variations of $\tilde{z}_m$, $\tilde{U}$, and $\tilde{B}$ with nondimensional streamwise distance $\hat{x}$ for salinity current with $d = 10^{-6}$ mm and turbidity currents with d = 0.05 and 0.1 mm. An increasing trend of $\tilde{z}_m$ with $\hat{x}$ is evident for all the cases. In Figure 5a, the $\tilde{U}$ in salinity current increases slowly with $\hat{x}$, becoming invariant of $\hat{x}$ for $\hat{x}$ > 45 with a constant value $\tilde{U}$ = 1.064 due to the vanishing acceleration. However, $\tilde{B}$ is invariant of $\hat{x}$ with a constant value $\tilde{B}$ = 1, since the net sediment flux in salinity current disappears as it is revealed from equation (54). On the contrary,

Figures 5b and 5c illustrate the self-accelerating behaviour (an increasing trend of $\tilde{U}$ with $\hat{x}$) for the turbidity currents due to an increasing trend of $\tilde{B}$ with $\hat{x}$. It is apparent from Figures 5b and 5c that the self-acceleration and the net sediment flux increase with an increase in sediment size in turbidity currents. The $\tilde{z}_m(\hat{x})$-, $\tilde{U}(\hat{x})$-, and $\tilde{B}(\hat{x})$-curves obtained from the classical formulations [*Graf and Altinakar*, 1998] have similar trends with marginally overestimated results from those obtained from the present model.

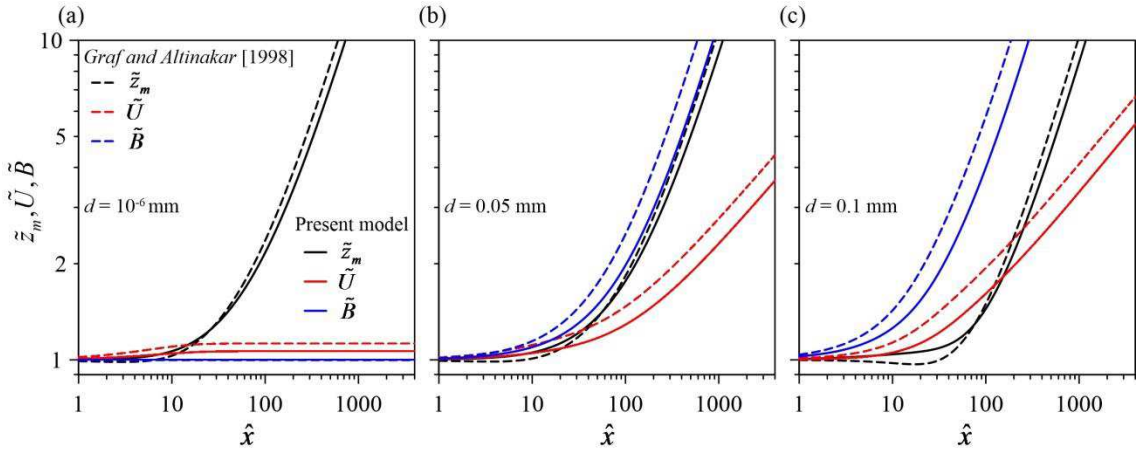

Fig. 5. Variations of $\tilde{z}_m$, $\tilde{U}$, and $\tilde{B}$ with $\hat{x}$ in a salinity current with (a) $d = 10^{-6}$ mm, and turbidity currents with (b) $d = 0.05$ mm and (c) $d = 0.1$ mm.

It is already stated that the turbidity current is characterized by an erosional or a depositional mode depending on the flow conditions. As the sediment size increases, the nature of turbidity current changes from erosional to depositional mode, primarily due to the effects of the terminal fall velocity of suspended sediment particles. Therefore, for a given bed slope θ, there exists a transition from erosional to depositional mode of turbidity currents with an increase in sediment size. To investigate this phenomenon, the variations of $\tilde{z}_m$, $\tilde{U}$, and $\tilde{B}$ with $\hat{x}$ for turbidity currents with $d = 0.2$ and 0.3 mm are computed and shown in Figures 6a and 6b. The present model shows a transitional characteristic (erosional to depositional) with an increase in sediment size from $d = 0.1$ to 0.2 mm (see Figures 5c and 6a). However, the classical model of *Graf and Altinakar* [1998] predicts the turbidity current as erosional for $d = 0.2$ mm. On the other hand, Figure 6b shows an agreement between the present and *Graf and Altinakar*'s [1998] models, as the turbidity current is depositional for $d = 0.3$ mm in both the models.

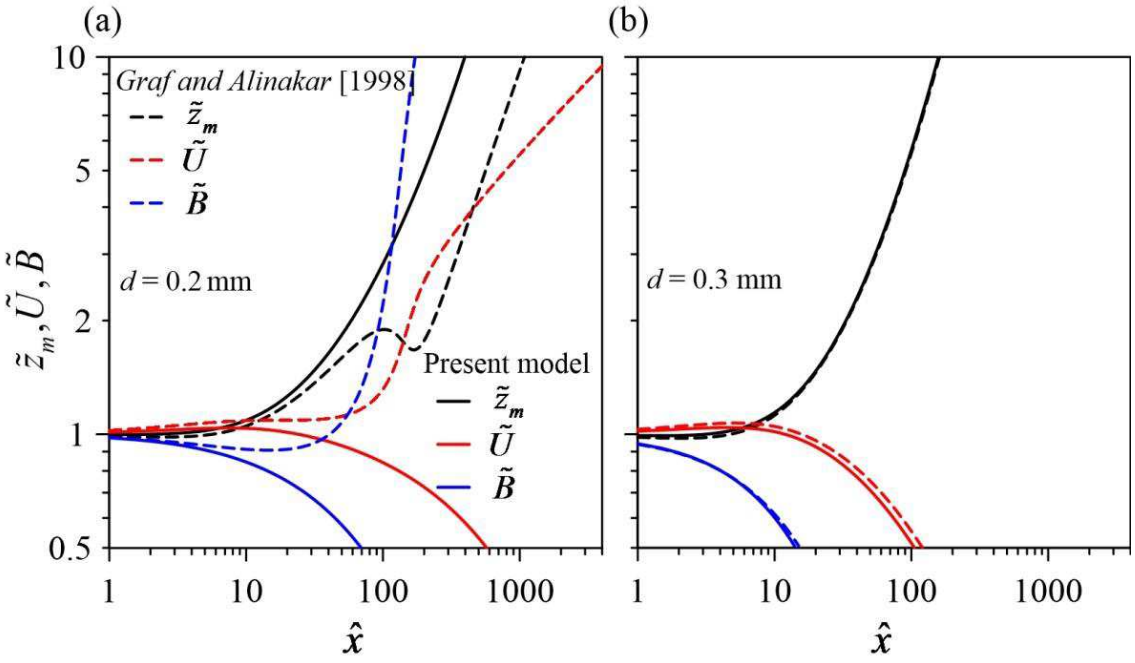

Fig. 6. Variations of $\tilde{z}_m$, $\tilde{U}$, and $\tilde{B}$ with $\hat{x}$ in turbidity currents with (a) d = 0.2 mm and (b) d = 0.3 mm.

Figures 7a–7c depict the variations of $\tilde{\mathrm{Ri}}$ and $\tilde{C}$ with $\hat{x}$ for salinity current with d = 10^{-6} mm and turbidity currents with d = 0.05 and 0.1 mm. The $\tilde{\mathrm{Ri}}$ gradually decreases with $\hat{x}$ in the initial stage, becoming constant (supercritical flow regime) with an increase in $\hat{x}$ for all the cases. In Figure 7a, the $\tilde{C}$ for salinity current follows a decreasing trend over the entire range of $\hat{x}$, since no sediment is introduced in the current and $\tilde{z}_m$ continuously increases with $\hat{x}$. In Figure 7b, the $\tilde{C}$ for turbidity current with d = 0.05 mm slowly decreases with $\hat{x}$. On the other hand, in Figure 7c, the $\tilde{C}$ for turbidity current with d = 0.1 mm increases with $\hat{x}$ due to a positive net sediment flux, attaining a maximum value $\tilde{C}$ = 1.722 at $\hat{x}$ = 120 and then decreases with $\hat{x}$ even though $\tilde{B}$ has an increasing trend there (see Figure 5c). The decreasing trend of $\tilde{C}$ in Figure 7c is attributed to the continuous rapid growth of $\tilde{z}_m$. The $\tilde{\mathrm{Ri}}(\hat{x})$- and $\tilde{C}(\hat{x})$-curves obtained from the classical model [*Graf and Altinakar*, 1998] have similar trends with a slight variation from those obtained from the present study.

To demonstrate the transitional characteristic of turbidity currents, the variations of $\tilde{\mathrm{Ri}}$ and $\tilde{C}$ with $\hat{x}$ for d = 0.2 and 0.3 mm are calculated and plotted in Figures 8a and 8b. The transitional characteristic (erosive to depositional) of the turbidity currents is found with an increase in sediment size from d = 0.1 to 0.2 mm (see Figures 7c and 8a).

However, according to the model of *Graf and Altinakar*, the turbidity current still shows an erosional mode for d = 0.2 mm. On the other hand, for d = 0.3 mm, both the models predict the turbidity current as depositional (Figure 8b).

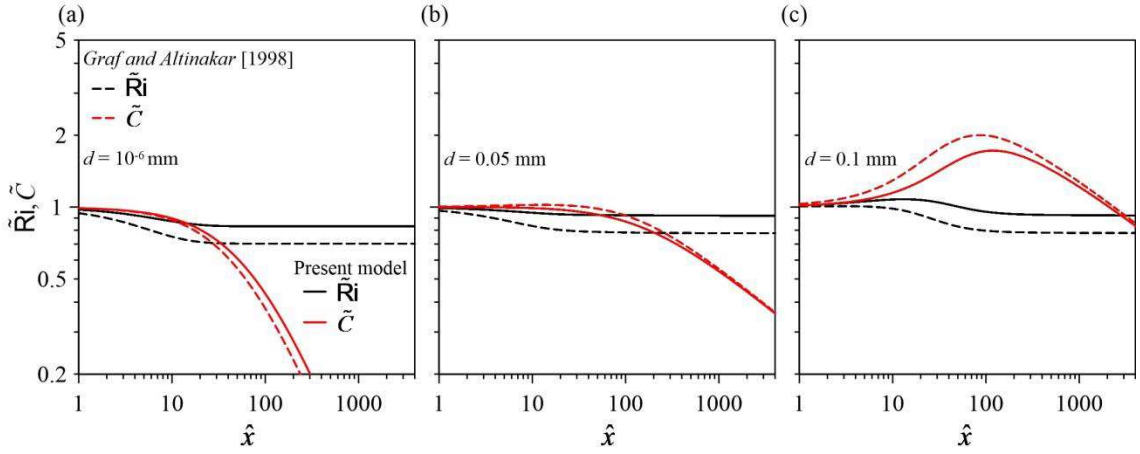

Fig. 7. Variations of $\tilde{R}i$ and $\tilde{C}$ with $\hat{x}$ in a salinity current with (a) $d = 10^{-6}$ mm, and turbidity currents with (b) d = 0.05 mm and (c) d = 0.1 mm.

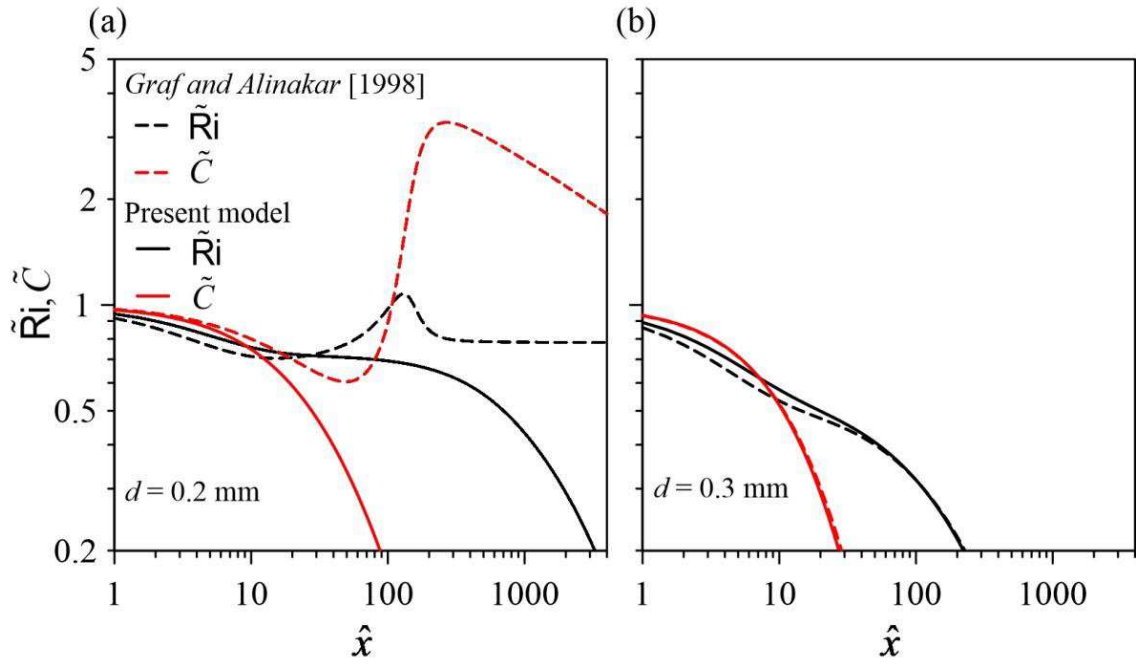

Fig. 8. Variations of $\tilde{R}i$ and $\tilde{C}$ with $\hat{x}$ in turbidity currents with (a) d = 0.2 mm and (b) d = 0.3 mm.

The Richardson number is a good indicator to identify the flow regime [subcritical flow (Ri > 1) or supercritical flow (Ri < 1)], and in turn, the turbidity current characteristics (erosional or depositional mode). Figures 9a–9c show the variations of $\tilde{R}i$ with $\hat{x}$ for different θ in salinity current with $d = 10^{-6}$ mm and turbidity currents with d = 0.05 and 0.1 mm. It is revealed from Figures 9a–9c that for smaller values of θ ($\leq 0.8^{o}$), the $\tilde{R}i$ abruptly increases with $\hat{x}$ for all the cases, while for larger values of θ

(≥ 2º), it increases for θ = 2º and decreases for θ = 5–45º with $\hat{x}$, becoming invariant of $\hat{x}$ for a large $\hat{x}$. Therefore, to obtain a supercritical flow (independent of $\hat{x}$), it is required to overcome a certain threshold value of bed slope θ that depends on the sediment size. It is evident that the $\tilde{R}i$ in salinity current (Figure 9a) attains a constant value earlier than in turbidity currents (Figures 9b and 9c). The $\tilde{R}i(\hat{x})$-curves obtained from the classical model [*Graf and Altinakar*, 1998] have similar trend with slightly underestimated results from those obtained from the present study for larger values of θ (≥ 2º), but slightly overestimated results for smaller values of θ (≤ 0.8º).

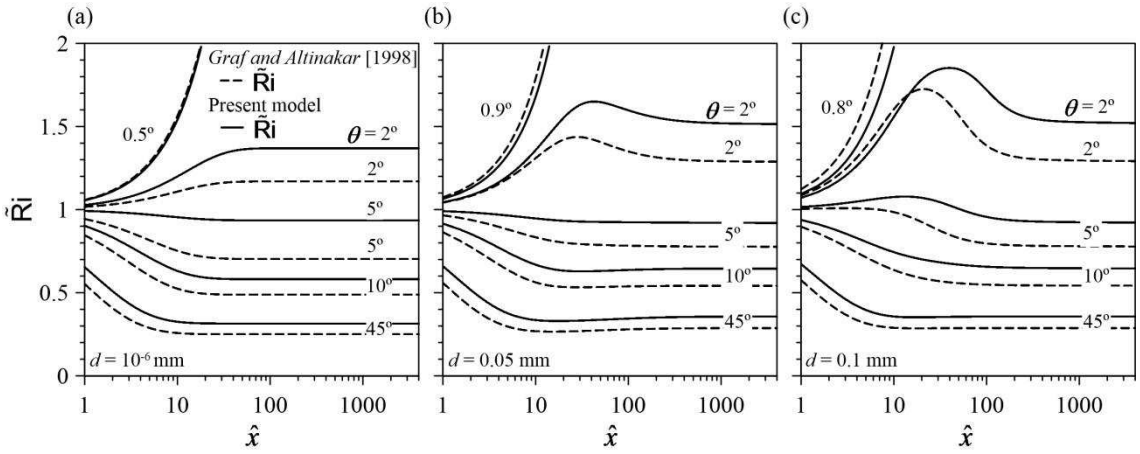

Fig. 9. Variations of $\tilde{R}i$ with $\hat{x}$ for different bed slopes θ in a salinity current with (a) $d = 10^{-6}$ mm and turbidity currents with (b) d = 0.05 mm and (c) d = 0.1 mm.

Figures 10a and 10b show the variations of $\tilde{R}i$ with $\hat{x}$ for different θ in turbidity currents with d = 0.2 and 0.3 mm. In Figure 10a (d = 0.2 mm), both the present and *Graf and Altinakar*'s [1998] models agree well in predicting $\tilde{R}i$ for θ = 2º, but differ for θ = 5º. For θ > 5º, the $\tilde{R}i$ has a supercritical flow tendency (independent of $\hat{x}$), while for θ < 5º, it decays asymptotically toward zero. With an increase in sediment size (d = 0.3 mm), the damping of $\tilde{R}i$ is noticeable with θ, while the supercritical flow is achieved at θ = 45º (Figure 10b). The $\tilde{R}i(\hat{x})$-curves obtained from the classical model [*Graf and Altinakar*, 1998] have similar trend with slightly underestimated results from those obtained from the present study, except for θ = 5º for which an overestimated result is obtained.

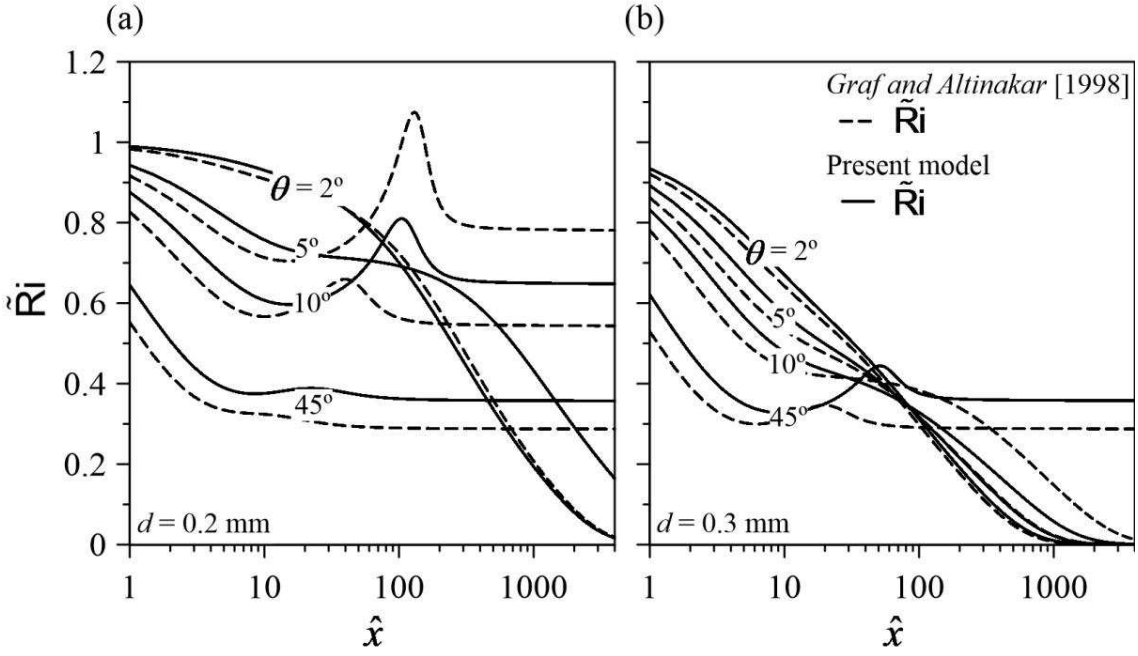

Fig. 10. Variations of $\tilde{Ri}$ with $\hat{x}$ for different bed slopes θ in turbidity currents with (a) d = 0.2 mm and (b) d = 0.3 mm.

The variations of $\tilde{Ri}$ with θ at $\hat{x}$ = 4000 (last node of computational domain) for salinity current with $d = 10^{-6}$ mm and turbidity current with d = 0.1 mm are plotted in Figure 11. The results obtained from the present model are compared with the formulations of *Graf and Altinakar*, [1998]. For a given initial condition, the turbidity currents can only maintain the supercritical flow ($Ri < 1$) if θ exceeds a threshold value, as shown in Figure 11. The $\tilde{Ri}(\theta)$-curves obtained from the classical model [*Graf and Altinakar*, 1998] have similar trend with slightly underestimated results from those obtained from the present study.

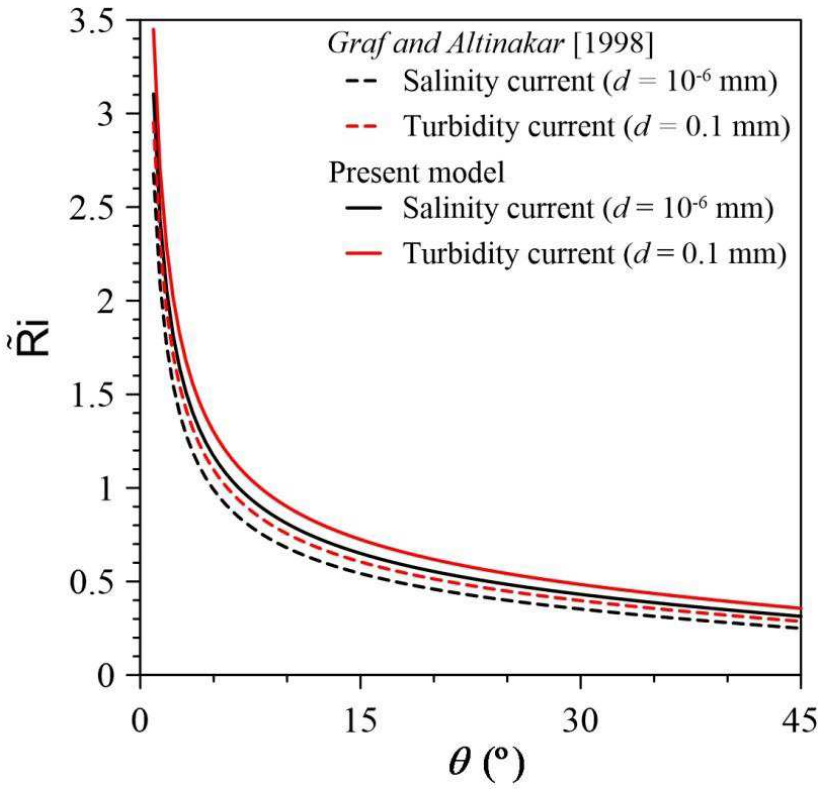

Fig. 11. Variations of $\tilde{\mathrm{Ri}}$ with θ at $\hat{x}$ = 4000 in a salinity current with $d = 10^{-6}$ mm and a turbidity current with d = 0.1 mm.

Figure 12 displays the variations of nondimensional growth rate $\mathrm{d}\,\tilde{z}_m/\mathrm{d}\,\hat{x}$ of turbidity currents with θ at $\hat{x}$ = 4000 for salinity current with $d = 10^{-6}$ mm and turbidity current with d = 0.1 mm. In these cases, the present model slightly underestimates the growth rate from that obtained from *Graf and Altinakar*'s [1998] model. The ratio of average growth rate of the turbidity current to that of the salinity current is determined as 0.66 (approximately), while from the classical model of *Graf and Altinakar* [1998], this ratio is obtained as 0.67. However, *Akiyama and Stefan* [1985] reported the ratio as 0.65.

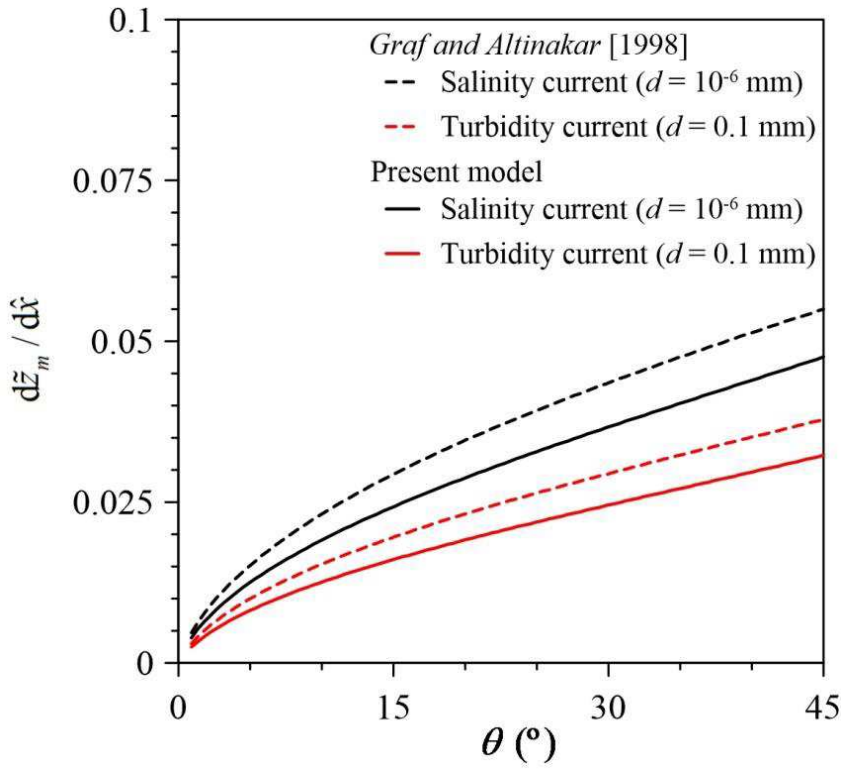

Fig. 12. Variations of d $\tilde{z}_m$ /d $\hat{x}$ with θ at $\hat{x}$ = 4000 in a salinity current with $d = 10^{-6}$ mm and a turbidity current with d = 0.1 mm.

9. Discussion

The present model of turbidity current is not merely based on empirical relationships, but it provides an insight into the physics of the fluid flow. The velocity and concentration distributions reported earlier were typically based on self-similarity functions obtained by treating the depth-averaged variables in the moments of the integral scales. Following the analysis by *Parker et al*. [1986], a satisfactory depth-averaged model was classical model [*Graf and Altinakar*, 1998]. In particular, the knowledge of the velocity and concentration distributions are required to treat the equations of fluid mass, sediment mass, and fluid momentum balance.

The expression for the velocity distribution is derived in Section 3. Using the experimental velocity data of turbidity and salinity currents reported by various investigators, the unknown parameters involved in the velocity distribution function are determined. However, the velocity distributions in a flow over bedforms have a departure from this trend, since the maximum velocity shifts upward in this case [*Sequeiros et al.*, 2010]. It is relevant to mention that the generalized expression (equation 11) for the velocity distribution can also be applicable to the flow over bedforms, if the unknown parameters are adjusted according to the experimental data.

Moreover, the unknown parameters involved in the velocity distribution are reduced to a single unknown parameter by means of the boundary conditions and the empirical relations. From the velocity distribution, the flow parameters such as nondimensional depth-averaged velocity, momentum (Boussinesq) and energy (Coriolis) coefficients are determined as 0.52, 1.465, and 2.366, respectively. In contrast, according to *Altinakar et al.* [1996], the nondimensional depth-averaged velocity was found as 0.769 showing a 50% overestimation of the present value. As a result of which the momentum and energy coefficients affect the moments of the integral scales of the governing equations. So, they need to be taken into account for a better performance of the model.

The concentration distribution is likewise treated and derived in Section 4. Following an analogous derivation to the velocity distribution, a single function for the concentration distribution involving a single unknown parameter is proposed by applying the boundary conditions and the empirical relations. The concentration distribution is based on the near-Gaussian distribution proposed by *Altinakar et al*. [1996] for the outer-layer of the turbidity currents. After an appropriate treatment, the near-Gaussian distribution is used over the entire range of the turbidity current layer. So, two separate concentration distributions in the inner- and outer-layer, which make the formulation rather complicated, are no longer required. The experimental data used in the analysis is chosen from the same experiments used for the velocity distribution. Therefore, the level of vanishing velocity at the interface between the turbidity current and the ambient fluid is known and the ordinate of the concentration distribution is rescaled accordingly. From the viewpoint of the suspended sediment motion, little is known about the background mechanism of the suspended sediment concentration in turbidity currents. Within the inner-layer where the velocity distribution follows a classical boundary layer flow, the concentration distribution is expected to adopt a traditional concentration distribution, as proposed by *Rouse* [1937]. However, according to the experimental data trend, the concentration at the bed can be approximated with a finite value [*Altinakar et al.*, 1996]. Within the outer-layer, the concentration distribution has a decreasing trend with the vertical distance leaving a finite value at the interface between the turbidity current and the ambient fluid. Accordingly, the moments of the integral scales defined in equation (5) are performed neglecting the concentration distribution in the ambient fluid layer.

Using the velocity and concentration distributions, the characteristics of turbidity current are further analyzed. In Section 5, the turbulent diffusivity in turbidity currents is estimated using the diffusion equation of the suspended sediment concentration. The Reynolds shear stress in turbidity currents is computed applying the Boussinesq hypothesis. The Reynolds shear stress distribution is in agreement with the theoretical study reported by *Stacey and Bowen* [1985]. Applying the diffusion equation to the suspended sediment motion, the turbulent diffusivity distribution is also obtained. In contrast to the present observations, the study of *Stacey and Bowen* [1985] considered a linear bridge to join the bimodal type of turbulent diffusivity distribution following *Launder and Spalding* [1972]. This linear bridge was explained from the viewpoint of the Prandtl's mixing length theory for turbidity currents. In fact, nothing can be firmly stated in this aspect, since little is known about the characteristics of the turbulent length scales in turbidity currents. However, the present study is free from the consideration of a linear bridge.

The present model provides the gradually-varied flow formulations given in Section 6. The variations of the nondimensional turbidity current depth, velocity, concentration, reduced sediment flux, and Richardson number with nondimensional streamwise distance obtained from the present model are compared with those obtained from the classical model [*Graf and Altinakar*, 1998]. The variations of $\tilde{z}_m$, $\tilde{U}$, $\tilde{C}$, and $\tilde{B}$ are, in general, underestimated by the present model as compared to those obtained from the classical model, leading to milder transitions than in the classical model. The variation of $\tilde{\mathrm{Ri}}$ is, in contrast, overestimated. Consequently, it can be interpreted that the present model is able to describe a greater strength of erosional turbidity currents without the implication of greater values of $\tilde{z}_m$, $\tilde{U}$, $\tilde{C}$, and $\tilde{B}$. Additionally, the point of departure from the erosional to depositional turbidity current appears earlier in the present model than in the classical model with respect to the median size of sediment particles, as inferred from Figures 6 and 8. The reason is attributed to account for the self-preserving type distributions of velocity and concentration in the present model. It is one of the main differences between the present and the classical models. Besides, the difference in prediction of $\tilde{\mathrm{Ri}}$ for different bed slopes θ is analyzed in Figure 11. In addition, the same trend is found for the growth rate $\mathrm{d}\tilde{z}_m/\mathrm{d}x$ of turbidity currents in Figure 12 by analyzing the ratio of the growth rates in salinity to turbidity currents. These

characteristics are generalized for a wide range of θ and in turn, it can be stated that the present model in general performs similarly to the classical model.

Last but not the least, the results on the gradually-varied flow parametric variables in turbidity currents with erosional or depositional mode could not be compared with the observed data due to lack of experimental or field data. However, in spite of some approximations adopted in the analysis, this model, at least, fulfils the purpose of describing clearly the characteristics and the behavior of turbidity currents. This corollary is further discussed in Appendix C through an auxiliary calculation following the recommendation of *Parker et al*. [1986]. The present three-equation model does not fail in predicting turbidity currents from ignition point and, in turn, does not violate the four-equation TKE balance [*Hu et al*., 2015]. Besides, in view of the self-preserving type of velocity and concentration laws that are validated by the experimental data and used to develop the gradually-varied flow relationships, perhaps a more than a qualitative rationality can be claimed for the computed results.

10. Conclusions

A physically based hydrodynamic analysis for the turbidity currents over a plane bed is presented using the classical three-equation model (depth-averaged fluid continuity, sediment continuity, and fluid momentum equations) and considering the self-similar characteristics of the streamwise velocity and concentration distributions. According to the classical theory of sediment-laden flow, the governing equations of turbidity currents are presented in generalized forms by using the moments of the integral scales. To perform the integrals, the velocity and concentration distributions are assumed as single functions over the entire turbidity current layer. Using the experimental data of salinity and turbidity currents over plane beds, the unknown parameters involved in the velocity and concentration distributions are evaluated. Importantly, the velocity and concentration distributions are of self-preserving type, as they correspond closely to the wide range of experimental data in fully developed flows. The values of the typical flow parameters, such as depth-averaged velocity, momentum, and energy coefficients are evaluated from the velocity distribution. From the velocity and concentration distributions, the turbulent diffusivity and the Reynolds shear stress distributions are determined using the diffusion equation of suspended sediment concentration and the Boussinesq hypothesis. The turbulent diffusivity distribution is found to follow a different trend to that reported in the literature [*Stacey and Bowen*, 1988], while the

Reynolds shear stress distribution agrees well with the previous observations [*Dey et al*., 2010].

Using the velocity and concentration distributions in the moments of the integral scales, a generalized model for unsteady-nonuniform turbidity currents is developed. Then, the gradually-varied flow formulations for steady-nonuniform turbidity currents are derived from the generalized model with suitable closure relationships. The different parametric variables (current depth, velocity, concentration, reduced sediment flux, and Richardson number) of turbidity currents obtained from the present model are compared with those obtained from the model of *Graf and Altinakar* [1998]. The dependency of the parametric variables of turbidity currents on the sediment size and the bed slope including the transitional feature of turbidity currents from erosional to depositional mode is especially focused. The threshold value (erosional to depositional mode) of the streamwise bed slope that ensures a supercritical flow is highlighted for different sediment sizes. However, for depositional turbidity currents carrying larger sediment sizes, no threshold value of the bed slope is obtained. The ratio of growth rate of the turbidity current to that of the salinity current predicted by the present model is found almost similar to those obtained from previous models.

The limitations of this study are as follows:

(1) The expressions for self-preserving distributions of velocity and concentration are calibrated using the limited available experimental data reported by some investigators. Use of more experimental data could improve the accuracy of these expressions.

(2) The diffusion equation of suspended sediment concentration for uniform flow is applied for solving the gradually varied turbidity current equations. Thus, the turbidity current is assumed to be a pseudo-uniform flow.

(3) The suspended sediment concentration is assumed to be sufficiently small to apply the Boussinesq approximation, and thus the kinematic viscosity equals its value for clear water.

(4) The present study does not take into account the effects of bedforms on turbidity current over sediment beds.

Nevertheless, the present model is believed to be a powerful tool to analyze the characteristics of fully developed turbidity currents. It not only provides more

comprehensive insights into the vertical structure of the currents, but also the generalized formulation of unsteady-nonuniform turbidity currents and parametric variations of gradually-varied turbidity currents. In addition, it provides additional evidences to claim in favour of the three-equation model.

11. Acknowledgements

This study was supported by the Spanish project CTM2013-45666-R, Ministerio de Economía y Competitividad. The first author is thankful to the Ministerio de Educación, Cultura y Deporte, Spain, for grant (FPU12/04795) to visit to the Indian Institute of Technology (IIT) Kharagpur. Data supporting Figures 2 and 3 are available in *Altinakar et al.* [1996], *Sequeiros et al.* [2010], and *Nourmohammadi et al.* [2011], as also acknowledged in the corresponding figure legends.

Appendix A: Turbulent Kinetic Energy (TKE) Budget

The depth-averaged equation of TKE budget of turbidity currents is as follows [*Parker et al.*, 1986]:

$$\frac{\partial}{\partial t}\int_0^\infty k\mathrm{d}z+\frac{\partial}{\partial x}\int_0^\infty uk\mathrm{d}z=P_T-\int_0^\infty \varepsilon\mathrm{d}z-\frac{1}{2}\Delta_s g w_s\int_0^\infty c\mathrm{d}z$$

$$-\Delta_s g\left[\frac{\partial}{\partial t}\int_0^\infty\int_z^\infty c\mathrm{d}z\mathrm{d}z+\frac{\partial}{\partial x}\int_0^\infty\int_z^\infty uc\mathrm{d}z\mathrm{d}z+\int_0^\infty c\frac{\partial}{\partial x}\left(\int_0^z u\mathrm{d}z\right)\mathrm{d}z\right]\cos\theta, \qquad (1)$$

where k is the TKE, P_T is the average TKE production rate, and ε is the TKE dissipation rate.

The link of equation (A1) with the three-equation model was expressed by *Parker et al.* [1986] through the bed shear stress. The entrainment coefficient, $E_s = E_b/w_s$, is related to the state of the turbulence, as it can be inferred from equation (7) and is given as a function of the level of turbulence K, which is the depth-averaged TKE. Thereby, *Parker et al.* [1986] assumed

$$u_{*b}^2=\alpha_1 K, \qquad (2)$$

where α_1 is the proportionality parameter, which is assumed to be constant for a given flow. In addition, following *Parker et al.* [1986], one can write

$$\varepsilon_0 z_m=\int_0^\infty \varepsilon\mathrm{d}z=U^3\left[\frac{1}{2}E_w\left(1-\mathrm{Ri}-2\frac{K}{U^2}\right)+\alpha_1\frac{K}{U^2}\right], \qquad (3)$$

$$P_T=Pz_m\ . \qquad (4)$$

The integrals of equation (A1) are defined as

$$I_6=\int_0^\infty\int_z^\infty uc\mathrm{d}z\mathrm{d}z,\ I_7=\int_0^\infty c\frac{\partial}{\partial x}\left(\int_0^z u\mathrm{d}z\right)\mathrm{d}z,\ I_8=\int_0^\infty k\mathrm{d}z,\ \ I_9=\int_0^\infty uk\mathrm{d}z. \qquad (5)$$

Then, the generalized form of equation (A1) is given by

$$\frac{\partial I_8}{\partial t}+\frac{\partial I_9}{\partial x}=(P-\varepsilon_0)z_m-\frac{1}{2}\Delta_s g w_s I_3-\Delta_s g\left(\frac{\partial I_5}{\partial t}+\frac{\partial I_6}{\partial x}+I_7\right)\cos\theta. \qquad (6)$$

Including equation (A1) in the turbidity current model, the large values of E_s damp the turbulence state and hence stabilizes the values of K and E_s, which is unpredictable

by a three-equation model [*Parker et al.*, 1986]. However, in order to obtain a solution for equation (A6), additional information is required. The TKE distribution belongs to integrals I_8 and I_9. Unfortunately, little is known about the legitimate TKE distribution in turbidity currents. Although there exist some approximations of the TKE distribution in turbidity currents [*Islam and Imran*, 2010], they are not generalized. Besides not only the expression for TKE distribution is required in a complete four-equation model, but also an initial value of TKE is a prerequisite to initiate the computation. In fact, it was clearly pointed out by *Parker et al.* [1986] that the initial value of TKE for the computation requires a number of assumptions. Therefore, it is rather uncertain to provide a reliable initial value of TKE. In addition, the type of distributions assumed for the velocity and the concentration makes it difficult to perform the other integral scales. In fact, integral I_7 is not possible to be integrated in terms of a function of z, as the hypergeometric series functions appear, e.g., Kummer confluent hypergeometric functions. Also, in order to perform the integration of I_6, a similar continuous function is assumed for the product of the nondimensional velocity and concentration as $\hat{u}\hat{c} = 10.5\eta^{0.75}(1-\eta)^5$. Thereby, I_6 is

$$I_6 = \int_0^\infty \int_z^\infty uc\,\mathrm{d}z\mathrm{d}z = \int_0^{z_m} \int_z^{z_m} uc\,\mathrm{d}z\mathrm{d}z \simeq 10.5 U_m C_m z_m^2 \int_0^1 \int_\eta^1 \eta^{0.75}(1-\eta)^5\,\mathrm{d}\eta\mathrm{d}\eta = 0.086 U_m C_m z_m^2 . \quad (7)$$

Thus, equation (A1) is finally modified as

$$\begin{aligned} &\frac{\partial I_8}{\partial t} + \frac{\partial I_9}{\partial x} = (P - \varepsilon_0) z_m \\ &-\Delta_s g \left\{ 0.264 w_s C_m z_m - \left[0.134 \frac{\partial (C_m z_m^2)}{\partial t} + 0.086 \frac{\partial (U_m C_m z_m^2)}{\partial x} + I_7 \right] \cos\theta \right\} . \end{aligned} \quad (8)$$

The consideration of equation (A8) may enhance the performance of the turbidity current model [*Parker et al.*, 1986]. Notwithstanding, realizing the drawbacks, the inclusion of this equation can be avoided by adopting proper closure relationships in three-equation model.

Appendix B: The Moments of the Integral Scales

With the unknown parameters, the velocity and concentration distributions obtained from equations (16) and (31) are given as

$$\hat{u} = 4.284\eta^{0.6}(1-\eta)^{2.2}, \tag{A1}$$

$$\hat{c} = 1.486\exp(-4\eta^{1.5}). \tag{A2}$$

Therefore, the moments of the integral scales are

$$I_1 = \int_0^{\infty} u\mathrm{d}z = \int_0^{z_m} u\mathrm{d}z = U_m z_m \int_0^1 \hat{u}\mathrm{d}\eta = 4.284 U_m z_m \int_0^1 \eta^{0.6}(1-\eta)^{2.2}\mathrm{d}\eta = 0.52 U_m z_m, \tag{A3}$$

$$I_2 = \int_0^{\infty} u^2\mathrm{d}z = \int_0^{z_m} u^2\mathrm{d}z = U_m^2 z_m \int_0^1 \hat{u}^2\mathrm{d}\eta = 18.35 U_m^2 z_m \int_0^1 \eta^{1.2}(1-\eta)^{4.4}\mathrm{d}\eta = 0.396 U_m^2 z_m, \tag{A4}$$

$$I_3 = \int_0^{\infty} c\mathrm{d}z = \int_0^{z_m} c\mathrm{d}z = C_m z_m \int_0^1 \hat{c}\mathrm{d}\eta = 1.486 C_m z_m \int_0^1 \exp(-4\eta^{1.5})\mathrm{d}\eta = 0.528 C_m z_m, \tag{A5}$$

$$I_4 = \int_0^{\infty} uc\mathrm{d}z = \int_0^{z_m} uc\mathrm{d}z = U_m C_m z_m \int_0^1 \hat{u}\hat{c}\mathrm{d}\eta$$

$$= 6.365 U_m C_m z_m \int_0^1 e^{-4\eta^{1.5}} \eta^{0.6}(1-\eta)^{2.2}\mathrm{d}\eta = 0.396 U_m C_m z_m, \tag{A6}$$

$$I_5 = \int_0^{\infty}\int_z^{\infty} c\mathrm{d}z\mathrm{d}z = \int_0^{z_m}\int_z^{z_m} c\mathrm{d}z\mathrm{d}z = C_m z_m^2 \int_0^1\int_\eta^1 \hat{c}\mathrm{d}\eta\mathrm{d}\eta$$

$$= 1.486 C_m z_m^2 \int_\eta^1\int_\eta^1 \exp(-4\eta^{1.5})\mathrm{d}\eta\mathrm{d}\eta = 0.743 C_m z_m^2. \tag{A7}$$

Appendix C: A Comparison between Three-Equation and Classical Four-Equation Models

According to *Parker et al*. [1986], the self-accelerating currents are wrongly predicted by means of the former classical three-equation models [*Ellison and Turner*, 1959]. On the contrary, they are satisfactorily simulated by introducing the TKE budget equation in the model. In this regard, Figures 7b and 15 are taken from *Parker et al*. [1986] (see Figures C1 and C2, respectively) to assess the performance of the three-equation model of this study. Figure C1 shows the development of the turbidity current characteristics from *ignition*. The term *ignition* in turbidity current is defined by *Parker et al*. [1986] as the self-acceleration through an entrainment of bed sediment. The curve illustrates how the three-equation model of *Parker et al*. [1986] fails to represent the behaviour of the current. However, the three-equation model of this study does not describe such a rapid increase in the sediment transport as obtained by *Parker et al*. [1986]. In addition, Figure C2 depicts how the present model corresponds to the estimations by four-equation model of *Parker et al*. [1986] rather than to follow the hydraulic jump trend obtained from the classical three-equation model of *Parker et al*. [1986].

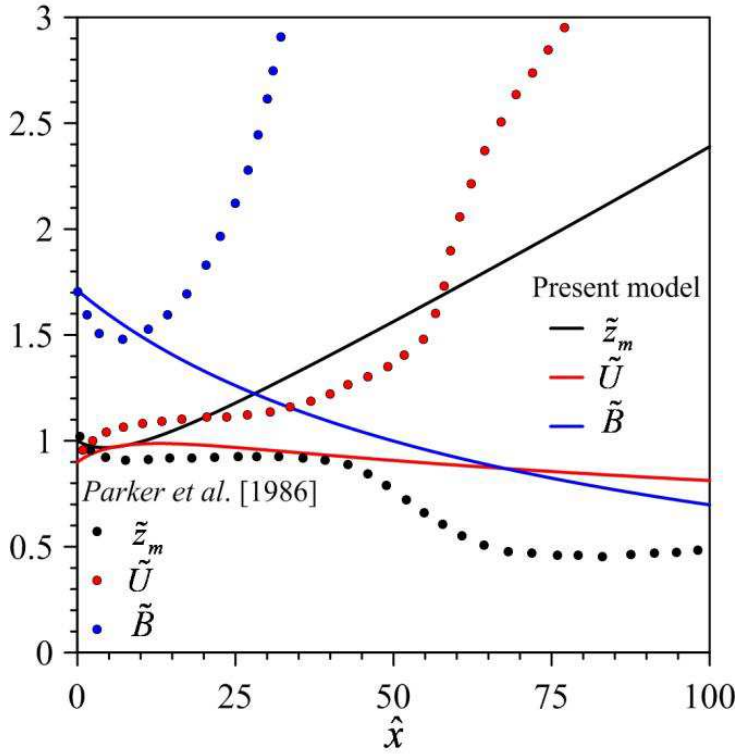

Fig. C1. Variations of $\tilde{z}_m$, $\tilde{U}$, and $\tilde{B}$ with $\hat{x}$ in a turbidity current showing the comparison between the present model and *Parker et al*. [1986].

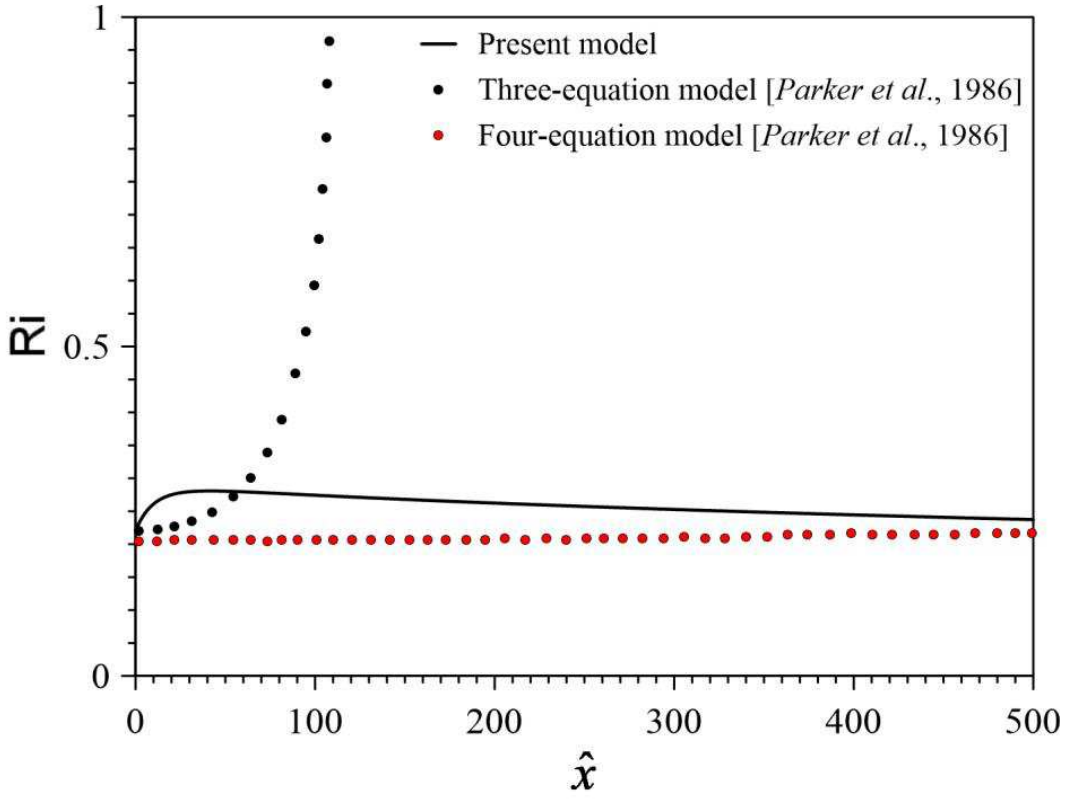

Fig. C2. Variation of Ri with $\hat{x}$ in a turbidity current showing the comparison between the present model and *Parker et al*. [1986].

12. Notation

B = reduced sediment flux

$\tilde{B}$ = nondimensional reduced sediment flux (= B/B_0)

B_0 = initial condition of B

C = depth-averaged concentration

$\hat{C}$ = C/C_m

$\tilde{C}$ = nondimensional depth-averaged concentration (= C/C_0)

C_0 = initial condition of C

C_m = suspended sediment concentration at $\eta = \eta_w$

c = suspended sediment concentration in turbidity current at z

c' = fluctuations of c

$\hat{c}$ = c/C_m

c_0 = sediment concentration at bed

$\hat{c}_0$ = c_0/C_m

c_b = reference sediment concentration

$\overline{c'w'}$ = Reynolds flux of suspended sediment particles

D_b = deposition rate of sediment

d = median size of sediment particles

E_b = erosion rate of sediment

E_s = entrainment coefficient of sediment particles from bed

E_w = entrainment coefficient of ambient fluid

g = gravitational acceleration

I_{1-8} = moments of integral scales

K = level of turbulence

k = turbulent kinetic energy (TKE)

P_T = average TKE production rate

Re_p = particle Reynolds number [= $(\Delta_s g d^3/\upsilon^2)^{0.5}$]

Ri = Richardson number

$\tilde{\mathrm{Ri}}$ = relative Richardson number (= $\mathrm{Ri}/\mathrm{Ri}_0$)

Ri_0 = initial condition of Ri

t = time

U = depth-averaged velocity

$\hat{U}$ = U/U_m

$\tilde{U}$ = nondimensional depth-averaged velocity (= U/U_0)

U_0 = initial condition of U

U_m = maximum velocity

u = streamwise velocity of turbidity current at z

$\hat{u}$ = u/U_m

u_{*b} = shear velocity

w = vertical velocity component

w' = fluctuations of w

w_h = vertical velocity component at top of turbidity current

w_s = terminal fall velocity of suspended sediment particles

x, z = Cartesian coordinates

$\hat{x}$ = x/z_{m0}

Z = Rouse number [= $w_s/(\kappa u_{*b})$]

z_m = turbidity current depth

$\tilde{z}_m$ = nondimensional turbidity current depth (= z/z_{m0})

z_{m0} = initial condition of z_m

z_w = position of maximum velocity

α = energy (Coriolis) coefficient

β = momentum (Boussinesq) coefficient

χ, ξ = exponents in velocity distribution

Δ_s = submerged relative density

ε = TKE dissipation rate

ε_t = turbulent diffusivity

$\hat{\varepsilon}_t$ = $\varepsilon_t/(ku_{*b}z_m)$

$\Gamma(s)$ = Euler gamma function

$\Gamma(a, s)$ = incomplete gamma function

η = z/z_m

η_w = z_w/z_m

κ = von Kármán constant

λ, ϕ, ζ = unknown parameters in concentration distribution

λ_D = Darcy-Weisbach friction factor

θ = streamwise bed slope

ρ = mass density of fluid-sediment mixture [= $\rho_a + (\rho_s - \rho_a)c$]

ρ_a = mass density of ambient fluid

ρ_s = mass density of sediment particles

σ = coefficient

τ = Reynolds shear stress

$\hat{\tau}$ = $\tau/(\rho u_{*b}^2)$

$\tilde{\tau}$ = $\hat{\tau}$ (u_{*b}/U_m)

υ = kinematic viscosity of fluid

13. References

Ahrens, J. P. (2000), A fall-velocity equation, *J. Waterw. Port Coastal Ocean Eng.*, *126*(2), 99–102.

Akiyama, J., and H. Stefan (1985), Turbidity current with erosion and deposition, *J. Hydraul. Eng.*, *111*(12), 1473–1496, doi: 10.1061/(ASCE)0733-9429(1985)111:12(1473).

Altinakar, M. S., W. H. Graf, and E. J. Hopfinger (1993), Water and sediment entrainment in weakly depositing turbidity currents on small slopes, in *Proceedings of the 5th Congress*, Int. Assoc. Hydraul. Res., vol. 2, Tokyo, Japan.

Altinakar, M. S., W. H. Graf, and E. J. Hopfinger (1996), Flow structure in turbidity currents, *J. Hydraul. Res.*, *34*(5), 713–718, doi: 10.1080/00221689609498467.

Ashida, K., and S. Egashira (1975), Basic study on turbidity currents, *Trans. Jpn. Soc. Civ. Eng.*, *237*, 37–50.

Bagnold, R. A. (1962), Auto-suspension of transported sediment; turbidity currents, *Proc. R. Soc. London, Ser. A*, *265*(1322), 315–319.

Bonnefille, R., and J. Goddet (1959), Etude des courants de densité en canal, in *Proceedings of the 8th Congress*, Int. Assoc. Hydraul. Res., vol. 2, Montreal, Canada.

Chang, H. K., and J. C. Liou (2001), Discussion of 'The fall-velocity equation', *J. Waterw. Port Coastal Ocean Eng.*, *127*(4), 250–251.

Dey, S. (2014), *Fluvial hydrodynamics: Hydrodynamic and sediment transport phenomena*, Springer, Berlin.

Dey, S., T. K. Nath, and S. K. Bose (2010), Submerged wall jets subjected to injection and suction from the wall, *J. Fluid Mech.*, *653*(June), 57–97, doi: 10.1017/S0022112010000182.

Dietrich, W. E. (1982), Settling velocity of natural particles, *Water Resour. Res.*, *18*(6), 1615–1626, doi: 10.1029/WR018i006p01615.

Dutta, S., C. Pantano-Rubino, M. I. Cantaero, M. H. Garcia, and G. Parker (2012), Effects of self-stratification on turbidity currents: A large eddy simulation

approach, in *Proceedings of the XIX International Conference on Water Resources*, pp. 1–10, University of Illinois at Urbana-Champaign.

Ellison, T. H., and J. S. Turner (1959), Turbulent entrainment in stratified flows, *J. Fluid Mech.*, *6*(3), 423–448, doi: 10.1017/S0022112059000738.

Felix, M. (2001), A two-dimensional numerical model for a turbidity current, in *Particulate gravity currents*, edited by W. McCaffrey, B. Kneller, J. Peakall, special publication, International Association of Sedimentologists, *31*, 71–81.

Fukushima, Y., G. Parker, and H. M. Pantin (1985), Prediction of ignitive turbidity currents in Scripps submarine canyon, *Mar. Geol.*, *67*(1–2), 55–81, doi: 10.1016/0025-3227(85)90148-3.

García, M. H. (1993), Hydraulic jumps in sediment-driven bottom currents, *J. Hydraul. Eng.*, *119*(10), 1094–1117, doi: 10.1061/(ASCE)0733-9429(1993)119:10(1094).

Graf, W. H. (1971), *Hydraulics of sediment transport*, McGraw-Hill, New York.

Graf, W. H., and M. S. Altinakar (1998), *Fluvial hydraulics*, John Wiley and Sons, New York.

Guo, J. (2002), Logarithmic matching and its applications in computational hydraulics and sediment transport, *J. Hydraul. Res.*, *40*(5), 555–565, doi: 10.1080/00221680209499900.

Hallermeier, R. J. (1981), Terminal settling velocity of commonly occurring sand grains, *Sedimentology*, *28*(6), 859–865, doi: 10.1111/j.1365-3091.1981.tb01948.x.

Hu, P., Z. Cao , G. Pender, and G. Tan (2012), Numerical modelling of turbidity currents in the Xiaolangdi reservoir, Yellow River, China, *J. Hydrol.*, *464–465*, 41–53, doi: 10.1016/j.jhydrol.2012.06.032.

Hu, P., T. Pähtz, and Z. He (2015), Is it appropriate to model turbidity currents with the three-equation model? *J. Geophys. Res.*, *120*, 1153–1170. doi: 10.1002/2015JF003474.

Inman, D. L., C. E. Nordstrom, and R. E. Flick (1976), Currents in submarine canyons: an air-sea-land interaction, *Annu. Rev. Fluid Mech.*, *8*, 275–310, doi: 10.1146/annurev.fl.08.010176.001423.

Islam, M. A., and J. Imran (2010), Vertical structure of continuous release saline and turbidity currents, *J. Geophys. Res.*, *115*, C08025, doi: 10.1029/2009JC005365.

Lai, Y., J. Huang, and K. Wu (2015), Reservoir turbidity current modeling with a two-dimensional layer-averaged model, *J. Hydraul. Eng.*, 04015029, doi: 10.1061/(ASCE)HY.1943-7900.0001041.

Launder, B. E., and D. B. Spalding (1972), *Mathematical models of turbulence*, Academic press, New York.

Lizhong, Y., Y. Junqi, and W. Yafei (2011), Simulation of gravity currents using the thermal lattice Boltzmann method, *Int. J. Numerical Methods Fluids*, *66*(9), 1174–1182, doi: 10.1002/fld.2308.

Mahdinia, M., B. Firoozabadi, M. Farshchi, A. G. Varnamkhasti, and H. Afshin (2011), Large eddy simulation of lock-exchange flow in a curved channel, *J. Hydraul. Eng.*, *138*(1), 57–70, doi: 10.1061/(ASCE)HY.1943-7900.0000482.

Mastbergen, D. R., and J. H. Van Den Berg (2003), Breaching in fine sands and the generation of sustained turbidity currents in submarine canyons, *Sedimentology*, *50*(4), 625–637, doi: 10.1046/j.1365-3091.2003.00554.x.

Normark, W. R., and F. H. Dickson (1976), Man-made turbidity currents in Lake Superior, *Sedimentology*, *23*(6), 815–831, doi: 10.1111/j.1365-3091.1976.tb00110.x.

Nourmohammadi, Z., H. Afshin, and B. Firoozabadi (2011), Experimental observation of the flow structure of turbidity currents, *J. Hydraul. Res.*, *49*(2), 168–177, doi: 10.1080/00221686.2010.543777.

Parker, G., M. H. Garcia, Y. Fukushima, and W. Yu (1987), Experiments on turbidity currents over an erodible bed. *J. Hydraul. Res.*, *25*(1), 123–147, doi: 10.1080/00221688709499292.

Parker, G., Y. Fukushima, and H. M. Pantin (1986), Self-accelerating turbidity currents, *J. Fluid Mech.*, *171*(October), 145–181, doi: 10.1017/S0022112086001404.

Piper, D. J. W., P. Cochonat, and M. L. Morrison (1999), The sequence of events around the epicentre of the 1929 Grand Banks earthquake: initiation of debris flows

and turbidity current inferred from sidescan sonar, *Sedimentology*, *46*(1), 79–97, doi: 10.1046/j.1365-3091.1999.00204.x.

Pratson, L. F., J. Imran, G. Parker, J. P. M. Syvitski, and E. Hutton (2000), Debris flows vs. turbidity currents: a modeling comparison of their dynamics and deposits, in *Fine-grained turbidite systems*, edited by A. H. Bouma and C. G. Stone, *Am. Assoc. Petrol. Geol.*, Memoir 72, special publication 68, 57–71.

Prestininzi, P., G. Sciortino, and M. L. Rocca (2013), On the effect of the intrinsic viscosity in a two-layer shallow water lattice Boltzmann model of axisymmetric density currents, *J. Hydraul. Res.*, *51*(6), 668–680, doi: 10.1080/00221686.2013.819532.

Rouse, H. (1937), Modern conceptions of the mechanics of turbulence, *Trans. Am. Soc. Civ. Eng.*, *102*(1), 463–505.

Sequeiros, O. E., B. Spinewine, R. T. Beaubouef, T. Sun, M. H. García, and G. Parker (2010), Characteristics of velocity and excess density profiles of saline underflows and turbidity currents flowing over a mobile bed, *J. Hydraul. Eng.*, *136*(7), 412–433, doi: 10.1061/(ASCE)HY.1943-7900.0000200.

Shringarpure, M., M. I. Cantero, and S. Balachandar (2012), Dynamics of complete turbulence suppression in turbidity currents driven by monodisperse suspensions of sediment, *J. Fluid Mech., 712*(December), 384–417, doi: 10.1017/jfm.2012.427.

Stacey, M. W., and A. J. Bowen (1988), The vertical structure of density and turbidity currents: theory and observations, *J. Geophys. Res.*, *93*(C4), 3528–3542, doi: 10.1029/JC093iC04p03528.

Stefan, H. (1973), High concentration turbidity currents in reservoirs, in *Proceedings of the 15th Congress*, Int. Assoc. Hydraul. Res., pp. 341–352, Istanbul, Turkey.

Sumner, E. J., and C. K. Paull (2014), Swept away by a turbidity current in Mendocino submarine canyon, California, *Geophys. Res. Lett.*, *41*(21), 7611–7618, doi: 10.1002/2014GL061863.

Turner, J. S. (1973), *Buoyancy effects in fluids*, Cambridge University Press, Great Britain.

Wang, H., N. Bi, Y. Saito, Y. Wang, X. Sun, J. Zhang, and Z. Yang (2010), Recent changes in sediment delivery by the Huanghe (Yellow River) to the sea: causes and

environmental implications in its estuary, *J. Hydrol.*, *391*(3–4), 302–313, doi:10.1016/j.jhydrol.2010.07.030.

Wu, W. (2008), *Computational river dynamics*, Taylor and Francis, London.

Wu, W., and S. S. Y. Wang (2006), Formulas for sediment porosity and settling velocity, *J. Hydraul. Eng.*, *132*(8), 858–862, doi: 10.1061/(ASCE)0733-9429(2006)132:8(858).

Zhang, R. J., and J. H. Xie (1993), *Sedimentation research in China*: *Systematic selections*, China Water and Power Press, Beijing.